Effect of Milling on Size Reduction and Microstructural Changes to Gamma-Alumina

Sandra Rutendo Chauruka

Submitted in accordance with the requirements for the degree of

Doctor of Philosophy

The University of Leeds

Institute of Particle Science and Engineering

School of Chemical and Process Engineering

October 2015

Declaration.

The candidate confirms that the work submitted is her own, except where work which has formed part of jointly authored publications has been included. The contribution of the candidate and the other authors to this work has been explicitly indicated below. The candidate confirms that appropriate credit has been given within the thesis where reference has been made to the work of others. Chapter 4 is based on work from a jointly authored publication. The work in this publication is attributable to the author of this thesis and contribution of other authors was in the way of proof reading and corrections.

Title of publication: Effect of mill type on the size reduction and phase transformation of gamma-Alumina

Name of authors: S.R. Chauruka, A. Hassanpour, R. Brydson, K.J. Roberts, M. Ghadiri and H. Stitt

Date of publication: 29 September 2015

Journal details: Chemical Engineering Science, Volume 134, Pages 774–783

Sandra R. Chauruka October 2015

Acknowledgements

Special thanks to my supervisors Dr Ali Hassanpour, Professor Rik Brydson and Professor Kevin Roberts for their advice and input throughout the course of this project. I am also grateful to Professor Mojtaba Ghadiri for acting as a consultant in this project and assisting with advice and guidance.

I would like to thank the EPSRC for project funding and access to solid state Nuclear Magnetic Resonance at Durham University. I would also like to thank Johnson Matthey for project funding top up as well as support throughout the project in the way of quarterly project meetings and access to planetary ball milling and characterisation methods.

Special thanks is also extended to the University of Leeds microscopy group for use of transmission electron microscopy and scanning electron microscopy. I would also like to thank Suzanne Patel and Particles CIC laboratory for use of BET nitrogen adsorption. Many thanks to Simon Lloyd and all the technicians at the University of Leeds for advice on many occasions as well as practical help.

I would also like to extend gratitude to Professor Junya Kano, Dr Colin Hare and Dr Ali Hassanpour for assisting with Discrete Element Method simulation results on the planetary ball mill and the single ball mill.

I am very grateful to my family, particularly Grace Chauruka, my mother and Jonisayi Chauruka my brother, for all the support from the beginning to the end of this project.

Special thanks to my husband Walter Hama for cheering me on to the finish of this project. Without his support, completion would have not been possible.

Dedication

This thesis is dedicated to my late father, Edson Chauruka (1957-1999), who at birth, saw the potential in me and never ceased to reiterate it in the time I spent with him. This thesis is also dedicated to my husband, Walter Hama and my unborn baby Nia-Louise Hama.

Abstract

This thesis sets out to evaluate the effects of milling on the microstructural changes to gamma-Alumina, a well-used catalyst support. It reviews the literature as it relates to the characterisation that has been done so far on this material, different milling methods and effects of milling.

The review section considers the strengths and weaknesses of previous work in the areas of structural characterisation of gamma-Alumina as well as reports on the effects of milling of the material with particular interest in size reduction and phase transformation.

Working from the base of current knowledge, experiments that can fill in the gap identified from the review are designed. The material under investigation is characterised as received for particle size and morphology and this gives a base for further experimental investigations.

Various experiments are designed centred around exposure of gamma-Alumina to different milling conditions. These include the use of different mills, variation of milling conditions and isolation of stress modes. Furthermore, results from Discrete Element Method simulations of one selected mill, provided by Professor Junya Kano of Tohoku University in Japan are analysed for energy quantification. Data processing of the results of the operation of a second mill, simulated by Discrete Element Method at the University of Leeds by Dr Colin Hare and Dr Ali Hassanpour is also used to quantify energies associated with the milling process.

It is concluded that microstructural changes to gamma-Alumina are very much energy driven processes. The jet mill has proven a worthy candidate for size reduction in small scale processes. The size reduction analysis shows that gamma-Alumina requires the presence of a dispersive agent such as water or compressed air for efficient size reduction. The characterisation work combined with the simulation results show that the amount of energy dissipated into the microstructure of gamma-Alumina during a collision governs the extent of microstructural effects.

Results also show that with the supply of different energies to milling processes, mechanical energy can achieve a phase transformation from gamma-Alumina to alpha-Alumina similar to that achieved by calcination where delta-alumna and theta-Alumina are observed as intermediate phases. Simulation also provides a tool for prediction and selection of milling processes appropriate for the required end product.

Table of Contents

List of Tables

List of Figures

Abbreviations

DEM	Discrete element method
HRTEM	High resolution transmission electron microscopy
XRD	X-ray diffraction
BET	Brunauer, Emmett and Teller method
TEM	Transmission electron microscopy
IR	Infra-red
NMR	Nuclear magnetic resonance
NVS	Neutron vibrational spectroscopy and
PGAA	Prompt gamma activation analysis
SAXS	Small angle x-ray scattering
Al	Aluminium
BPR	Ball-to-powder ratio
PCA	Process control agent
FCC	Face centred cubic
BCC	Body centred cubic
HCP	Hexagonal close packed
DTA	Differential thermal analysis
SAED	Selected area electron diffraction
HR	High resolution
TGA	Thermogravimetric analysis
DSC	Differential scanning calorimetry
FTIR	Fourier transformed infra-red
SEM	Scanning electron microscopy
SSA	Specific surface area
PSD	Particle size distribution
ICDD	International centre for diffraction data
FWHM	Full width a half maximum intensity
ZB	Zirconia ball
SBM	Single ball mill
PBM	Planetary ball mill
JM	Jet mill
SSV	Stainless Steel vessel
SLR	Solids-liquid ratio
SSB	Stainless Steel ball
AlV	Aluminium vessel
CCP	Cubic close packed
MAS	Magic Angle Spinning
D_N	Nth particle
F	Force
Λ	gamma
A	alpha
Θ	theta
Δ	delta
Al_2O_3	Alumina
H_V	Vickers hardness

Notation

Measurement

nm	Nanometre
mm	Millimetre
μm	micrometre
in	Inches
ml	Millilitres
L	Litres
g	Grams
min	Minutes
m	Metres
J	Joules
^oC	Degrees Celsius
K	Kelvin
kJ	Kilojoules
kg/hr	kilograms per hour
lb/hr	pounds per hour
m^2/g	specific surface area
MPa	megapascal
pH	degree of acidity
g/l	grams per litre
kV	Kilovolt
cm^3/g	cubic centimetre per gram
D	Diameter
ρ	Density
kN	kilo newtons
N	Newtons
hr	Hour
g/cm^3	grams per cubic centimetre
s	Seconds
GPa	gigapascals
MPa	megapascals

Mill Parameters

N_b	number of balls
D_b	diameter of balls
ρ_b	density of milling balls
W_p	rotational speed of mill disc
W_v	vial rotational speed
D_v	diameter of vial
h_v	height of vial
rpm	revolutions per minute
D_0	particle size before milling
D_t	particles size at time t
D_l	limit of particle size

Mill Parameters

K_p	milling rate constant
W	mass of sample
r_B	radius of milling balls
μ	coefficient of frition
E_i	impact energy of milling balls
υ_r	velocity of collisions
F_n	forces acting on collisions
n	number of collisions
E_w	specific impact energy
h	height of pot
d_m	diameter of pot
Vm	volume of pot
R	revolution radius
r	rotation to revolution speed ratio
N_f	revolution speed
t_i	cumulative time of impact energy
f	specified frequency
m_p	powder weight
u	relative displacement

Crystallographic

$D_{crystallite}$	diameter of crystallite
k	bragg constant
FWHM	full width at half maximum
h k l	crystal planes
d-spacing	spacing between crystal planes
n	order of reflection of x-rays
λ	wavelength of x-rays
θ	bragg angle

Adsorption

S_t	total surface area of adsorbate
A_x	cross sectional area of adsorbate
$\bar{m}$	adsorbate molecular weight
p	equilibrium pressure
p_0	saturation pressure at adsorbate temperature
W	quantity of adsorbed gas
W_m	quantity of adsorbed gas in monolayer
C	bet constant
E_1	heat of adsorption of first layer
E_L	het of adsorption of second layer
s	slope of bet plot
i	intercept of bet plot

Chapter 1

Introduction

An introduction into the research project is given, which includes background of the work, the research question, objectives and methodology used. The Chapter also gives information on how the project was managed as well as the structure of the thesis.

1 Introduction

1.1 Background of Research

When chemical reactions occur, new materials are formed from the precursors. The chemical reaction may occur at a very slow rate or require certain conditions such as very high temperature and pressure, making it sometimes not feasible. Catalysts are materials that can help to overcome these barriers and make the reaction either feasible or more efficient and eventually, can reduce costs. Catalysts come in many forms and can exist as solid, liquid or gas depending on the reaction they are to be used in. The amount of catalyst required for any reaction is dependent on the kinetics of the reaction.

There are many applications for catalysts including the automotive and the process industries. Catalyst supports are materials that are used to carry a catalyst before its usage. The catalyst is usually embedded or adsorbed onto the catalyst support by a number of methods. The catalyst support under investigation in this work is gamma-Alumina and is used as a support for various catalysts. A suitable catalyst support should have desirable surface and crystalline properties that can result in the catalyst attaching to its surface. These properties can include good pore volume and pore size distributions as well as favourable arrangement of atoms in the crystal structure that allows attachment of a catalyst to its surface. The choice of a catalyst support is dependent on the type of catalyst to carry. Gamma-Alumina is used as either a catalyst itself or catalyst support.

In this work, the focus is on its use as a catalyst support. Gamma-Alumina has desirable properties because in addition to its low cost and high mechanical strength, it also has high surface area and good pore volume and pore size distribution. This allows the embedding catalyst to penetrate rapidly and uniformly into the catalytic sites. The typical individual grain sizes of gamma-Alumina in the micro-aggregates used in commercial applications ranges from 5 to 50 nanometres (Sinkler *et al.*, 2006). Figure 1.1 below shows a schematic of the use of gamma-Alumina as a catalyst support.

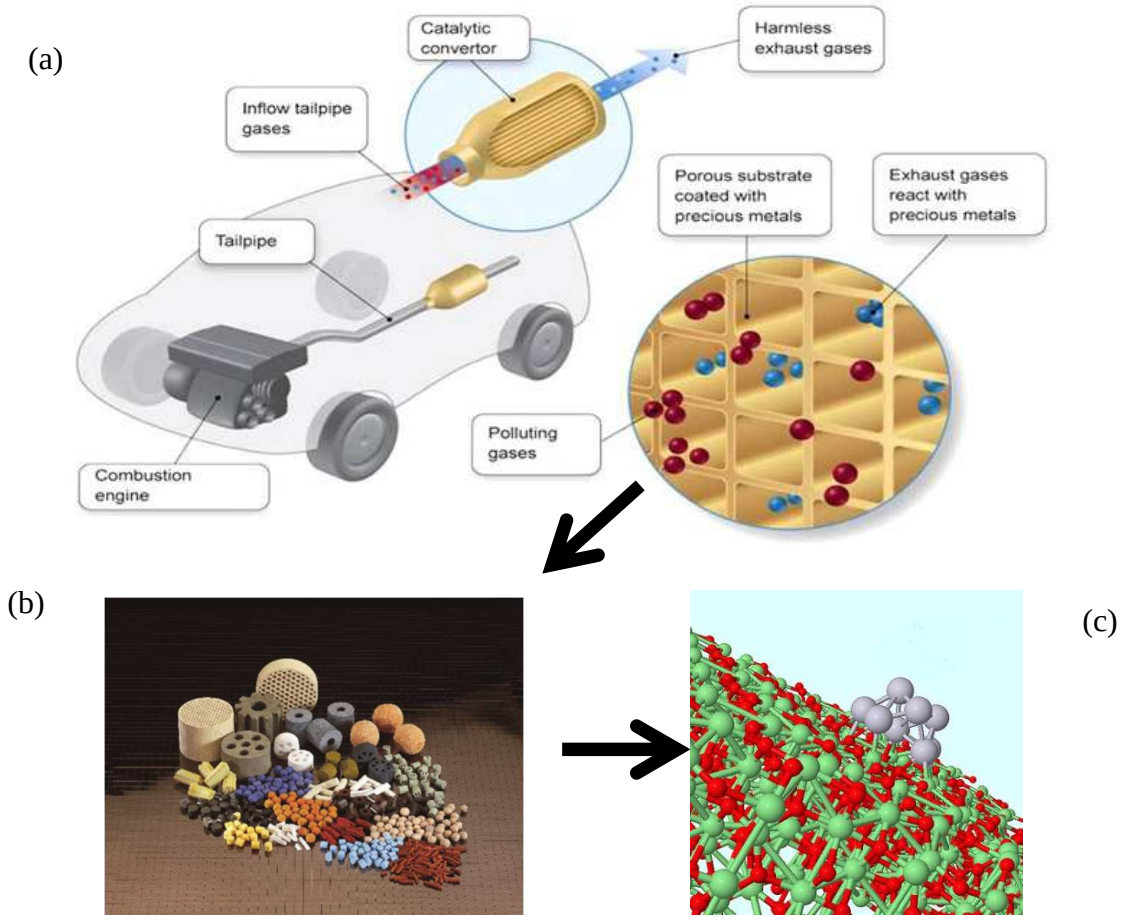

Figure 1.1: Schematic of the use of gamma-Alumina as a catalyst support showing (a) the use of a catalytic converter in fuel combustion with an insert showing the substrate with catalyst support and catalyst (Umicore Precious Metals Refining, 2015), (b) the substrates with walls coated with catalyst support and catalysts (Lloyd, 2011) and (c) a layer of gamma-Alumina catalyst support with a platinum catalyst embedded on the surface (Argonne National Laboratory, 2009)

Gamma-Alumina is prepared to the desirable particle size by milling. However, in addition to the particle size, the desired properties of the final product are not always consistent and as expected. These properties include the physical and morphological properties that affect the material's end use as a catalyst support. During size reduction, the crystalline structure of gamma-Alumina is affected and this in turn alters the characteristics of the material. The microscopic changes that occur to the material due to the milling process are however not well understood.

There is also a lack of information in the literature on the effect of milling on the aforementioned properties and as a result, finding the most appropriate milling device and the process conditions is highly empirical, time consuming and expensive. If the effect of milling on the material properties of the product is established, this would eliminate the

lengthy empirical approach in the selection of the milling conditions. The main motivation for this research work is to find a correlation between the milling process conditions and the final milled product properties. This correlation coupled with the creation of a predictive model of the milling process using DEM can offer better control of the process.

1.2 Scope of work

The lack of information on the actual interactions of the milled material with the mill during process runs brings about a deductive reasoning approach where the theory states that the energy has an effect on the physical properties of the material but the actual energies involved and the interactions are not well understood. A hypothesis can be extracted that assumes that if the energy supplied into the material during milling is known and its effect is observed, a relationship between energy and property changes can be formulated. With this in mind, it brings about a single question that underpins the entirety of this work;

'What are the physical property effects of different mills and milling variables on the product and how can these effects be related to the energy supplied by milling?'

An attempt to fully answer the research question is displayed in this thesis by way of meeting the following objectives;

i. Characterising the particle size and particle shape, available surface area and crystal structure before and after milling
ii. Determining the range of impact energies that occur during milling
iii. Formulating a mechanistic relationship between the milling environment and the physical properties of the milled product

The methodology chosen for fulfilling the research question and subsequent objectives involves a four step process; milling of the material→ characterisation of product physical properties → modelling of milling parameters → determination of relationship between product properties and milling parameters. This approach employs characterisation methods such as XRD and laser diffraction to analyse milling effects on the physical properties of the material after size reduction using different milling techniques such as planetary ball milling and air jet milling. Simulation of some of the employed milling techniques by Discrete Element Method will supply a range of impact energies within the mill that can be related to the milling effects observed by characterisation. This methodology explores a new area of research which relates milling process conditions with product properties through direct

knowledge of the mechanical energies supplied. Figure 1.2 shows a project map of how the objectives will be fulfilled.

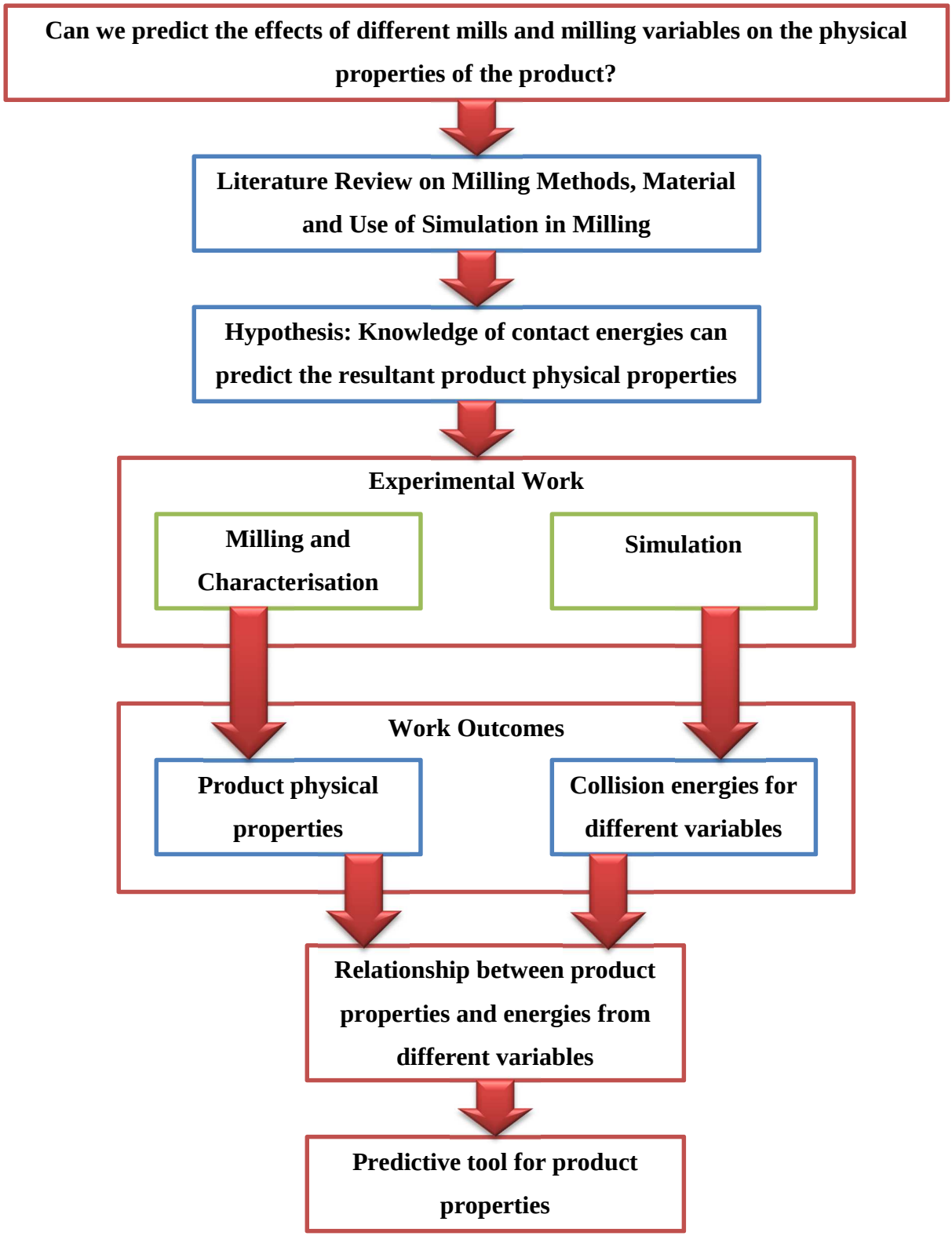

Figure 1.2: Project map showing how objectives are met in the thesis

1.3 Project Management

The research is an Engineering and Physical Sciences Research Council (EPSRC) funded project with Johnson Matthey as an industrial sponsor. The funding for the project from Johnson Matthey was under the direction of Dr. Dave Thompsett. The majority of the experimental work was carried out at the University of Leeds. The main supervisor was Dr Ali Hassanpour with Professor Kevin John Roberts and Professor Richard Drummond-Brydson as co-supervisors and Professor Mojtaba Ghadiri as a consultant.

The industrial mentors from Johnson Matthey in charge of the project were Dr. Hugh Stitt and Dr. Alison Wagland. Some milling experiments were carried out at Johnson Matthey's Chilton site in Billingham under the supervision of Dr. Michele Marigo. Other milling experiments were carried out at Johnson Matthey Technology Centre in Reading under the supervision of Dr. Jose Villoria and Dr. Jhonny Rodriguez. Characterisation work was also carried out at the same site under the supervision of Dr. Dogan Ozkaya. All modelling simulations of the planetary ball mill were carried out by Dr. Junya Kano at Tohoku University in Japan.

Quarterly meetings were held in each year of the life of the project at different locations. A presentation was prepared for every meeting. Work carried out in the three months before the meeting was presented and new objectives were set for the following three months.

1.4 Structure of the Thesis

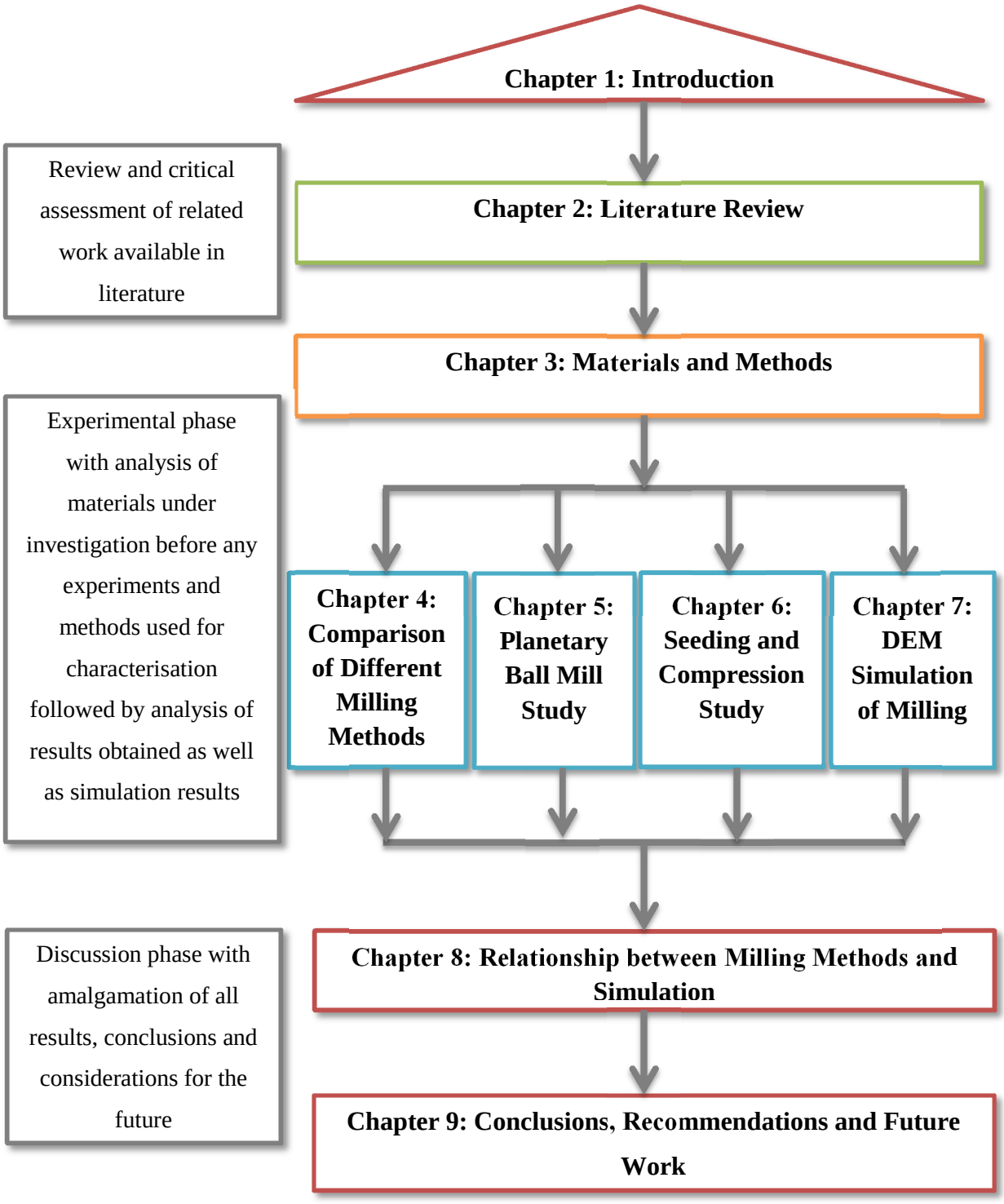

Figure 1.3: Structure of thesis with interlinking showing relationships of chapters

The contents of the thesis structure diagram in Figure 1.3 can be briefly described as follows; *Chapter 2* consists of a literature review on all topics that are relevant to the work carried out.

The chapter is composed of three main areas for review; properties and characterisation of the material under investigation, milling methods and reported effects of milling the material.

Chapter 3 presents detailed characterisation on the properties of the material under investigation in this project. Characterisation methods selected for use are briefly described. Preparation of gamma-Alumina samples for characterisation and the main findings on the particle size, surface area and crystal morphology of the material under investigation are presented.

Chapter 4 consists of a comparison of three selected milling methods; jet milling, single ball milling and planetary ball milling. The effect of these mills on the properties of the material under investigation such as particle size, surface area and crystal morphology is examined.

Chapter 5 builds on the observations in *Chapter 4* of the planetary ball mill samples. It provides a detailed analysis of the phase change observed during initial milling investigations in *Chapter 4*. Milling using the planetary ball mill is investigated further by a variation of milling process conditions to derive the effect of the stress mode provided by the planetary ball mill on the properties of the material under investigation. The effect of milling aids is also investigated in this chapter.

Chapter 6 is made up of two main sections; seeding experiments and compression testing. The effect of planetary ball milling in the presence of corundum Alumina is investigated along with the effect of compression by mimicking impact energy effects observed in *Chapter 5*.

Chapter 7 provides the range of impact energies involved during milling in the single ball mill and planetary ball mill. The experimental findings on how the different mills affect the properties of the material under investigation are related to the impact energies dissipated during milling.

Chapter 8 serves to amalgamate the results of the entire project and provides a simplified explanation of how to relate the changes to properties observed in gamma-Alumina with the stress modes imposed by different mills and the impact energies provided by the mills. The chapter serves to unify all the results presented in previous chapters and *Chapter 9* serves to provide recommendations for milling gamma-Alumina as well as future work that can be carried out as the aim of this research work is to understand how milling affects the properties of gamma-Alumina.

Chapter 2

Literature Review

A summary of the literature available on how gamma-Alumina is derived from its precursors, the structure of the material and milling work that has been carried out on gamma-Alumina is presented. Different millings methods are reviewed and a critical analysis of milling effects on gamma-Alumina is outlined. The effect of milling aids is also reviewed before a summary is given.

2 Literature Review on Gamma-Alumina as a Catalyst Support, Milling Methods and Effects of Milling

2.1 Introduction

The most popular application of catalysts to the wider non-scientific community is within the car exhaust system. Although this is true and highlights one application of catalysts, it is important to note that approximately up to 90 % of chemical products are manufactured using a catalytic process (Chorkendorff and Niemantsverdriet, 2006). Examples of chemicals and products common in our daily lives manufactured by the use of catalysts include fertilizers, detergents, plastics, automotive fuels and pharmaceuticals (Somasundaran, 2006). Many other successful applications of catalysts include pollution prevention and reduction. The highly advantageous use of a catalyst is the faster, less energetically involving process route that it provides as opposed to a catalyst-free process (Chorkendorff and Niemantsverdriet, 2006).

The importance of catalysis to human beings does not go even further than our own physical bodies. When food is ingested, required compounds for the function of the human body are extracted from it through the occurrence of chemical reactions within cells. These reactions are made possible by the existence of enzymes; which are molecules that ensure faster rates of reactions within the body (Bettelheim *et al*., 2009). Catalysts can exist as discrete atoms and/or molecules, enzymes or on solid surfaces. Catalysts that exist on solid surfaces require a favourable surface for their attachment known as a catalyst support. Catalyst supports are made up of three parts; a support, a catalytically active phase and a promoter.

The catalytically active phase is the region where the reaction occurs and includes the catalyst itself. Common catalysts include metals, metal oxides and sulphides. The promoter is a material added to the supported catalyst to aid in inhibiting processes that limit the catalyst life cycle as well as to improve properties of the supported catalyst. In order for a material to be classed as a good catalyst support it has to possess properties such as a high surface area, good pore volume and pore size distribution, high degree of purity, good thermal stability and good chemical stability (Regalbuto, 2006). These properties determine the success of their use in reactions e.g. a highly porous support with a large surface area allows for easy diffusivity of reactants during chemical reactions (Somasundaran, 2006).

The use of a catalysts support also makes economic sense in the use of precious metal catalysts such as platinum and palladium. These materials are embedded on inert catalyst support surfaces as nanometre sized molecules reducing the overall cost of the supported catalyst. The high porosity of the catalyst support is crucial in this case (Chorkendorff and Niemantsverdriet, 2006). Supported catalysts come in many different shapes and forms; spheres, pellets, aggregates or honeycomb substrates and some of these examples are shown in Figure 2.1 (Somasundaran, 2006).

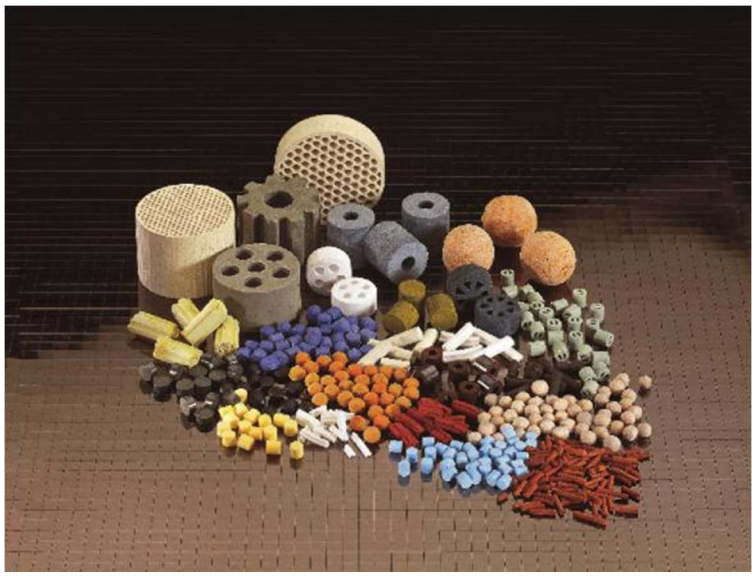

Figure 2.1: Different types of supported catalysts (Lloyd, 2011)

The support; which we are particularly interested in in this project, can be made from different materials such as Alumina, magnesia, silicates, Zirconia, titania and other metal oxides. Where a catalyst is highly active, lower surface area supports may be required and therefore catalyst support selection is governed by the end use of the supported catalyst (Somasundaran. 2006). This project is centred on the use of gamma-Alumina as a catalyst support.

Alumina is used as a coating for the substrate and both the coating and the substrate make up the catalyst support. The substrate is usually a honeycombed and thin walled structure which is immersed into the Alumina slurry to apply the coating, air dried to remove excess coating, dried and calcined before end usage. The Alumina slurry has to have high solids content, i.e. large amount of solids per every part liquid. Viscosity is also very important to aid adhesion of the Alumina to the substrate as well as to achieve high Alumina slurry loadings (Blachou *et al*., 1992). According to Dwyer and Pesansky (1975) Alumina slurry with good adherence to substrate can be made by mixing 45 to 70 weight percent Alumina trihydrate with 4 to 18

weight percent polysiloxane resin and 18 to 35 weight percent toluene. This was done for 12 hours and was used to coat a ceramic honeycombed structure with 20 channels per square inch (Blachou *et al.*, 1992).

The project also covers particular interest on how milling as a manufacturing route, affects the end properties of the support. It is therefore necessary to understand the existence of gamma-Alumina, its properties, how milling may affect them and to determine the most suitable manufacturing routes of the material. This chapter focuses on work that has been carried out related to properties of gamma-Alumina, effects of milling on the material, different suitable milling methods as well as how a better understanding of the gamma-Alumina can contribute to selection of better milling processes for the material.

2.2 Gamma-Alumina as a Catalyst Support

2.2.1 Production of Transition Aluminas from Bauxite Ore

Gamma-Alumina is part of a family of different Alumina phases called the transition Aluminas. In order to fully understand the structure of gamma-Alumina, it is important to look into the synthesis of the material from its precursor. Gamma-Alumina is derived from boehmite, an Alumina hydrate. There are several types of Alumina hydrates which include gibbsite, bayerite, boehmite and diaspore. The precursors themselves are derived from bauxite, which is the mineral ore mined from the ground. Bauxite exists as a soft red clay composed of Alumina, ferric oxide, titania, silica and calcia. The Bayer process is used to extract Alumina hydrates from bauxite. It can be seen in Figure 2.2 that the different Alumina hydrate phases exhibit different properties in terms of their crystal structures and mechanical properties such as hardness (Cardarelli, 2008).

Phase	Chemical formula	Crystal system	Therm. stability range	Density ($kg.m^{-3}$)	Mohs hardness	Tenacity	Average refractive index (n_D)
Gibbsite (hydrargillite)	α-$Al(OH)_3$	Monoclinic	<100	2420	2.5–3.5	Tenacious	1.57–1.59
Bayerite	β-$Al(OH)_3$	Monoclinic	<100	2530	n.d.	Tenacious	1.58–
Nordstrandite	γ-$Al(OH)_3$	Triclinic		2450	3		1.590
Boehmite	γ-AlO(OH)	Orthorhombic	100-350	3010	3.5–4	Highly tenacious	1.65–1.67
Diaspore	α-AlO(OH)	Orthorhombic	100–350	3440	6.5–7	Brittle	1.70–1.75

Figure 2.2: Properties of different Alumina hydrates (Cardarelli, 2008)

In order to derive the transition Aluminas, the Alumina hydrates are calcined to temperatures of up to 1100^{o}C to 1400^{o}C. Each type of hydrate yields alpha-Alumina as the final stable phase. As shown in Figure 2.3, between the hydrate and alpha-Alumina, many different Alumina phases exist and the calcined hydrate determines the phases existent between it and the final alpha-Alumina phase (Cardarelli, 2008).

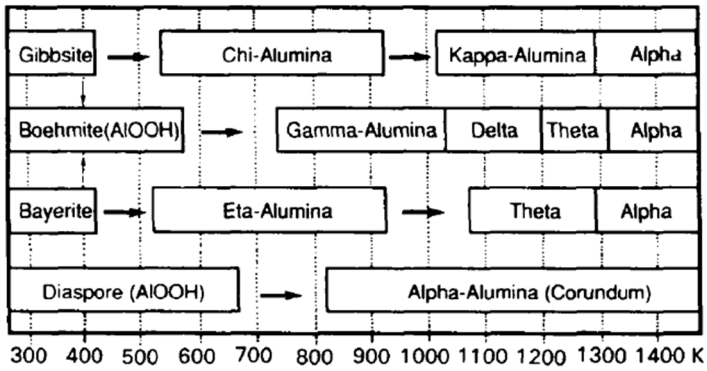

Figure 2.3: The family of transition Aluminas (Zhou *et al.*, 1991)

2.2.2 Properties of Boehmite-Derived Aluminas

Boehmite-derived Alumina can exist in four states which include three transition states; gamma (γ), delta (δ) and theta (θ) and the final thermodynamically stable alpha (α) Alumina. Wang *et al.* (1998) investigated production of transition Aluminas from dehydrating boehmite for use as catalysts and catalyst supports. They observed the production of gamma-Alumina in the ranges of 350^{o} to 700^{o} C as the first transitional phase when boehmite is dehydrated, followed by delta-Alumina at temperatures of 800^{o} to 1000^{o} C followed by theta-Alumina at 1000^{o} to 1200^{o} C and finally the thermodynamically stable structure of alpha-Alumina at temperatures over 1200^{o}C (Wang *et al.*, 1998).

The structure of the transition Aluminas which includes gamma-Alumina have been described to have cubic close packing of oxygen anions and their differences come about in the arrangement of cations in the crystal structure. Theta Alumina was described to be monoclinic in structure and alpha-Alumina was described as rhombohedral. In terms of structure, the changes in structure during dehydration can be attributed to the rearrangement of aluminium ions and the exchange of vacant octahedral and tetrahedral sites. This rearrangement may be driven by configuration entropy minimisation(Wang *et al.*, 1998) . High Resolution Transmission Electron Microscopy (HRTEM) was used in the work by Wang *et al.*, (1998) to show how the ordering of vacant octahedral sites changes among the

transition Aluminas. Figure 2.4 shows vacancies observed and they concluded that vacant aluminium sites were located only on the octahedral sites and none on the tetrahedral sites.

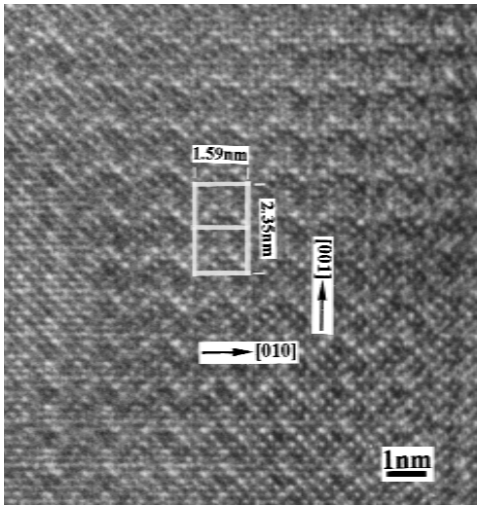

Figure 2.4: HRTEM image of vacancies located on the (011) and (011) planes of Alumina, forming a characteristic zigzag configuration (Wang *et al.*, 1998)

2.2.3 Morphology and Properties of Gamma-Alumina

With the knowledge of how gamma-Alumina is derived from its precursor, it is necessary to analyse existent knowledge on the structure and properties of gamma-Alumina. Knowledge of the structure of the material from other researchers' perspective can provide a platform to begin research activities on the material. When boehmite is calcined, the transformation to gamma-Alumina is topotactic, resulting in a similar cubic close-packed structure as shown in Figure 2.5. Further calcination at higher temperatures of up to 1100°C results in hexagonal close-packed alpha-Alumina.

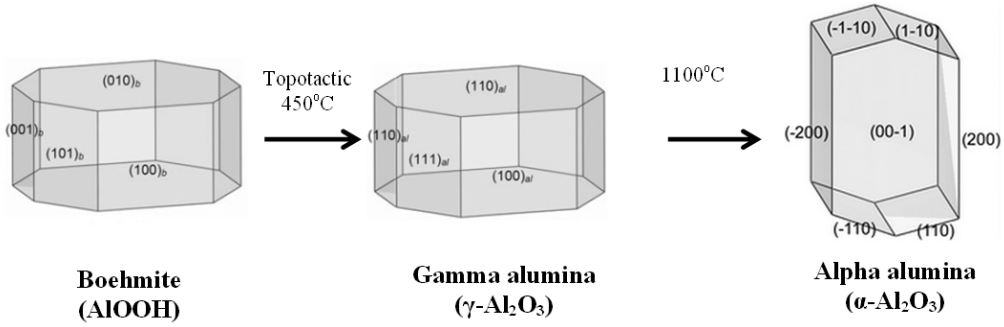

Figure 2.5: Topotactic Transformation of Boehmite to Gamma-Alumina after Calcination at Temperatures of 450°C to 700°C

The transformation from Boehmite to gamma-Alumina occurs by a series of steps of structural transformation. Two major steps are involved in this process which include; an initial collapse of the Boehmite structure followed by hydrogen transfer and water extraction. The transformation is a diffusion controlled mechanism which involves counter-migration of Al cations and protons with the crystallographic formation of voids in a cubic close-packed structure. Gamma-Alumina is finally achieved in this process by gradual filling of tetrahedral cation sites with Aluminium which also results in the formation of vacancies and the existence of Aluminium on both octahedral and tetrahedral sites (Rozita *et al.*, 2013).

Various methods have been used to characterise gamma-Alumina including X-ray diffraction (XRD), BET adsorption, Transmission Electron Microscopy (TEM), Infra-red spectroscopy, Nuclear Magnetic Resonance spectroscopy (NMR), neutron vibrational spectroscopy (NVS), prompt gamma activation analysis (PGAA) and small angle x-ray scattering (SAXS). Despite considerable work that has been done on characterising gamma-Alumina, its structure is still not yet well defined. Gamma-Alumina is often described as a defect spinel and the defect is in the ordering of the cations and the presence of vacancies (Trueba *et al*., 2005). A spinel structure with the formula $MgAl_2O_4$ is a cubic close-packed structure containing 56 atoms (32 oxygen and 24 metal atoms) per unit cell. Gamma-Alumina in turn, contains only $53_{1/3}$ atoms (32 oxygen, $21_{1/3}$ Al and $2_{2/3}$ vacancies) per unit cell (Rozita *et al.*, 2013).

The structure is described to have only trivalent Al cations in the spinel type structure. This means the structure of gamma-Alumina does not completely satisfy the structure of an ideal spinel. Its oxygen atoms are in a lattice that is built by cubic close packed oxygen layers stacked together, while Al atoms occupy the octahedral and tetrahedral sites. This order does not however balance the stoichiometry so the structure also contains vacancies to balance the charge of gamma-Alumina. The ordering of these vacancies is however still not well defined and is attributed to the complexity of the structure of the material (Trueba and Trasatti, 2005). There has been extensive work to determine the structure of gamma-Alumina. Previous work on the material shows that the structure of gamma-Alumina; cubic or tetragonal, is determined by the precursor used.

Sinha *et al*. (1956) reports gamma-Alumina as a cubic spinel and the same is reported by Levin *et al*. (1997) and McPherson (1973). If amorphous boehmite is used, a cubic structure with a tetragonal distortion has been observed (Wilson, 1979), (Wilson *et al*., 1980). A tetragonal structure only was observed by Paglia *et al*. (2004a), Paglia *et al*. (2004b) and Tsuchida *et al*. (1980) and this is in agreement with recent work by Rozita *et al*. (2013). They

observed that the material belongs to the tetragonal space group, $I4_1/amd$. The crystal structure of γ-Al_2O_3 is the main reason why the material is suitable for use as a catalysts support as the vacancies within the material give a desired porous morphology. The presence of these vacancies, as well as the cubic close-packed structure of the material, are crystalline properties worth considering when assessing the effect of mechanical energy on the material. The possibility of shear and diffusional nucleation events due to supplied energy needs to be addressed. Jefferson (2000) studied the surface activity of ultrafine gamma-Alumina particles. TEM revealed that the structure of gamma-Alumina is metal terminated which is unexpected for metal oxides. Rozita *et al* (2013) also observed this. This explains another reason why the material is well suited as a catalyst support as precious metal can easily disperse on its surface. When the catalysts metals are dispersed on the surface of gamma-Alumina, they can dissolve in the metal outer layer which releases aluminium ions that move to the interior of the particle and stabilise the dispersed particle onto its surface (Jefferson 2000). Trueba and Trassati (2005) reviewed aspects to be taken into account on improving the properties of gamma-Alumina as a catalyst support. Gamma-Alumina derived from amorphous precursors is reported to be more thermally stable to temperatures of up to 1200^{o}C. The structure of cubic Gamma-Alumina can be shown in Figure 2.6 below (Trueba and Trasatti, 2005).

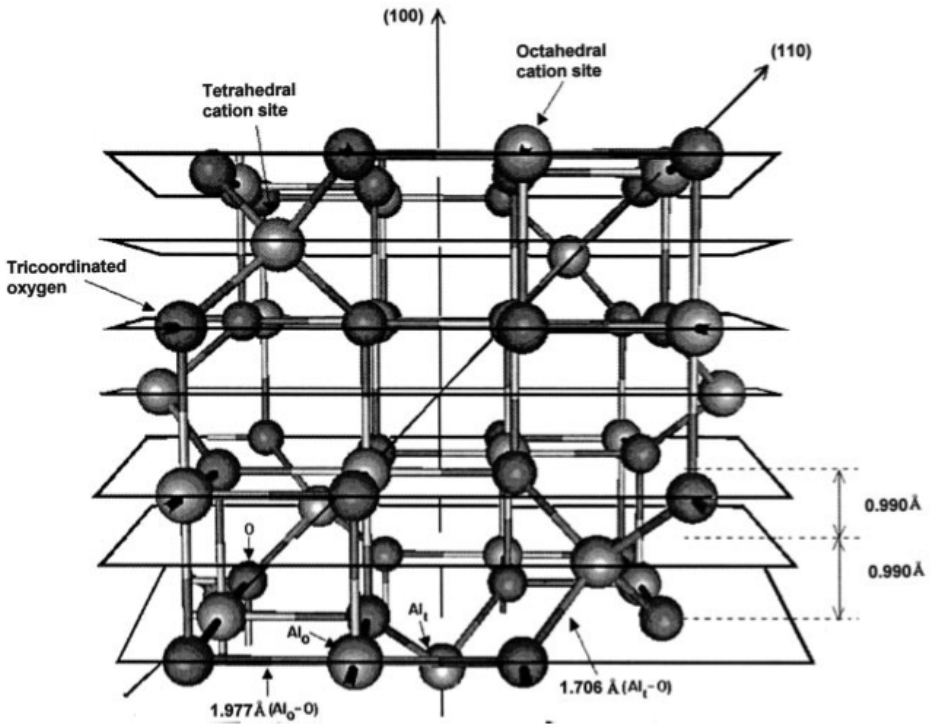

Figure 2.6: Cubic spinel structure of Gamma-Alumina (Trueba and Trasatti, 2005)

Some researchers have reported that there is a small difference between gamma-Alumina and delta-Alumina that is not very distinct and this difference has been described to be in the ordering of the Al atoms and vacancies as gamma- Alumina is described to have vacancies in octahedral and tetrahedral sites whilst delta-Alumina only has vacancies in the octahedral sites (Wilson et al., 1980). With the vast work done on characterising gamma-Alumina some authors have described gamma-Alumina from XRD, NMR and TEM to have vacancies in its octahedral sites (Wang *et al*., 1998), some have disputed this and defined them to be in the tetrahedral sites (Wilson, 1979) whilst other have concluded that they are distributed between tetrahedral and octahedral sites (Wilson *et al*., 1980). The gamma-Alumina structure has also been reported to defeat the spinel type structure by having sites usually vacant in spinel type materials occupied in the gamma-Alumina material (Zhou *et al*., 1991). It has also been reported that the degree of Al content in the Alumina determines the pore size distribution, crystallinity and surface area of the material. A material with a high Al content is more likely to have a high surface area and low crystallinity (Trueba and Trasatti, 2005).

Despite gamma-Alumina existing with a large surface area, there are added advantages with reducing the size of gamma-Alumina particles before catalyst attachment such as an increase in binding sites for the catalyst. In order to achieve the desired particle size, it is important to select a mill that is appropriate for the material especially considering the vast selection of mills available.

2.3 Milling Methods

Size reduction of gamma-Alumina is mainly achieved by wet or dry milling. In the milling process, the particle size is reduced by fracturing under an applied energy. Energy for the process of milling is normally applied by mechanical means. However, the applied energy usually exceeds the energy that is actually required for particle breakage to the desired size by far. This brings about a term called energy utilisation which determines the efficiency of milling processes, representing how much the surface area of particles has increased per unit of required energy for the breakage of particles (Kwan *et al*., 2005).

It is difficult to directly determine the proportion of applied energy in mills which is consumed for particles breakage and one of the reasons is due to the complexity of strain and stress fields and the impact incident energy that every single particle experience in the mill. The impact energies among the particles are widely distributed and hence difficult to

determine. In the work carried out by Kwan *et al*., (2005), it was found that the movement of the ball in a single ball laboratory scale mill is dependent on the milling frequency, ball size, mill orientation and the amount of sample that has been loaded into the mill with the ball (Kwan *et al*., 2005).

The complexity of morphology of particle samples as well as distribution in particles size and material properties affect the mill product even when the same amount of energy is applied to particles. The energy which can be directly used for particle breakage could be as low as 10% of applied energy, due to dissipation of energy as a result of friction, noise, heat and vibration in the mill during operation as well as plastic deformation of the particles (Kwan *et al*., 2005).

During milling, the theory of comminution can be used to describe the process that occurs. Initial elastic deformation results in dislocation formation in the material. Micro-cracks can also be observed in this phase. Dislocation density continues to increase until it reaches a yield point. At this point, plastic deformation occurs according to the material properties. At the stage of plastic deformation, dislocation migration can be observed along with sliding of structural units and change of orientation. Amorphisation can also occur at this stage. Size reduction in materials is limited by the primary particle size of the material. At this particle size, continued grinding often results in only plastic deformation. The equilibrium state of milling can also be reached during this stage of milling where the rate of size reduction equals the rate of aggregation or agglomeration. In materials that expel water molecules during grinding, stable oxygen bridges such as Al-O-Al have also been observed to form. This is a sign of chemical reactions initiated by mechanical energy (Juhasz, 1998).

Milling is a widely used industrial operation common for cases where size reduction of particles is required (Reid *et al*., 2008). It can also be known as grinding and involves the size reduction of particles smaller than 10 mm. There is a vast range of mill types available commercially and the choice of mill is based on a variety of factors, such as properties of the material to be milled, e.g. failure mode, and the required product particle size (Angelo *et al*., 2008). Figure 2.7 shows an array of size reduction equipment available for different combinations of feed and product particle sizes (Neikov *et al*., 2009).

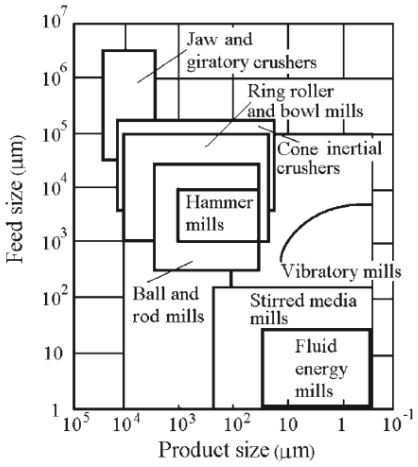

Figure 2.7: Size reduction equipment available for different combinations feed size and product particle size (Neikov *et al*., 2009)

The diagram also gives insight into mill selection for a certain degree of size reduction required. It can be seen that the most appropriate mills for size reduction of gamma-Alumina are the ball and rod mills, stirred media mills, vibratory mills and fluid energy mills as the material before catalysis is within the size ranges of 10^1 to 10^2 microns. The mills can be further classified depending on whether a milling medium such as water is required; wet or dry milling. Rod and ball mills can be used for both wet and dry milling. Vibratory mills are most commonly used for keeping powders dispersed during dry milling. Fluid energy mills use a fluid as the grinding media and are used for dry milling. Stirred media mills are most common for wet milling to very fine particle sizes less than 1 micron.

High energy mills can give insight into how mechanical energy affects the structure and properties of gamma-Alumina powders. It is therefore of great interest to select mills that dissipate a high amount of energy per contact. In this case, the ball mill and the fluid energy mills are the mills which arouse the greatest interest and in particular the planetary ball mill, the vibratory mill and the fluid energy jet mill. Ball mills, vibratory mills, rod mills and jet mills can be used to achieve particles less than 1 mm in diameter (Rosennqvist, 2004) but for ultrafine dry milling, e.g. particles (d_{90} = <10 µm), vibratory ball milling, planetary ball milling (Mio *et al*., 2009) and fluid energy/ air jet milling (Midoux *et al*., 1999) are commonly used methods. In these mills particle size is reduced by impact, shear, attrition or compression or a combination of them (Balaz *et al*., 2013). The stresses may affect product attributes in different and often ‘unexpected’ ways through mechanochemical activation, so an understanding of the mill function on the product characteristics is highly desirable for optimising product functionality.

2.3.1 Ball Milling

Ball milling achieves size reduction by a combination of shear stresses and impact stresses. The proportions of the combination may vary according to the way in which the mill works. There are numerous types of ball mills which include shaker, attritor, tumbler, drum, canon, planetary and stirred ball mills. Ball mill containers are often cylindrical. Size reduction by shear is achieved when the balls roll along the walls of the milling container and impact is often achieved when the milling balls drop onto the powder beneath them by gravitational force (Varin *et al.*, 2009). The main variable that is often manipulated to vary the extent of size reduction is the speed of the mill. The critical speed of the ball mill where no size reduction is achieved can be expressed according to Equation 2.1.

$$\mathbf{N_c = 42.3/D^{1/2}} \qquad \textbf{Equation 2.1}$$

Where N_c is the revolutions per minute (RPM) and D is the diameter of the milling container in metres and the ball diameter is much smaller than the mill diameter. When a ball comes in contact with the material being milled, there is kinetic energy transfer from the ball to the material. A relationship between the kinetic energy, E, mass of the milling balls, m and the velocity of the milling ball, v is shown in Equation 2.2.

$$\mathbf{E = (½)\ mv^2} \qquad \textbf{Equation 2.2}$$

The equations also show that the main factors governing the amount of kinetic energy transferred to the material being milled are the mass of the balls and the velocity. The mass of the balls can vary from material to material and materials with higher density can provide more energy per impact. The velocity of the ball can be varied by the speed of the mill and mills which can achieve velocities higher than gravitational force can provide more energy in impacts that occur when milling

2.3.1.1 Ball Milling Process Variables

During selection of an appropriate mill, it is important to consider all variables that may affect the outcome of the product. When listed, apart from already discussed mill type selection, the process variables worth considering during milling are;

- Mill material
- Milling speed
- Filling of milling jar
- Milling time

- Milling media
- Ball-to-powder ratio
- Milling atmosphere
- Process control agents
- Temperature rises

Figure 2.8 shows the different milling parameters worth considering during the process of mill selection.

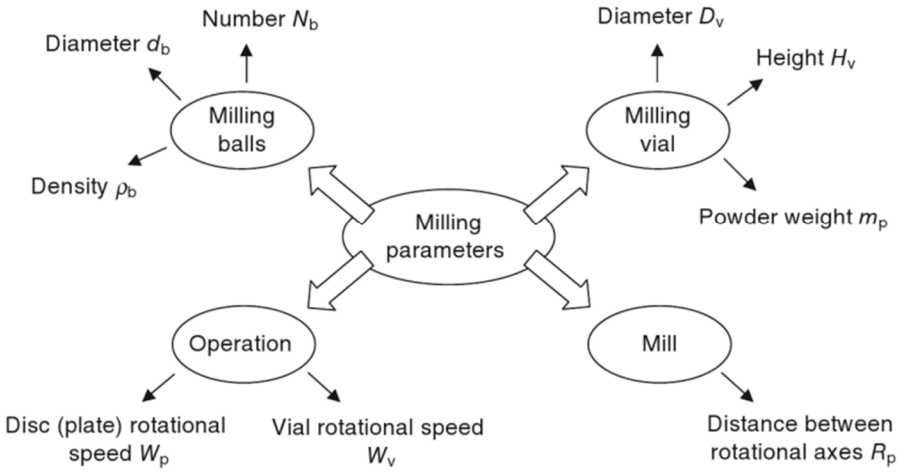

Figure 2.8: Milling parameters that affect outcome of product (Sopicka-Lizer, 2010)

Here the different variables to be considered during milling are briefly discussed.

2.3.1.1.1 Mill Material

The properties of the milling jar or chamber and milling media material are important during the design of a milling process. A mill made of a material with a high hardness value and high density can achieve smaller particle sizes than one made of a lower hardness material due to the energy provided at every contact during milling. In ball mills, the impact and shear of the milling medium with the wall of the milling jar can, however, cause wear. This results in contamination of the milled powder. It is therefore important to consider the material of the jar and its effects on the milled product. With the wide variation of mill materials available such as tungsten carbide, Zirconia, Agate and Alumina to name a few, it is important to have full knowledge of the properties of the material to be milled as well as the size reduction required (Aliofkhazraei, 2015).

2.3.1.1.2 Milling Speed and Mill Jar Filling

A chosen milling speed determines the amount of energy imparted into the milling jar or chamber. A higher milling speed results in a greater amount of energy available for the sample material. In fluid energy mills, the pressure of the fluid determines the intensity of the milling and a high pressure results in more energy input to the sample material. In ball mills, two limitations exist which determine the maximum speed that can be applied to the mill. The first is a critical speed above which milling media does not move in the milling jar and hence no energy is imparted into the sample material. Temperature rise due to high energy impacts can also be a limitation. In high energy ball milling processes, it is necessary to stop the mill periodically to allow cooling. Other modern mill designs include a cooling system. The temperature rise that occurs can be an advantage for processes that require diffusion or a disadvantage where undesired decomposition or phase transformation can occur (Aliofkhazraei, 2015).

2.3.1.1.3 Mill Filling

In ball mills, for efficient transfer and distribution of energy from the mill to the powder, it is important to have a reasonable amount of space in the milling jar or chamber after filling. This provides space for contact between the mill and powder. The recommended filling is up to 30% of the mill. This varies from mill to mill. The size of the milling media also affects the mill filling. Where larger diameter milling balls are required, a smaller number may be used and the number of balls is often measured according to their mass. In fluid energy mills such as the air jet mill, the feed rate of the powder determines the amount of powder in the milling chamber. A high feed rate can result in mill ‘choking’ where the powder blocks the inlet and causes flow back up the feed chute of the mill (Aliofkhazraei, 2015).

2.3.1.1.4 Milling Duration

Choice of milling duration if often selected after determining other milling variables such as the milling speed. The length of time selected affects the outcome of the product in terms of the size reduction, morphology effects and level of contamination from milling tools. The powder properties can also determine the milling time. Friable materials may not require long mill times as compared to harder materials (Aliofkhazraei, 2015).

2.3.1.1.5 Milling Media

When choosing milling media for ball milling processes, three main variables are considered; the size or diameter, the material they are made of and the amount of them or their mass. The

larger the diameter of the milling media, the greater the amount of energy dissipated at every impact. In terms of material choice, harder materials or materials with higher density values can impart a larger amount of energy than softer materials. Common materials used are Stainless Steel, hardened steel, Agate, Zirconia, tungsten carbide and Alumina. Although smaller diameter media do not dissipate a large amount of energy, their size results in smaller particle sizes as they do not promote cold welding of particles as much as larger media. Contamination also occurs from milling media more so in cases where the milled powder is brittle. It is recommended to use monosized milling balls although higher impact energies have been observed where the milling ball diameters were varied (Aliofkhazraei, 2015).

2.3.1.1.6 Ball-to-Powder Ratio

The ball-to-powder ratio (BPR) is important in ball milling and is the selected ratio of the ball mass to the powder mass. It can be varied from 1:1 to 220:1 and the mass of the balls is often the higher value. This ratio also determines the efficiency of the milling process as it affects the amount of energy that is transferred from the balls to the powder. Where a high BPR is used, the impact energies to the powder are higher and this is often used for mechanochemical reactions where higher energies are required. The ratio of 10:1 is the most common although the desired product almost always determines the selection of the BPR (Aliofkhazraei, 2015).

2.3.1.1.7 Milling Environment and Process Control Agents (PCA)

The milling environment encompasses the use of milling aids and milling mediums. Milling can be carried out in air or in other environments such as in argon or cryogenic. Variation of the environment is usually done in cases where certain attributes are required in the milled powder such as specific surface properties. Ball milling can also be carried out wet or dry. Wet milling achieves finer particles although it results in higher levels of contamination from the mill to the powder. The wet medium can be water or other solvents such as alcohols. Process controls agents (PCAs) are also commonly used where certain properties of the powder being milled may need preserving. They include lubricants such as stearic acid, magnesium stearate or zinc stearate to name a few. Both wet milling and PCAs can aid in reducing friction to the powder and hence slow down processes such as amorphisation and phase transformation.

2.3.1.1.8 Temperature Rises

It is important to consider temperature rises during milling as this is often discussed in two parts. There is the overall bulk temperature that is often recorded in the milling jar and there is the localized temperature rises that occur at every impact during milling. Different mill types and mill sizes result in different ranges of energies and higher energy mills result in high bulk temperature increments. Most recorded temperatures in the planetary ball mill do not exceed 473 K. The localized temperature rises are, however, reported to be much higher than the bulk temperatures. They have been reported to exceed 1273 K although no direct measurement of them is yet possible. Due to the assumption of such high temperatures, thermally driven reactions that occur mechanochemically are often reported to be linked to these localized temperature rises.

From the ball milling process variables discussed, it is clear that for most of them, one cannot be separated from the other and the selection of one can directly or indirectly influence the other. As an example, the choice of BPR, milling speed, milling material and filling all affect the amount of energy that is transferred from the mill to the powder and hence all have a direct impact on the product achieved. It is therefore clear that prior knowledge of the properties of the sample and desired product is important for selection of milling process variables. Two mills that encompass all the milling variables discussed are the planetary ball mill and the vibration mill. These are high energy ball milling processes efficient for the size reduction of semi-brittle and brittle materials.

2.3.2 Vibratory Milling

Vibratory milling is a variation of ball milling and all milling principles reviewed in ball milling apply. The added advantage of this method is that it includes the mechanism of vibration to the milling vessel after the milling media and material has been loaded. This can give an added advantage over conventional ball milling by increasing the mobility of both the material and the milling media and hence encouraging more collisions and interactions. Vibratory milling is faster and smaller particle sizes can be achieved with this method. The two motions that aid vibratory milling to perform better than conventional ball milling is that a cascading or mixing action is imposed on the contents of the mill and that shear and impact of material between grinding media is promoted. Mills can be lined with different materials to reduce contamination. These mill types can also be used for cleaning metal parts (Richerson and Lee, 2005).

2.3.3 Fluid Energy Milling

Fluid energy milling is a dry process that is popular in industry as it is efficient and scalable. Particles are mainly reduced by particle-to-particle collisions although some particles can be reduced by particle-wall collisions. The jet mill or air classifying mill is a type of fluid energy mill. In this mill, air enters a circular chamber through different inlets at high velocity due to the compressed air that is used in the mill. The sample to be milled rotates around the chamber and exits through a classifier where the desired particle size is screened. The mill uses centrifugal force by the design of the circular milling chamber and particles are forced to travel to the centre of the chamber. Larger particles are pushed back to the outer walls were they experience greater size reduction until the required size is achieved.

The mills can achieve very fine particles that can range between 1 micron and 30 microns. These types of mills are very popular in pharmaceuticals as they are readily cleanable by dismantling parts and have low levels of contamination from the milling tools. An added advantage is that there is little heat build-up in these mills as opposed to ball milling processes. Other applications of fluid energy mills include size reduction in cosmetic products, precious metals, ceramics and pigments (Liu, 2008). The fluids can be used for these mill types include nitrogen, compressed air, superheated steam and any other gas that is compatible with the materials of the mill. The velocities of the fluids are sonic or near sonic. The design of the chamber also works to reduce particle-wall impacts and hence the reason why less contamination is achieved.

Another measure that can be taken that is process specific is a choice of material to line the mill. Materials such as Zirconia, polyurethane, rubber or steel can be used depending on the properties of the material to be milled as well as the desired end product properties. Issues with this method mainly arise in the collection of milled samples as they are often collected in filter material bags that often clog up quickly. Typical milling data for materials commonly milled in fluid energy mills is shown in Table 2.1 (Richerson and Lee, 2005). Size reduction in fluid energy mills is mainly by two stress modes; impact and attrition. One design of a fluid energy milling chamber can be shown in Figure 2.9 (Gad, 2008). Agglomeration and aggregation can also occur but this is usually due to the fine particles ‘coming together’ in the collection bag after the milling chamber. Wettability of the milled particles can also be an issue but can be overcome by adding a hydrophilic carrier in the samples (Augsburger and Hoag, 2008). This is because fine particles produced by fluid energy milling often have a high surface charge and can therefore agglomerate.

Table 2.1: Typical data for materials commonly milled by fluid energy milling

Material	Mill Diameter		Grinding Medium	Material Feed Rate		Average Particle Size Obtained	
	cm	in.		kg/hr	lb/hr	μm	in.
Al_2O_3	20.3	8	Air	6.8	15	3	0.00012
TiO_2	76.2	30	Steam	1020	2250	<1	<0.00004
TiO_2	106.7	42	Steam	1820	4000	<1	<0.00004
MgO	20.3	8	Air	6.8	15	5	0.0002
Coal	50.8	20	Air	450	1000	5–6	~0.00025
Cryolite	76.2	30	Steam	450	1000	3	0.00012
DDT 50%	61.0	24	Air	820	1800	2–3	~0.0001
Dolomite	91.4	36	Steam	1090	2400	<44	<0.0018
Sulfur	61.0	24	Air	590	1300	3–4	~0.00014
Fe_2O_3	76.2	30	Steam	450	1000	2–3	~0.0001

Another method to counteract this is milling at elevated humidity. This reduces the amorphous content in the materials as well producing crystalline samples. The humidity levels used range between 30% and 70% (Colombo *et al.*, 2012).

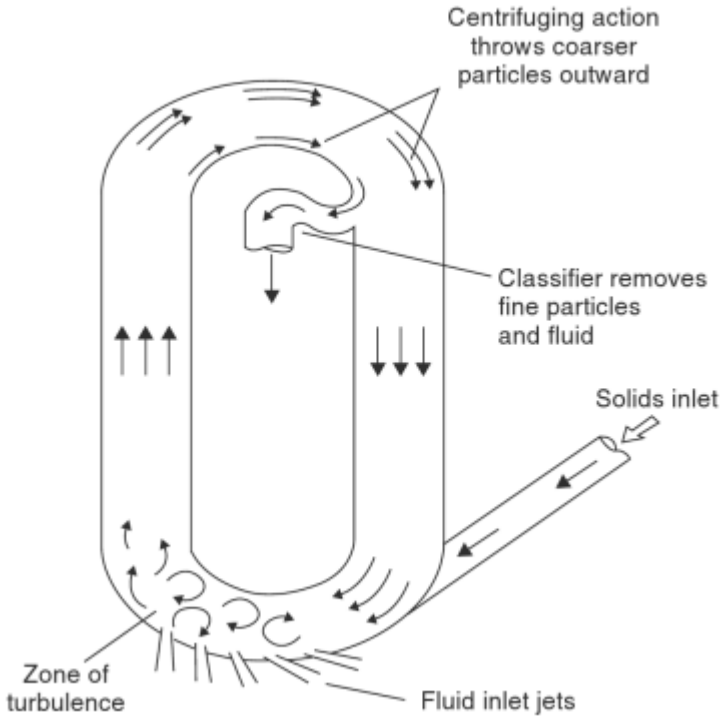

Figure 2.9: Milling chamber in a fluid energy mill

2.4 Milling Effects on Gamma-Alumina

2.4.1 Size Reduction

The surface properties of a material change when its size is reduced to the nanometre scale because the percentage of atoms at the surface increases. Catalysis increases the rate of a chemical reaction by promoting the mixing of reactive chemicals or lowering the optimum reaction temperature and activation energy. For metal catalysts, the chemical reactions often occur at its surface; therefore size reduction is an essential part in making the catalysts. This is because once the catalyst size has been reduced, its activity increases as it has different surface properties including more exposed atoms at its surface (Rozita *et al*., 2010).

An example would be gold; which is a poor catalyst in significantly large sizes but in sizes of less than 10 nm in diameter, its activity significantly increases and can be used for chemical reactions such as the oxidation of carbon dioxide. Due to the activity that occurs on catalysts during chemical reactions, especially highly reactive catalysts, catalyst particles with no catalyst support can agglomerate which is undesired; therefore a catalyst support can be used with the catalyst. Gamma-Alumina is used as a catalyst support because it a typical surface area of 100 to 350 m^2/g and is thermally stable up to 1000^oC. The crystal structure of a catalyst support can also change when it is reduced in size (Rozita *et al*., 2010).

Gamma-Alumina is described as a defect spinel and when it is reduced to nanoparticle size, it is usually expected to maintain its spherical shape to minimize surface energy and attain stability. However, it has been observed that when gamma-Alumina is reduced in size, it tends to adopt cubeoctahedral or octahedral crystal shapes with distinct surface facets. The two mentioned shapes of spherical and cubeoctahedral arrangements can be seen in Figure 2.10.

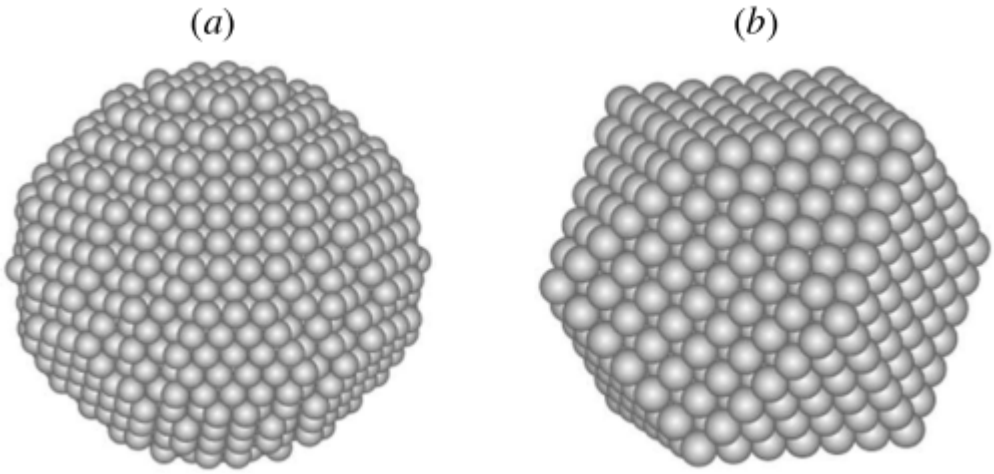

Figure 2.10: Models of morphologies of crystals with (a) showing expected spherical structure after gamma-Alumina size reduction and (b) showing observed cubeoctahedral shapes after size reduction (Jefferson, 2000).

When gamma-Alumina particles are reduced in size, their stoichiometry is altered as there will be a significant number of atoms at the surface compared to the total atoms in the particle and the way the particle terminates, i.e. whether it is on a metal or oxygen plane is variant. Even though gamma-Alumina is a popular material used for a variety of purposes, its structure and the changes that occur as a result of size reduction still have not been fully clarified. Changes to the surface characteristics and properties of gamma-Alumina due to size reduction can affect the reactivity and in turn catalytic activity of the metal adhered to its surface.

Different analytical methods are available to determine the properties of the product and feed gamma-Alumina. The techniques available for use are gas adsorption to determine the surface area and porosity of gamma-Alumina using the BET method, differential thermal analysis (DTA) to get more information on phase transitions between 50 and 1400^{o}C and x-ray diffraction (XRD) and selected area electron diffraction (SAED) methods to determine the structural information of the metal particles. Transmission electron microscopy (TEM) can be used to determine particle morphology, size and size distribution whilst high resolution (HR) TEM can be used to analyse the crystallinity of the particles (Rozita *et al.*, 2010).

2.4.2 Deformation in Crystals

Atomic arrangements of crystalline materials can be described by the seven crystal systems. These are further divided into fourteen Bravais lattices which are shown in Figure 2.11. Although these lattices grouped crystal structures into fourteen systems, there are hundreds of crystal structures that fully define crystals. A crystal structure is defined by lattice parameters its unit cell. This can be defined as the smallest unit of a crystal structure although it is made up of atoms. A unit cell is defined by the number of atoms in it, the coordination number and the packing factor of the atoms in the unit cell. Face centred cubic (FCC) and hexagonal close packed (HCP) structures have the closest packing of atoms. Coordinates and Miller indices are used to define the points, directions and planes within a crystal structure. X-ray diffraction and Transmission Electron Microscopy are the best methods for analysing and determining crystal structures (Askeland and Wright, 2013).

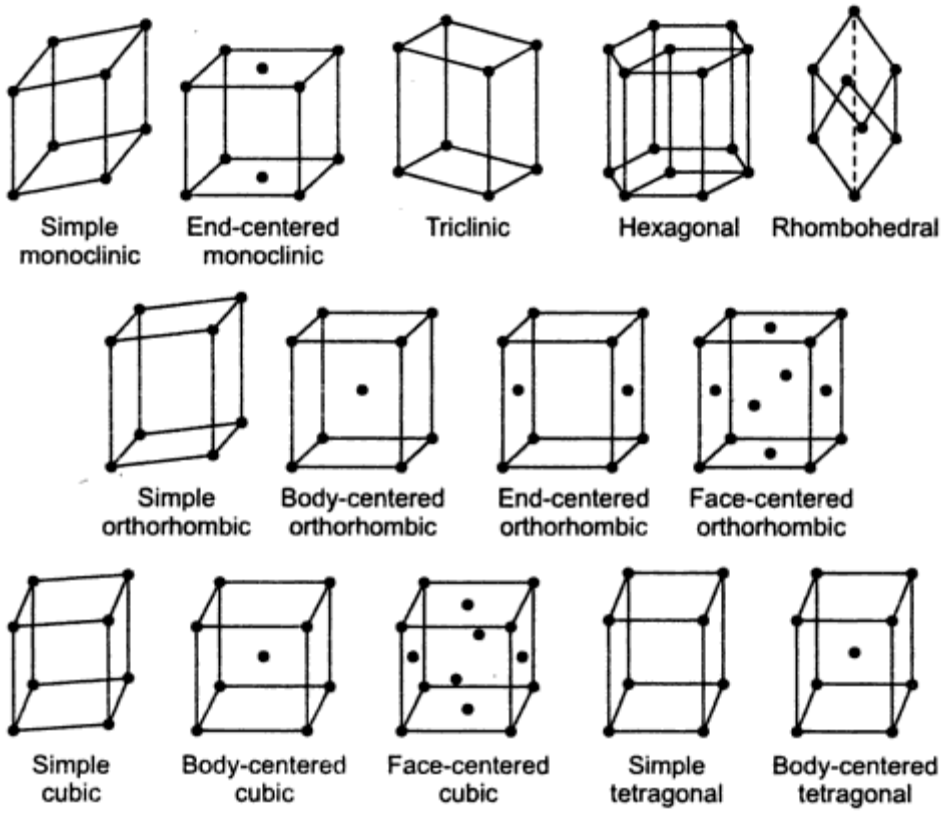

Figure 2.11: Illustration of the fourteen Bravais lattices (Wadhwa and Dhaliwal, 2008)

Defects exist within materials and these defects can affect the properties of the material. The main defects that exist are point defects, dislocations and surface defects. Point defects are localized disruptions to the atomic arrangement in a crystal structure. They come in many forms such as vacancies, interstitial atoms, substitutional atoms, Frenkel defects and Schottky

defects. As highlighted earlier in this review, gamma-Alumina contains vacancies within its crystal lattice and hence an understanding of their effects is necessary. The movement of atoms when they gain energy or when impurities are introduced often causes defects (Askeland and Wright, 2013).

Vacancies can be described as the space that is left due to an atom missing from the normal site in the crystal structure. Materials with vacancies have high entropy and hence higher thermodynamic stability. In metal alloys, vacancies are commonly due to solidification at high temperatures or radiation damage. An increase in temperature with a crystalline sample results in an increase in vacancies. Dislocations are imperfections in a crystal that provide points of weakness. When a sufficient shear stress is applied to a crystal structure, the plane that contains the dislocation line and the Burgers vector is known as a slip plane.

Slip is the process by which a dislocation moves through the body of a crystal structure. Full motion of a dislocation through a crystal in the slip plane results in the formation of a step at the edge in the slip direction. Dislocations can lead to plastic deformation in metals. Plastic deformation is the irreversible change to the structure of a material after the causal applied load is removed. In order for slip to occur, the critical resolved shear stress (CRSS) of the slip plane must be reached and only then can plastic deformation occur (Askeland and Wright, 2013).

In FCC materials, the main slip plane is the {111} as this is the closest packed plane and the slip direction n is <110>. This can be shown in the diagram in Figure 2.12. FCC materials have 12 slip systems in total of which four are unique to the {111} plane. The more slip systems a material has, the higher its ductility. HCP materials are in turn brittle as they have fewer slip systems (Callister, 2007).

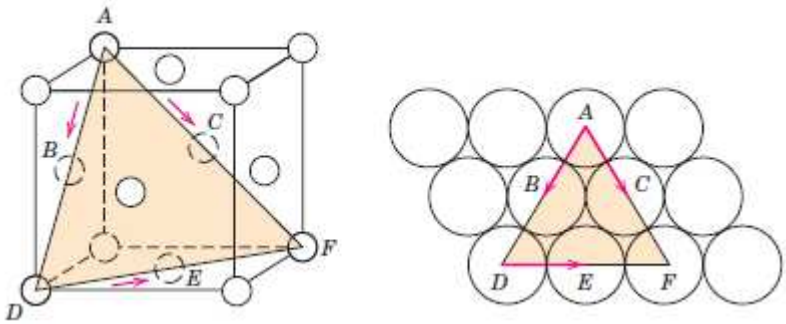

Figure 2.12: Slip plane and slip direction in FCC crystal structures (Callister, 2007)

Some metallic materials also deform by twinning. Twinning is induced by shear stress and can result in atomic displacements where the atoms on one side of a plane mirror the positions on the other side of the twin boundary. The occurrence of twinning is shown in Figure 2.13 (Callister, 2007).

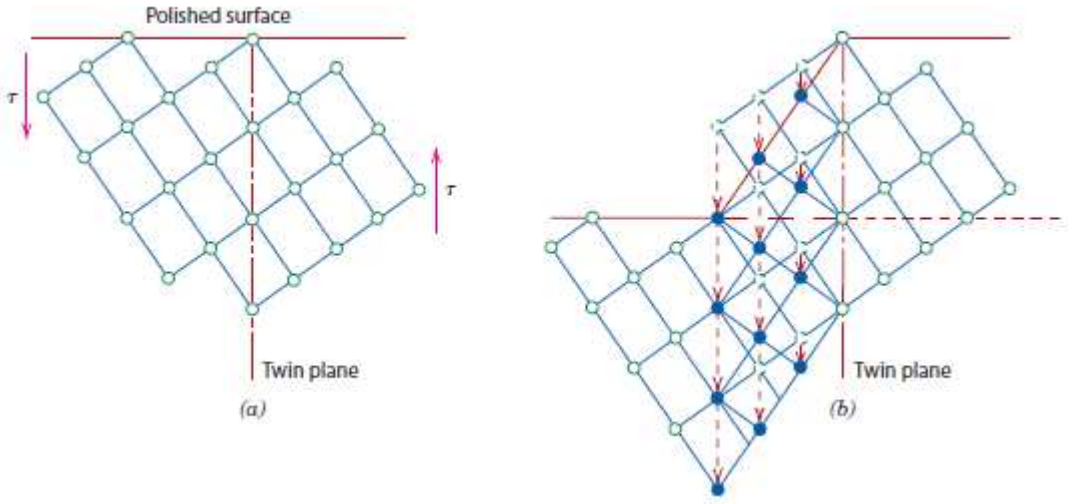

Figure 2.13: Occurrence of twinning in metals (Callister, 2007)

Twinning occurs in a specific direction on a specific plane which is determined by the crystal structure of the material. The difference between twinning and deformation by slip is that in twinning, the deformation is homogenous. The crystallographic orientation above and below the slip plane in slip remains the same whereas in twinning there is reorientation. Slip also occurs over longer distances than twinning. Twinning is most common in BCC and HCP metals (Callister, 2007). Deformation systems are important in milling processes that involve shear as these types of stresses can result in transformation of a material. They also allow better understanding of the occurrence of transformation in a material including the planes of the crystal as well as the direction. The influence of milling on the phase transformation of gamma-Alumina is reviewed in the next section.

2.4.3 Phase Transformation of Gamma-Alumina during Milling

According to Sopicka-Lizer (2010), mechanochemical activation can cause microstructural changes to materials and existent lattice imperfections can result in phase transformations or amorphization. Mechanochemistry encompasses chemical reactions that are initiated by the absorption of mechanical energy (Šepelák *et al*., 2007). High energy ball milling has been reported to induce mechanochemical phase transformations and reactions, the conditions of high stresses during milling are envisaged to play a major role in such phase transformations

(Šepelák *et al*., 2007). The stresses on powder during high energy ball milling can reach pressures of the order of 200 MPa. No record has been made of contact temperatures that occur during milling but it is assumed that the temperatures can reach hundreds of degrees.

Mechanochemistry can also induce different kinds of transformations such as polymorphic transformations and grain boundary disordering. It can also cause defects such as crystallographic shear plane defects. Shear stress is known to induce defects within materials. A combination of shear stress, resultant defects and localized temperature rise can result in increased atomic mobility and phase change. A selection of milling conditions determines the type of defects in the material and the material properties of the milling tools also determine the type of transformation achieved during the milling duration (Šepelák *et al*., 2007). A good example is yttrium oxide (Y_2O_3) which when ground with Zirconia tools transforms from a bixbyite to a fluorite structure. When ground with steel tools, a monoclinic phase is observed, which becomes amorphous with prolonged milling. This difference in transformations based on milling conditions could be related to the range of energies supplied to the material by the different milling tools (Šepelák *et al*., 2007).

Liu *et al*. (2005) investigated on the phase transformation of mechanically milled nanosized gamma-Alumina and found that the milled samples had a large number of defects generated by milling. The defects also lowered the temperatures and activation energies of phase transformation by promoting nucleation and diffusion. The defect accumulation on the samples also showed a logarithmic dependence on milling time (Liu *et al*., 2005). The transformation of aluminium oxide materials falls under polymorphic transformations.

Zielinski *et al*. (1993) reported on the phase transformation from gamma-Alumina to alpha-Alumina by the use of the SPEX mill. Different milling tools were used which included hardened steel, tungsten carbide and Zirconia. They observed phase transformation in all cases with faster transformation rates in the experiments with denser milling tools. From this they concluded that the density of the milling material provides varied impact energies and hence different rates of phase transformation. They also varied the milling atmosphere; air and argon, and observed greater agglomeration rates in the argon atmosphere reflecting that oxygen aids in preventing agglomeration. This work highlights a few variables to consider during milling of gamma-Alumina; milling tools mechanical properties and the milling atmosphere. The main methods of analysis used by Zielinski *et al*. (1993) were XRD and

BET. From XRD results they observed peaks matching alpha-Alumina after milling. From BET results they observed a reduction in surface area as well as a change in the pore size and pore structure of the material. They related the observed phase transformation to martensitic-type transformations.

Kostic *et al*. (2000) also carried out work on the phase transformation from gamma-Alumina to alpha-Alumina by the use of a vibrating disc mill. The interesting outcome of this work was the observed transformations which followed those observed by calcination of boehmite; boehmite → gamma-Alumina → delta-Alumina→ theta-Alumina → alpha-Alumina. In Zielinski *et al*. (1993) there is no mention of intermediate phases. This brings about the interesting but missing link in the research carried out on gamma-Alumina transformations so far; the energies supplied by different mills and milling variables and how they affect the outcome of the product. Additionally, evidence of phase transformation due to milling, similar to that achieved by thermal dehydration of boehmite, has been reported in works by Wang *et al*. (2005) and Duvel *et al.* (2011).

Interestingly, Wang *et al.* (2005) used a similar SPEX mill as that used by Zielinski *et al*. (1993) and did not observe phase transformation until alpha-Alumina was added as seed to the experiments. The difference in the way the experiments were carried out is in the material of the milling tools (Stainless Steel vs hardened steel) as well as the ball-to-powder (BPR) ratios used. When Zielinski *et al*. (1993) used hardened steel, transformation was observed after 8 hours of milling but when Wang *et al.* (2005) used Stainless Steel, no transformation was observed even after 20 hours of milling. Wang *et al*. (2005) states the BPR ratio as 10: 1.

Zielinski *et al*. (1993) does not give the BPRs used but with the given sample mass of ~4 g and the densities of the three materials used; hardened steel, tungsten carbide and Zirconia, the calculated BPRs are 30:1, 65:1 and 12:1 respectively. The ratio used for the steel was 3 times higher than that used by Wang *et al.* (2005). It is also important to note that phase transformation was observed with Zirconia although it has a BPR close to that used by Wang *et al.* (2005). Therefore these two works add the influence of BPR and milling tool materials as variables that need consideration when selecting an appropriate milling procedure for gamma-Alumina.

The work by Wang *et al.* (2005) also highlights an interesting leap in the quest to understand the mechanochemical phase transformation of gamma-Alumina; the influence of alpha-Alumina seed. Although the quantity is not stated, Wang *et al.* (2005) observed phase

transformation when a small fraction of alpha-Alumina was added before milling. Bodaghi *et al*. (2008) also carried out work on the milling of gamma-Alumina and observed no phase change after 30 hours of milling in the Fritsch Pulverisette 7 planetary ball mill. In this work, hardened steel was the milling material used and a BPR of 30:1 was used. With these conditions being similar to those used by Zielinski *et al*. (1993) with the SPEX mill, the two main factors that come to mind is the range of energies provided by the two different mills which is influenced by the milling speed selected as well as the size and orientation of milling jars/ vessels. The milling speeds were not stated in both works. Bodaghi *et al*. (2008) however reported the occurrence of phase change of gamma-Alumina to alpha-Alumina only after the addition of alpha-Alumina seeds into the mill and concluded that the alpha-Alumina seeds act by reducing the transition temperature and activation energy for alpha-Alumina to nucleate. The experimental work carried out by Bodaghi *et al*. (2008) also shows that the milling media used was not of the same size. This may well have had an effect on the mechanochemical effects observed.

Notable work on gamma-Alumina phase transformation by high energy ball milling is that of Duvel *et al.* (2011). Their focus was on the change in pentacoordinated Al (Al_5) sites with different milling conditions. It is important to note that they used a planetary ball mill at 600rpm with 140 monosized balls and a BPR of 27:1. These variables determine the range of energies supplied to gamma-Alumina in their experiments.

Their observations were an increase in Al_5 Alumina with high energy ball milling by use of solid state NMR. They also observed the influence of milling parameters on the outcome of the milled product. They concluded that due to the need for a critical gamma-Alumina crystal size for phase transformation, the properties of the gamma-Alumina pre-milling can determine the phase of the milled product. Duvel *et al.* (2011) highlight that the initiation of phase transformation may be from the existence of these Al_5 sites which are basically aluminium atoms on octahedral sites that have been exposed on the surface due to particle breakage in milling. These surfaces are highly likely energetic and hence would favour the structure with the least energetic state; which in this case would be hcp over ccp structure.

It is noteworthy in the work by Duvel *et al*. (2011) that adding alpha-Alumina seed did not result in full phase transformation as what was observed by Wang *et al.* (2005) and Bodaghi *et al.* (2008). It can however, also raise the influence of the milling speed chosen. Because a high milling speed of 600 rpm was used, the possibility of cold-welding occurring is high and

this can influence the availability of gamma-Alumina surfaces for phase transformation. If gamma-Alumina phase transformations observed from different research work are listed, Table 2.2 shows the observations of the final phases after milling.

Table 2.2: Phase transformations observed after high energy ball milling of Gamma-Alumina (Wang *et al*., 2005)

Starting phase	Mill	Milling condition	Milling time (h)	Final phase
γ-Al_2O_3	Fritsch Pulverisette 9	Tungsten carbide grinding set, 1000 rpm	2	δ-Al_2O_3
δ-Al_2O_3	Fritsch Pulverisette 9	Tungsten carbide grinding set, 1000 rpm	10	θ-Al_2O_3
γ-Al_2O_3 surface area > 80.3 m^2/g	SPEX8000	Hardened steel/tungsten carbide vials and balls, in air/argon	10	α-Al_2O_3
κ-Al_2O_3/χ-Al_2O_3	SPEX8000	Hardened steel/tungsten carbide vials and balls	< 10	α-Al_2O_3
γ-AlOOH (Boehmite)	Fritsch Pulverisette 7	Tungsten carbide vial and balls, 10 balls with a diameter of 10 mm, the powder is 1 g, in air	2.5	α-Al_2O_3
$Al(OH)_3$ (Gibbsite)	Fritsch Pulverisette 7	Tungsten carbide vial and balls 10 balls with a diameter of 10 mm, the powder is 1 g, in air	7	α-Al_2O_3
γ-Al_2O_3	SPEX8000	WC vial and balls, BPR5:1	10	α-Al_2O_3
γ-Al_2O_3	SPEX8000	WC vial	24	γ-Al_2O_3
γ-Al_2O_3, < 10 μm, poor crystallinity	Fritsch Pulverisette 5	Hardened steel vials, in air, BPR15:1, 200 rpm	56	α-Al_2O_3

McArdle and Messing (1993) have demonstrated the effect of seeding boehmite with α-Fe_2O_3, a material isostrutural to alpha-Alumina. They achieve alpha-Alumina through this process. As the boehmite to alpha-Alumina transformation is topotactic, the structure of boehmite and alpha-Alumina are similar. Their results can therefore be compared in seeding experiments to gain an understanding of changes in crystallographic arrangements with addition of energy. The results of their investigation are shown in Figure 2.14 and show that the transformation follows a sigmoidal pattern. There is an initial stage in the phase transformation were the rate is slow, followed by faster transformation rates and a plateau when full phase transformation has been achieved. Their experiments were carried out using calcination which is different from milling used in the experiments in this thesis. If however, these results are comparable with milling results, it can be suggested that mechanical energy from milling has a similar effect as thermal energy from calcination can likewise overcome the energy barrier for phase transformation.

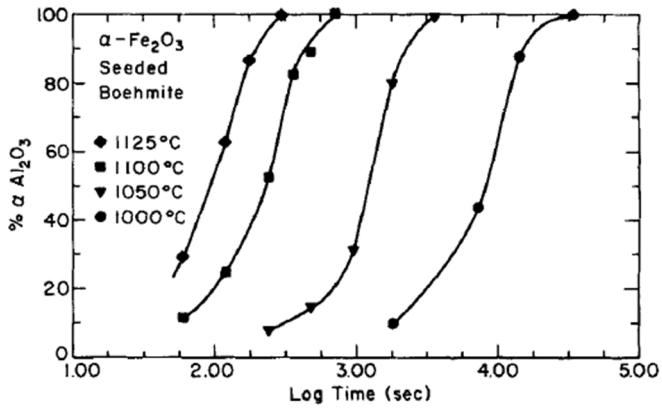

Figure 2.14: Isothermal transformation kinetics of boehmite-derived Alumina from α-Fe_2O_3 seeded samples (McArdle and Messing. 1993)

McArdle and Messing (1993) also observed a decrease in surface area with the formation of α-Al_2O_3 in seeded boehmite as shown in Figure 2.15.

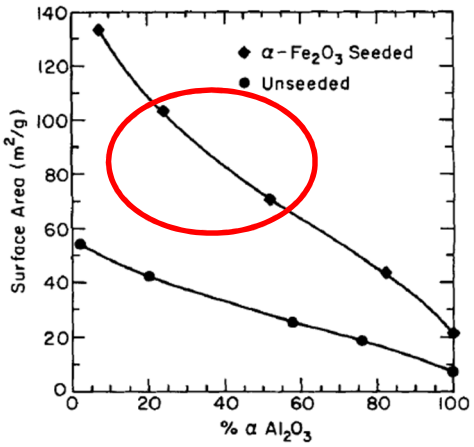

Figure 2.15: Reduction in surface area with formation of α-Al_2O_3 observed by McArdle and Messing (1993)

Bagwell *et al.* (2001) assessed the possible factors that are involved during the transformation of theta-Alumina to alpha-Alumina. The structures of theta and gamma differ in the degree of dehydroxylation. Both materials, however, still exist in the ccp structure. It is therefore beneficial to consider the findings in this work. They considered two methods of nucleation of alpha-Alumina from theta-Alumina; shear nucleation and diffusional nucleation. The shear nucleation model considered brings to consideration the work of Kachi *et al.* (1963). They developed the synchro-shear model and based it on the orientation relationship of $(111)\gamma//(0001)\alpha$, $[1\bar{1}0]\gamma//[01\bar{1}0]\alpha$. They proposed shearing of the oxygen lattice in the $\langle 112 \rangle$ direction with the shift of Fe^{3+} ions simultaneously results in a shift from ccp to hcp structure.

It can be highlighted that the identification of an orientation relationship alone is not enough evidence to classify the nucleation method as shear. However, as a review it is important to understand different observations of previous work done. Bye and Simpkin (1974) investigated the influence of chromium (Cr) and iron (Fe) on the transformation from gamma-Alumina to alpha-Alumina. They concluded that Cr reduced the rate of conversion from theta-Alumina to alpha-Alumina and Fe increased it. They also observed that the presence of Cr^{6+} accelerated the rate of conversion from gamma-Alumina to theta-Alumina. Their observations favoured the synchro shear model.

The synchro shear model requires the growth of gamma-Alumina crystals to a critical size before phase transformation can occur. Bagwell *et al*. (2001) disputes the theory for a need for growth to a critical size at the end of the review paper and supports diffusional nucleation. Their argument is based on the requirement of a habit plane between the matrix and nucleating phases which would result in shear of an entire crystal that has reached a critical size. They rather support the argument of diffusional nucleation due to this argument and due to the observation that in TEM images of alpha-Alumina presumably formed by shear nucleation, no stacking faults are present and the only visible defects are pores entrapped during growth.

The work of Duvel *et al*. (2011) and the work of Bodaghi *et al*. (2008) on seeded gamma-Alumina samples provide a platform for the argument of diffusional nucleation. As this is a process that occurs from the surface of crystallites, the observation made by Duvel *et al*. (2011) on the increase of Al_5 sites supports diffusional nucleation by means of providing nucleation sites for the growth of alpha-Alumina. Providing alpha-Alumina seeds, also carried out by Duvel *et al*. (2011) and Bodaghi *et al*. (2008), also provides nucleation sites for alpha-Alumina to grow. Duvel *et al*. (2011) also report that additives such as lanthanum oxide (La_2O_3) inhibit the formation of alpha-Alumina. They observed that Al_5 also reduced in the samples when additives were used during milling. The assumption to this is that the additives bind onto potential nucleation sites and inhibit the formation of alpha-Alumina. Orientation relationships reported by Bye and Simpkin (1974) also exist in diffusional nucleation and therefore cannot be used to support shear nucleation alone.

Mechanical energy from milling also includes the influence of different stress modes on the material being milled. The review on milling methods has shown that in different mills, different stress modes are imposed on the particles. Bagwell *et al*. (2001) highlights that the

transformation from theta-Alumina to alpha-Alumina involves a decrease in volume of the material of approximately 10%. Any processes that involve the application of pressure such as compression would favour the transformation to a more stable state. Koruderlieva and Platchkova (1997) investigated the effect of compression on the thermally driven phase transformation of gamma-Alumina to alpha-Alumina. They tested different pressures of 30, 60 and 140 MPa. They found that an increase in the amount of pressure resulted in an increase in the rate of phase transformation. This work highlights the influence of mechanical energy in phase transformation. The transformation has always been looked at as a thermally driven process.

The influence of mechanical energy brings about the argument of whether the heat energy is the predominant factor or whether a critical energy supply to the process in either form (heat or mechanical) can initiate the process of phase transformation. It is also of interest to understand whether the process of phase transformation occurs in a similar way whether heat or mechanical energy is used. When heat is supplied, gamma-Alumina is dehydroxylated and eventually results in the formation of alpha-Alumina. With mechanical energy, the exposure of metal terminated surface by breakage along with shear and compression forces can be assumed to encourage the formation of alpha-Alumina as a less energetic state. Both energy supplies have one thing in common; nucleation of alpha-Alumina from aluminium sites.

The factor that all experimental investigations carried out on gamma-Alumina have is the evidence of trial and error. It clearly shows that there are no working principles to start from for the milling of gamma-Alumina. The apparent gap in the need to know the range of impact energies supplied by different milling variables does not go unnoticed. If the energy can be estimated by inputting milling parameters into simulation software, the trouble of trial and error can be eliminated. Threshold energies for achieving milled products with certain properties can be calculated and used as benchmarks during milling processes. It is therefore still necessary to carry out an in depth investigation into the effect of size reduction mechanisms brought about by different stress modes such as shear, impact, and compression on the surface and morphology or structure of the material. Having achieved this, simulation of the experimented energies can provide the much required energies which lack in the research that has been carried for gamma-Alumina.

2.4.4 Effects of Wet-Milling

Having reviewed the effects of dry milling on the properties of gamma-Alumina, it is of interest to review any work done on wet milling. There is a gap in literature on wet milling of gamma-Alumina and hence a review of related oxides and hydroxides has been carried out. The addition of water as a milling medium greatly affects the milling environment including the collision energies that are transferred from milling balls to particles. Stenger *et al.* (2005b) carried out nano-milling of alpha-Alumina using a 1 L stirred media mill with a torque sensor shaft to measure the number of revolutions and an ultrasonic spectrometer to measure temperature, pH, conductivity and particle size distribution simultaneously. In this experimental setup, the suspension material to be ground continuously circulates between the grinding chamber, the stirred vessel, and the ultrasonic spectrometer. A pH regulator vessel was also attached to alter the pH of the suspension for electrostatic stabilization by adding additional ions as required after it has passed through the ultrasonic spectrometer (Stenger *et al.*, 2005b).

The main aim of their work was to achieve stable alpha-Alumina nanoparticles by wet milling. Alpha-Alumina was wet milled in a system that was recording electrochemical properties and pH of the system in-situ in order to achieve electrostatic stabilisation and produce stable nanoparticles. They concluded that operational milling conditions have to be controlled as much as the suspension stability parameters to achieve nanoparticles by wet milling. The results also showed that if suspensions of Alumina are stabilized during milling, nanoparticle sizes of up to 10 nm can be achieved.

Decreasing the size of the grinding media also led to better grinding results as that improved particle-grinding media interactions for smaller alpha-Alumina particle sizes. A high solids mass fraction also improved the milling results due to an increased contact between particles and grinding media, but this is however limited by viscosity effects as the viscosity of the suspension is much higher at high solids content and could reduce the efficiency of particle breakage (Stenger *et al.*, 2005b). This work raises a few factors to consider when milling Alumina; the suspension stability, solids mass fraction and viscosity of the suspension. It is apparent that size reduction has an effect on these factors. As size reduction occurs, the viscosity is expected to increase and with this, the energetics of the particle-milling media collisions would be expected to change.

Stenger *et al*. (2005a) also investigated the mechanochemical changes of the Alumina during the milling process as the stresses that occur in the mill can lead to phase transformations and amorphisation. The stresses in the mill were identified to cause changes from Alumina to Alumina hydroxide. However, the Alumina hydroxide was observed to dissolve at pH less than 5 (Stenger *et al.*, 2005a). The main issues faced with milling to submicron range are particle-particle interactions which in turn result in increased viscosity and agglomeration of particles (Stenger *et al.*, 2005a). These effects can lead to no particle breakage despite addition of energy input. Schönert (1988) carried out a study on the breakage of brittle materials and estimated that the minimum particle size for breakage of brittle materials is in the range of 10 nm to 100 nm depending on the properties of the material. The results of the work by Stenger *et al*. (2005a) however showed that nanometer range particles of Alumina could be achieved and the control of particle-particle interactions was identified to affect the milling greatly.

Damm *et al*. (2011) investigated on the formation of free radicals during the wet milling of Alumina, as a desirable property as it would result in the milled product having properties that are required for the end use. One example given was the direct initiation of polymerisation reactions for the preparation of modified polymer nanoparticles. The material used for their experiments was Alumina with d_{50} of 300nm. A laboratory scale stirred mill with different size of Zirconia beads as the milling media was used for the milling experiments. The Alumina was wet milled with water as the aqueous phase. A solution of 2,2-diphenyl-1-picrylhydrazyl (DPPH) in water was added to the mill (it bleaches when in contact with a free radical and can hence be detected by UV spectroscopy) to show the extent of free radical formation (Damm *et al.*, 2011).

To characterise the Alumina sample, other methods were employed including BET nitrogen adsorption method for the specific surface area, zetasizer for particle size and SEM for morphology of the particles. Damm *et al.* (2011) concluded that particle breakage and mechanical activation of the particle surface both contribute to the generation of free radicals. This gives the benefit that the free radicals produced during milling of Alumina can be used to activate polymerization of acrylic acid and acryl amide which in turn can be used in the formation of hydrogels for use in medical engineering. Of relevance is the formation of free radicals during the milling of Alumina which can be further investigated into whether these have any effect on the end product and whether they can lead to a variance of product properties (Damm *et al.*, 2011).

Pourghahramani *et al.* (2008) also investigated the effect of grinding on the structural changes of hematite sample. Changes to the material structure can be attributed to permanent rearrangement of the crystal lattice as well as structural alterations to the grains of the material. The main characterisation techniques used by Pourghahramani *et al.* (2008) were BET nitrogen adsorption (Brunauer *et al*., 1938), X-ray diffraction (XRD), Thermal Gravimetric Analysis (TGA), Differential Scanning Calorimetry (DSC) and Fourier Transform Infra-red (FTIR). After the milling process, the results showed that the size reduction process resulted in higher specific surface area, smaller crystallites, higher physical broadening and increased x-ray amorphous material. The results also showed greater size reduction in wet milling than in dry milling (Pourghahramani *et al.*, 2008).

An investigation of the influence of operating parameters such as solids concentration, initial size of particles and stirrer speed on the final size distribution and specific energy consumption during wet milling of Alumina hydrate was carried out by Frances and Fadhel (2001).The conclusions drawn from the work show that the operating parameters affect the product during wet milling. They concluded that a slurry of a higher density will require a higher specific energy to obtain a fixed median size. They also concluded that if the feed particles are large, more energy will be required to reach a desired degree of fineness of the product. Also in conclusion, if the mill was run at a high stirrer speed, the grinding rate would also be high as well as the specific energy consumed (Fadhel and Frances, 2001).

Blachou *et al.* (1992) investigated the wet milling of Alumina using hydrochloric acid (HCl) as the solvent. The work by Blachou *et al*. (1992) was aimed to produce stable colloidal dispersions after wet milling of Alumina. Kinetics of reaction and the effect of acid concentration in the milling were also investigated. They also investigated the effects of solids loading, pH and particle size distribution on the viscosity of the slurry formed. The apparatus used in the wet milling experiment was a Pascal ceramic mill and granulometric analysis was carried out after this. A Brookfield viscometer which is a device that employs rotational viscometry was used to measure the viscosity of the Alumina suspension. They confirmed that change in the acid concentration does not change the properties of the wet milled product. The viscosity of the Alumina suspension was found to be dependent on the pH of the materials during milling. They also highlighted that the reason why Alumina is favoured as a catalyst support is due to its high surface area and good porosity characteristics.

The conclusions drawn from the experiments show that gamma-Alumina yields the smallest particles as compared to the hydrated Alumina used in the experiments (Blachou *et al.*, 1992).

The results from the work done on wet milling of Alumina do not report extensive mechanochemical effects. Pourghahramani *et al.* (2008) reports x-ray broadening but does not report any observations of a new material and Stenger *et al.* (2005a) reports on the formation of a hydroxide. This shows that water has an effect on the surfaces of Alumina during milling which can aid in reducing stresses that can initiate phase change. Better understanding of the interaction of water with the surfaces of gamma-Alumina can shed more light into this. The interaction of water with particles during milling can be in different forms as shown in Figure 2.16.

According to Stenger *et al*. (2005a,b), the presence of water can have an effect on particle-particle interactions during milling. Various factors determine the effect of water on a material during milling which include; mill variables such as time and speed, amount of water added as well as the existence of the material before milling such as its surface and crystalline properties (Balaz *et al*., 2013).

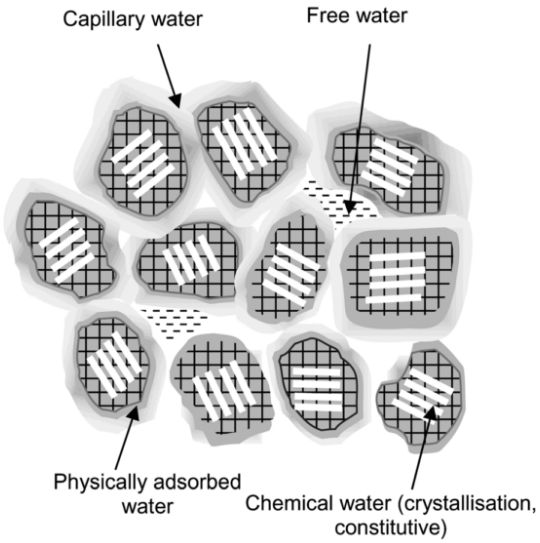

Figure 2.16: Different interactions of water with particles during milling (Balaz *et al.*, 2013)

Water is a polar liquid, and its presence during milling can promote fine milling due to a breakdown of aggregates to primary particles (Juhasz, 1998). However, if the milled product is desired in dry powder form, water added to the mill during milling can be minimized to reduce energy consumption through the drying process. Mechanochemical reactions in wet

milling are often observed when the solids to liquid ratio is very high, often 70% or higher. A higher solids-loading results in higher frictional stresses which initiate mechanochemical reactions. Wet milling is seen as more favourable to its efficiency at size reduction than dry milling as less energy is consumed for smaller particle size distributions (Balaz *et al*., 2013).

2.5 Summary

Milling is a necessary process in the production of gamma-Alumina catalyst supports and different milling methods have been analysed such as planetary ball milling, vibration milling and jet milling. This chapter has covered the properties and uses of catalysts and catalyst supports. It has provided reasons as to why gamma-Alumina is a good choice for a catalyst support. The origins of the material have been explored as well as the structure and morphology of the material. It is clear from this review that during milling, a set of different variables such as mill speed, milling material, ball-to-powder ratio and milling environment need to be understood and well selected in order to achieve a product with the desired properties.

Apart from the importance of mill variables, it is also important to understand how different mills and their variables can affect the structure of the material. There is evidence from different works that have been explored (Zielinski *et al*., 1993, Duvel *et al*., 2011, Wang *et al*., 2005) that high energy milling can result in mechanochemical effects such as phase transformation from gamma-Alumina to alpha-Alumina. It has also been highlighted in the works of Duvel *et al*. (2011) and Balaz *et al.* (2013) that the addition of PCAs in the mill such as water or surface modifying agents can reduce the effects mechanical energy has on the material being milled. The method of trial and error is very much evident in all the milling work reviewed. The need for energy quantification during milling processes as well as a relationship between the energy and mill variables is an area that needs addressing to better understand the effects of milling gamma-Alumina.

The planetary ball mill, vibratory ball mill and jet mill have been selected for use in this project after careful review of literature. Although the SPEX mill is well documented in work pertaining to phase transformations, it would not achieve the required particle size and is not available and hence was not selected in the subsequent studies. The work of Zielinski *et al.* (1993) may also reflect as though significant ground has been covered in understanding gamma-Alumina. The work, however only reports the use of XRD and BET and a shortfall in other useful methods such as TEM as well as further analysis of XRD such as use of Rietveld

refinements can expose more information proving a deeper understanding of the subject. Other studies have also covered the effects of seeding with alpha-Alumina during milling. There are gaps in this work such as a report of the BPRs and milling speeds used. Such information can build a better picture of the process and this can only be achieved by producing a better reported piece of work with all the variables concerned.

Laser diffraction is also in use in conjunction with SEM to derive the size of gamma-Alumina particles and SEM is in use for the shape of the particles before and after milling. Knowledge of the particle size reduction after milling is important in analysing the efficiency of the milling process parameters used for size reduction of the particles. TEM and XRD methods are also included in the characterisation work to determine the crystallite sizes and composition of the gamma-Alumina particles and XRD will also be used in future work to determine lattice strain and vacancies within the samples.

It is important to determine crystallite sizes before and after milling in this work to analyse if there is any reduction in crystallite sizes due to milling or whether the milling results in only breakage of agglomerates. Determining the compositions of the samples also gives clarity to whether any new compounds are formed due to milling which can in turn change properties of gamma-Alumina after milling. BET is also in use to find the specific surface area of gamma-Alumina particles before and after milling to assess any increase in surface area of the gamma-Alumina particles due to milling. This method is important in determining whether the milling method is effective in increasing surface area of the gamma-Alumina particles which is a desirable property for use of the sample as a catalyst support.

A decent attempt to fill in this gap involves an initial understanding of the gamma-Alumina material by characterisation. This can be followed by an analysis of the effects of high energy milling in different mills to analyse different stress modes. Once the effect of different stress modes is analysed, the effect of isolated milling variables can also be analysed as well as isolated stress modes. At this stage, if the milling variables experimented are simulated, a relationship can derived between the collision energies and milling effects observed. Trial and error can be eliminated by providing threshold energies for mechanochemical effects. This attempt is shown in Chapters 3 to 8 of this thesis.

Chapter 3

Characterisation of Gamma-Alumina

An introduction to selected milling methods for use in the project is given. Characterisation methods selected for use are briefly described. Preparation of gamma-Alumina samples for characterisation and the main findings on the particle size, surface area and crystal morphology of gamma-Alumina are presented.

3 Materials and Methods

3.1 Introduction

In order for a material to be selected for use as a catalyst support, it needs to possess properties that make it suitable i.e. high surface area, porous morphology as well as chemical and thermal stability in chemical reactions. Gamma-Alumina is a common choice as it possesses all of the mentioned properties. It is however, necessary to reduce the agglomerate size of gamma-Alumina particles in order to create more surface area for catalyst attachment. This project aims to address the problems associated with poor catalyst attachment due to a change in the structure of the material.

An in-depth analysis of the material before and after milling will give a better understanding of the effects of milling on the macrostructure, microstructure and crystal structure of gamma-Alumina. It is therefore necessary to have an initial understanding of gamma-Alumina before milling energy is applied. This will provide detail on the initial existence of the material and hence provide a platform for comparison, should there be any changes in gamma-Alumina after milling. To achieve an understanding of gamma-Alumina, the knowledge of both physical and surface properties is necessary and hence this chapter consists of detailed descriptions of the test material, properties and the methods used to derive these properties. A discussion of the analysed properties is followed by a conclusion on the morphology of gamma-Alumina.

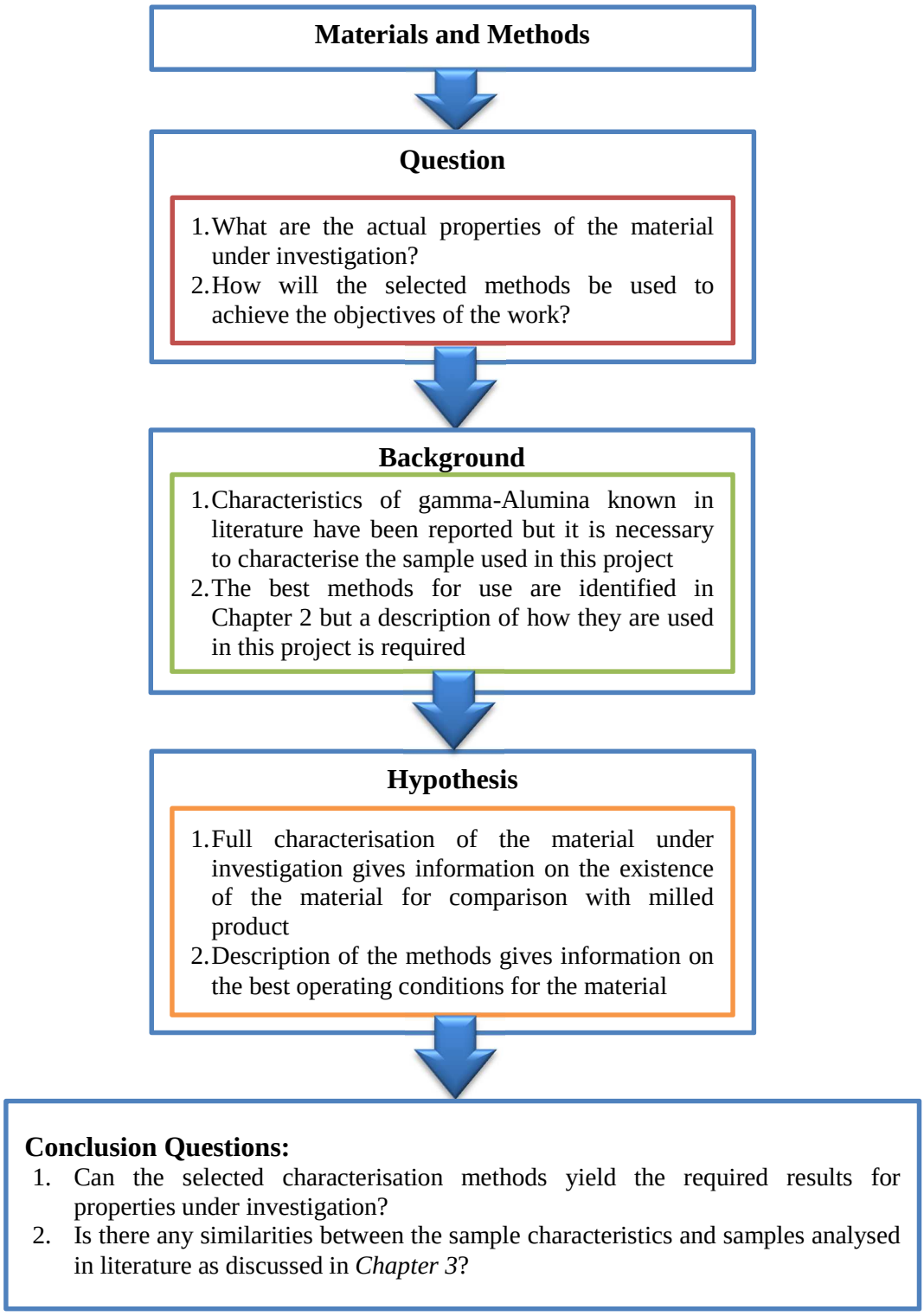

Figure 3.1: Hypothesis formulation for *Chapter 3*

3.2 Milling Methods

Following a review of milling methods in Chapter 2, the three selected milling methods are briefly described in this section.

3.2.1 Planetary Ball Milling

The planetary ball mill is one such mill that can achieve higher forces than gravitational force (50 times more) (Varin *et al*., 2009). It is classified as a high energy ball mill and it is commonly used for mechanical alloying (Lu *et al*., 2013) and the production of metal and composite powders (Angelo *et al*., 2008). It is made up of a revolving base disk and one or more (up to 4) rotating milling pots. The revolving disk rotates in a direction opposite to the milling pot (which rotate about their own axis) hence the name planetary. Popular laboratory scale planetary ball mill manufacturers are Fritsch GmbH and Retsch.

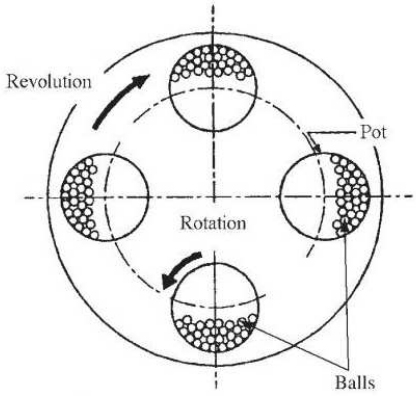

Figure 3.2: Schematic diagram showing pot motion in the planetary ball mill (Neikov *et al*., 2009)

The large centrifugal force created during rotation of the mill disk and milling pots reduces particle size of materials. The mill pots and milling media are available in different material types e.g. tungsten carbide, Zirconia, hardened steel, Stainless Steel, Agate and corundum Alumina. It is recommended to use the same material for the milling pot and milling balls to avoid cross contamination and more effective milling has been shown when monosized milling balls are used. Figure 3.2 shows a schematic of 4 milling pots on the rotating disk of a planetary ball mill with direction of revolution of the rotating disk and pots.

The planetary ball mill is a high energy mill (Angelo *et al*., 2008), where shearing is more prevalent than high velocity collisions. Shear and impact are the stress modes it is best known to apply to powders during milling. Shear occurs when the powder being ground and milling balls roll against the inner wall of the milling pot due to the centrifugal forces supplied by the

motion of the mill. The impact forces arise from the motion of the milling balls as they are thrown from one side of the milling pot to another when the milling pot rotates. Because of this, an increase in the speed of the mill results in an increase in impact and shear forces as the milling balls move at a faster speed (Lu *et al*., 2013).

It is important to note that when high milling speeds are used in the planetary ball mill, the milling pot and its contents can increase in temperature up to 120^{o}C within a short time of between 30 and 60 minutes. It is therefore important to monitor closely the temperature rise and allow adequate cooling of the milling pot before resuming longer mill times (Lu *et al*., 2013). Materials that degrade with high temperatures may also be unsuitable for size reduction with this mill type. Manufacturers such as Retsch have created modified versions of the planetary ball mill that include a cooling system as well as temperature and pressure monitors.

Another factor apart from milling speed that affects the intensity of milling is the size of the milling balls. Various sizes are available from 1 mm up to 30 mm depending on the diameter of the milling pot to be used. An increase in the milling balls diameter can increase the impact energies achieved. However, for the same size milling balls, a change in material from a softer material such as Agate to a harder material such as tungsten carbide can also increase the impact energy in the milling process (Lu *et al*., 2013).

3.2.2 Vibration Milling

The vibratory mill is another type of ball mill that can be classified as high energy and it was created to cut down the milling duration where fine powders are required. In terms of stresses from the mill, both impact stresses and shear stresses are present. Size reduction is caused by the motion of the milling balls and further enhanced by the vibration of milling jar. The mills vary in size from laboratory scale of 12 ml to industrial scale from 50 litres up to 250 litres (Angelo *et al*., 2008). Two common laboratory scale mills are the SPEX 8000 and the Retsch MM200 mills. Figure 3.3 shows the ball and milling container movement of the Retsch MM200 mill.

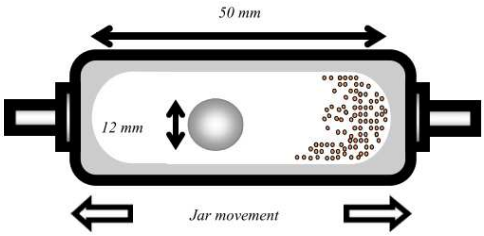

Figure 3.3: Schematic diagram showing ball and powder motion in the single ball mill (Kwan *et al*., 2003)

In vibratory ball milling using the Retsch MM200, short duration collisions dominate and the energy generated by the mill is determined by the chosen milling frequency. Size reduction is by impact, shear and attrition in the Retsch MM200 mill. The SPEX mill differs from the Retsch mill in the motion of the balls as shown in Figure 3.4. There is the presence of an upward movement due to the curvature of the vessel during milling and hence three perpendicular motions are achieved in this mill (Neikov *et al*., 2009).

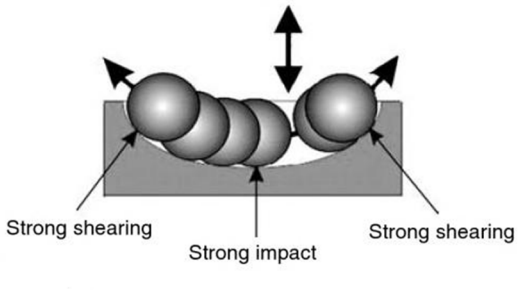

Figure 3.4: Ball motion in the SPEX mill (Neikov *et al*., 2009)

The Retsch MM200 is a single ball mill whilst the SPEX can use multiple milling balls. For research purposes, an investigation of different energies supplied by different mills could yield more varied results if the Retsch MM200 single ball shaker mill is compared with either the SPEX or the planetary ball mill and both the SPEX and the planetary ball mill can produce more energy due to the possibility of using multiple milling balls. Due to availability, the planetary ball mill is used in this work.

3.2.3 Fluid Energy Milling

Another method of milling that can produce high energy and is worth exploring is fluid energy or jet milling. This involves the use of highly pressurised air or steam as fluid energy. The principle of size reduction is mainly particle-particle collisions and some particle-wall

collisions which result in fracture of particles. The milling zones of these mill types include nozzles which are the inlets for the pressurised fluid, and an inlet for the material. The fluid and the material enter the milling zone simultaneously and the material particles are accelerated at sonic velocities resulting in collisions and size reduction (Angelo *et al*., 2008). The nozzles are often made from a wear resistant material such as tungsten carbide (Neikov *et al*., 2009).

In the design of jet mills, Equation 2.2 still governs the kinetic energy supplied during milling. Most modern design jet mills include a classifier that controls the maximum size of the product. Any particles larger than this size are redirected into the milling zone by centrifugal forces for further size reduction. The stress modes that effect size reduction in the jet mill are mainly impact, by way of particle-particle and particle-wall collisions and attrition (Angelo *et al*., 2008).. Figure 3.5 shows the movement of feed and compressed fluid in the operation of a spiral jet mill.

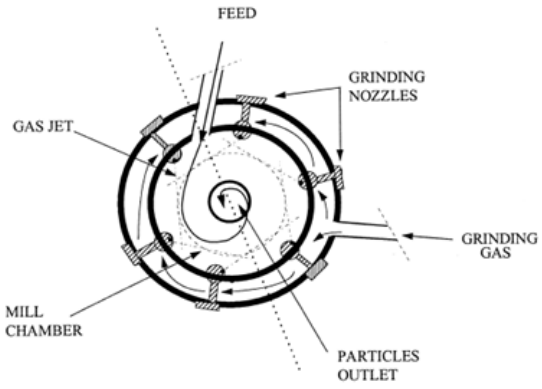

Figure 3.5: Schematic diagram showing movement of powder through the milling chamber in the spiral jet mill (Mio *et al*., 2001)

The jet mill can achieve fine particle sizes less than 5 microns although an initial particle size of 150 microns is recommended. Hence the use of the jet mill may require pre-milling use of other mills to reduce size if the particles are much larger than 150 microns. Due to the nature of reduction (fracture from particle-particle collisions), sphere-shape and cubic materials can be reduced in size more efficiently than plate-like or needle-shaped particles (Angelo *et al*., 2008). Apart from initial particle size and shape, other factors to consider when using the jet mill include moisture content, friability, hardness and flammability for safety purposes. Jet milling is also classified as high energy milling (Neikov *et al*., 2009).

3.3 Characterisation Methods

From previous work on gamma-Alumina reviewed in Chapter 2, five characterisation methods have been selected. A brief description of the methods as well as the theory behind their working principles is given.

3.3.1 Laser Diffraction Technique

Laser diffraction is a particle sizing technique that is in use extensively in this work to determine particle size distributions of gamma-Alumina samples before and after milling. This technique involves the use of a laser beam to determine the size of particles in a sample. As particle pass through the laser beam in the equipment, they scatter light at an angle related to their size. Small particles scatter light at wide angles with low intensity whilst larger particles scatter light at narrow angles with higher intensity (Malvern. 2012). The device to be used in this work is a Mastersizer 2000 and the principles behind its functioning are shown in Figure 3.6.

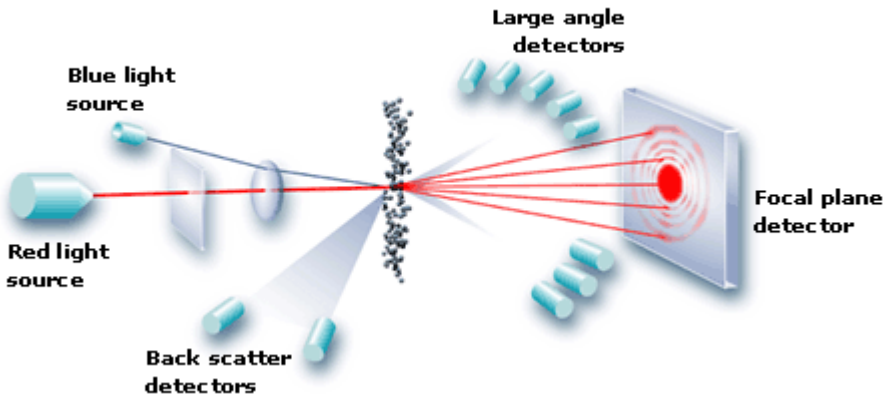

Figure 3.6: Internal setup of the Mastersizer 2000 laser diffraction equipment showing the ligt source and detectors when a sample goes through the equipment(Malvern. 2012)

The setup of a typical laser diffraction system involves a laser of fixed wavelength, a sample dispersed in a suitable dispersant and a series of detectors. The detectors can take a range of measurements from 0.02 degrees to 135 degrees (Malvern. 2012). Figure 3.7 shows the results of the particle size distribution derived from analysing a gamma-Alumina sample. In this work, laser diffraction, using a Malvern Mastersizer 2000, has been carried out for particle size analysis, using water as carrier medium. The samples were dispersed using in-built ultrasound and measured at an average obscuration of 12%.

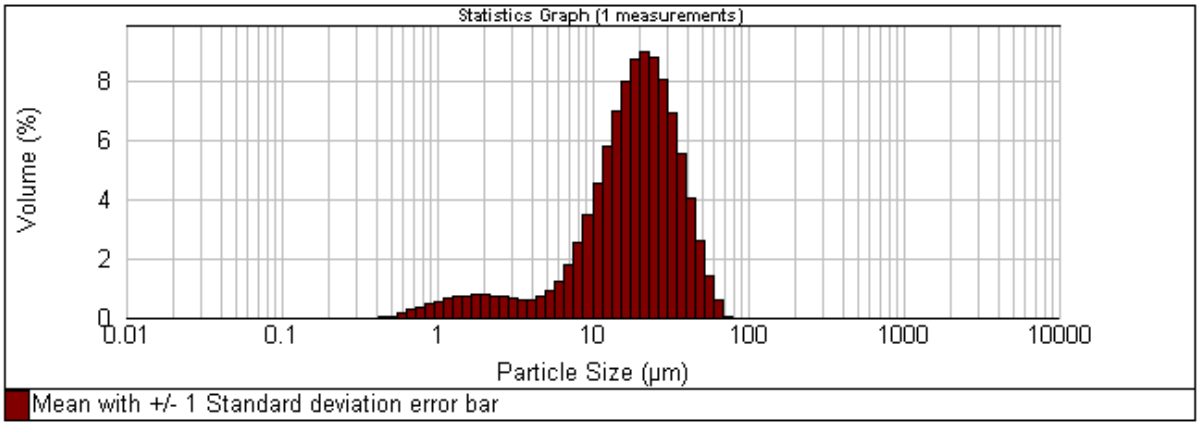

Figure 3.7: Particle Size Distribution of Fine Gamma-Alumina Sample from Mastersizer 2000

3.3.2 Scanning Electron Microscopy

Scanning electron microscopy is in use in this work to analyse the size of gamma-Alumina particles as well as the shape and surface appearance of the particles. It is being used in conjunction with laser diffraction particle sizing to determine the sizes of gamma-Alumina particles before and after milling. The advantage of using both methods will come in the ability to compare and validate results obtained from the different pieces of equipment which use different principles to obtain sizes of particles.

A scanning electron microscope (SEM) is a type of microscope that scatters electrons onto a target and produces an image of the target. The SEM has a high resolution which allows imaging of closely packed particles. The SEM operates by producing a beam of electrons at the top of the microscope by use of an electron gun. The electron beam travels down the microscope in a vertical path that is in a vacuum. The beam also passes through lens and an electromagnetic field which act to keep the beam in its vertical path until it hits the target. Upon hitting the target, electrons and x-rays are ejected from the sample and are all collected by detectors which then convert them into a signal that is used to produce the image in a similar mechanism as that of a television screen (Purdue University. 2010).

Samples to be analysed using SEM have to be prepared before being put under the microscope. Preparation of the samples depends on the type of material to be analysed. Metals can be analysed by putting them through the microscope without prior preparation as they are conductive but non-metals have to be coated with a conductive material before analysis. This coating is usually done using a sputter coater and the coating metals used are gold, platinum or palladium. The sputter coater uses argon gas to displace the metal ions from

a foil which fall onto the sample and form a thin nanolayer of the desired height. The sample can then be analysed using SEM (Purdue University. 2010). Figure 3.8 shows an illustration of a scanning electron microscope.

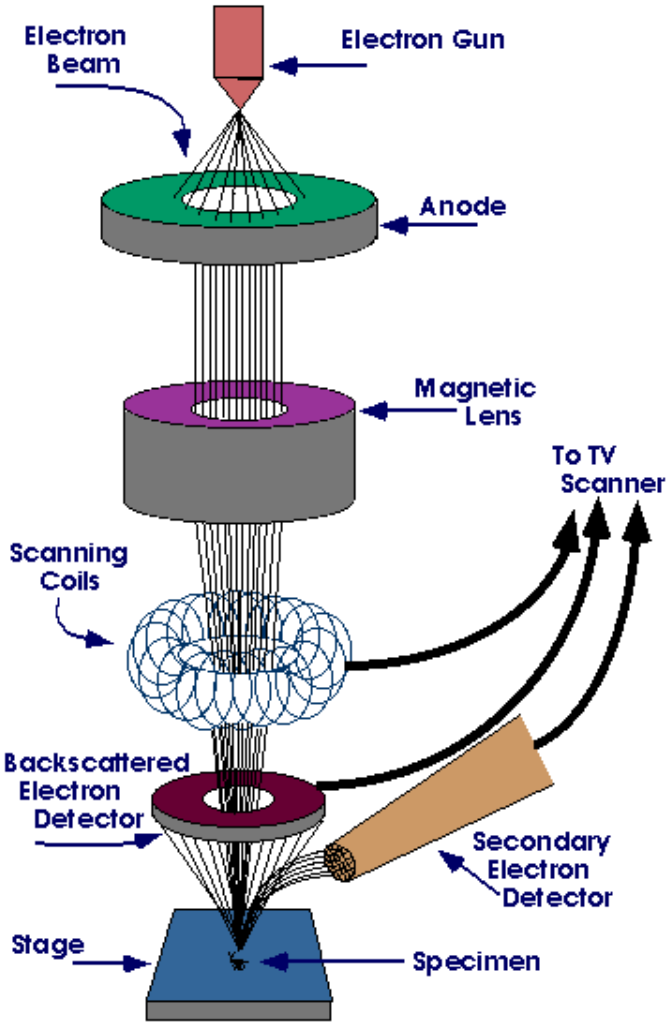

Figure 3.8: Illustration of a Scanning Electron Microscope (Purdue University. 2010)

In this work, SEM analysis is carried out using a Carl Zeiss EVO MA15 scanning electron microscope at 20 kV in secondary and backscattered imaging mode. Carbon tabs were coated with powder samples and placed on SEM metal stubs. Sample stubs were sputter-coated with a conductive layer of gold before analysis to prevent charging. SEM quantitative analysis was carried out using Gatan Digital Micrograph Particle Analysis Software. Average particle sizes were calculated from the derived size distributions of a minimum of 500 particles. The coefficient of variation was also derived by dividing the average particle size with the standard deviation of the size distributions.

3.3.3 X-Ray Diffraction

X-ray diffraction (XRD) involves the scattering of incident x-ray photons to atoms in their crystal lattice. As the x-rays are scattered they give off a constructive interference from which information on the structure of the crystals of the material can be derived. XRD can be used to determine the composition, crystallite sizes, lattice strain and vacancies within a sample. XRD is in use in this work on milled and non-milled gamma-Alumina samples to derive crystallite sizes and detect any phase changes within the material by matching diffraction results with reference files from the Powder Diffraction File. Any changes to the material detected by x-ray diffraction will be quantified by matching the changes with other expected materials within the sample such as impurities and precursors to fully characterise every milled sample Bragg's law can be used to derive lattice spacings within crystal lattices by use of Equation 3.1 below;

$$n\lambda = 2d \sin \Theta \qquad \textbf{Equation 3.1}$$

where n is the order of reflection, an integer, λ is the wavelength of the x-rays, dependant on the x-ray source, d is the space between the crystal planes also known as the d-spacing and Θ is the angle between the beam incident ray and the normal to the reflecting lattice plane. The d-spacing of crystallographic planes can then be derived from the angle, Θ at which the angle leaves the crystal plane. With this method, unknown substances can also be identified by matching results derived from the diffraction with known patterns for different compounds available in the International Centre for Diffraction Data (ICDD) database. As well as d-spacing results, other properties of a material can also be determined which include single particle size and degree of crystallization. Bragg's law can also be displayed in the schematic in Figure 3.9;

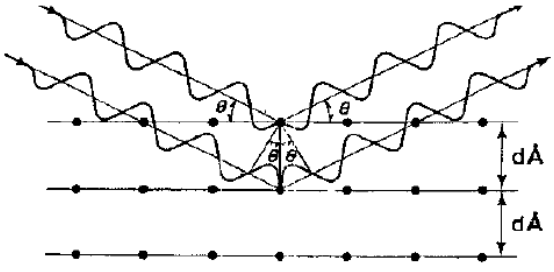

Figure 3.9: Schematic representing Bragg's Law (Ramachandran *et al.*, 2001)

Crystal sizes can also be calculated from x-ray diffraction data. This is mostly favourable when a sample possesses long range order and hence produces clear diffraction peaks representing perfect crystals (Ramachandran et al., 2001). The crystal sizes can be calculated using Scherrer's equation as in Equation 3.2 below;

$$\textbf{Crystallite size; } D_{crystallite} = \frac{K\lambda}{B\cos\Theta} \qquad \textbf{Equation 3.2}$$

Where K is a constant often 0.9, λ is the x-ray wavelength, B is the full peak width at half its maximum intensity (FWHM) and Θ is the Bragg angle. The result obtained from this equation is a reliable estimate that can be used to have an idea of crystallite sizes at different peak intensities. Different x-ray setups are available which use different radiation targets including MO, Cu, Co and Fe targets. The main components in the setup of a modern diffractometer include x-ray protected housing, a goniometer, x-ray tubes and filters, a detector, an x-ray generator and a high-voltage transformer for x-ray tubes (Ramachandran et al., 2001). The setup can be shown in Figure 3.10.

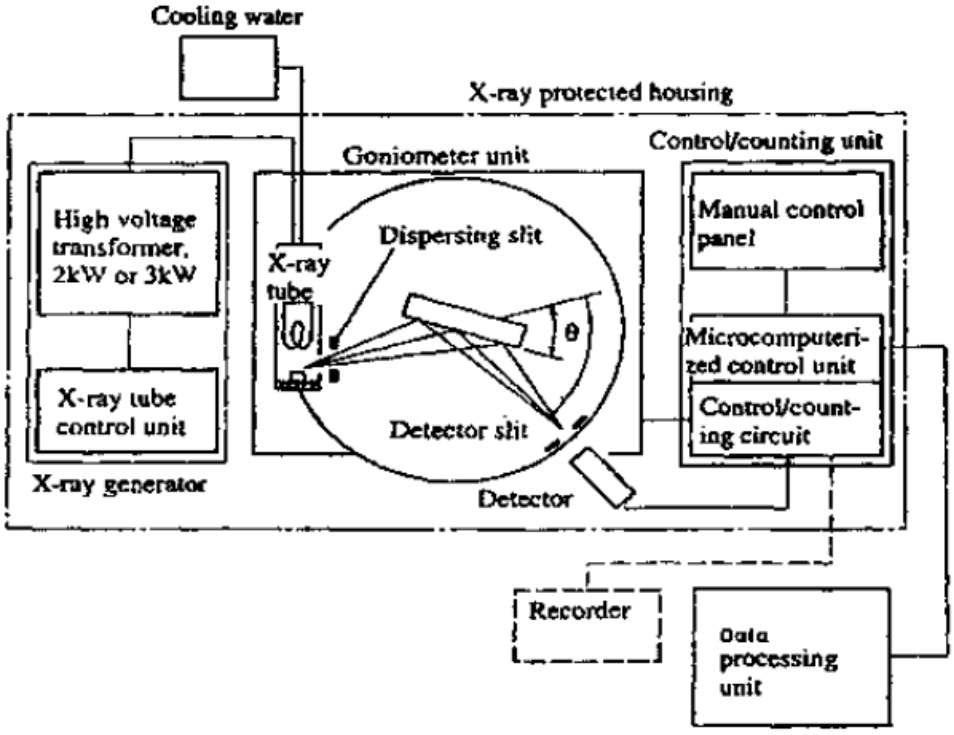

Figure 3.10: Schematic of X-ray Diffractometer (Ramachandran et al., 2001)

In this work, XRD using the Bruker D8 Advance with monochromatic CuKα radiation (λ=0.154 nm) and a 2θ range of 10^o to 90^o, was employed for crystal phase analysis. Further

XRD analysis was carried out by estimating the crystallite size using Scherrer's equation, Xpert Highscore software was used for all XRD analysis including the deriving of proportions of transitional Aluminas in the samples. XRD average crystallite sizes were estimated by selecting 7 peaks corresponding to the dominant Alumina phase and using Scherrer's equation.

3.3.4 Transmission Electron Microscopy

TEM is in use in this work to investigate the surface properties of gamma-Alumina samples before and after milling. The main properties under investigation using TEM include crystallite sizes, composition and surface structures. This method is in use in conjunction with XRD to compare results of crystallite sizes obtained and validate the results as the methods use different working principles.

TEM is a branch of electron microscopy where a beam of electrons as opposed to light is used to produce images of specimen magnified to a high resolution. The use of an electron beam provides the advantage that electrons have a much higher resolving power as opposed to light. TEM and SEM both use electron microscopy with the difference lying in the electrons that are captured during the imaging. In SEM secondary electrons are captured providing information on shape of particles in samples whereas in TEM transmitted electrons are captured giving the internal structure of the particles. The image below showing various types of analyses that can be carried out using x-rays and electrons, shows the differences in interactions of beams with the specimen material (Aguilera et al, 1999).

The illustration in Figure 3.11 shows how TEM beams differ from all other analyses methods as they are transmitted through the sample. TEM equipment can also be described as an inverted light microscope with the illumination coming from the electron gun instead of a lamp. At the top of the device, an electron gun is heats and emits a beam of high velocity electrons. The voltage that is applied to heat the electron gun can be anything between 40 kV and 100kV. The beam is deflected by a magnetic lens and transmits through the specimen. The final image is focussed on a photographic plate or fluorescent screen. The device also has a pump connected to it to maintain a high vacuum in order for the electrons to travel long distances. Because of the mechanism of the TEM device, only samples that are strong enough to resist beam damage can be examined. Figure 3.12 shows a comparison between a TEM and a light microscope (Aguilera et al, 1999).

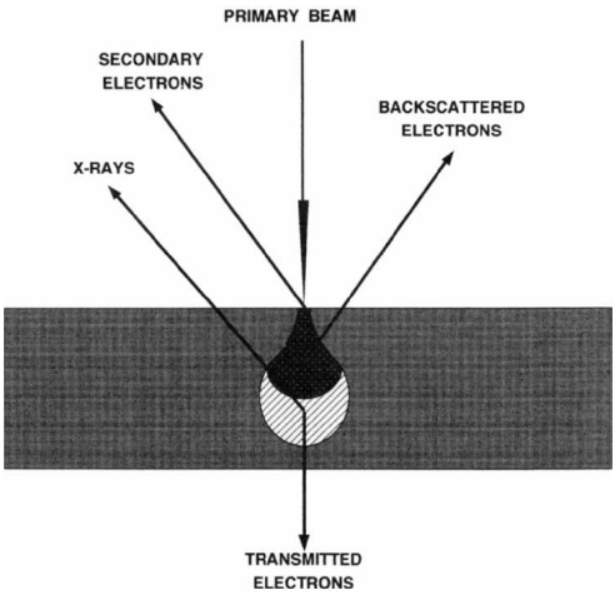

Figure 3.11: Illustration of interactions of beams of electrons and x-rays with specimen material (Aguilera et al, 1999)

In this work, TEM using the FEI CM200 field emission transmission electron microscope, operated at 200 kV, was used to characterise the crystallite morphology of gamma-Alumina samples. Further quantitative analysis of primary particle size and shape was also carried out using Gatan Digital Micrograph. TEM average particle sizes were calculated quantitatively by sizing 30 particles from TEM images.

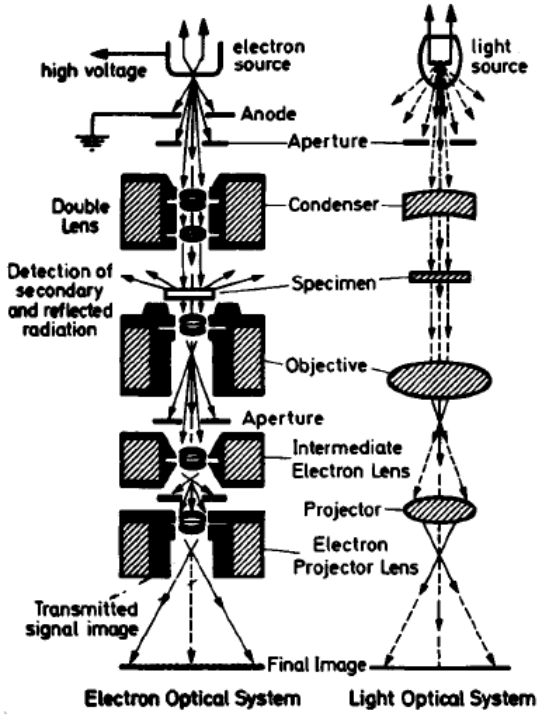

Figure 3.12: Comparison between TEM and Light Microscopy (Aguilera et al, 1999)

3.3.5 BET Theory

The BET method is in use in this work to determine the specific surface area of gamma-Alumina particles before and after milling to assess for any changes to the surface area due to milling. The BET method is based on the physical adsorption of gas molecules on a solid surface. This adsorption mechanism for calculation of available surface area on materials is based on a calculation of the amount of adsorbate molecules that are required to make a single molecular layer on the surface of a specimen material. BET acronym is derived from Brunauer, Emmett and Teller (BET), who extended Langmuir's theory (Langmuir, 1918) to multilayer adsorption in 1938. When the amount of gas adsorbate molecules exposed to the surface of an adsorbent is known, an addition of the amount of adsorbate molecules adsorbed onto a specimen will give the surface area of the specimen. When adsorbate molecules adsorb onto a specimen, there is no distinct point in the process were one monolayer of the molecules is achieved on the surface of the material. The BET method however allows the derivation of this point where one monolayer exists on the surface of the specimen (Lowell et al, 2004).

When physical adsorption is occurring, the more energetic sites on the surface of the specimen are occupied by adsorbate molecules first at low pressure and as the pressure is increased, other sites on the specimen are then occupied by the molecules. BET theory assumes that the adsorbate layer on the specimen and the vapour of the adsorbate are in dynamic equilibrium. This means that the first monolayer on the specimen will be in equilibrium with the vapour and if there are two layers or more, the uppermost layer will be in equilibrium with the vapour. This assumption means that in every layer of adsorbate on the surface of the specimen, there will be equal adsorbate molecules (Lowell et al, 2004). The BET equation used in calculating surface areas is given as Equation 3.3;

$$\frac{1}{W[\frac{P}{P_0}-1]} = \frac{1}{W_m C} + \frac{C-1}{W_m C}\left(\frac{P}{P_0}\right) \qquad \textbf{Equation 3.3}$$

Where P is the equilibrium pressure and P_0 is the saturation pressure of adsorbates at the adsorption temperature, W is adsorbed gas quantity, W_m is the monolayer adsorbed gas quantity and C is the BET constant which is shown as Equation 3.4;

$$C = \frac{E_1 - E_L}{RT} \qquad \textbf{Equation 3.4}$$

Where E_1 is the heat of adsorption of the first layer to adsorb onto the specimen material and E_L is the heat of adsorption of the second and higher layers and equals the heat of liquefaction (Lowell et al, 2004). The BET equation is used to plot an adsorption isotherm of $1/W\ [(P_0/P)-1]$ against P/P_0 which produces a straight line which is usually within the ranges of $0.05 \leq P/P_0 \leq 0.35$. The slope of the straight line is given as Equation 3.5;

$$s = \frac{C-1}{W_m C} \qquad \textbf{Equation 3.5}$$

Where C is the BET constant, s is the slope of the BET plot and W_m is the monolayer adsorbed gas quantity. The intercept of the BET plot is also given as Equation 3.6;

$$i = \frac{1}{W_m C} \qquad \textbf{Equation 3.6}$$

Where i is the intercept, C is the BET constant and W_m is the monolayer adsorbed gas quantity. From calculating s and i as above, the adsorbed monolayer weight, W_m can be calculated as Equation 3.7;

$$W_m = \frac{1}{s+i} \qquad \textbf{Equation 3.7}$$

From this, the total surface area, S_t can then be calculated as Equation 3.8;

$$S_t = \frac{W_m \bar{N} A_x}{\bar{M}} \qquad \textbf{Equation 3.8}$$

Where A_x is the cross sectional adsorbate area, $\bar{M}$ is the adsorbate molecular weight, $\bar{N}$ is Avogadro's number and W_m is the adsorbed monolayer weight (Lowell et al, 2004).

For a BET experiment to be run, the adsorbent sample is first added to a glass vessel and degassed to remove any moisture and impurities within the sample. This can be done for up to 16 hours to ensure that the surface of the adsorbate is free from contaminants. A small sample size of about 0.5 g is used and after degassing, the sample is then attached to the surface area measurement device. A dewar of liquid nitrogen is placed at the bottom of the sample glass tube to cool the sample and maintain a low temperature in order to promote interaction between the solid adsorbent surface and the gas adsorbate (Barron, 2012).

The adsorbate gas, nitrogen in this case is injected into the glass vessel in calibrated amounts. Before and after every measurement is taken, helium gas is used to quantify the dead volume in the sample glass vessel as it does not interact with the adsorbent. The amount of adsorbed

gas depends on the available surface area, temperature, pressure and interactions of the gas with the solid surface area. Relative pressures of less than atmospheric pressure are also maintained in the glass vessel by maintaining a partial vacuum in the vessel. Pressure transducers exist on the BET equipment which measure the changes in pressure caused by the adsorption process. When the saturation pressure is reached, adsorption seizes and the sample is then heated to release all the adsorbed nitrogen. The amount of this nitrogen is quantified and used to plot one of the BET isotherms of relative pressure against quantity of nitrogen adsorbed.

The desorption process is also recorded in the BET isotherms when the nitrogen is released from the sample during heating. Nitrogen gas adsorption-desorption isotherms will be used to derive surface areas for different gamma-Alumina samples (Barron, 2012). Adsorption isotherms have been classified by the International Union of Pure and Applied Chemistry (IUPAC) to describe six different sorption behaviours (Lowell et al., 2004). They range from Type I to type VI. BET analysis involves use of three of these isotherms namely type I, type II and type IV.

Type I isotherm describes microporous materials with pore diameters less than 2 nm such that only one monolayer is likely to form on the adsorbent, type II isotherm describes non-porous or macroporous materials where monolayer and multilayer formation is expected and this is the most common isotherm achieved in the BET technique and type IV isotherm is achieved in mesoporous materials with pore diameters of 2 nm to 50 nm and has a hysteresis loop which is a result of pore condensation. The six sorption isotherms can be shown in Figure 3.13 (Lowell et al., 2004). In this work, BET surface area measurements were carried out to analyse any changes in specific surface area in the different mills. This was done using BET nitrogen gas adsorption with the Micromeritics Tristar 2000. Samples were degassed at 400^{o}C for a total of 4 hours prior to analysis. BET particle sizes were estimated from specific surface area (SSA) by use of Equation 3.9.

$$\mathbf{D_{particle}\ (nm) = 6/(\rho * SSA)} \qquad \textbf{Equation 3.9}$$

$D_{particle}$ is the particle size in nm, ρ is the density in gm^{-3} and SSA in m^2g^{-1} is the specific surface area derived from BET.

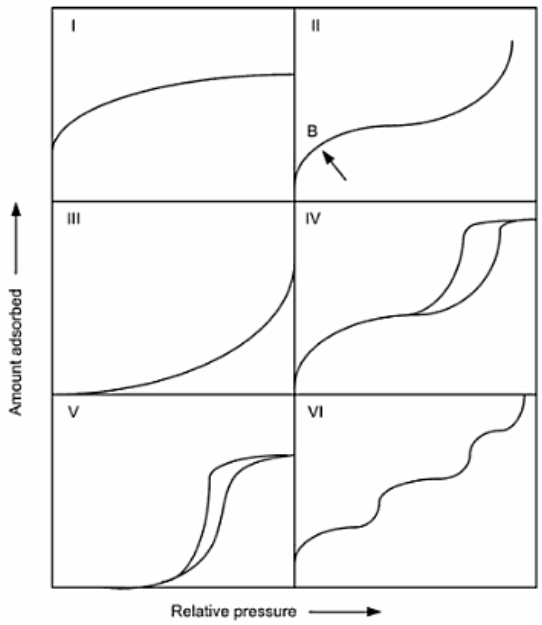

Figure 3.13: IUPAC classification of sorption isotherms (Lowell et al., 2004)

3.3.6 Solid-state NMR

Nuclear Magnetic Resonance (NMR) spectroscopy can be defined as the study of molecules by recording the interaction between the nuclei of molecules placed in a strong magnetic field and radiofrequency electromagnetic radiations. This is also known as the 'Zeeman effect' as it was first discovered by Zeeman. Radiofrequency radiation, which is the type of radiation used in NMR is at the lowest energy end of the electromagnetic spectrum. It involves energies of the order of 10^6 Hz. In electromagnetic radiation, each quantum of radiation is called a photon and a photon possesses a discrete amount of energy that is directly proportional to the frequency of the radiation.

Radiations below the visible region are incapable of breaking bonds and so radio-frequency radiations fall in this region. In order for a particle to absorb a photon of electromagnetic radiation, the particle must possess a uniform periodic motion with a frequency that matches the frequency of the absorbed radiation. Constructive interference of the oscillations of the particle follows this process and the system can be said to be in resonance. Absorption of radio-frequency radiation occurs at this stage. NMR can then be described as the immersion of nuclei in a magnetic field which is followed by matching their frequency with the frequency of electromagnetic radiation to ensure that energy absorption occurs (Rahman *et al*., 2015). The main working principle of NMR is in the magnetic properties of atomic nuclei. The resonance signal is the spectral line that is recorded from the radio-frequency

receiver after the absorption of energy is detected. For absorption of energy to occur, there must be an interaction of the nuclear magnetic moment with an external magnetic field which leads to a nuclear energy level diagram. This is because magnetic energy of the nucleus is restricted to certain discrete values called eigenvalues which are associated with eigenstates (only states an elementary particle can exist). The diagram in Figure 3.14 shows how a resonance signal is generated from a sample.

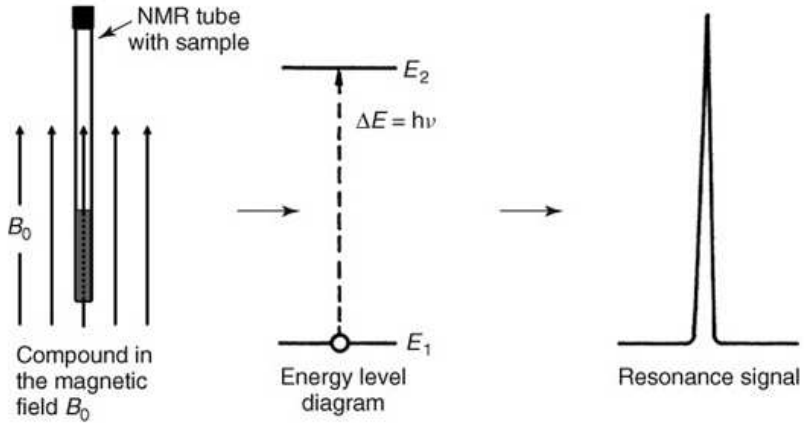

Figure 3.14: Generation of a resonance signal in solid-state NMR spectroscopy

A spectrum can be generated for any atoms whose nuclei have a magnetic moment higher than zero. When a resonance signal is generated, the area under the signal is proportional to the number of protons that give rise to the signal and this can be measured by integration. Proton resonances can form singlet peaks but can also sometimes form triplets and quartets by splitting as a result of spin-spin coupling. Spin-spin coupling is caused by a magnetic interaction between different nuclei. Because protons reside in different chemical environments, different resonance signals can be found for protons. They are separated by chemical shift. Correlations of spectral parameters, chemical shift and spin-spin coupling can give the structure of chemical compounds as well as structure determination of unknown compounds.

Aluminium-Magic Angle Spinning-NMR (Al-MAS-NMR) has been selected as a characterisation method to identify aluminium cations in different chemical environments in both as-received and milled samples. This method can be used to identify different coordinations of Alumina cations. Magic Angle Spinning (MAS) is the technique used in solid-state NMR to improve identification and analysis of spectrum by spinning the samples at a set frequency at the magic angle. The magic angle (θ_m) is the angle at which $\cos^2 \theta_m =$

1/3 with respect to the direction of the magnetic field. MAS narrows the broad lines in the spectra obtained and hence improves the resolution (Günther, 2013). In this work, Al-MAS-NMR measurements were carried out using a Bruker Avance III HD NMR spectrometer. The external magnetic field used corresponded to an Al NMR resonance frequency of 195.25 MHz. A commercial 4 mm MAS probe was used in combination with 4 mm high speed rotors. These had an inner diameter of 2.5 mm. The spinning speed was set to 15 kHz. NMR spectra were recorded with a single pulse sequence with an excitation pulse length of 16 μs. The recycle delay was 5 s.

3.4 Test Material (γ-Al_2O_3)

Gamma-Alumina, which will be referred to as γ-Al_2O_3 in this thesis, is a commercially available material, manufactured by the dehydration of synthetic boehmite, which is, in turn, derived from sodium alkoxide. The γ-Al_2O_3 sample used is a high purity activated powder, manufactured by Sasol under the code Puralox SCFa-140. It is manufactured from a high purity boehmite-Alumina. The sample is available as an odourless, white powder.

3.5 Properties of γ-Al_2O_3

Finding a relationship between changes to γ-Al_2O_3 material properties and milling energy is of paramount importance. The generic physical properties of γ-Al_2O_3 are shown in Table 3.1. It is interesting to note that the melting temperature of γ-Al_2O_3 is high (2000^{o}C) and this provides thermal stability during reactions where γ-Al_2O_3 is used as a catalyst support.

Table 3.1: Physical Properties of Sasol SCFa-140 γ-Al_2O_3 (SasolTechData. 2012)

Property	**Value**
Melting point (^{o}C)	2000
Purity (%)	98
Impurities	La_2O_3, Na_2O
Loss of Ignition, H_2O (%)	2
Packed Bulk Density (g/l)	800-1000

The main properties that are of relevance to milling and the use of γ-Al_2O_3 as a catalysts support include particle size, surface area and crystal morphology. These are investigated in further detail by a full characterisation of the Puralox SCFa140 γ-Al_2O_3 sample.

3.5.1 Particle Size of γ-Al_2O_3

During milling processes where size reduction is the aim, the particle size of a material plays a crucial role. The initial and desired post-milling particle size can determine the appropriate mill to be used for size reduction as well as the energy required. Initial knowledge on the particle size distribution is required. Laser diffraction is a suitable method for analysis of particle size. The Hydro unit of the Mastersizer 2000 is used for particle size analysis. A small mass of γ-Al_2O_3, typically less than 0.5 g, is added to the dispersion tank. The dispersant used is water as γ-Al_2O_3 is insoluble in water.

The sample is stirred at 650 rpm in the tank with 50% ultrasound to aid in dispersing γ-Al_2O_3 particles. The sample is delivered to the optical unit at the machine pump speed of 1750 rpm. As particles pass the laser in the optical unit, the diameter of particles is calculated and reported as a particle size distribution. Analysed samples are disposed. The particle size distribution of γ-Al_2O_3 observed by laser diffraction is shown in Figure 3.15. The particle sizes are also reported according to particle sizes below which 10% (d_{10}), 50% (d_{50}) and 90% (d_{90}) of the total measured sample lies and this is shown in Table 3.2. D_{10}, d_{50} and d_{90} particle sizes given by the manufacturer of the γ-Al_2O_3 sample are also given in Table 3.2.

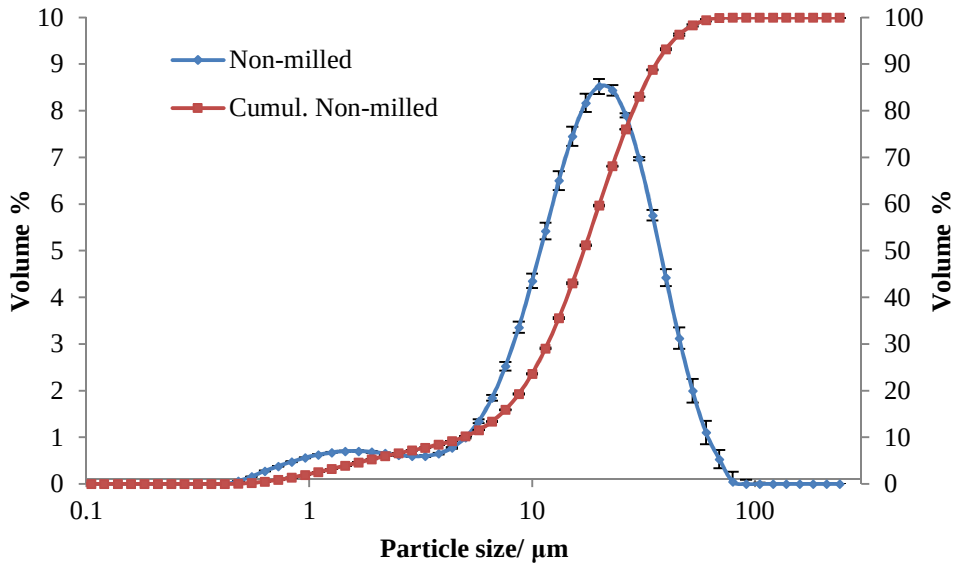

Figure 3.15: Particle Size Distribution and Cumulative Particle Size Distribution of γ-Al_2O_3 by Laser Diffraction

Table 3.2: Particle Sizes of γ-Al_2O_3 Given by Manufacturer and Determined by Laser Diffraction

γ-Al_2O_3 Sample	Particle size (μm)		
	D_{10}	D_{50}	D_{90}
Laser Diffraction	6.2	21.4	49.1
Manufacturer (Sasol)	5.9	19.5	45.3

As seen in Figure 3.15, the particle size distribution shows that the greater percentage of γ-Al_2O_3 particles lie below 100 μm. The manufacturer's particle sizes and particle sizes determined by laser diffraction are relatively similar. Laser diffraction is also used for characterisation of particle size in the milled product in subsequent chapters. The principle behind the particle size measurements by this laser diffraction technique is based on the Mie theory. It gives the equivalent sphere of the scattering intensity of a single particle detected during a measurement. Due to the assumption associated with this technique, the γ-Al_2O_3 particles were also analysed by SEM to observe the maximum projected area of particles and particle shapes.

SEM analysis is carried out using a Carl Zeiss EVO MA15 scanning electron microscope at 20 kV in secondary and backscattered imaging mode. Carbon tabs are coated with powder samples and placed on SEM metal stubs. Sample stubs are sputter-coated with a conductive layer of gold before analysis to prevent charging. SEM quantitative analysis has also been carried out using Gatan Digital Micrograph Particle Analysis Software (Gatan Digital Micrograph Offline, 2014). Average particle sizes were calculated from the derived size distributions of a minimum of 500 particles. The coefficient of variation was also derived by dividing the average particle size with the standard deviation of the size distributions. Irregular and spherical particles with smooth surfaces are observed in Figure 3.16. It can also be seen that the particles have a wide particle size distribution.

The coefficient of variation calculated from the rough quantitative analysis and shown in Table 3.3 shows a large variation in the particle sizes of γ-Al_2O_3 observed. It is appreciated that SEM particle sizing is not conclusive due to the nature of the method where the full sample may not be represented by the powder on a single SEM stub. However, it provides an idea of observable sizes as well as insight into the smallest particles in the sample. The smallest particle observed by laser diffraction and SEM is 0.4 μm and 0.2 μm respectively. A

full size distribution can be obtained from laser diffraction, however, further information on finer material within the sample is better analysed by SEM.

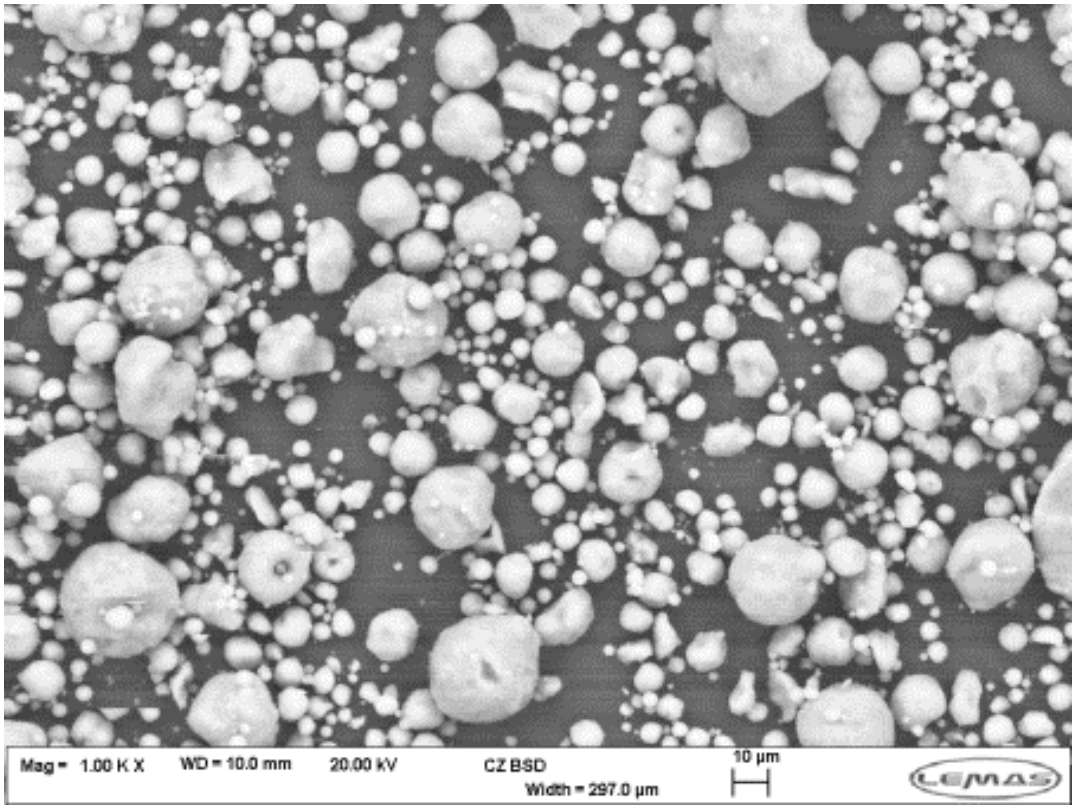

Figure 3.16: Scanning Electron Micrograph of γ-Al_2O_3 Particles

Table 3.3: SEM Number-based Quantitative Particle Size Analysis for γ-Al_2O_3

Number-based Average Particle Size (µm)	11.4
Coefficient of Variation	0.9
Smallest observed particle (µm)	0.2

3.5.2 Specific Surface Area of γ-Al_2O_3

The specific surface area of γ-Al_2O_3 is derived from nitrogen adsorption using the Brunauer, Emmet and Teller (BET) method. The BET method used is based on the physical adsorption of nitrogen gas molecules on the γ-Al_2O_3 surface. The equipment used for this method is the Micromeritics Tristar ASAP-2000. The adsorption mechanism for calculation of available surface area is based on a calculation of the amount of nitrogen adsorbate molecules that are required to make a single molecular layer on the surface of γ-Al_2O_3. When a BET experiment is run, the γ-Al_2O_3 sample, typically 0.5 g is first added to a glass vessel and degassed at 400^oC for 4 hours to remove any moisture and impurities within the sample. Liquid nitrogen

is used to cool the sample and maintain a low temperature in order to promote interaction between the solid adsorbent γ-Al_2O_3 surface and the nitrogen gas adsorbate (Barron, 2012). Once attached to the BET equipment, nitrogen gas is injected into the samples in calibrated amounts. Before and after every measurement is taken, helium gas is used to quantify the dead volume in the sample glass vessel as it does not interact with the adsorbent. The amount of adsorbed nitrogen gas depends on the available surface area, temperature, pressure and interactions of the gas with the solid surface area of γ-Al_2O_3. Relative pressures of less than atmospheric pressure are also maintained in the glass vessel by maintaining a partial vacuum in the vessel. Pressure transducers exist on the BET equipment which measure the changes in pressure caused by the adsorption process. When the saturation pressure is reached, adsorption seizes and the sample is then heated to release all the adsorbed nitrogen.

The amount of this nitrogen is quantified and used to plot one of the BET isotherms of relative pressure against quantity of nitrogen adsorbed. The desorption process is also recorded in the BET isotherms when the nitrogen is released from the sample during heating. Calculations of specific surface area are made from the amount of nitrogen adsorbed at specific relative pressures. Pore sizes and pore volumes are also derived using this method. Figure 3.17 shows the plot of nitrogen adsorbed onto γ-Al_2O_3 surfaces at specific relative pressures. The graph shows a large amount of nitrogen adsorbed. The values of specific surface area, pore size and pore volume derived are also shown in Table 3.4.

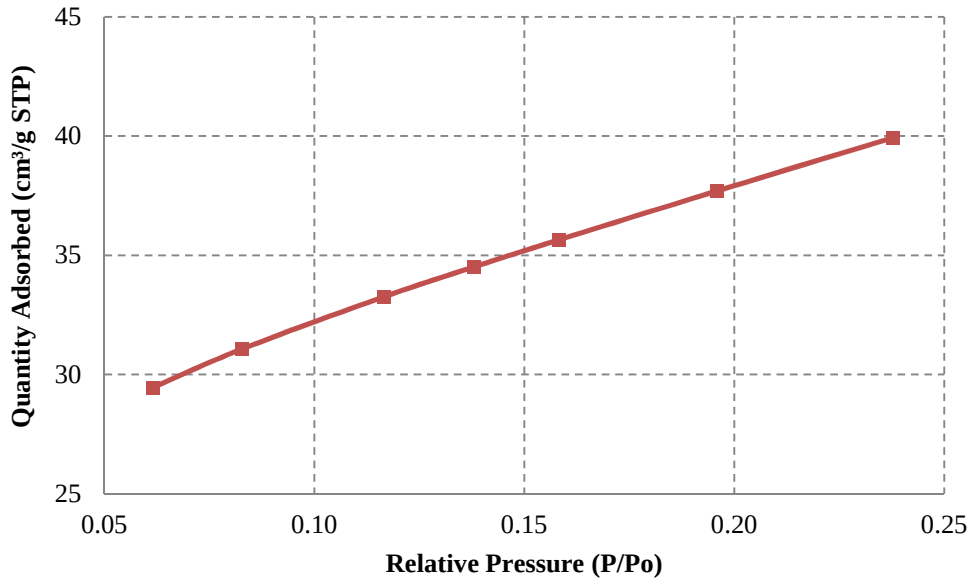

Figure 3.17 Graph showing Relative Pressure of Nitrogen against Amount of Nitrogen: Adsorbed onto the γ-Al_2O_3 Surface

Table 3.4: Specific Surface Area, Pore Size and Pore Volume of γ-Al_2O_3

Specific Surface Area (m^2/g)	145
Pore Size (nm)	13.85
Pore Volume (cm^3/g)	0.47

The BET method can be used to estimate primary particle sizes from specific surface area (SSA) by use of Equation 3.9.

$$D_{particle}\ (nm) = 6/(\rho * SSA) \qquad \text{Equation 3.9}$$

Where $d_{particle}$ is the particle size in nm, ρ is the density in g/m^3 and SSA in m^2/g is the specific surface area derived from BET. It should be noted that this estimated particle size assumes spherical particles with surfaces that come in contact over a minute area. It does not give an accurate value but a range in which the particle sizes fall. The method also assumes monosized particles. Table 3.5 shows a calculated particle size of 13.6 nm highlighting the existence of γ-Al_2O_3 as very small crystallites. If the pore size and primary particle size are compared, it can be seen that their sizes are similar, 13.85 nm and 13.6 nm respectively. This reflects that γ-Al_2O_3 has relatively large pores. The pore volume is also observably large. XRD and TEM can be used to verify the size of primary particles of γ-Al_2O_3.

Table 3.5: BET Particle Size of γ-Al_2O_3

Sample	BET Primary Particle Size (nm)
A-R	13.6

3.5.3 Crystal Morphology of γ-Al_2O_3

Particle size as measured by laser diffraction shows the agglomerate size of γ-Al_2O_3 particles. In order to gain an idea of the primary particle size, shape and bulk crystal structure, X-ray diffraction (XRD) and Transmission Electron Microscopy (TEM) are used to characterise γ-Al_2O_3. XRD is used for phase identification and to analyse the bulk crystal structure and crystallite size of the material, whilst TEM is used to observe primary particle size and shape, and crystallinity of γ-Al_2O_3. The principle of XRD is based on the scattering of incident x-ray photons to atoms in their crystal lattice. As the x-rays are scattered they give off a constructive interference from which information on the structure of the crystals of the material can be derived. XRD can be used to determine the composition, crystallite sizes,

lattice strain and vacancies within a sample. A sample holder is filled with powder sample creating a flat surface at the top. The sample holder is placed in the XRD machine and run with monochromatic CuKα radiation (λ=0.154 nm) at a 2θ range of 10^o to 90^o. Figure 3.18 shows the XRD diffractogram for γ-Al_2O_3 derived from the Bruker D8 Advance Powder Diffraction equipment and when fitted using Xpert Highscore Software (Panalytical B.V. Highscore with Plus Option, 2014) matches to ICDD reference file 00-010-0425 for γ-Al_2O_3.

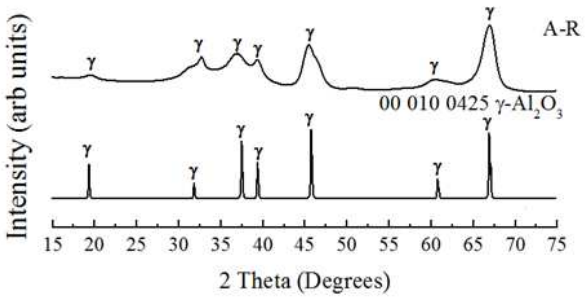

Figure 3.18: XRD Diffractograms showing the γ-Al_2O_3 sample and ICDD Reference File 00-010-0425 for γ-Al_2O_3

Broad peaks are observed suggesting that the crystallites of γ-Al2O3 are relatively small. Equation 3.2 shows the Scherrer equation (Cullity and Stock, 2001) used to estimate the crystallite sizes of γ-Al_2O_3. As shown in Table 3.6, the calculated crystallite sizes of γ-Al_2O_3 range from 5-16 nm.

Table 3.6: Peak Positions, D-spacing, Crystallite Sizes and hkl for all γ-Al_2O_3 Peaks Matching to ICDD Reference File 00-010-0425 for γ-Al_2O_3

Peak	2 Theta (º)	d-spacing (nm)	Crystallite size (nm)	h	k	l
1	19.7	0.45	11.3	1	1	1
2	31.1	0.29	11.5	2	2	0
3	32.8	0.27	15.4	1	1	2
4	36.9	0.24	5.8	3	1	1
5	39.6	0.23	11.8	2	2	2
6	45.5	0.20	8.7	4	0	0
7	60.2	0.15	11.4	5	1	1
8	67.3	0.14	6.7	4	4	0
9	84.9	0.11	12.0	4	4	4

The calculated XRD average crystallite size from the peaks observed and shown in Table 3.6 is 10.51 nm. TEM is used as a complimentary method to analyse crystallite sizes of γ-Al_2O_3. The TEM used is the FEI CM200 field emission transmission electron microscope, operated

at 200 kV. TEM is a branch of electron microscopy where a beam of electrons as opposed to light is used to produce images of specimen magnified to a high resolution. The use of an electron beam provides the advantage that electrons have a much higher resolving power as opposed to light. In TEM, transmitted electrons are captured giving the internal structure of the particles.

The γ-Al_2O_3 powder sample is dispersed in methanol and placed in at ultrasonic bath for 5 mins. A single drop of the dispersion in then placed on a holey copper TEM grid. The TEM grid is placed on the sample holder and inserted in the microscope. From the TEM micrograph of γ-Al_2O_3 in Figure 3.19, the γ-Al_2O_3 sample appears to be made up of plated primary particles. The particles can appear as needles depending on their orientation on the copper grid when TEM analysis is carried out. The crystallite sizes observed by TEM are below 30 nm and hence support the crystallite size estimates calculated from XRD.

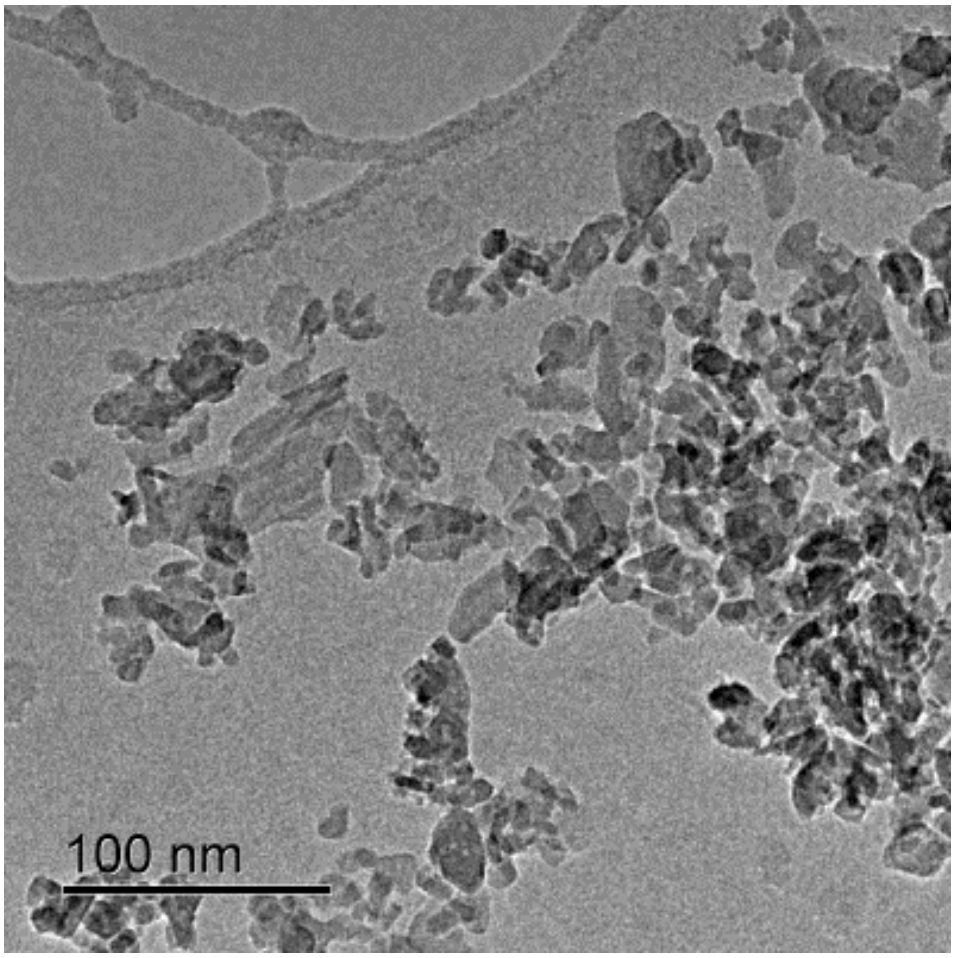

Figure 3.19: TEM Micrograph of γ-Al_2O_3

A TEM average particle size can also be calculated by selecting 10 TEM micrographs and carrying out a rough quantitative analysis of crystallite sizes using Gatan Digital Micrograph (Gatan Digital Micrograph Offline, 2014). The observed primary particle size shown in Table 3.7 is 16.9 nm.

Table 3.7: Average particle size, Coefficient of Variation and Aspect Ratio from TEM images of γ-Al_2O_3

Average particle size (nm)	16.9
Coefficient of variation	0.5
Aspect ratio	2.5

Al-MAS-NMR is also used identify the different environments the aluminium cations exist in in the samples before and after milling. It is mainly useful in this project for identifying whether Al cations are in octahedral, pentahedral or tetrahedral sites. This is valuable in identifying any changes that will have occurred to the material during milling. The NMR results shown in Figure 3.20 also show that the aluminium atoms in the sample are shared between tetrahedral and octahedral sites with a greater percentage in octahedral sites.

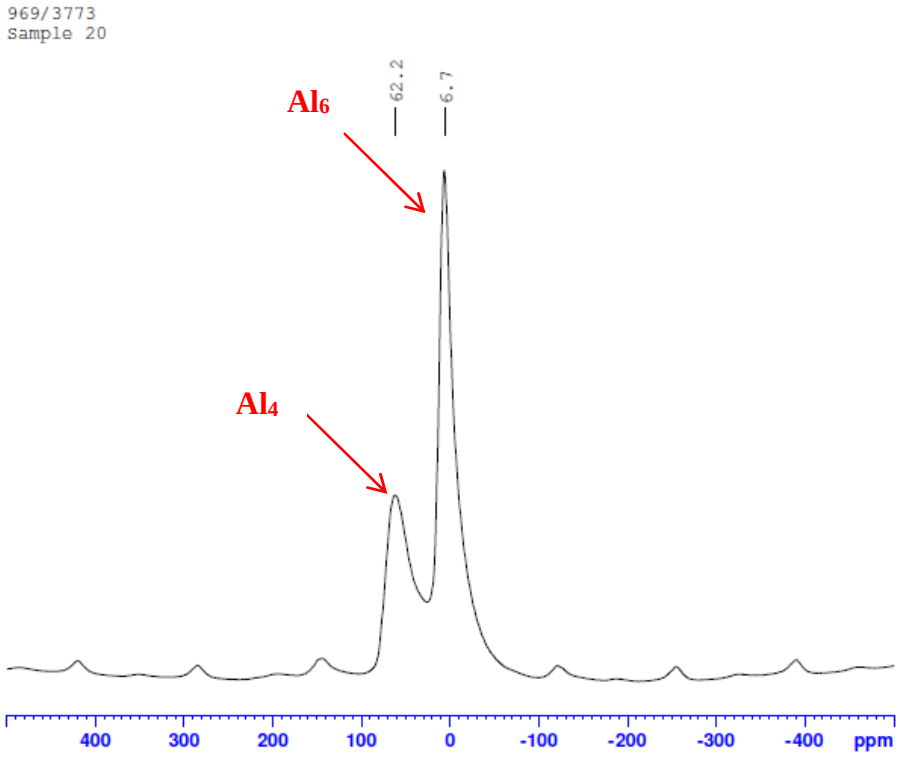

Figure 3.20: NMR results of A-R γ-Al_2O_3

3.6 Discussion

There is reasonable agreement between the laser diffraction particle size results and the manufacturer's particle sizes and hence laser diffraction has been adopted for use in particle sizing in subsequent chapters. The particle sizes observed by laser diffraction are in the micron range. When compared with the primary particles derived by XRD and observed by TEM in the nanometre range, it is clear that the γ-Al_2O_3 sample is composed of very large agglomerates of much smaller primary particles. With an appreciation of the difference in technique principles of SEM and laser diffraction, the SEM micrographs show that the sizes observed by laser diffraction are reliable as the particles observed were in the range of the particle size distribution derived from the Mastersizer 2000.

SEM also proves to be a necessary complimentary method for particle size and shape as it shows particles smaller than those observed by laser diffraction and a mixture of spherical and irregular shapes. The BET method used to derive specific surface area shows a large surface area for γ-Al_2O_3 which compliments the material's suitability for use as a catalyst support. The small crystallite sizes observed by BET, TEM and XRD are the main reason as to why γ-Al_2O_3 has a large specific surface area. A comparison of the primary particle sizes observed by these three methods is shown in Table 3.8.

In general, there is reasonable agreement, qualitatively, between the sizes derived using the 3 techniques as the principles of measurement of the methods are different. The primary particles are single crystal in nature, as suggested in TEM bright field images. Looking at Table 3.8, it is important to note that the γ-Al_2O_3 crystallite sizes estimated from XRD using the Scherrer's equation are smaller than those observed by TEM owing to presence of a core-shell structure within γ-Al_2O_3 primary particles with a surface disordered shell surrounding a more ordered crystalline core as observed by (Rozita *et al.*, 2014).

Table 3.8: Primary Particle Sizes as Observed using TEM and Estimated from XRD and BET

TEM Primary Particle Size average (nm)	XRD Crystallite Size average of 7 peaks (nm)	BET Primary Particle Size (nm)
10.5	9.7	13.6

3.7 Conclusions

The characterisation of γ-Al_2O_3 has been carried out with a focus on three main properties; particle size, surface area and crystal morphology. It is important to achieve the desired particle size reduction during milling whilst preserving the crystal morphology of the material as a change in morphology can result in a loss of surface area. It is therefore necessary to fully characterise a material before milling in order to have a base from which milled products can be compared. Successful characterisation has been displayed in this chapter and has given a reasonably complete insight into the existence of the γ-Al_2O_3 sample before milling. It is now of particular interest to further focus on the shift in particle sizes in laser diffraction in order to quantify size reduction after milling and complement this method with particle shape and size analysis with SEM. Figure 3.21 shows a plan of how the experimental objectives will be achieved.

BET gives the specific surface area and it is of interest to observe how surface area is affected by size reduction of agglomerates. If any changes occur to the crystallinity of the material, these should be observed in XRD diffractograms as well as crystallite observation under TEM. BET can also shed light on crystal morphology changes as different materials can exhibit different surface areas, and hence, should phase change as that observed in previous work detailed in Chapter 2 occur, this will also be marked by a difference in surface area. Characterisation and analysis of milled γ-Al_2O_3 by use of these methods will be carried out in the following chapter.

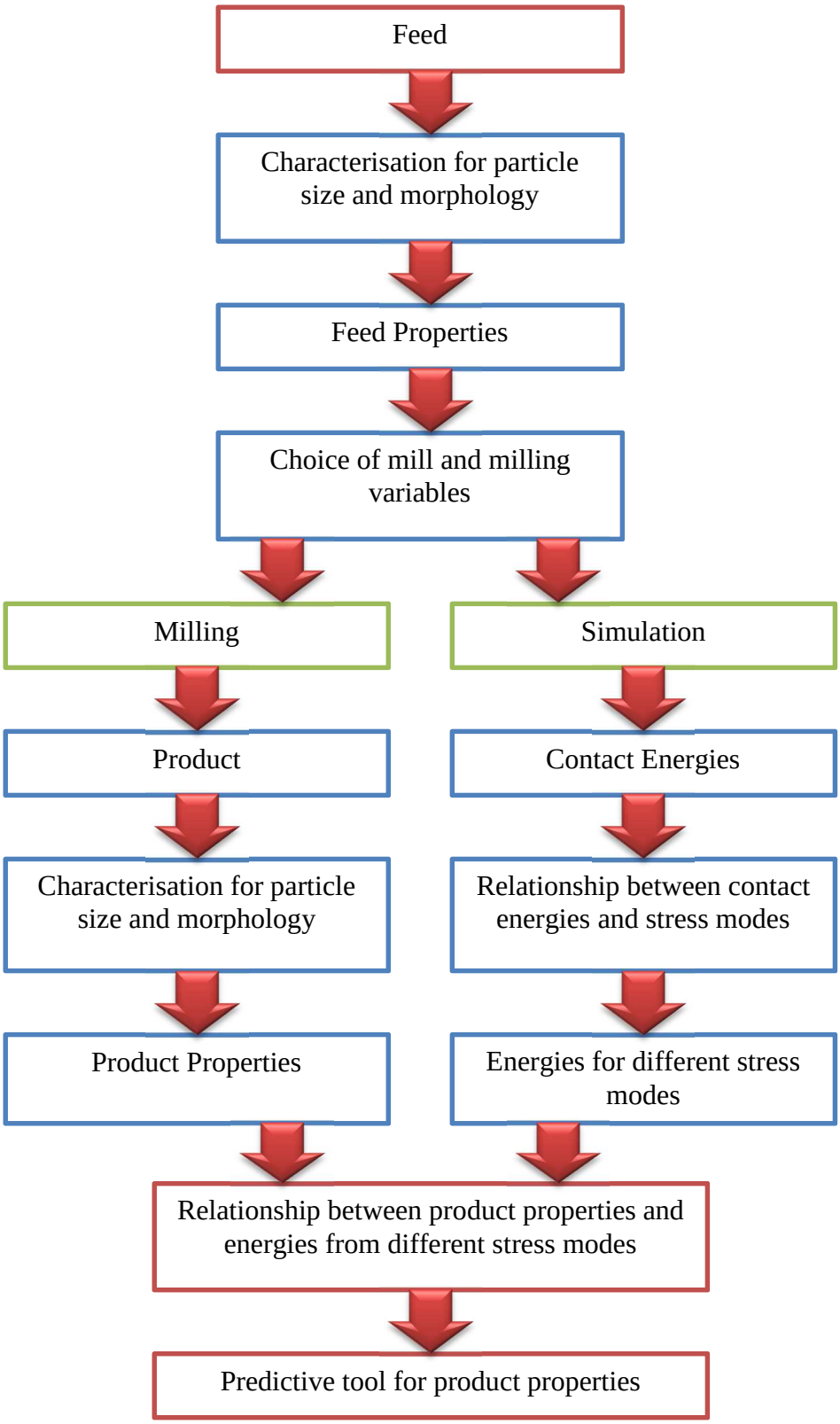

Figure 3.21: Project Plan

Chapter 4

Comparison of Different Milling Methods

A comparison of three selected milling methods; jet milling, single ball milling and planetary ball milling. The effect of these mills on the properties of gamma-Alumina such as particle size, surface area and crystal morphology is investigated. Further analysis of the results is also carried out to relate the mechanism of milling to the properties' changes observed.

4 Comparison of Different Milling Methods

4.1 Introduction

The effect of mill type on particle size, surface area and crystal morphology of γ-Al_2O_3 is presented. The reasoning behind choice of different mills is based on investigating the effect of impact energies provided by different stress modes i.e. impact and shear stresses. The desired agglomerate particle size required for use of γ-Al_2O_3 in catalysis is a d_{90} of less than 10 μm. Due to the hardness and semi-brittle failure mode of γ-Al_2O_3, high energy milling is required to achieve the desired fineness. Air jet milling and ball milling are widely used high energy milling methods as discussed in Chapter 2. The three methods selected for milling γ-Al_2O_3 are spiral jet milling, single ball milling and planetary ball milling.

The Hosokawa Alpine 50AS, a spiral air jet mill that reduces particles by impact, was used. The mill operates using compressed air and an investigation into how air aids in reducing particles can shed more light into the behaviour of γ-Al_2O_3 during milling. For single ball milling, the Retsch MM200 single ball mill was used. The mill reduces particles by impact and shear using a single ball as milling media. The behaviour observed by milling with a single ball can be expectedly different from milling using compressed air and hence the two impact mills are a good choice for comparison. The Fritsch P7 was the planetary ball mill selected for use and this mill reduces particles mainly by shear and impact. The mill uses balls as milling media and hence the effect of both increased milling media and shear stress can also be investigated.

This chapter is organised as follows. Firstly, the milling devices used and the experimental procedures are described. Preliminary tests for optimum milling conditions are presented with results of the selected conditions. This is followed by a particle size analysis of the conditions selected for jet milling, single ball milling and planetary ball milling. The effects of milling on specific surface area and crystal morphology are also presented. A discussion of all the results in the chapter is given and conclusions on the effects of the different mills on γ-Al_2O_3 are presented. This chapter has been published and the corresponding authors have been acknowledged in the introduction (Chauruka *et al*, (2015).

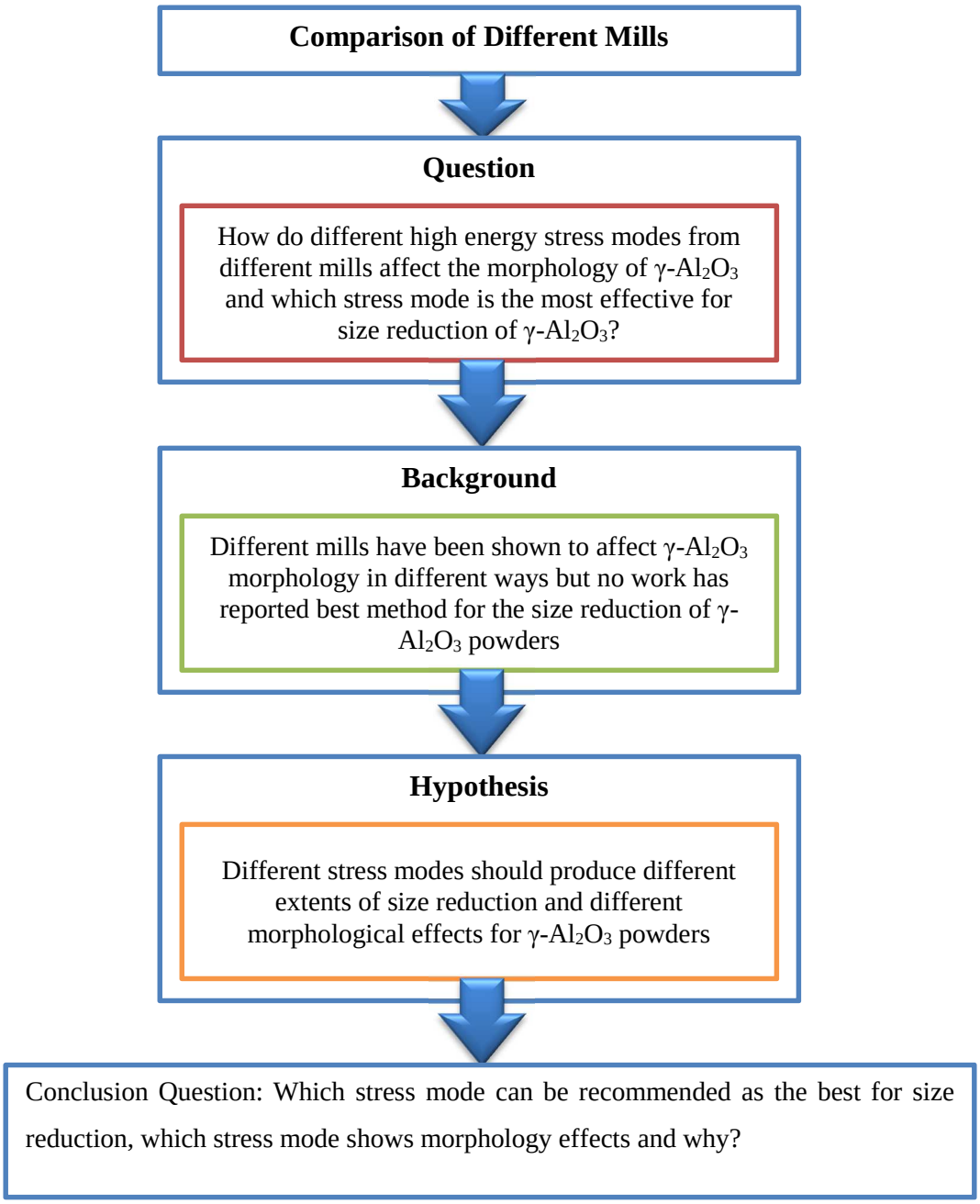

Figure 4.1: Hypothesis formulation for *Chapter 4*

4.2 Experimental Devices and Procedures

4.2.1 Spiral Jet Milling

The setup of the Hosokawa Alpine 50AS spiral jet mill is shown in Figure 4.2 and includes a small feed hopper at the top were the sample is fed in through. The mid part of the mill contains the grinding chamber which has two compressed air inlets. One inlet allows injection pressure through while the other allows the grinding pressure through. The injection compressed air pressure valve is opened first to allow for suction pressure. The grinding pressure valve is then opened and set at a pressure at least 2 bar less than the injection pressure to allow suction of the sample into the mill.

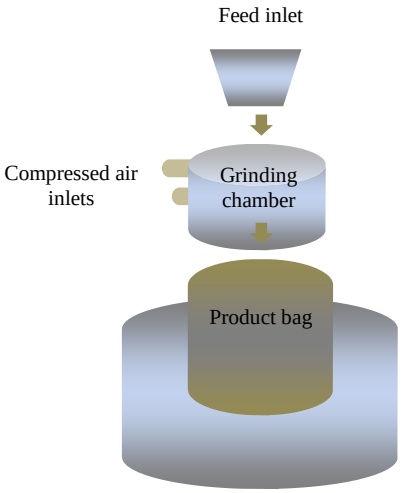

Figure 4.2: Illustration of the Setup of the Spiral Jet Mill

As the sample is fed through the inlet, it is sucked into the grinding chamber where the grinding air pressure results in particle-wall and particle-particle interactions which lead to breakage of the material. The material is then released from the grinding chamber through the outlet and is collected in the product bag at the bottom. The mill can then be opened and product recovered. Compressed air to the mill is supplied through the laboratory's compressed air pipeline at a maximum pressure of 7 bar. This pressure means the maximum achievable grinding pressure through this supply is 4 bar. The image of the mill is shown in Figure 4.3.

Figure 4.3: Photograph of the Alpine A50S Jet Mill

4.2.2 Single Ball Milling

The Retsch MM200 single ball mill has two attachments for ambient milling. Size reduction of the particles occurs by vibration of the milling jar when the machine is running. The milling jars compatible with the mill and used in the investigation were 11 ml in volume. A schematic of the milling jar with dimensions is shown in Figure 4.4.

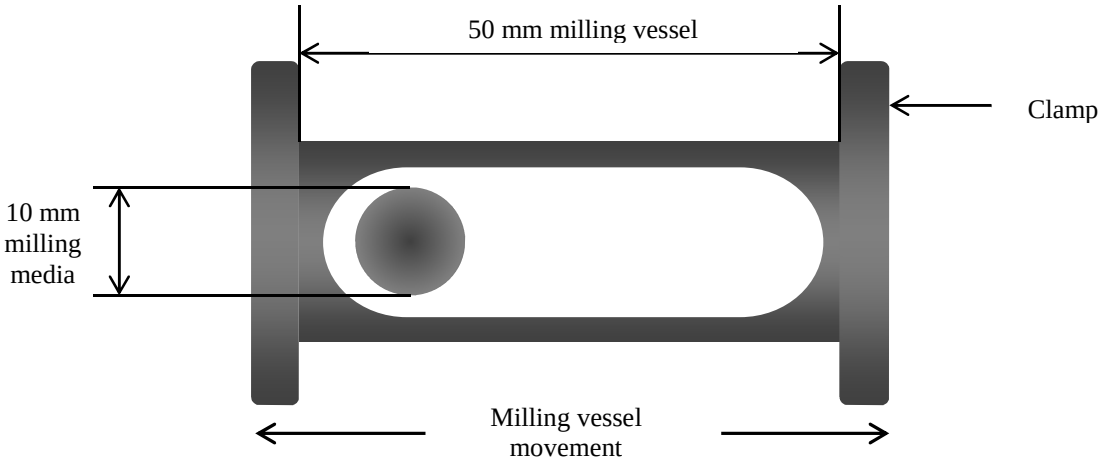

Figure 4.4: Retsch MM200 Single Ball Mill

Stainless Steel and aluminium milling jars are used. Milling media is also varied to assess the effect of different milling material on the size reduction and morphology of the product particles. The milling media used are single balls, 10 mm in diameter and made from Stainless Steel and Zirconia. The milling frequency of the mill can be varied between 3 and 30 Hz. For the experiments, 30 Hz is used. Sample masses are varied between 0.5 g and 2 g depending on the ball-to-powder ratio to maintain a ratio of 10:1 respectively. The time for

the experimental runs is varied from 1 to 1200 min. A diagram representing the setup of the milling vessel and movement during operation and the milling device is shown in Figure 4.5.

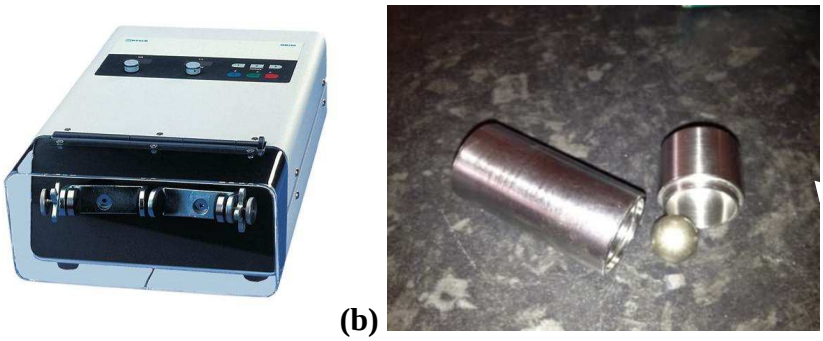

(a) **(b)**

Figure 4.5: Photographs showing (a) Vibration Milling Device and (b) Milling Vessel with Milling Media

During milling experiments, a measured mass of sample is transferred into the milling jar of size 11 ml. The milling media, a single 10 mm diameter Stainless Steel or Zirconia ball is added into the jar. The jar is sealed with the lid before clamping the jar onto the Retsch single ball mill and the jar is secured tightly using the clamps and the safety cover is placed onto the machine. The frequency of the vibrations is set to 30 Hz and the desired mill time is set. Milling is commenced and after every experimental run, the milled product is transferred into a small glass vial ready for characterisation. The experiment is repeated for different time intervals from 1 min up to 1200 minutes. Milling vessels and media are varied according to the conditions shown in Figure 4.6.

Stainless Steel has a higher density than Zirconia and aluminium. Zirconia, however, has a higher hardness value than Stainless Steel and it is therefore of interest to analyse which material property of milling media takes precedence in the single ball mill. Aluminium is also used to observe whether a good size reduction can be achieved with minimal contamination in the sample as this is a common problem in ball milling.

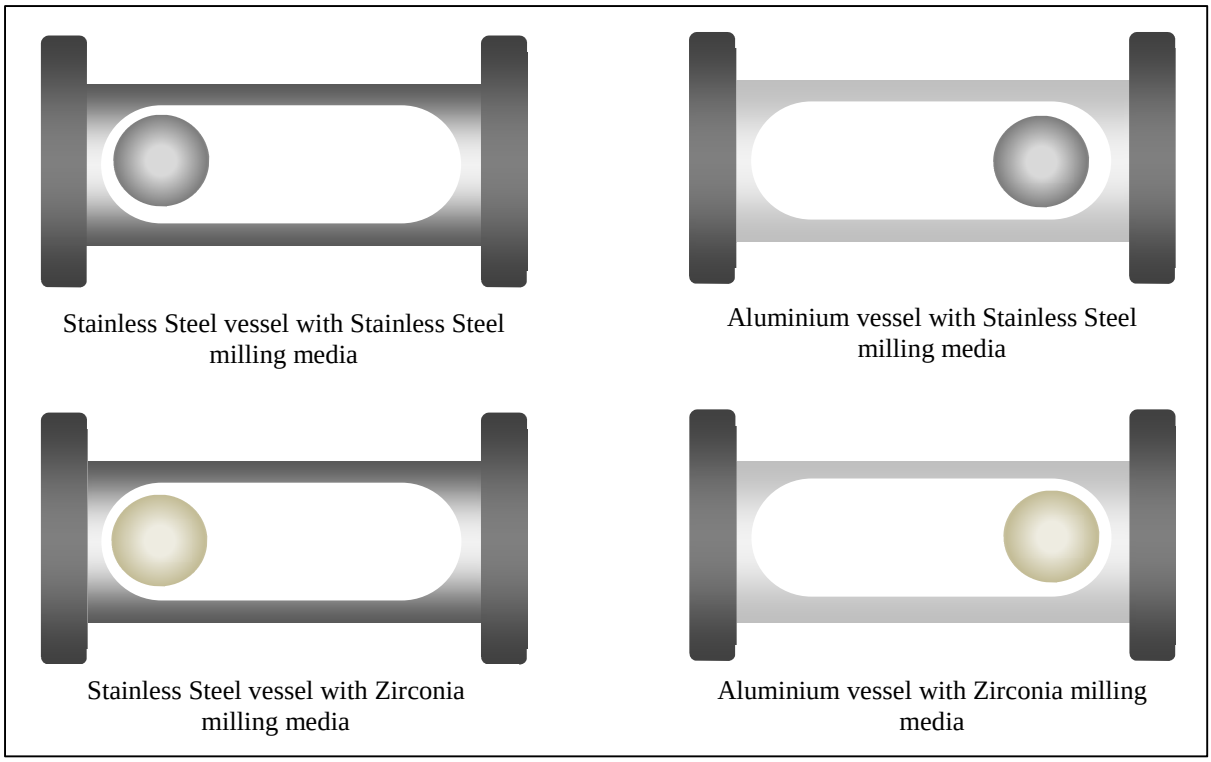

Figure 4.6: Experimental Setup Representations for Four Different Milling Conditions used on the Single Ball Mill (SBM)

4.2.3 Planetary Ball Mill

The Fritsch P7 planetary ball mill, shown in Figure 4.7, is used for a milling time study. Two 45 ml Zirconia vessels, each with 3 Zirconia balls as milling media, are used. The mill is run at 700 rpm for milling times of 15 minutes to 300 minutes. The ball-to-powder ratio used is 10:1; 2 g of powder sample and 20 g of milling media. The diameter of the milling media is 15 mm. During an experimental run, the milling vessels are filled with powder samples and milling media for up to two thirds of the total volume of the vessel. The milling vessels are sealed with Zirconia lids and tightly clamped on the mill. The safety hood is closed and the time and speed of milling is set. The machine is run for the required milling time. The machine is regularly checked during milling to ensure the milling vessels are tightly clamped. The temperature rise that occurs during milling is also closely monitored with a thermometer to ensure the safety during the experiment. After an experimental run, the milling powders are collected and characterised for particle size and morphology.

Figure 4.7: Photograph of Fritsch P7 Planetary Ball Mill

4.3 Preliminary Milling Experiments

In order to select the most suitable conditions for milling, preliminary tests were carried in mills where optional materials and conditions were available for use. It is important to select the most effective milling conditions as they can reflect the highest energy utilisation for size reduction of γ-Al_2O_3. This can determine whether the mills used can achieve the desired particle size distribution with a d_{90} of 10 μm and whether they cause any changes to the structure of γ-Al_2O_3 at the optimum conditions. For the Retsch MM200 single ball mill, milling jars made of Stainless Steel and aluminium were available with milling media made of Stainless Steel and Zirconia. It was necessary to test combinations of these materials to find the most effective milling combination. For the Hosokawa Alpine 50AS, the compressed air injection and grinding pressures can be varied. The milling rate can also be varied. A compressed air pressure study and feed rate study was carried out to assess for the most effective milling conditions. For the Fritsch P7 planetary ball mill, the only materials available were the Zirconia milling jar with 15 mm Zirconia milling balls. No preliminary study was carried out for this mill. The ball-to-powder ratio (BPR) used was 10:1.

4.3.1 Spiral Jet Mill Preliminary Tests

Preliminary milling tests with the Hosokawa Alpine 50AS included the variation of injection and grinding pressures in order to define a milling method. The input pressures used for the mill can be shown in Table 4.1. It is recommended to maintain a difference of at least 2 bar between the injection and grinding pressures. This is necessary in order to promote continuous suction of the sample from the feed chute of the mill and avoid ‘choking’ the mill.

Table 4.1: Input Pressures for Jet Mill Preliminary Tests

Condition	Injection Pressure/ bar	Grinding Pressure/ bar
1	4	2
2	6	3
3	6	4

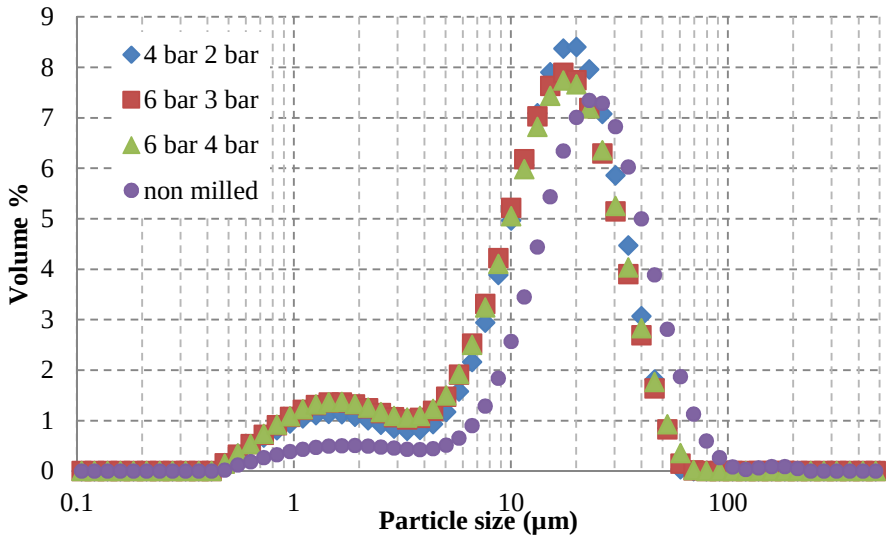

Figure 4.8: Particle Size Distributions for γ-Al_2O_3 Milled at Different Injection and Grinding Pressures

The results in Figure 4.8 show a bimodal PSD. The main focus on these results was to pick a condition with the greatest percentage of fine material, hence the smaller left peak on the bimodal graphs was analysed. The combination of injection and grinding pressure with the greatest percentage of small particles was the 6 bar 4 bar combination. This pressure combination was used for further jet milling as it achieved smaller particle sizes after milling as compared to the other pressures. The preliminary tests shown in Figure 4.8 were carried out by running the samples through the mill once. It was also identified from these tests that jet milled samples would have to be re-fed into the mill repeatedly until the desired particle size was achieved.

4.3.2 Single Ball Mill Preliminary Tests

A preliminary material study was carried out using the single ball mill to assess the extent of size reduction that could be achieved using different materials for the milling vessels and milling media. This was done in order to select the milling equipment that would result in the greatest extent of size reduction. Table 4.2 shows the summary of preliminary experiments carried out. In order to assess the extent of size reduction, the Mastersizer 2000 (MS2000) Hydro was used with water as a dispersant and ultrasound to obtain a particle size distribution (PSD) before milling and after every milling test carried out. The particle sizing was repeated twice for accuracy by collecting 3 samples for sizing from 3 different areas within a milled sample and error bars representing this were included in all PSDs. All preliminary tests were carried out at a milling frequency of 30 Hz for milling durations between 1 min and 1200 min.

Table 4.2: Preliminary Experiments with the Single Ball Mill

Experiment Number	Milling Vessel	Milling Media	Abbreviation
1	Stainless Steel	Stainless Steel	SSV SSBall
2	Stainless Steel	Zirconia	SSV ZBall
3	Aluminium	Stainless Steel	AlV SSBall
4	Aluminium	Zirconia	AlV ZBall

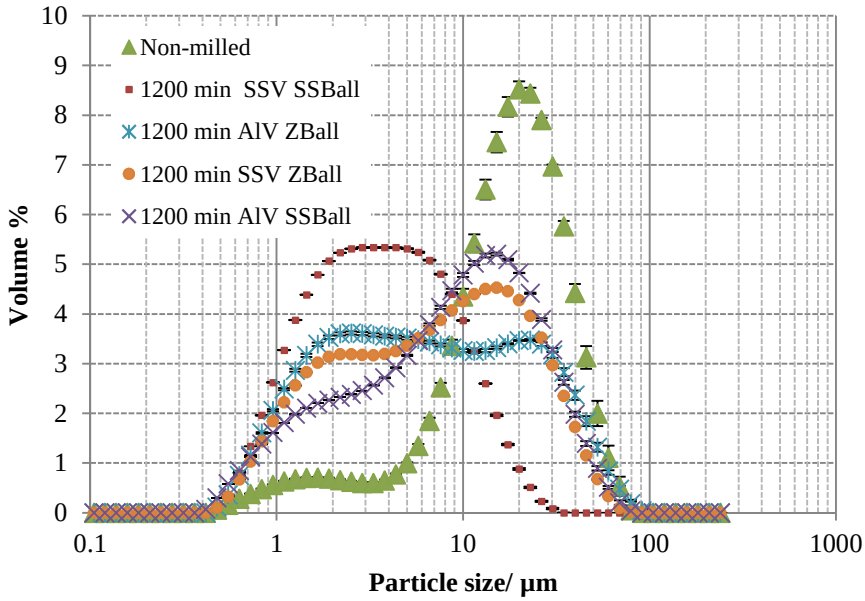

Figure 4.9: PSD of as-received γ-Al_2O_3 and after milling in conditions in Table 4.1

Figure 4.9 shows the PSD of as-received (A-R) γ-Al_2O_3 and after milling in Stainless Steel and aluminium with Stainless Steel milling media and Zirconia (ZrO_2) milling media. The PSD analysis can be shown more clearly in the cumulative PSD graphs in Figure 4.10. The cumulative PSD in Figure 4.10 show more clearly that there is an overlap in the AlV SSBall, AlV ZBall and SSV ZBall samples. All three samples achieved similar particle size reduction. The SSV SSBall sample however had the smallest particles. This shows that the smallest particles were achieved by milling in a Stainless Steel vessel with Stainless Steel milling media. Further analysis was carried out by calculating a milling rate for all conditions. A first order milling rate equation was used to compare the milling results by expressing the d_n (n = 10, 50, 90) of the samples measured with respect to time as shown in Equation 4.1 (Kwan et. al., 2005).

$$\frac{(D_t - D_l)}{(D_0 - D_l)} = \exp(-K_p t) \qquad \textbf{Equation 4.1}$$

D_t is the dn of the milled sample, D_l is the d_n at the milling limit where further milling results in no size reduction, D_0 is the d_n of the sample before milling, t is the milling duration and K_p is the milling rate constant. In order to calculate a milling rate, mill times, t of 10, 30, 60, 600 and 1200 min were used. Table 4.2 outlines the values used for calculation of the (D_t - D_l /D_0 - D_l) parameter and Figure 4.11 shows the milling rate (K_p) for the different milling conditions used.

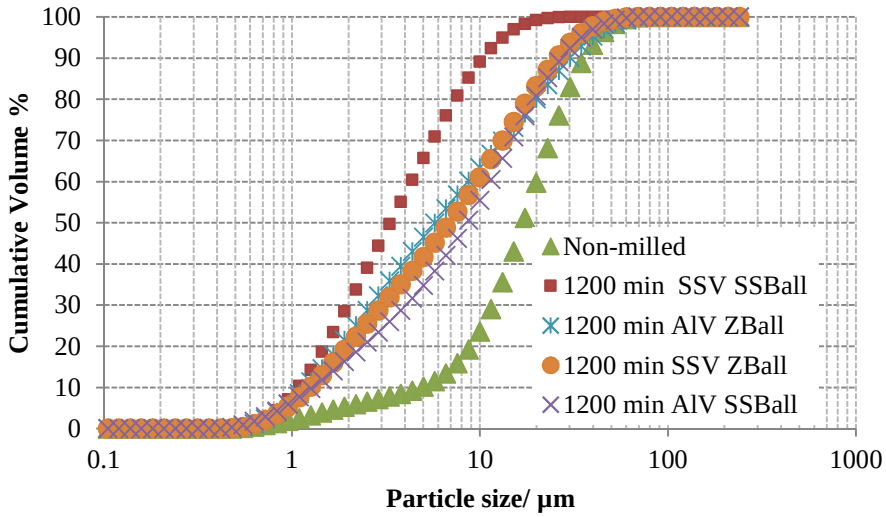

Figure 4.10: Cumulative PSD for A-R γ-Al2O3 and for milling combinations in Table 4.2

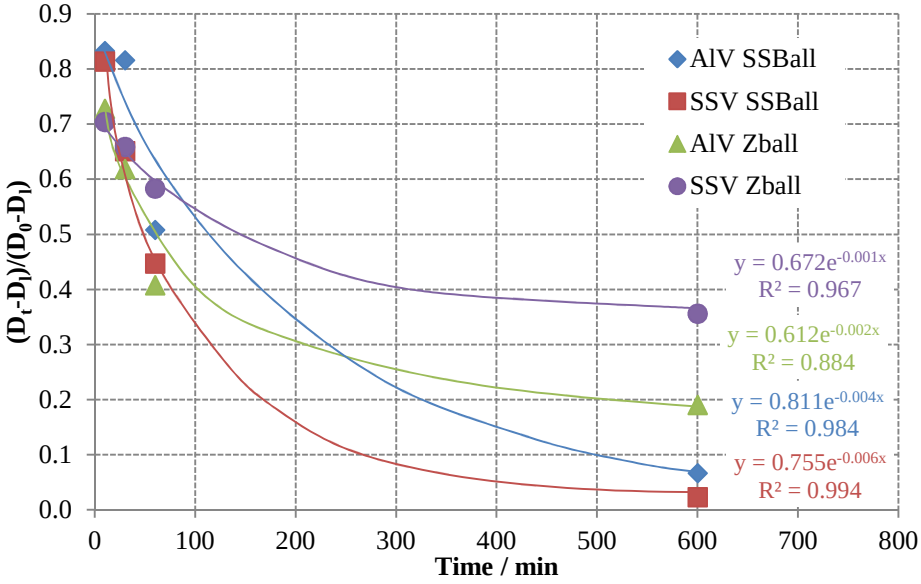

Figure 4.11: Graphs showing the milling rates of γ-Al_2O_3 according to milling conditions in Table 4.2

The results in Figure 4.11 show the milling rates according to Equation 4.1. A good agreement with the milling rate model by Kwan *et al* (2000) is observed for all samples. This shows that the size reduction of γ-Al_2O_3 follows a first order rate equation. The results also show that the SSB SSV condition has the highest milling rate and hence is the most efficient of the four milling conditions used.

Samples of γ-Al_2O_3 from SBM preliminary tests were also analysed by SEM using the Carl Zeiss EVO MA15 scanning electron microscope. This analysis was carried out in order to assess the effect of milling on the particle size and shape of γ-Al_2O_3 particles. Figure 4.12 shows the SEM micrograph of γ-Al_2O_3 particles before milling. The particles appear spherical with smooth surfaces and there is very little or no presence of fines (less than 1 µm) in the sample.

Figure 4.12: SEM micrograph of γ-Al_2O_3 particles before milling

The SEM images of the four milling conditions tested (Table 4.2) after 1200 min of milling are shown in Figure 4.13. Figure 4.13 shows SEM images for samples with PSDs shown in Figure 4.9, where the smallest PSD was observed in the SSB SSV sample. This can also be observed in Figure 4.13(a) which, when compared to Figure 4.13(b), (c) and (d) shows the smallest particles. The least amount of size reduction was observed in the AlV SSB sample by laser diffraction (Figure 4.9) and this can also be observed in Figure 4.13(c). The SEM results were in agreement with laser diffraction particle sizing and show a similar trend in size reduction from smallest to largest of SSB SSV → AlV ZB→SSV ZB → AlV SSB. The

results confirm that milling with Stainless Steel milling media in a Stainless Steel vessel gives the smallest particles and hence this combination is used in further experiments.

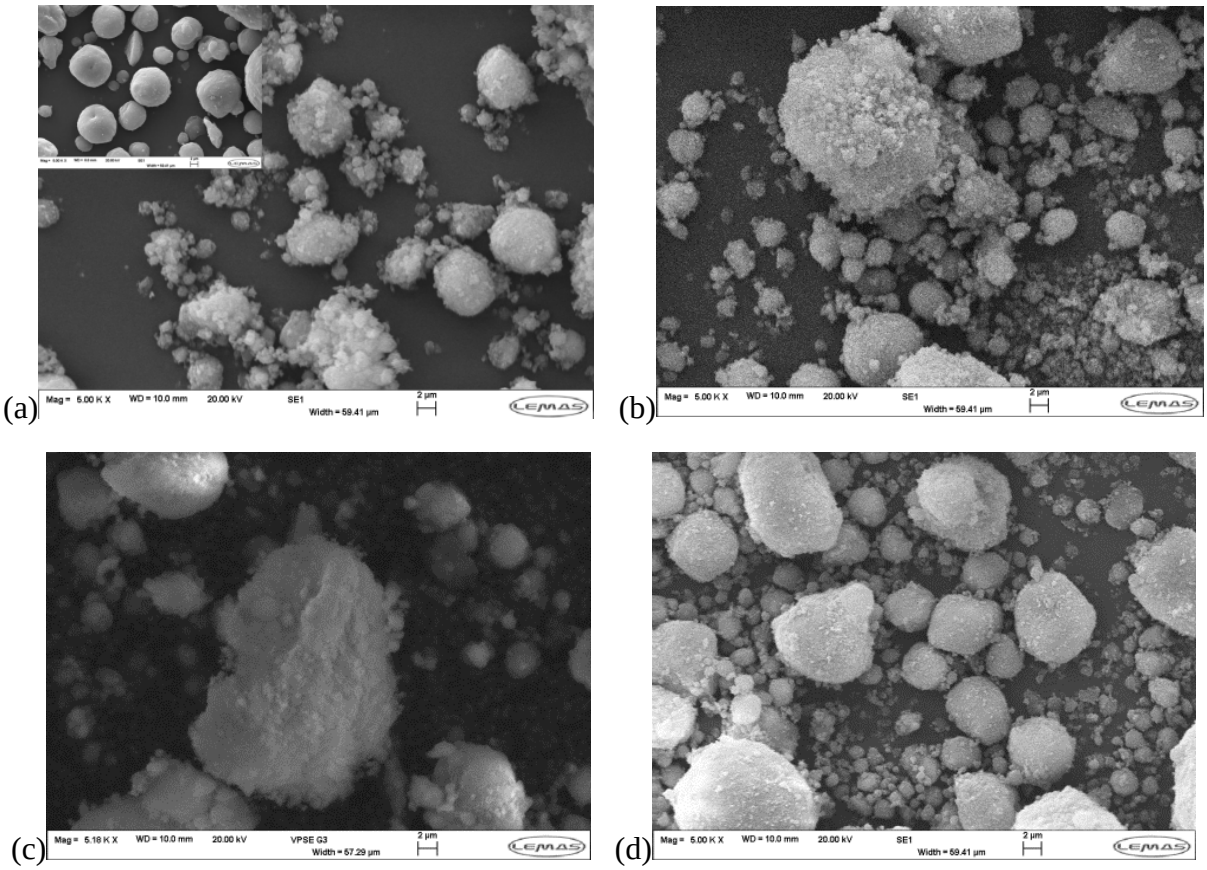

Figure 4.13: SEM images of sample before milling (insert in (a)) and SBM samples after 1200 min of milling with (a) Stainless Steel vessel and media, (b) Stainless Steel vessel and Zirconia ball, (c) Aluminium vessel and Stainless Steel ball and (d) Aluminium vessel and Zirconia ball

4.4 Particle Size Analysis of Three Milling Methods using Laser Diffraction

4.4.1 γ-Al_2O_3 Particles Before and After Milling in the Jet Mill

Samples of γ-Al_2O_3 were fed through the JM for a total of 20 passes. Samples were collected for particle size analysis after 5, 10 and 15 passes. Figure 4.14 shows the particle size distribution (PSD) and cumulative PSD of the particles. As shown in Table 4.3, there was a significant size reduction between the as-received (A-R) samples and the sample after 20 passes also shown by the measured characteristic sizes of the particles where the A-R sample had a d_{90} of 49.10 µm and the 20 pass sample had a d_{90} of 2.89 µm.

Table 4.3: Characteristic sizes (d_{10}, d_{50} and d_{90}) of the A-R sample and samples milled by the jet mill for 5, 10, 15 and 20 passes

Sample	Particle size (µm)		
	D_{10}	D_{50}	D_{90}
A-R	6.2	21.4	49.1
5 pass	0.9	3.6	16.2
10 pass	0.9	4.7	12.3
15 pass	0.7	1.8	10.7
20 pass	0.6	1.2	2.9

The cumulative PSD in Figure 4.14b also showed an initially fast rate of size reduction between the A-R sample and the 5 pass sample which then reduced for subsequent passes; the 5 pass, 10 pass and 15 pass samples all showed a more continuous reduction in larger particles. Finally, the 20 pass sample showed a marked reduction in larger particles within the sample as the bimodal distribution in Figure 4.14a showed only a small peak for particles larger than 6 µm.

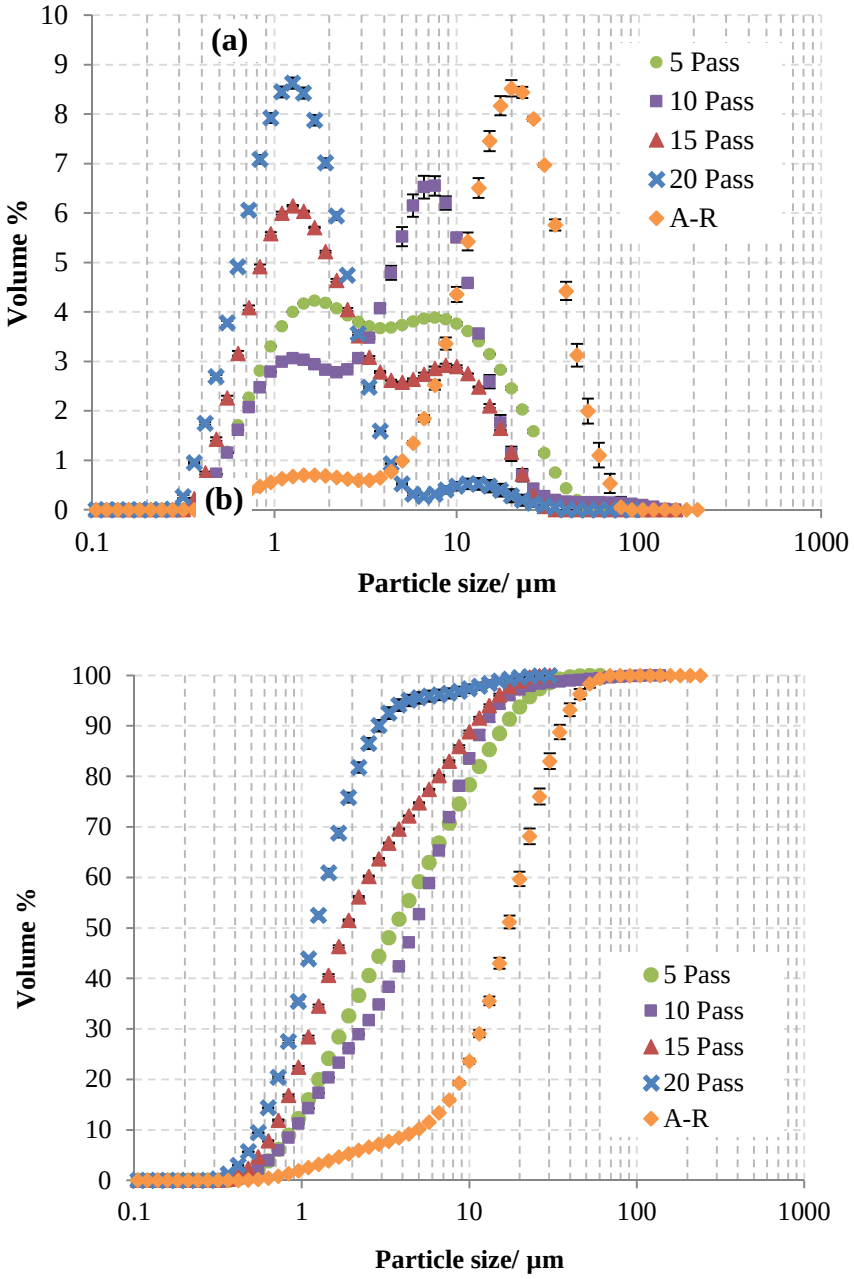

Figure 4.14: PSD of jet milled γ-Al_2O_3 samples showing (a) the PSD distribution and (b) the cumulative PSD after 5, 10, 15 and 20 passes through the jet mill

Particles larger than 6 µm in the 20 pass sample highlight the importance of manipulating the feed rate of the sample into the mill as this can aid in reducing the number of non-milled particles after running a sample. Further milling was not carried out as the desired particle size was achieved (d_{90} = <10 µm) after 20 passes through the JM.

4.4.2 γ-Al_2O_3 particles before and after dry milling in the SBM

Figure 4.15 shows the PSD of samples milled using the SBM with Stainless Steel milling vessel and Stainless Steel milling media. The characteristic sizes at different mill times are shown in Table 4.4. The results show particle size reduction with increased milling time; the decrease in large particles being evident by the movement of the tail of the PSD graphs to smaller sizes with increased milling time.

Table 4.4: Characteristic sizes (d_{10}, d_{50} and d_{90}) of the A-R sample and samples milled by the single ball mill for 60, 600 and 1200 min

Sample	Particle size (µm)		
	D_{10}	D_{50}	D_{90}
A-R	6.2	21.4	49.1
60 min	1.6	10.7	52.5
600 min	1.4	5.4	20.0
1200 min	1.2	4.1	11.5

The cumulative PSD also shows a significant size reduction between 60 min and 600 min of milling but a less significant difference between 600 and 1200 min. Interestingly, the PSD after 60 min milling showed larger particles than in the A-R sample. This is presumably due to adhesion of fine particles with high surface energy on the surfaces of larger agglomerates. Further milling up to 600 and 1200 min ensures the breakage of these larger particles without any significant difference in the particle size reduction achieved.

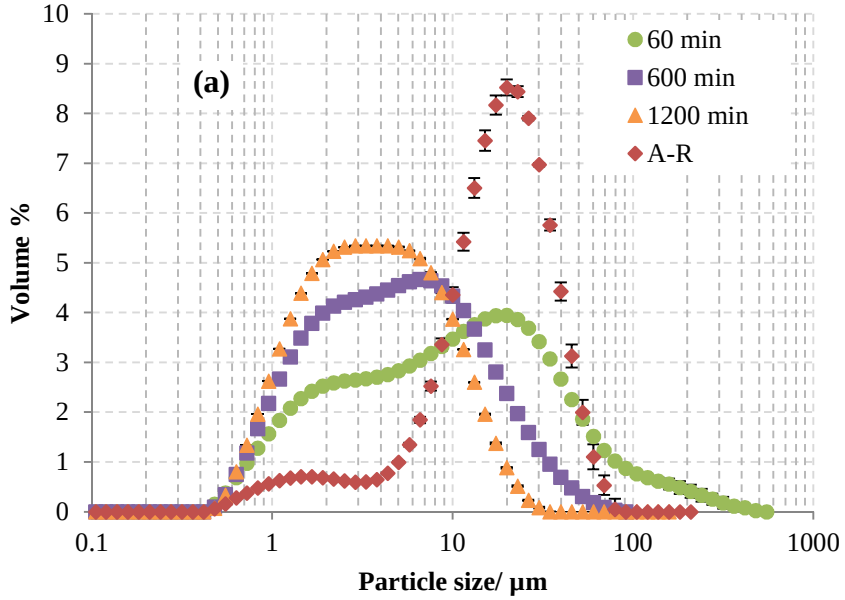

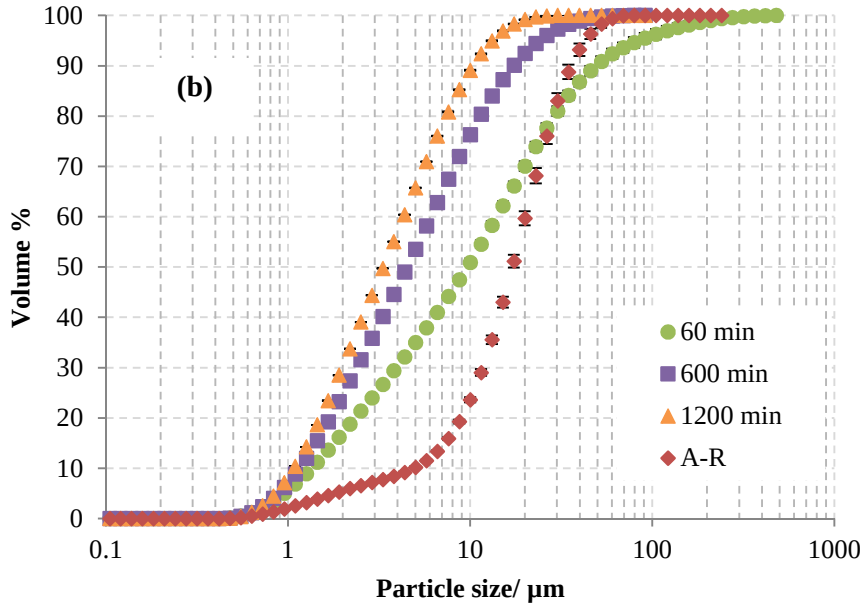

Figure 4.15: PSD of single ball milled γ-Al_2O_3 samples showing (a) the PSD distribution and (b) the cumulative PSD after 60, 600 and 1200 min of milling

4.4.3 γ-Al_2O_3 particles before and after dry milling in the PBM

Figure 4.16 shows the PSD of samples of γ-Al_2O_3 milled using the PBM at 700 rpm. The characteristic sizes at different mill times are shown in Table 4.5. The results show an initial significant decrease in particle size between the A-R sample and the sample after 10 mins of milling; further milling up to 300 min does not result in a significant decrease in particle size. A small increase in the volume of particles within the sample which is larger than the initial feed size is noted as milling time is increased. This is also observed in the 60 min single ball milled samples.

Table 4.5: Characteristic sizes (d_{10}, d_{50} and d_{90}) of the A-R sample and samples milled by the planetary ball mill for 10, 15, 30 and 300 min

Sample	Particle size (µm)		
	D_{10}	D_{50}	D_{90}
A-R	6.2	21.4	49.1
10 min	1.0	11.5	45.7
15 min	1.0	11.5	42.8
30 min	0.8	10.0	32.4
300 min	0.7	8.7	30.2

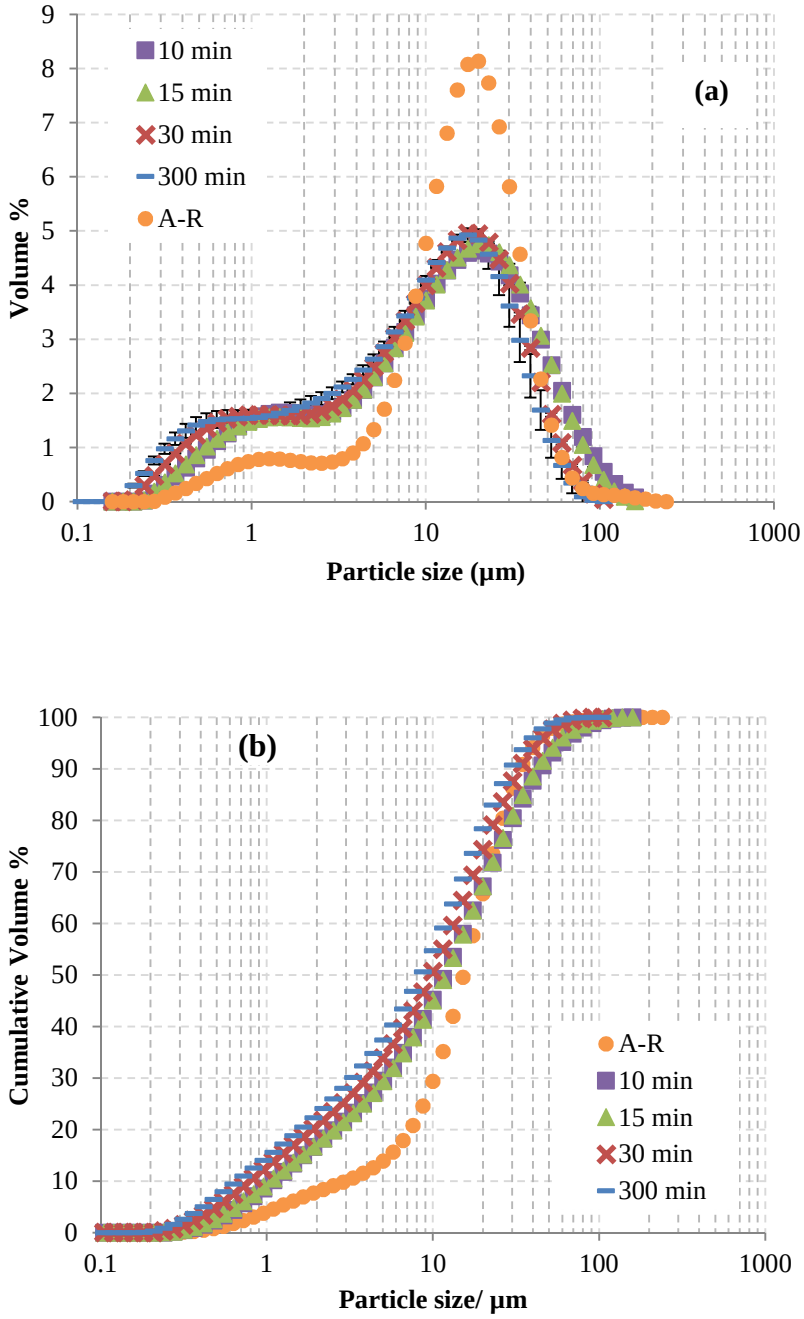

Figure 4.16: PSD of planetary ball milled γ-Al_2O_3 samples showing (a) the PSD distribution and (b) the cumulative PSD after 10, 15, 30 and 300 mins of milling

4.4.4 Comparison of Particle Size Reduction by Different Mills

Figure 4.17 shows a comparison of (a) the PSD and (b) the cumulative PSD of γ-Al_2O_3 particles as-received (A-R) and after milling in the PBM for 300min, SBM for 1200 min and JM for 20 passes.

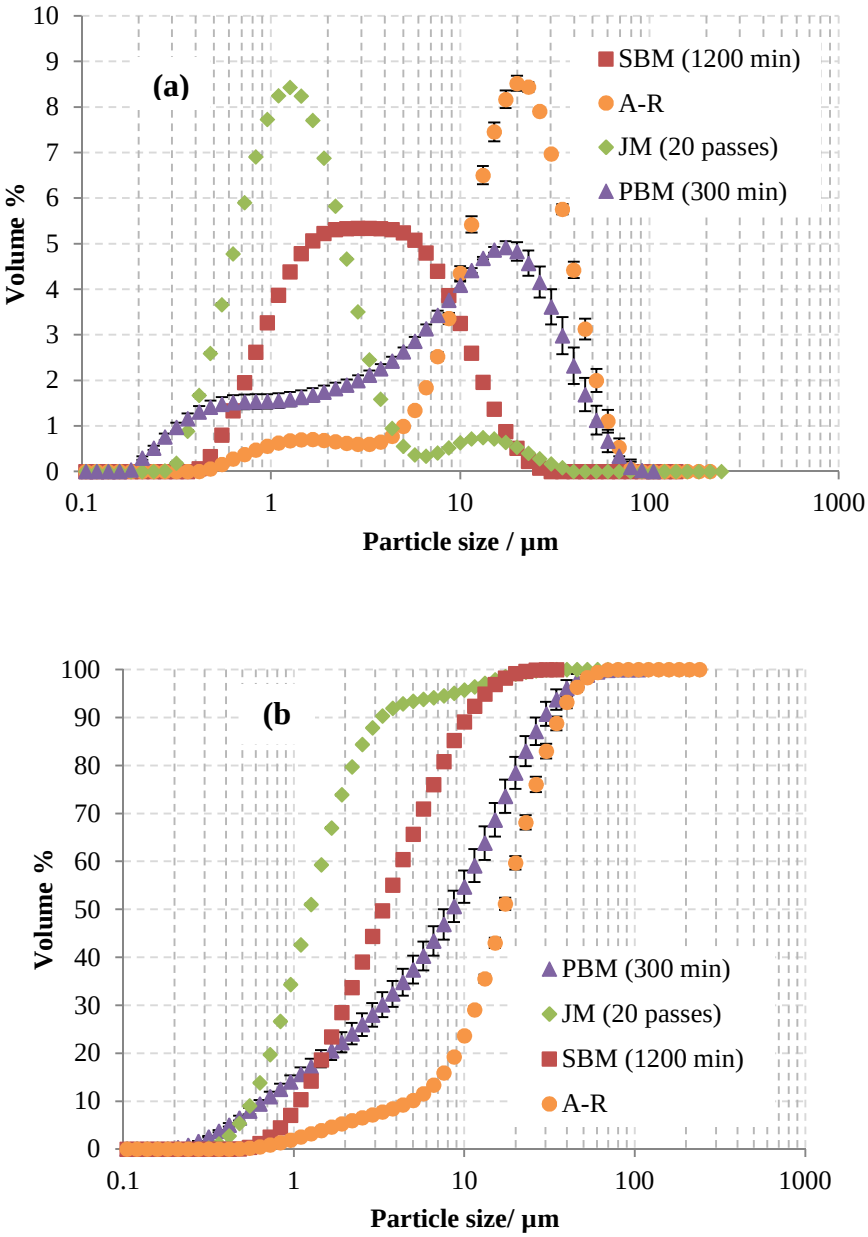

Figure 4.17: Size analysis results for γ-Al_2O_3 particles showing (a) PSD and (b) cumulative PSD of as-received (A-R) samples and after milling in the single ball mill (SBM) for 1200 min, planetary ball mill (PBM) for 300 min and jet mill (JM) for 20 passes

The PSDs in Figure 4.17a show that the greatest size reduction of particles was achieved with the JM, albeit this gave a bimodal distribution with a majority of fine particles accompanied by smaller distribution of larger particles. For the ball milled samples, the SBM samples had smaller particle sizes than the PBM samples. However the PBM samples showed the greatest amount of fines in all the milled samples, evident in the cumulative curves shown in Figure 4.17b. The characteristic sizes can be shown in Table 4.6. Considering the d_{90} particle sizes of the PBM, SBM, JM and A-R samples, the JM method appears more suitable for dry milling of γ-Al_2O_3 particles.

Table 4.6: Characteristic sizes (d_{10}, d_{50} and d_{90}) of the A-R sample and samples milled by the SBM, PBM and JM

Sample	Particle size (µm)		
	D_{10}	**D_{50}**	**D_{90}**
A-R	6.2	21.4	49.1
PBM	0.7	8.7	30.2
SBM	1.9	4.1	11.5
JM	0.6	1.2	2.9

The particles from the JM samples show a steady decline in average particle sizes with further milling as observed in Figure 4.14 and show no increase in particle size after a certain period of milling as that observed with the SBM and PBM in Figure 4.15 and. The compressed air used for milling with the JM appears to aid in keeping the particles fairly dispersed as breakage occurs in the milling chamber. The short residence time in the milling chamber also reduces the possible number of contacts particles can have. This results in consistent particle size reduction.

The PSD results for SBM samples (Figure 4.15) and PBM samples (Figure 4.16) show only a small reduction in size with increased milling time. This is between 600 and 1200 min for SBM (Figure 4.16) and 15 and 300 min for PBM (Figure 4.16). This is due to particles reducing in size to a critical value where the equilibrium state of milling is achieved. In this state, whilst particles are reduced in size by the milling energy supplied, at this critical size, the fines produced and broken agglomerates begin to form larger agglomerates joined by weak van der Waals forces and eventually form aggregates joined by stronger chemical bonds (Balaz *et al*., 2013). This results in a reduced effectiveness of the milling process in terms of achieving size reduction. This can also result in the assembly of agglomerates larger than the initial maximum feed size as observed in both SBM and PBM.

According to the review done in Chapter 2, the mechanism of size reduction in the SBM and PBM is different; the SBM is reported to reduce particles mainly by impact whilst the PBM is mainly by both shear and impact. The shearing in the PBM continuously produces fines for all milling times, the agglomerates continue to grow as they are compacted onto the walls of the mill by the shearing and impact effect and this compaction onto the walls of the mill, results in strongly bonded agglomerates. This greatly reduces the effectiveness of the mill. The SBM, in turn, can initially produce fines when large agglomerates are broken at the initiation of milling as observed after 60 mins. This can result in larger agglomerates being formed by weak bonds between fines and larger broken particles, but prolonged size reduction by impact, results in breakage of these weakly bonded agglomerates and better size reduction than the PBM. This is also due to the added advantage of the vibration effect in the SBM. Further milling was not carried out after 20 passes in the JM as the desired particle size of a d_{90} less than 10 µm had been achieved. Conditions of PBM after 300 min, SBM after 1200 min and JM after 20 passes were used for further comparative analysis of the three mills.

4.5 Characterisation of Particle Morphology of Three Milling Methods by SEM Analysis

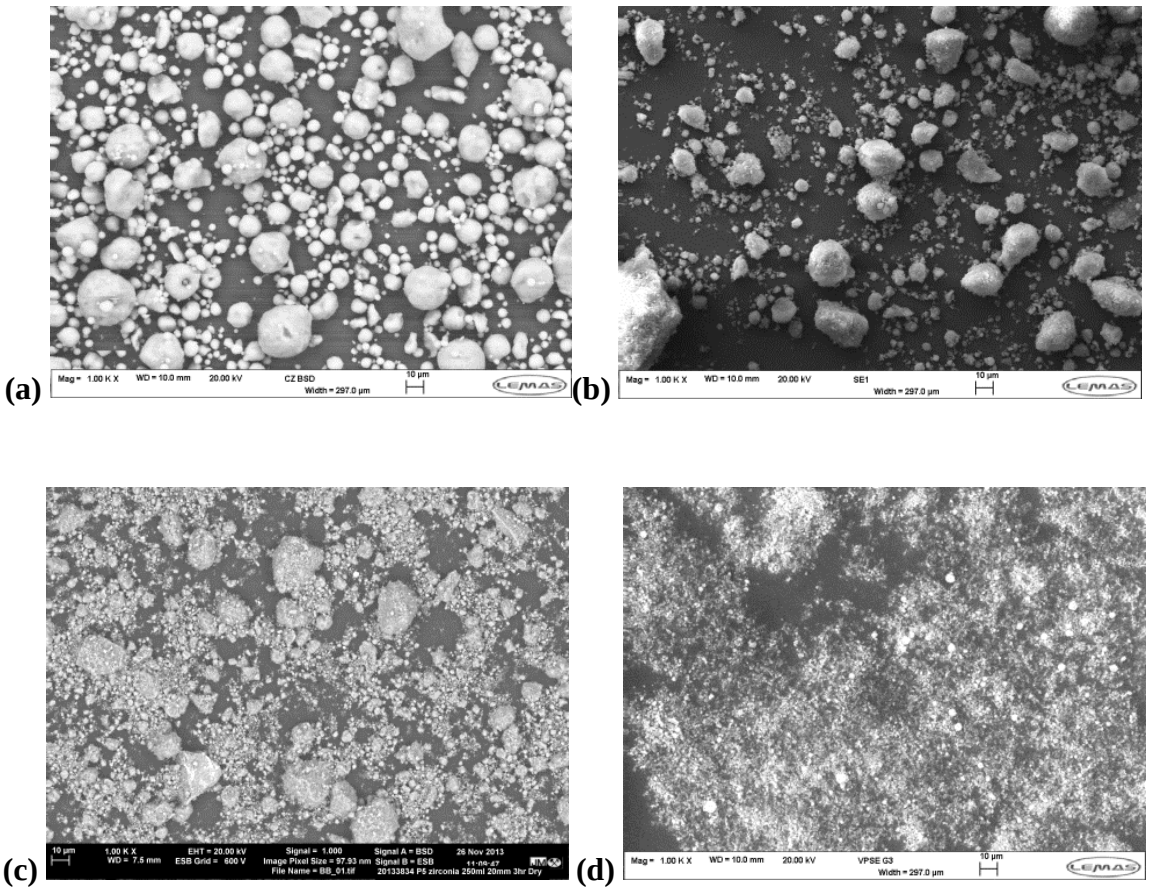

Figure 4.18: SEM imaging of γ-Al_2O_3 particles showing (a) A-R sample, (b) SBM sample after 1200 min of milling, (c) PBM sample after 300 min of milling and (d) JM sample after 20 passes through the jet mill

Figure 4.18 shows SEM images for samples before and after milling in the SBM for 1200 min, PBM for 300 min and JM for a total of 20 passes. As laser diffraction measures particle size at random orientation, SEM analysis was used to analyse the maximum projected area and shape of the particles. Figure 4.18a shows spherical agglomerates with smooth surfaces for A-R particles. After milling, the agglomerate shapes appeared less spherical and more random in terms of their shapes. The agglomerate surfaces also appeared rougher as shown in Figure 4.18b, c and d. An accumulation of very fine particles on the surfaces of the agglomerates in the PBM samples is shown in Figure 4.18c. This can reduce the efficiency of milling as broken particle reassemble to form large particles and this is also observed in the laser diffraction results in Figure 4.16 where an equilibrium state of milling is observed. Figure 4.18d for JM samples, when compared to Figure 4.18a-c at similar magnification,

shows much finer material. A rough number-based quantitative analysis of SEM micrographs was carried out for analysis of average particle sizes and large particles and is shown in Table 4.7.

Table 4.7: SEM number-based quantitative particle size analysis for PBM 300 min, SBM 1200 min, JM 20 passes and A-R samples

Sample	A-R	PBM	SBM	JM
Number-based Average Particle Size (µm)	11.4	5.2	5.1	3.8
Coefficient of Variation	0.9	3.7	1.4	1.0
Largest particle (µm)	70.7	161.6	73.9	38.4

This was carried out for verification of fines and larger particles observed in laser diffraction results. With an appreciation of the difference in the principles of the two sizing techniques, a similar trend to laser diffraction of size reduction of A-R→PBM→SBM→JM (from largest to smallest particles) was observed. The smallest particles were observed in the JM samples with majority of particles less than 3 µm as shown in Figure 4.18d. SEM micrographs of PBM samples showed a wide variation in the particle sizes and this is due to the large amount of fines observed in the SEM images of the sample. Apart from fines, the PBM sample also had particles larger than those observed in the A-R sample (106 µm observed from laser diffraction). This was also correlated with the formation of agglomerates larger than the A-R sample during PBM milling observed in laser diffraction results.

4.6 Characterisation of Surface Area using BET

BET surface area measurements were carried out for A-R, SBM after 1200 min, JM after 20 passes and PBM after 300 mins. According to Table 4.8, samples from the JM and SBM show a negligible difference in surface area when compared with the A-R sample. However there is a significant decrease in specific surface area for the PBM sample from 136.6 m^2/g observed in the A-R sample to 82.6 m^2/g.

Table 4.8: BET surface area measurements for A-R, PBM, JM and SBM samples showing specific surface area

Variable	**Sample**			
	A-R	**SBM**	**JM**	**PBM**
BET surface area (m^2/g)	136.6	144.1	147.5	82.6

Further analysis on the PBM samples was carried out by BET surface area measurements for the A-R sample and PBM samples milled for 60, 180 and 300 min as shown in Figure 4.19.

The results show a reduction in specific surface area with milling: from 136.6 m^2/g in the A-R sample to 119.8 m^2/g after 60 mins, 76 m^2/g after 180 min and finally 82.6 m^2/g in the 300 min milled PBM sample. The reduction in surface area in the PBM reflects a change in the structure of the sample during milling and will be further considered in the next section.

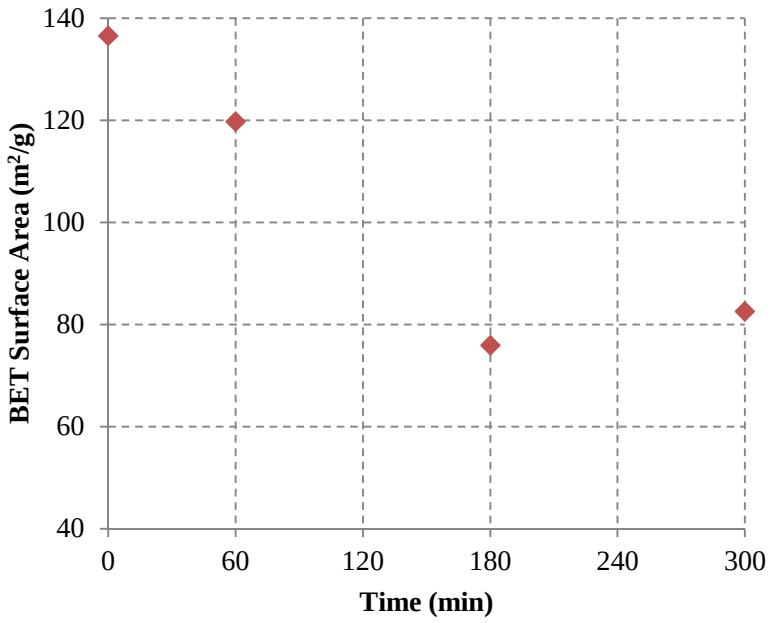

Figure 4.19: BET surface area measurements for PBM samples after 0, 60, 180 and 300 min of milling showing specific surface area

4.7 Phase Identification by XRD analysis

Figure 4.20 shows the XRD patterns of the A-R γ-Al_2O_3 sample and samples milled in dry state using SBM for 1200 min, PBM for 300 min and JM for 20 passes together with reference patterns for γ-Al_2O_3 and α-Al_2O_3 obtained from ICDD Database. XRD analysis of all samples shows similar diffractograms in the A-R, JM and SBM samples. These samples match well with ICDD reference file 00-010-0425 for γ-Al_2O_3 suggesting that the milling processes do not affect the crystal structure of the material. In contrast, the diffractogram of the PBM samples however show the majority of peaks matching to ICDD reference pattern 00-005-0712 for α-Al_2O_3 and some small peaks indicating a small amount of remaining γ-Al_2O_3 in the sample.

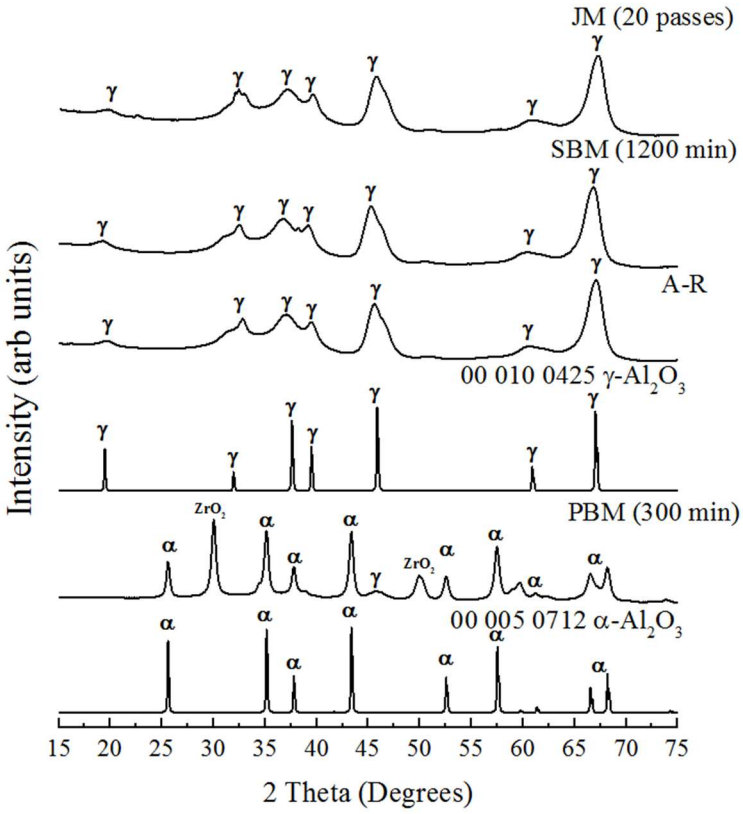

Figure 4.20: XRD patterns of Al_2O_3 showing α-Al_2O_3 ICDD reference pattern 00-005-0712, γ-Al_2O_3 ICDD reference pattern 00-010-0425, as-received γ-Al_2O_3 and γ-Al_2O_3 after milling in PBM (300 min), SBM (1200 min) and JM (20 passes)

This shows that dry planetary ball milling results in a change in the crystal structure of the material and induces a phase transformation from the γ- to the α-Alumina phase correlating with the reduction in the surface area observed in the BET surface area measurements shown in Figure 4.19. Additional peaks not corresponding to α- or γ-Al_2O_3 match to Zirconia (ZrO_2). This suggests contamination from the milling jar and milling media.

Table 4.9: Crystallite sizes estimated from XRD patterns for as-received and after milling in PBM (300 min), SBM (1200 min) and JM (20 passes)

γ	$d_{crystallite}$ (nm)			α	$d_{crystallite}$ (nm)
hkl	**A-R**	**JM**	**SBM**	**hkl**	**PBM**
111	10.2	7.5	15.3	012	30.3
222	12.3	11.8	13.4	024	19.8
400	9.7	8.8	19.3	113	23.9

As presented in Table 4.9, the crystallite sizes of the A-R and JM samples varied from 8 nm to 12 nm whilst the SBM γ-Al_2O_3 samples showed an approximate doubling in crystallite size showing growth of γ-Al_2O_3 during single ball milling. For PBM the estimated size of the transformed α-Al_2O_3 crystallites ranged between 20 nm and 30 nm indicating an increase in

the crystallite size due to phase transformation and correlating with the results observed by Kostic *et al.,* (2000). Figure 4.21 shows the XRD diffractograms for samples dry milled in the PBM for 30, 60, 180 and 300 min.

As milling time increased, the intensity of the α-Al_2O_3 peaks was observed to increase. This shows that the transformation from γ to α occurs progressively over time during milling rather than being an instantaneous change. The proportions of γ-Al_2O_3 and α-Al_2O_3 in the samples derived from XRD diffractograms are given in Table 4.10. Interestingly, the δ and θ states of Alumina were never observed at any milling time.

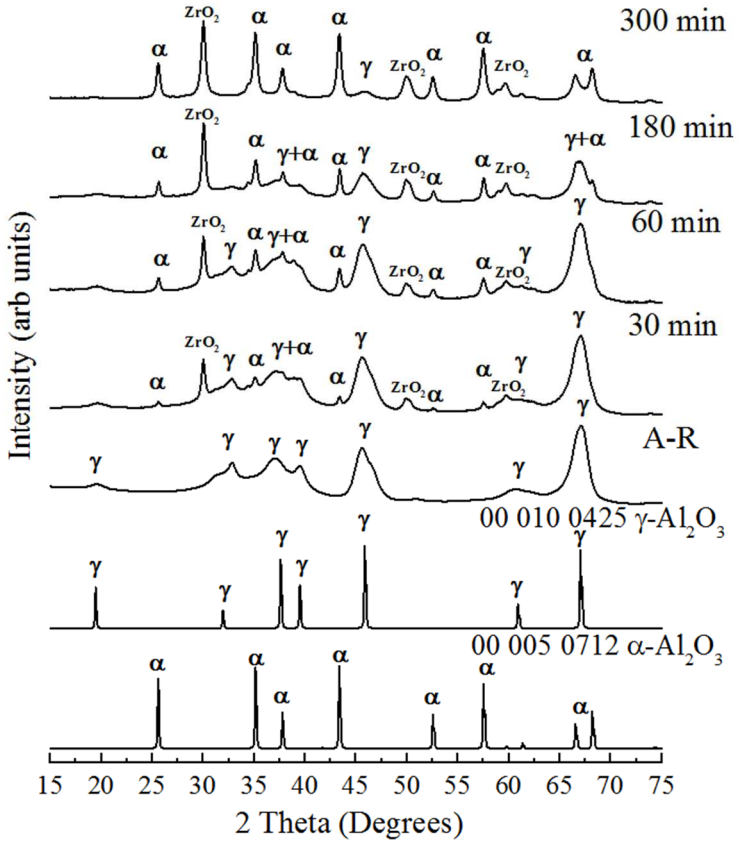

Figure 4.21: XRD patterns of Al_2O_3 showing α-Al_2O_3 ICDD reference pattern 00-005-0712, γ-Al_2O_3 ICDD reference pattern 00-010-0425, as-received γ-Al_2O_3 and γ-Al_2O_3 after milling in PBM for 30, 60, 180 and 300 min

As the samples in Figure 4.21 were milled without the addition of α-Al_2O_3 before milling, the results differ from the observations of Bodaghi *et al.* (2008), and show that with the appropriate milling conditions, α-Al_2O_3 can be produced mechanochemically without any seeding (Kostic *et al.,* 2000). ZrO_2 contamination was also observed to increase as milling progressed as the intensity of the ZrO_2 peak increased with prolonged milling times.

Table 4.10: Percentage of γ-Al_2O_3 and α-Al_2O_3 phases in PBM milled samples at 60, 180 and 300 min based on area under matched peaks by the use of Xpert Highscore software (Panalytical B.V. Highscore with Plus Option, 2014)

Sample	Phase Composition	
	% γ-Al_2O_3	% α-Al_2O_3
60 min	59	41
180 min	46	54
300 min	6	94

4.8 Characterisation of Particle Morphology by TEM Analysis

Figure 4.22 shows TEM bright field images of: (a) the as-received γ-Al_2O_3 and in (b), (c) and (d) the samples after dry milling in the JM for a total of 20 passes, SBM for 300 mins and PBM for 1200 min, respectively. In all cases it is clear that these secondary particles are composed of agglomerates of nanometre-sized single crystal primary particles. A rough quantitative analysis of the average particle sizes and shapes was carried out and is shown in Table 4.11.

Table 4.11: Average particle sizes, Coefficients of Variation and Aspect Ratios from TEM images of JM, PBM, SBM and A-R samples

Sample	A-R	JM	SBM	PBM
Average particle size (nm)	16.9	16.6	19.7	22.0
Coefficient of variation	0.5	0.2	0.2	0.2
Aspect ratio	2.5	2.5	1.7	1.1

The crystallite morphologies observed in the A-R sample appear plate-like with facetted edges; note elongated needle shapes are also observed depending on the orientation of the plate-like crystallites on the TEM support film. The JM sample was similar in size and morphology to the A-R sample as shown in Table 4.11. The SBM sample (Figure 4.22c) however shows a mixture of plate-like facetted crystallites and less elongated, more rounded crystallites. The sizes of the plate-like crystallites in the SBM sample have an average size of 17.2 nm whilst the more rounded crystallites had an average size of 22.2 nm.

The aspect ratio of the SBM samples (Table 4.11) is smaller than that observed in the A-R and JM samples. This suggests fracturing of elongated plates during SBM, which results in more equiaxed particles. Overall the primary crystals in the SBM samples appear slightly larger than those in the A-R and JM samples, providing evidence for coarsening of γ-Al_2O_3 particles with milling. This can be observed in Figure 4.22c. However, the PBM samples,

which from XRD had transformed to α-Al_2O_3, showed more octahedral-shaped crystallites with an average size of 22.0 nm and a coefficient of variation of 0.24 as shown in Figure 4.22d (ii) and Table 4.11.

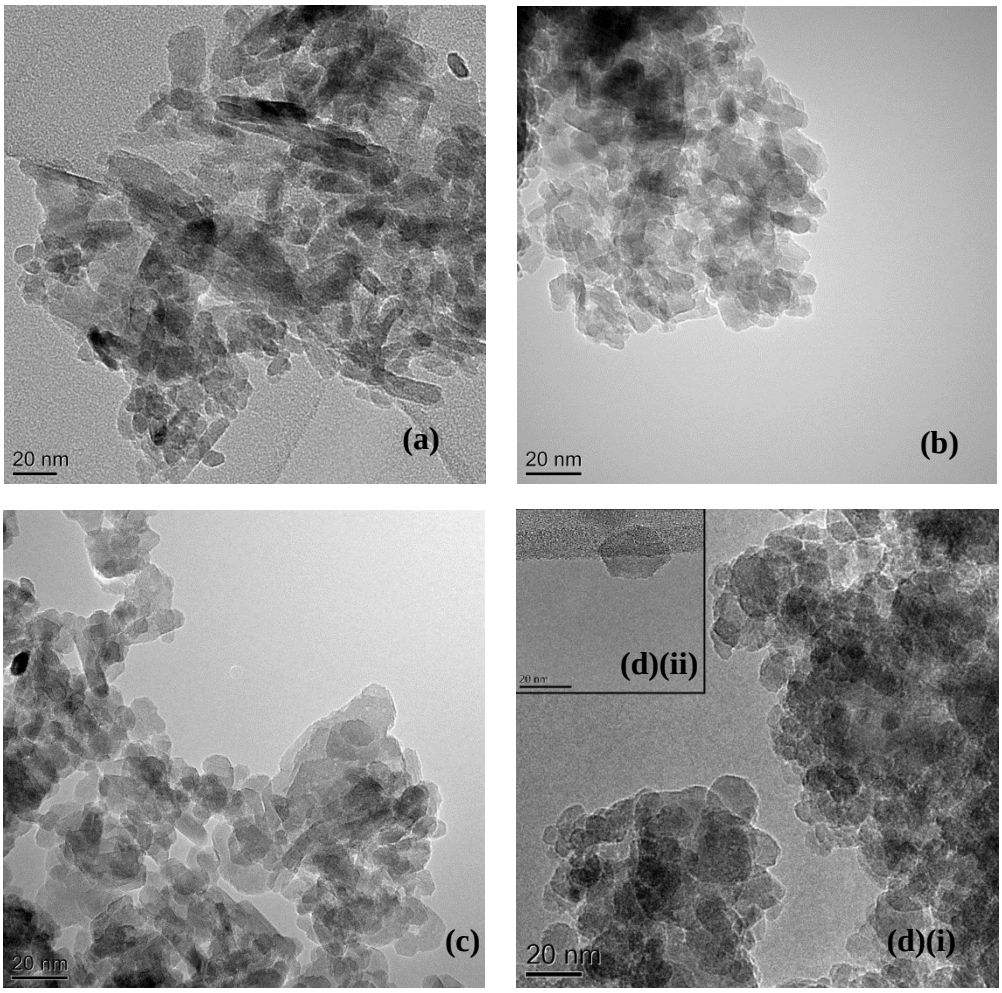

Figure 4.22: TEM micrographs illustrating the morphology of the γ-Al2O3 particles by bright field TEM showing (a) A-R, (b) JM after 20 passes, (c) SBM after 1200 min milling, (d)(i) PBM after 300 min milling and (d)(ii) inset of single crystal after 300 min milling in PBM

4.9 Characterisation of Chemical Environment by NMR Analysis

Solid-state NMR was used as a characterisation tool to better understand the structure of γ-Al_2O_3 samples after milling. Duvel *et al*. (2011) reported on a change in the sites of aluminium cations during milling. The results are shown in Figure 4.23. The arrows in Figure 4.23(a) show the peaks that represent aluminium cations in tetrahedral sites and octahedral sites. It can be observed that for A-R, SBM and JM samples, similar peaks are observed for the aluminium cations. The PBM sample however shows a smaller peak for the aluminium

cations in tetrahedral sites signifying a reduction in cations in these sites. This aligns well with the phase transformation observed as an increase in α-Al_2O_3 means that more aluminium atoms are in octahedral sites. α-Al_2O_3 exists as a hexagonal structure and hence all aluminium cations are in octahedral sites.

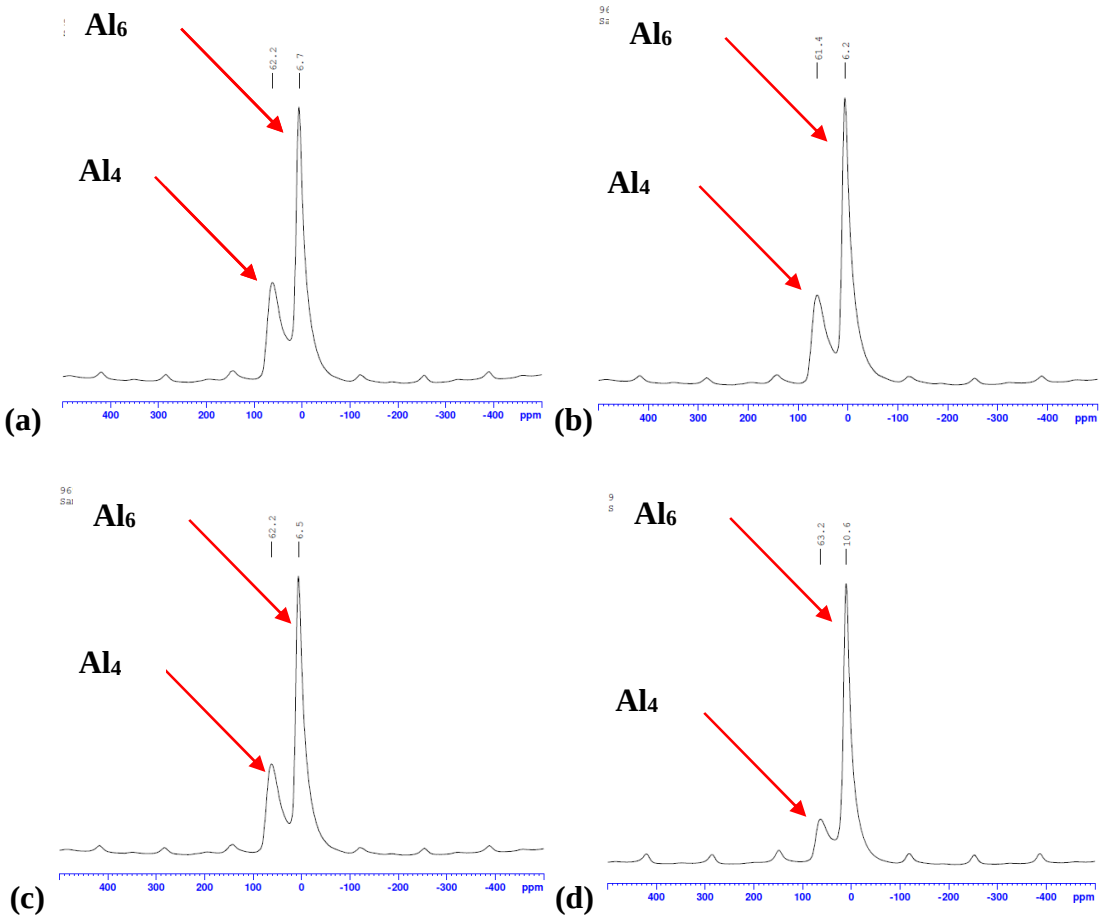

Figure 4.23: NMR results for samples (a)A-R and samples milled in the (b) JM, (c) SBM and (d) PBM

4.10 Discussion

Further analysis was carried out by a comparison of particle or crystallite sizes for A-R, JM (20 passes), PBM (300 min) and SBM (1200 min), derived from BET, TEM and XRD as shown in Table 4.12. In general, for all samples there is reasonable agreement, qualitatively, between the sizes derived using the three techniques as the principles of measurement of the methods are different. The primary particles are single crystal in nature, as suggested in TEM bright field images. It is important to note that the γ-Al_2O_3 crystallite sizes (Table 4.12) estimated from XRD using the Scherrer's equation are smaller than those observed by TEM owing to presence of a core-shell structure within γ-Al_2O_3 primary particles with a surface

disordered shell surrounding a more ordered crystalline core as observed by Rozita *et al.* (2013).

Table 4.12: Primary particle sizes as observed using TEM and estimated from XRD and BET

Sample	TEM Primary Particle Size average (nm)	XRD Crystallite Size average of 7 peaks (nm)	BET Primary Particle Size (nm)
A-R	16.9	9.7	13.6
SBM (1200 min)	19.7	13.6	12.9
JM (20 passes)	16.6	11.3	12.6
PBM (300 min)	22.0	25.0	22.5

Similar crystallite sizes were observed in the A-R and JM samples, whilst from XRD and TEM, SBM samples showed larger crystallites. The PBM samples showed the largest crystallite sizes averaging ca. 25 nm and these match primary crystal sizes for Boehmite-derived α-Al_2O_3 (Kim *et al*., 2007); here we also note that the TEM and XRD crystallite size data are closer in value, presumably due to the phase transformation to the α-Al_2O_3 crystal structure, which does not exhibit a disordered structure at the surface of the particles.

The formation of larger α-Al_2O_3 crystallites by a crystallographic rearrangement of the close packed planes of γ-Al_2O_3 from a cubic close packed to a hexagonal close packed structure that is stoichiometrically balanced with less vacancies results in a reduction in specific surface area (Table 4.8). The dehydration of Boehmite to form γ-Al_2O_3 is a topotactic transformation resulting in a similar crystal arrangement. Further dehydration results in less well-defined transition states (δ and θ phases), and α-Al_2O_3 is the final stable phase. However, mechanochemistry processes during milling appear to result in a transformation from γ-Al_2O_3 to α-Al_2O_3 without any observation of the intermediate δ and θ transition states (Figure 4.21). This transformation with an absence of δ and θ transitional Al_2O_3 phases was also observed by Tonejc *et al*. (1994) who observed χ and κ transitional states instead.

This suggests that a different mechanism to that of dehydration may be occurring during milling under the conditions used. It is observed that size reduction in the SBM and JM does not initiate phase change. However, the effect of shearing that is present in the PBM may be the main initiator of phase change by a possible shear-induced nucleation approach documented by Bagwell *et al*. (2001). In a shear mechanism, atoms in the region of

transformation shift a short distance into a new crystal arrangement (Bagwell *et al*., 2001). In this case, γ-Al_2O_3 exists as a cubic close-packed defective oxygen spinel structure with aluminium cations in interstitial positions in either octahedral or tetrahedral sites (or both) and vacancies.

The defective structure of γ-Al_2O_3 coupled with tri-axial stresses from the PBM can result in the movement of atoms by slip on close packed planes from the cubic close packed to the hexagonal close packed structure (Bagwell *et al*., 2001). Similar results to Duvel *et al*. (2011) of a reduction in aluminium cations in tetrahedral sites is observed in the NMR results. This confirms a change in the structural arrangement of the material as α-Al_2O_3 evolves during milling. Penta-coordinated aluminium cations are however not observed and a more in depth study with variation of milling variables is required as it can reveal whether this occurs during the process.

It can therefore be suggested that the mode of mechanical energy supplied; impact, shear, attrition, possibly determines whether mechanochemistry will occur. This can only be made conclusive by the study of isolated stress modes and by simulating impact energies during milling. Here, impact energy alone in the JM (a high impact energy mill) does not affect the structure of γ-Al_2O_3. A presence of limited shear stresses in the SBM (vibration milling) results in a small increase in crystallite size without transformation. This may arise via a possible growth of crystals to a critical size before shear-induced nucleation and transformation occurs, as stated by Bagwell *et al.* (2001) and observed by Dynys and Halloran (1979). This suggests that impact energy alone will not cause transformation. Growth of crystals in SBM samples shows that the shear stress supplied by the mill affects crystal morphology but is not sufficient to initiate phase transformation to α-Al_2O_3.

This work does not only highlight the stress mode but also the amount of energy supplied by each stress mode in each mill. Zielinski *et al*. (1993) observed phase transformation using a vibratory mill. The difference between the SPEX mill used by Zielinski *et al*. (1993) and the Retsch MM200 is that the SPEX milling jar is at an angle during milling while the Retsch MM200 milling jar remains horizontal as shown in Figure 4.24. The powder in the horizontal jar experiences less shear stress compared to that in the SPEX. It is also important to note that in the Retsch MM200 mill, only one single ball is used whereas the SPEX milling jar is large enough for more milling media, 10 mm or bigger in diameter. This also increases the amount of energy transferred into the powder. The difference is shown in Figure 4.24.The PBM

however supplies the adequate amount of shear stress which favours shear nucleation of α-Al_2O_3 from γ-Al_2O_3.

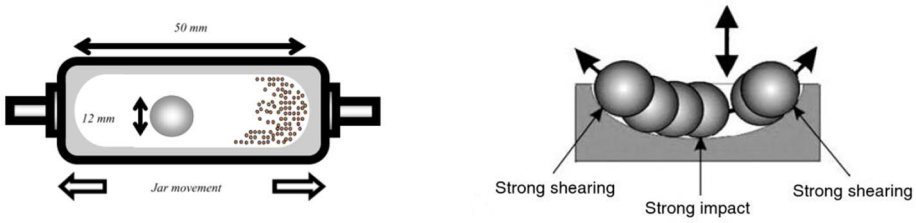

(a) **(b)**

Figure 4.24 : Difference between the (a) Retsch and (b) SPEX vibratory mill

4.11 Conclusions

Jet milling is a more suitable size reduction method for dry milling of γ-Al_2O_3 powders when compared with planetary ball milling and single ball milling, as it effectively reduces size without affecting the morphology of the material. Contamination of samples with ZrO_2 also occurs during planetary ball milling and is observed to increase with time. Dry planetary ball milling results in a phase change from γ to α-Al_2O_3 as observed by XRD patterns and octahedral crystal shapes in TEM. A significant loss of surface area from 136.6 m^2/g to 82.6 m^2/g is evident in the planetary ball mill samples, rendering the planetary ball mill as less suitable for size reduction of catalyst supports. The observation of transformation in planetary ball milled samples is likely to be caused by high shear stresses in the mill that result in shear nucleation and formation of α-Al_2O_3. This, however, requires further investigation which will be addressed in *Chapter 5* of this thesis. The single ball mill is also observed to cause a change in the morphology of γ-Al_2O_3 although it does not result in phase transformation. The observed changes are likely due to small movements of atoms at surfaces initiating phase transformation within the sample and hence causing crystals to appear larger. Further investigation is also required here and will be addressed in *Chapter 6* of this thesis.

Chapter 5

Phase Transformation in the Planetary Ball Mill

Milling gamma-Alumina using the planetary ball mill is investigated further by a variation of process conditions. The effect of the stress mode provided by the planetary ball mill on the properties of gamma-Alumina is derived from these investigations. A mechanism of phase transformation from gamma-Alumina to alpha-Alumina is proposed and further observations on the effect of milling material are also discussed in this chapter.

5 Phase Transformation in the Planetary Ball Mill

5.1 Introduction

Phase transformation from γ-Al_2O_3 to α-Al_2O_3 is observed in planetary ball milled samples as discussed in Chapter 4. This effect is caused by mechanochemical reactions that occur when mechanical energy is applied to γ-Al_2O_3. Mechanochemistry as detailed in Chapter 2 is often initiated by high energy ball milling. In order to better understand the interactions of powder samples with milling media and milling vessels in the planetary ball mill, it is necessary to conduct a study on the mill.

A variation of different conditions during milling, such as ball-to-powder ratio, milling media size and milling media and vessel material, can shed further light into the phase transformation observed. This is because, by varying different conditions, the impact energies supplied to the powder samples are also varied. It is then possible to deduce the milling conditions that effect phase transformation. More information on the range of impact energies supplied by different milling conditions can allow choice for the most suitable conditions for the desired product. It is also then possible to isolate the stress mode that effects phase transformation and come up with a mechanism of how the change is initiated and carried forward. Shear stress has been suggested in Chapter 4 as an initiator for phase transformation. This finding is however, inconclusive and requires further investigation. The effect of milling aids such as lubricants and water can also shed light into how additional substances in the mill affect the rate of phase transformation.

This chapter is organised as follows. Firstly, the milling devices used and the experimental procedures are described. A planetary ball mill time study is presented with results of the characterisation carried out after milling. This is followed by a milling material and milling media size study, which includes particle size analysis and morphology characterisation. Finally, an analysis of the effect of milling with aids such as water and zinc stearate is attempted. A discussion of all the results in the chapter is given and conclusions on the effects milling conditions in the planetary ball mill are given.

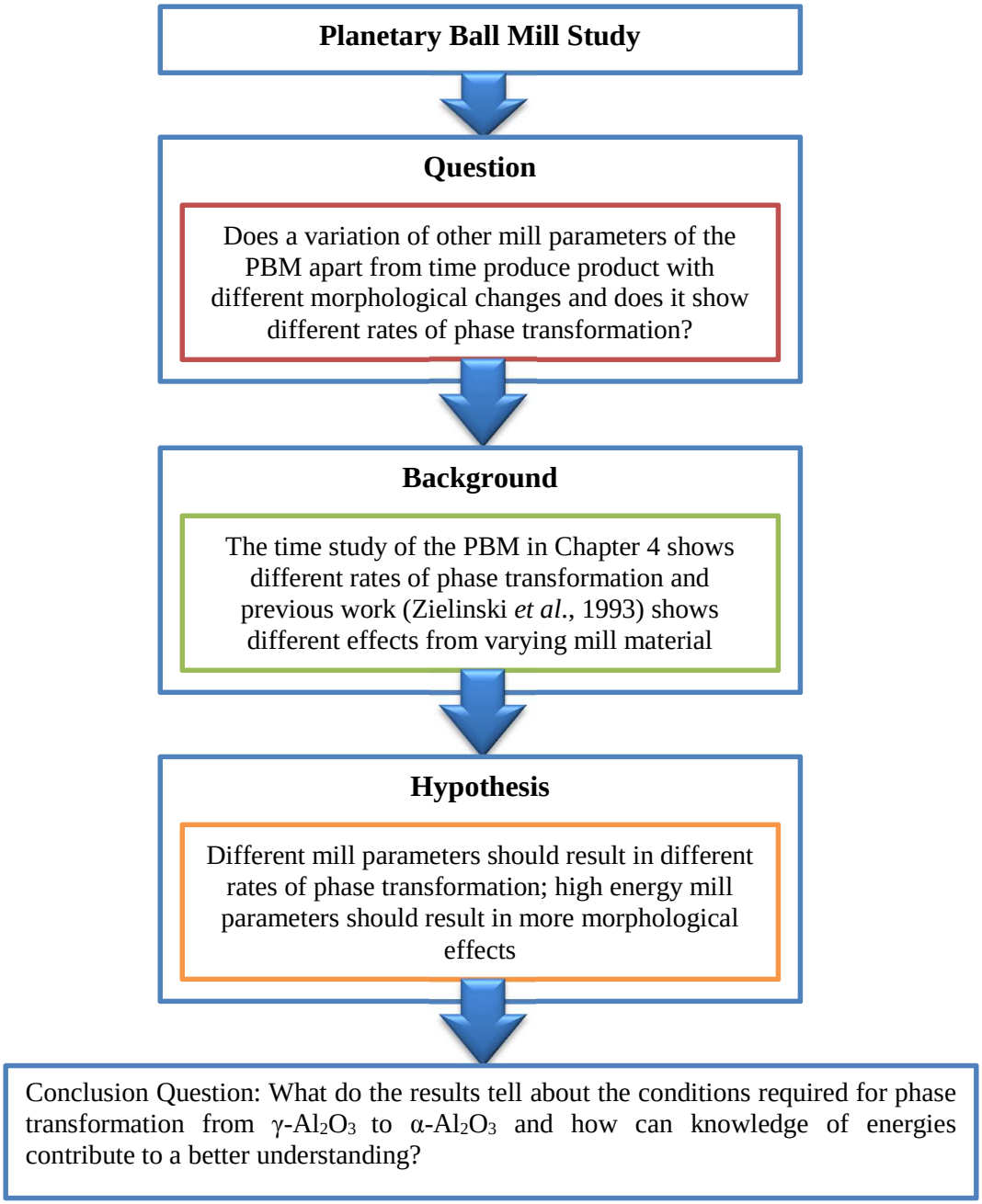

Figure 5.1: Hypothesis formulation for *Chapter 5*

5.2 Experimental Devices and Procedures

The Fritsch Pulverisette 7 mill detailed in section 4.2.2 has already been used for a planetary ball mill time study. A study of the effect of ball-to-powder ratio, milling media size and milling material is also carried out with the Fritsch Pulverisette 5 mill shown in Figure 5.2. The mill is operated at the maximum milling speed of 400 rpm. The volume of the milling vessels used is 250 ml and a ball-to-powder ratio of 10:1 is used. The milling vessels are filled up to two thirds of their total volume. Four different milling materials are tested; Agate, Zirconia, Stainless Steel and Alumina. In the milling material study, the milling media size used is a diameter of 20 mm.

Figure 5.2: Fritsch Pulverisette 5 Planetary Ball Mill

The milling media size study is carried out with Zirconia milling vessels and Zirconia milling media. The milling media size is varied from ~2 mm (1.5 -2.5 mm) to 20 mm and milled for 120 minutes. The milling vessel and milling media used for the experiment is shown in Figure 5.3.

(a) 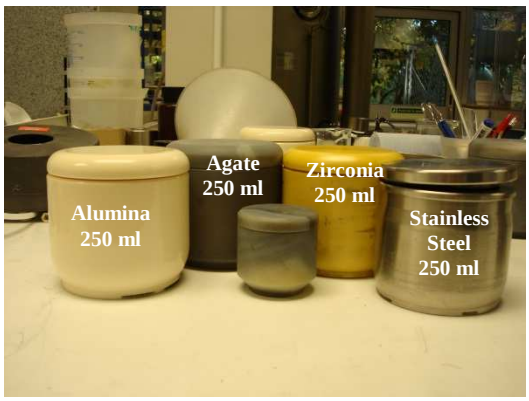

(b) 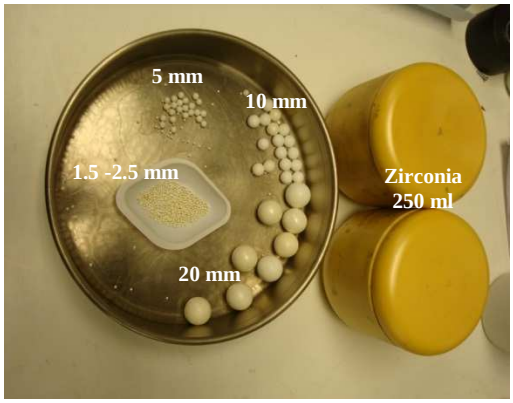

Figure 5.3: Milling vessels and milling media for ball-to-powder ratio, milling material and milling media size studies showing (a) all milling vessels and (b) Zirconia 250 ml milling vessels with 4 Zirconia milling media sizes

During an experimental run, the milling vessels are filled with powder samples and milling media and tightly clamped on the mill. The safety hood is closed and the milling time and milling speed are set. The mill is run with periodical checks every 20 minutes to ensure the milling vessels are tightly clamped and to ensure the temperature of the milling vessels is within safe limits. Table 5.1 is a detailed outline of the properties of all the milling vessels and milling media used in the experiments with the Fritsch Pulverisette 5 mill.

Table 5.1:Equipment Used for Fritsch P5 Planetary Ball Mill Study

Mill Type	Milling Tools					Milling Media
	Material	Size (ml)	Density (g/cm^3)	Youngs Modulus (GPa)	Vickers Hardness (GPa)	Diameter (mm)
Fritsch Pulverisette 5	Agate 99.9% SiO_2	250	2.65	70	7.85	20
	Sintered corundum 99.7% Al_2O_3	250	3.8	300	15.00	20
	Stainless Steel 17-19% Cr 8-10% Ni + Fe	250	7.8	200	5.30-6.47	20
						10
	Zirconium dioxide 95% ZrO_2	250	5.7	250	11.77	20
						10
						5
						1.5 – 2.5

The effect of milling aids such as water and zinc stearate is also studied in the Fritsch P5 and Retsch PM100 planetary ball mill with 20 mm milling media (shown in Figure 5.4). In this

study, the milling material was varied for wet milling in water. Zirconia milling vessels and milling media were used and the mills were operated at 400 rpm. A ball-to-powder ratio of 10:1 was maintained for all experiments.

(b)

Figure 5.4: Photographs showing (a) Retsch PM100 planetary ball mill and (b) various milling vessels and milling media with the Zirconia milling vessels and milling media used in experiments shown by a red asterisk

5.3 Ball-to-Powder Ratio Study in the Planetary Ball Mill

When loading the planetary ball mill with milling media and the material to be milled, it is important to add the two in a ratio that allows efficient milling of the material. Two ball-to-powder (BPR) ratios have been selected; 5:1 and 10:1 for use. An Agate milling vessel with Agate milling media were used for the investigation. After milling, the samples were characterised for particle size reduction and morphology changes by use of laser diffraction and XRD respectively. Table 5.2 shows the variables used.

Table 5.2: Variables for BPR Study in P5 Planetary Ball Mill

Dependant variables	Controlled variables		Independent variable	
% of α-Al_2O_3 D_{90} particle size	Ball size/ mm	20	BPR	10:1
	Material	Agate		
	Time/ hr	1, 3		5:1

5.3.1 Particle Size and Shape Analysis for BPR Study

Figure 5.5 and Figure 5.6 show the particle size distribution for the two samples milled with a varied BPR and characterised using laser diffraction. The results shown are after 3 hours of milling. It can be seen that a higher BPR of 10:1 achieves smaller particles. The 5:1 sample also shows particles larger than the A-R sample. The samples are further analysed by SEM imaging to observe the particle shapes as well as the morphology of the large particles observed in laser diffraction.

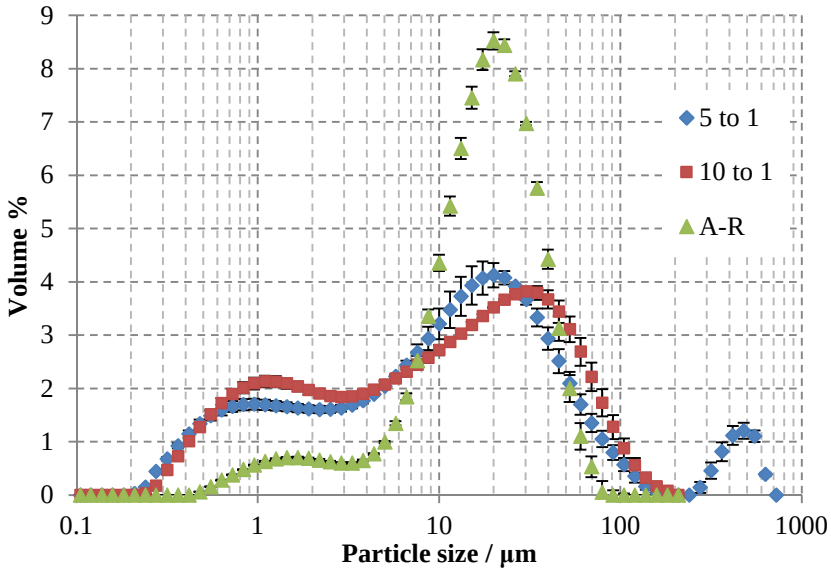

Figure 5.5: Particle size distribution for γ-Al_2O_3 samples milled in Agate with BPRs of 5:1 and 10:1 for 180 min

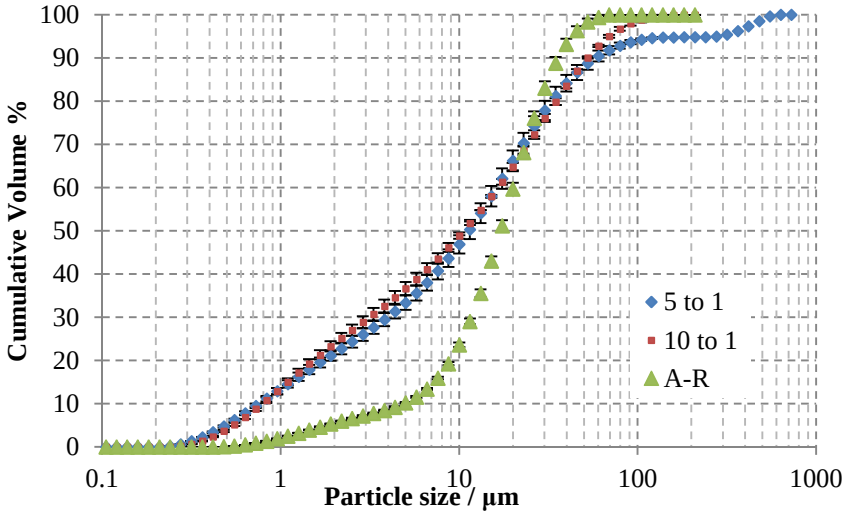

Figure 5.6: Cumulative particle size distribution for γ-Al_2O_3 samples milled in Agate with BPRs of 5:1 and 10:1 for 180 min

Figure 5.7 shows the SEM images for the samples milled at a BPR of 5:1 and 10:1. A large amount of fine material is observed in the 10:1 sample and this is not observed in the 5:1 sample. This shows that more efficient particle breakage occurs when a higher BPR is used.

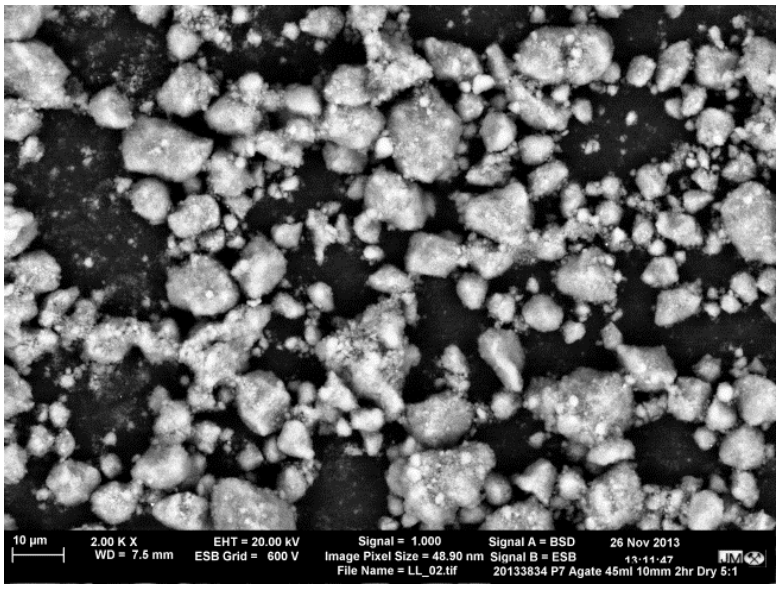

Figure 5.7: SEM images of BPR study samples showing powders milled at a BPR of (a) 5:1 and (b) 10:1

From the SEM images, a number based particle size distribution has been carried out to derive the amount of particles below 10 µm. It can be seen in Figure 5.8 that the sample with the 10:1 BPR has the largest number of fine particles. In terms of size reduction, a higher BPR is more favourable for achieving smaller particles. The sample with a ratio of 10:1 contains 50% less γ-Al_2O_3 powder than the 5:1 sample and this allows for better contact of

the sample with milling media and milling vessel walls. Increased contacts allow for more particle breakage and better size reduction. All results from this study show that a ratio of 10:1 can be used for size reduction of γ-Al_2O_3 powder. It is also; however, clear that milling with Agate does not achieve the required particle size reduction with a d_{90} of less than 10 µm. The sample only contains a minimal amount of small particles. It is, therefore, necessary to test different milling materials to assess if smaller particles can be achieved.

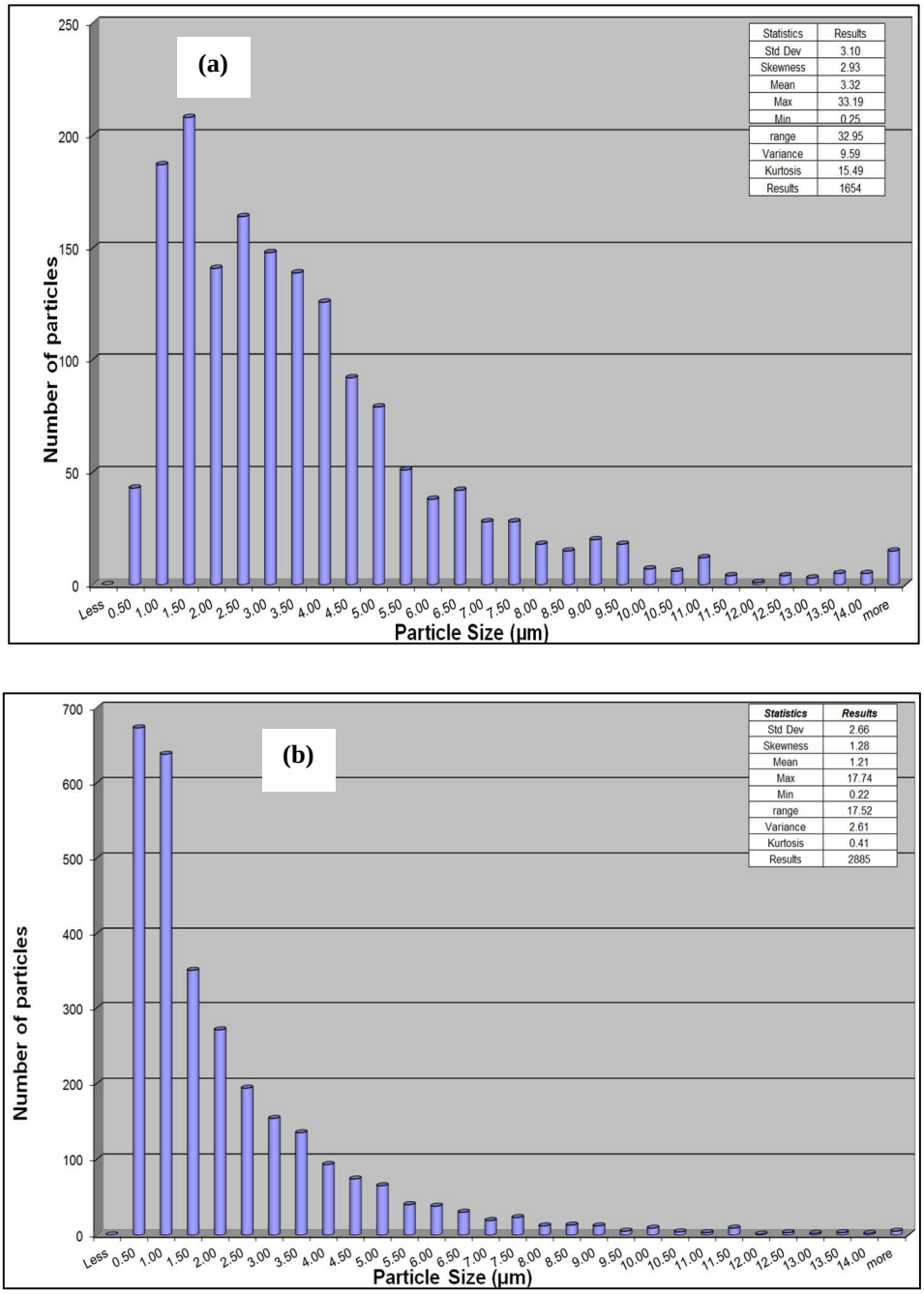

Figure 5.8: Number based particle size distribution of BPR study showing samples milled in Agate with a BPR of (a) 5:1 and (b) 10:1

5.3.2 Phase Identification by XRD Analysis

It is also of interest to investigate the effects of planetary ball milling on the morphology of γ-Al_2O_3 powders. XRD analysis has been used to assess whether a variation BPR affects the morphology of γ-Al_2O_3 powder. Figure 5.9 shows the XRD patterns for the samples milled at different BPRs. It is clear from comparing the A-R sample with the milled samples that milling in Agate does not initiate phase transformation. This could likely be due to the material properties of Agate i.e. low hardness and density, which result in lower energy impacts and hence the mechanical energy supplied is not enough to cause any phase change. The intensity of the silicon peak in the milled samples also highlights a high level of contamination. The 10:1 BPR sample has a higher level of contamination than the 5:1 sample. This shows that γ-Al_2O_3 powder is too abrasive for milling in Agate. A higher BPR results in more abrasion of the mill walls and milling media with the powder.

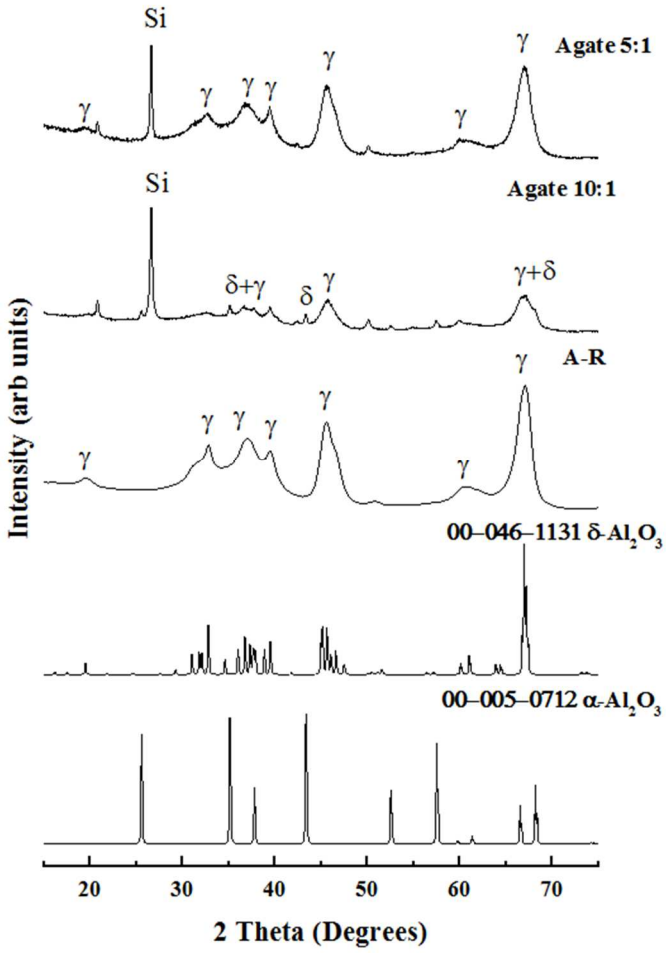

Figure 5.9: XRD Diffractograms for BPR Study showing γ-Al_2O_3 reference file 00-010-0425, A-R sample and γ-Al_2O_3 milled at a ratio of 5:1 and 10:1

5.4 Material Study in the Planetary Ball Mill

In order to have a better understanding of the phase transformation observed in the mill type study in Chapter 5, it is necessary to understand how γ-Al_2O_3 powders interact with different milling materials during milling. This has been done by selecting four different materials and milling using similar controlled variables. The conditions used in the milling material study are shown in Table 5.3. Having carried out the milling experiments, the milled samples are characterised for size reduction and morphology changes.

Table 5.3: Milling Conditions for Material Study In Fritsch P5 Planetary Ball Mill

Dependant variables	Controlled variables		Independent variable	
% of α-Al_2O_3 D_{90} particle size	Time/ hr	3	Material type	Agate
	Ball size	20 mm		Alumina
	Medium	Dry		Zirconia
	BPR	10:1		Stainless Steel

5.4.1 Particle Size and Shape Analysis of Milling Material Study

It is of interest to analyse the efficiency of the Fritsch P5 planetary ball mill in terms of size reduction in order to deduce whether the mill can achieve the required size reduction of less than 10 μm. Figure 5.10 shows the particle size distribution of the material study carried out and Figure 5.11 shows the cumulative distributions as derived from laser diffraction. Size reduction can be observed for all four conditions. There is however no significant difference in the size reduction achieved by the four different materials.

The results can also be further analysed by comparing the d_{10}, d_{50} and d_{90} particle sizes. As shown in Table 5.4, there is no significant difference in the size reduction observed in the Zirconia, Alumina and Stainless Steel vessels. It can, however, be observed that in the Agate vessel, the particle sizes are larger than in the other three materials. Agate shows to be less effective when compared with the other three milling materials. The d_{90} particle size in all vessels is larger than the A-R sample. This suggests that milling the PBM can result in re-agglomeration of particles.

Table 5.4: Characteristic sizes (d_{10}, d_{50} and d_{90}) of the A-R sample and samples milled by the Fritsch P5 mill in Zirconia, Agate, Stainless Steel and Alumina

Sample	Particle size (µm)		
	D_{10}	D_{50}	D_{90}
A-R	6.2	21.4	49.1
Agate	0.9	13.5	65.4
Stainless Steel	0.6	11.2	74.2
Alumina	0.6	9.6	63.4
Zirconia	0.6	10.1	65.2

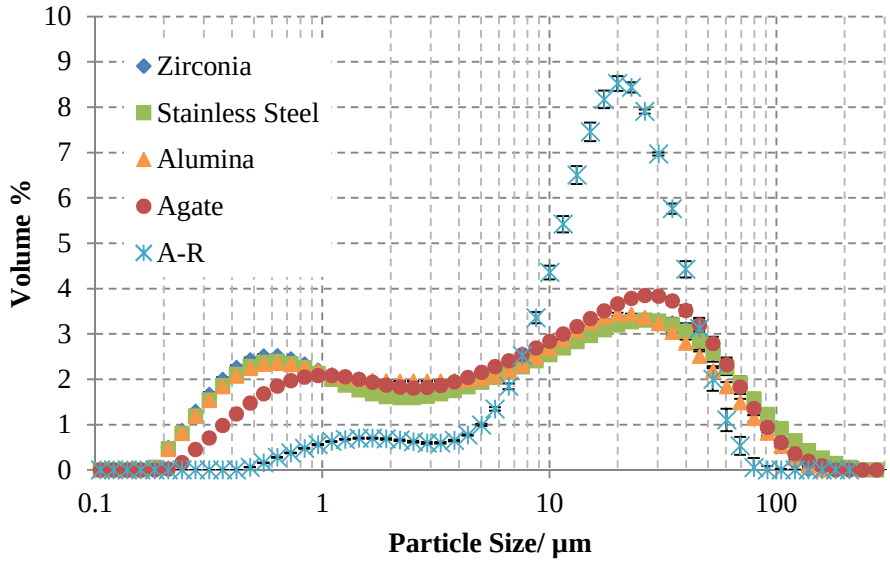

Figure 5.10: Particle size distribution for γ-Al_2O_3 samples milled in different milling materials

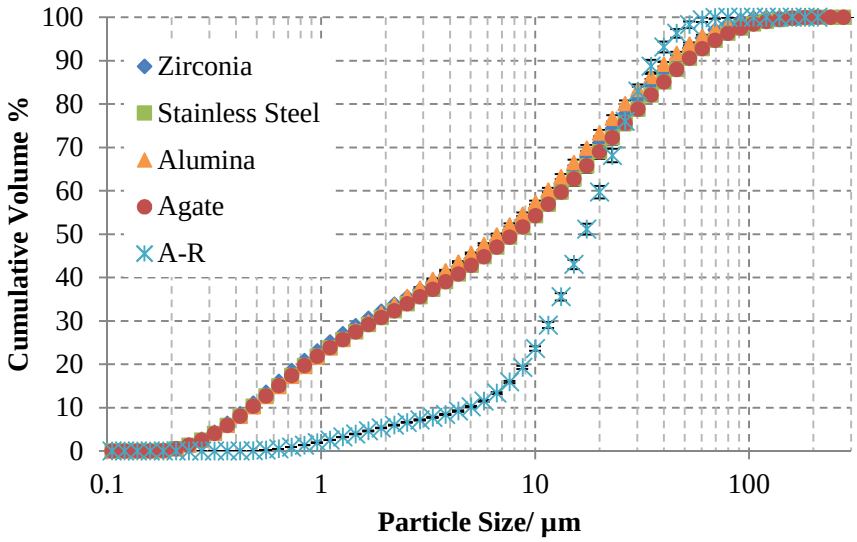

Figure 5.11: Cumulative particle size distribution for γ-Al_2O_3 samples milled in different milling materials

Although laser diffraction sheds light into the full particle size distribution of all samples, the Mie theory used for calculations for particle sizes, assumes spherical particles. It is therefore necessary to analyse the particles with SEM for particle shapes and sizes. Figure 5.12 shows the SEM images of the A-R sample and the four samples from the milling material study.

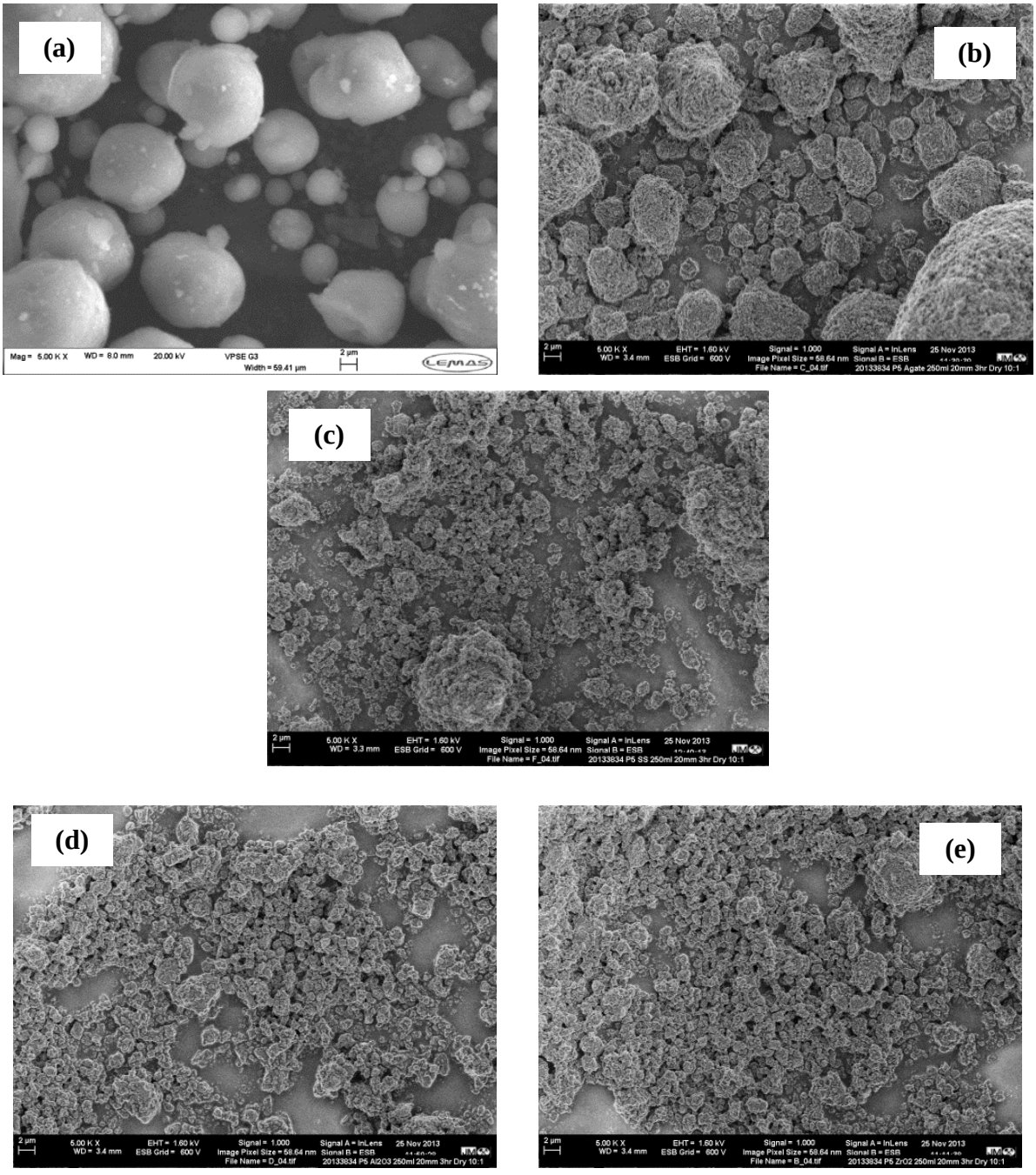

Figure 5.12: SEM imaging of γ-Al_2O_3 particles showing (a) Agate sample, (b) Stainless Steel sample, (c) Alumina sample and (d) Zirconia sample after 300 mins of milling

It can be observed from Figure 5.12 that the Agate sample has larger particles than the other three samples. There is, however, no significant observable difference in the particle sizes of

the Stainless Steel, Alumina and Zirconia samples. Large agglomerates of finely milled material are also observed in Stainless Steel sample suggesting re-agglomeration observed by laser diffraction. Although the A-R sample is composed of spherical particles with smooth surfaces, the particle shapes after milling are irregular with rough surfaces. Further analysis has been carried out on SEM images in Figure 5.12 to derive number based particle size distributions. These are shown in Figure 5.13 and it can be seen that the largest amount of fine material below 10 μm is obtained in the Zirconia milling vessel. A trend of size reduction can be derived from the number based distribution for frequency of particles less than 10 μm. It shows that the frequencies from largest amount to smallest amount follow; Zirconia →Alumina→ Stainless Steel→ Agate. This trend is similar to that observed by laser diffraction and an agreement in the results has been observed.

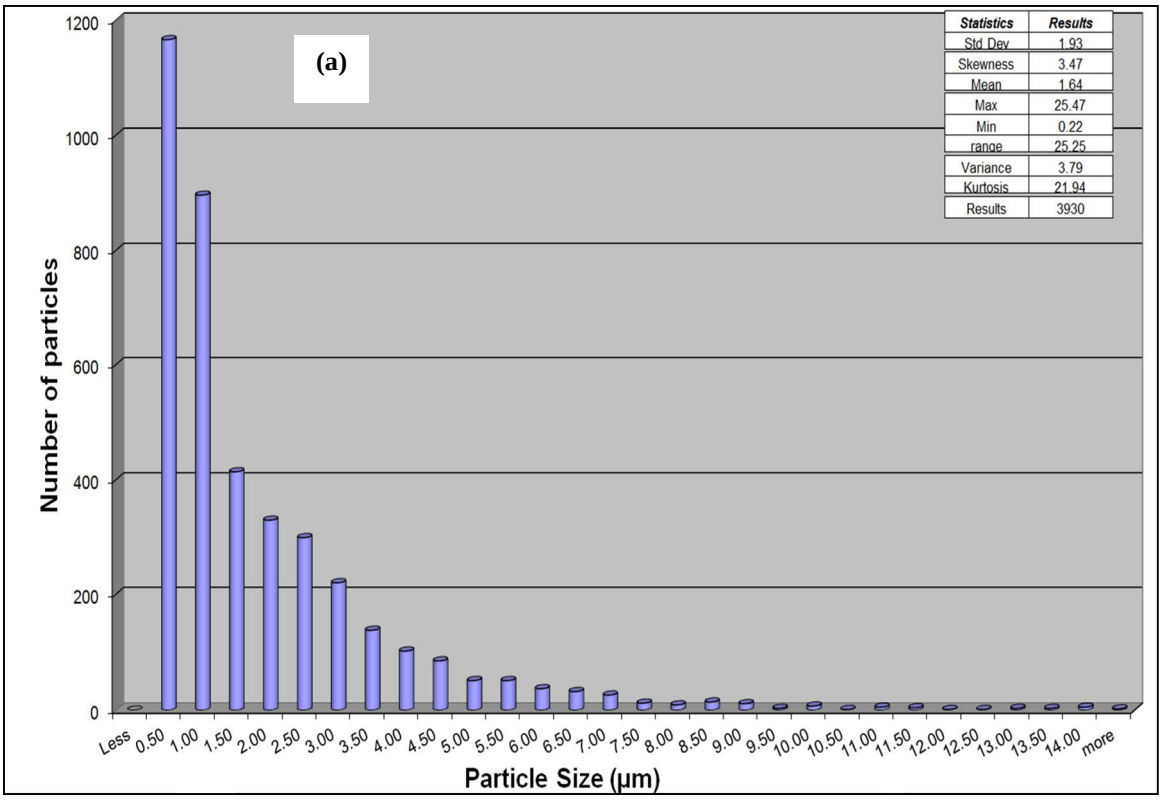
(a)
Statistics | Results
Std Dev | 1.93
Skewness | 3.47
Mean | 1.64
Max | 25.47
Min | 0.22
range | 25.25
Variance | 3.79
Kurtosis | 21.94
Results | 3930
Number of particles
0
200
400
600
800
1000
1200
Less 0.50 1.00 1.50 2.00 2.50 3.00 3.50 4.00 4.50 5.00 5.50 6.00 6.50 7.00 7.50 8.00 8.50 9.00 9.50 10.00 10.50 11.00 11.50 12.00 12.50 13.00 13.50 14.00 more
Particle Size (µm)

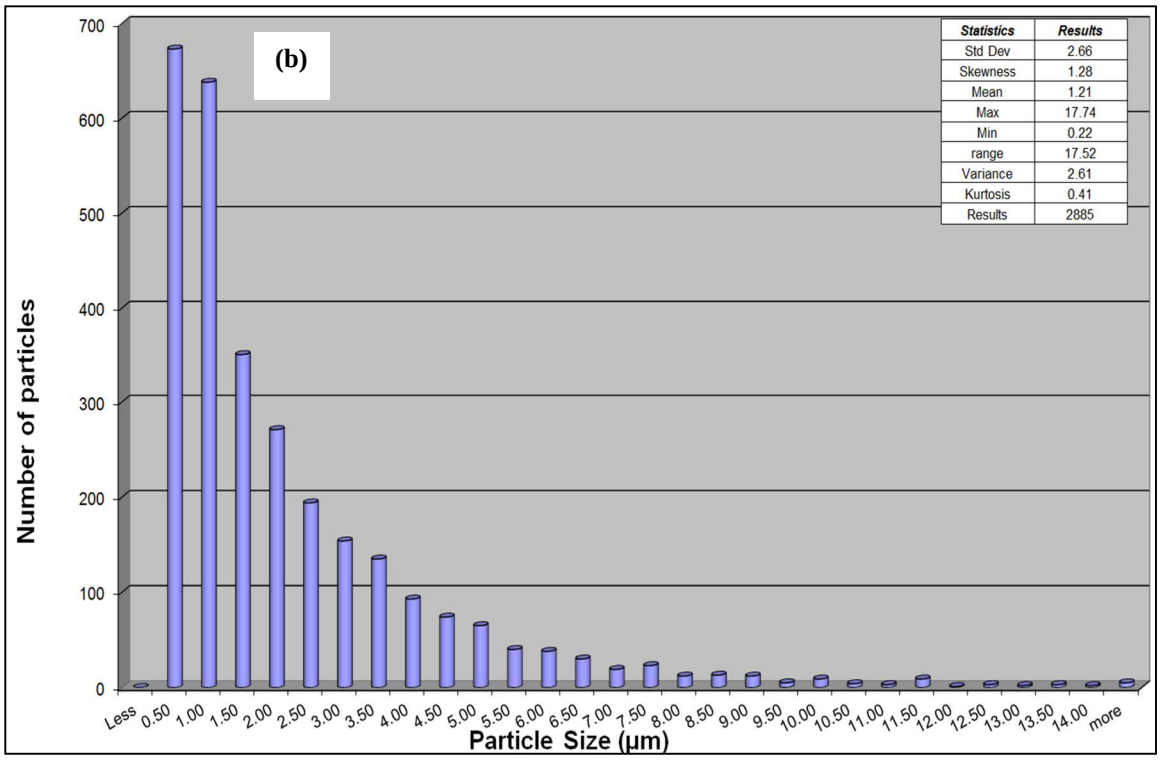
(b)
Statistics | Results
Std Dev | 2.66
Skewness | 1.28
Mean | 1.21
Max | 17.74
Min | 0.22
range | 17.52
Variance | 2.61
Kurtosis | 0.41
Results | 2885
Number of particles
0
100
200
300
400
500
600
700
Less 0.50 1.00 1.50 2.00 2.50 3.00 3.50 4.00 4.50 5.00 5.50 6.00 6.50 7.00 7.50 8.00 8.50 9.00 9.50 10.00 10.50 11.00 11.50 12.00 12.50 13.00 13.50 14.00 more
Particle Size (µm)

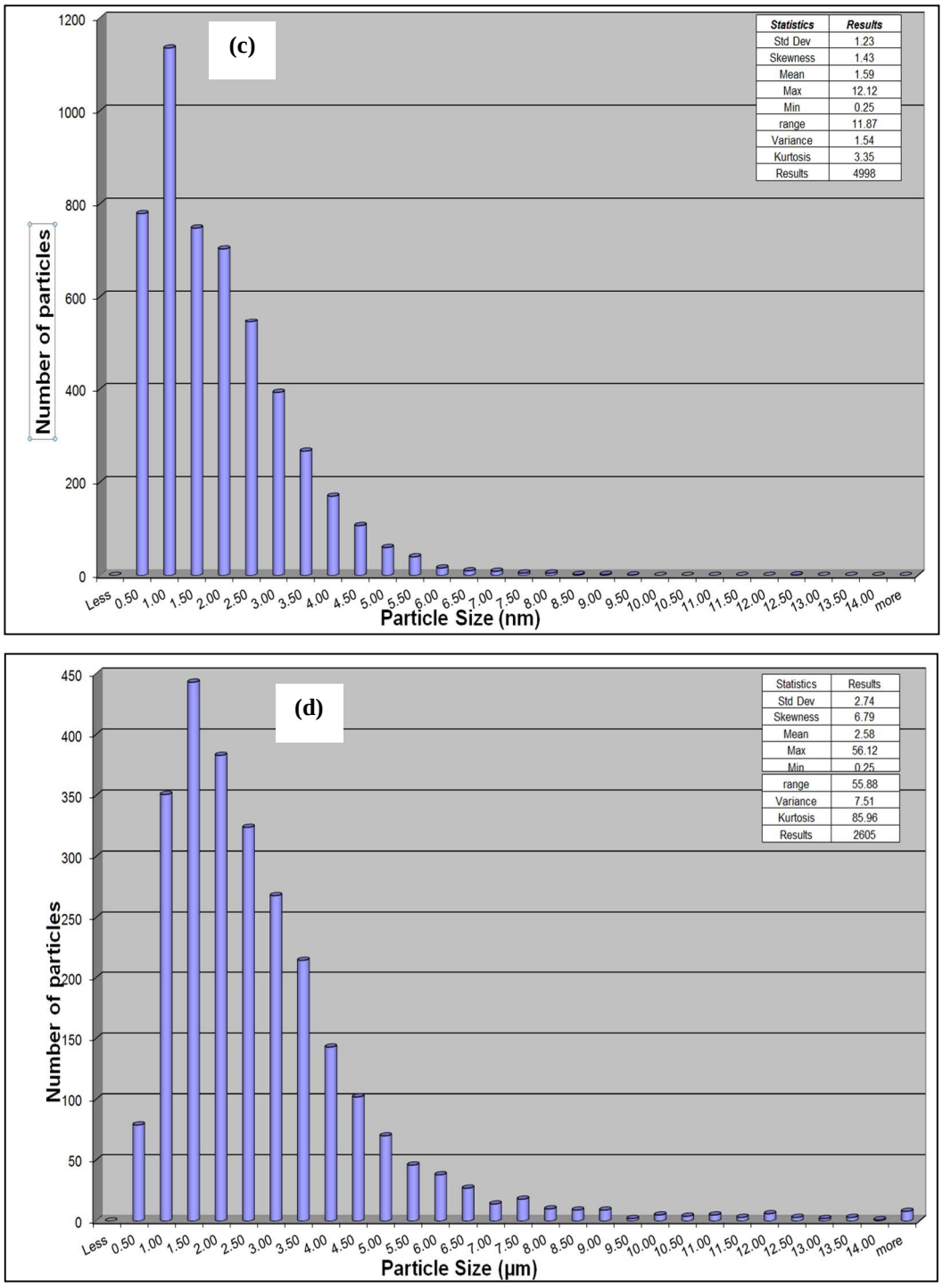

Figure 5.13: Number based particle size distributions of material study showing samples milled in (a) Zirconia, (b) Agate, (c) Alumina and (d) Stainless Steel

Although small differences in size reduction efficiency are observed in the four different materials with a trend of Zirconia →Alumina→ Stainless Steel→ Agate, overall there is no significant difference in the particle sizes achieved. It is therefore necessary to analyse the material further for morphological effects in the different mills which may include surface effects, crystallographic effects and levels of contamination.

5.4.2 Phase Identification of Milling Material Study

Phase transformation has been observed in the Fritsch P7 mill with Zirconia milling material. It is of interest to investigate the effect of different milling material in order to identify the main factors that result in the formation of α-Al_2O_3 from γ-Al_2O_3. XRD has been used for bulk crystal morphology analysis and the XRD diffractograms are shown in Figure 5.14. It can be observed from Figure 5.14 that the γ-Al_2O_3 sample milled in the Agate vessel resembles the pattern of the A-R sample. There is, however, contamination from the milling vessel and media. The γ-Al_2O_3 samples milled in the Zirconia and Alumina mills show phase transformation after 300 minutes of milling. The XRD diffractograms also match to the ICDD reference file 00-005-0712 for α-Al_2O_3. The sample milled in the Stainless Steel vessel resembles the pattern of A-R γ-Al_2O_3 but with small emerging peaks of α-Al_2O_3.

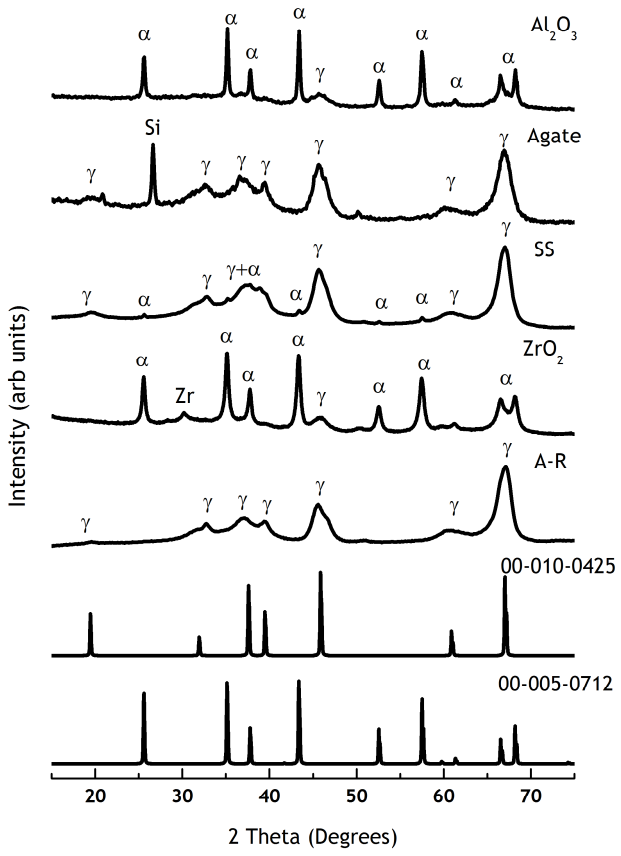

Figure 5.14: XRD patterns of Al_2O_3 showing α-Al_2O_3 ICDD reference pattern 00-005-0712, γ-Al_2O_3 ICDD reference pattern 00-010-0425, as-received γ-Al_2O_3 and γ-Al_2O_3 after milling in Agate, Zirconia, Alumina and Stainless Steel

Further analysis can be carried out by a calculation of the percentage estimates of each phase; α-Al_2O_3 and γ-Al_2O_3 in the sample by use of Rietveld refinement. Peaks not matched to γ-Al_2O_3 in the Agate sample were matched to δ-Al_2O_3.

Table 5.5: Percentage of γ-Al_2O_3 and α-Al_2O_3 phases for samples milled in Zirconia, Alumina, Stainless Steel and Agate vessels based on area under matched peaks by the use of Xpert Highscore software

Material	γ-Al_2O_3 (%)	α-Al_2O_3 (%)	δ-Al_2O_3 (%)
Alumina	48.2	51.8	-
Zirconia	34.2	65.6	-
Stainless Steel	51.0	48.3	-
Agate	61.0	0	34.8

Table 5.5 shows that the sample milled in the Alumina vessel has the second highest percentage of α-Al_2O_3. At this stage, although the Alumina material displays a fast rate of transformation, the Al_2O_3 from the milling material itself may be playing a role in the transformation. This has been previously reported by Bodaghi *et al*. (2008). This effect is analysed further by seeding experiments in Chapter 6. The Zirconia milling material has the largest amount of α-Al_2O_3 after 300 min of milling. No α-Al_2O_3 was observed in the Agate sample. However, 34.8% of the sample was composed of δ-Al_2O_3. All milling material experiments have been carried out with 20 mm milling media. It is of interest to analyse the effect of different milling media size using a material that initiates phase transformation.

XRD analysis highlights the presence of contamination in the samples. This can be an undesired effect if the mill material can affect the use of the final product. Further analysis has been carried out by TEM-EDX analysis to confirm the existence of contamination in the milled material. This can be shown in Figure 5.15. The analysis of contamination shows that γ-Al_2O_3 is abrasive in all four milling materials. According to the manufaturer, the abrasion resistance of the materials from most resistant to least resistant follows the trend of Zirconia → Alumina → Stainless Steel → Agate. The XRD results show a similar trend with very sharp peaks of Silicon observed in the Agate sample.

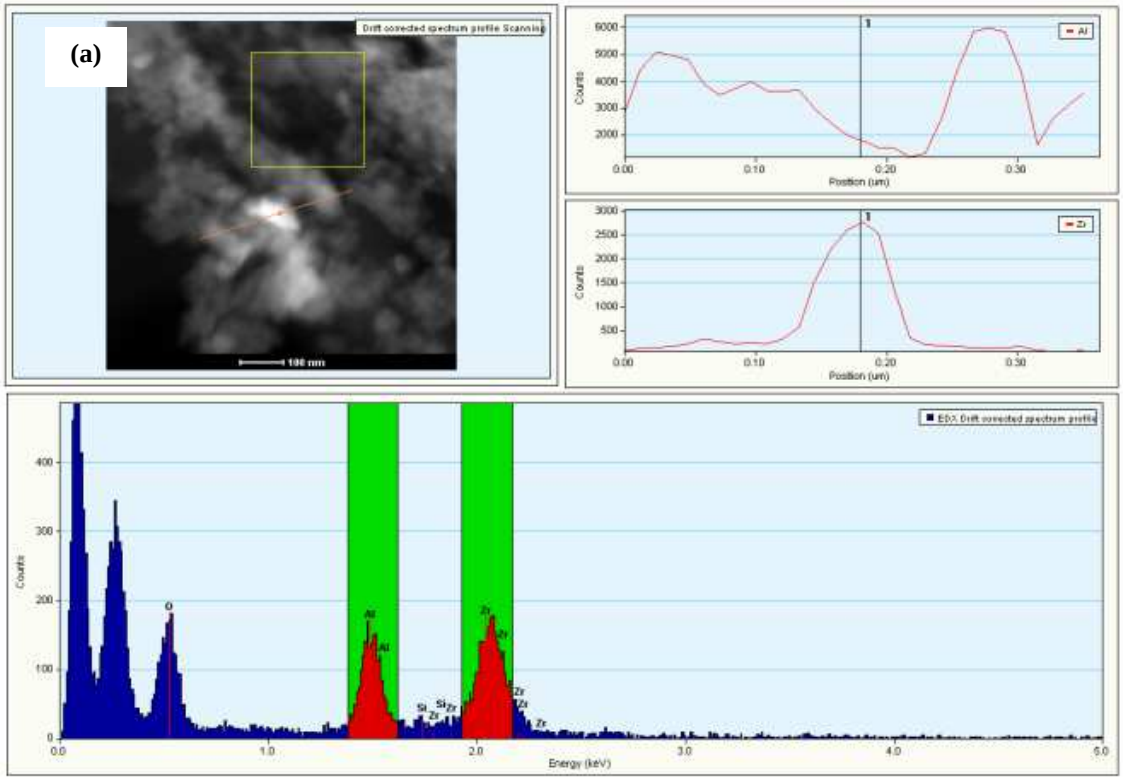

A line profile spectra1.emi - Thu Nov 28 16:06:00 2013

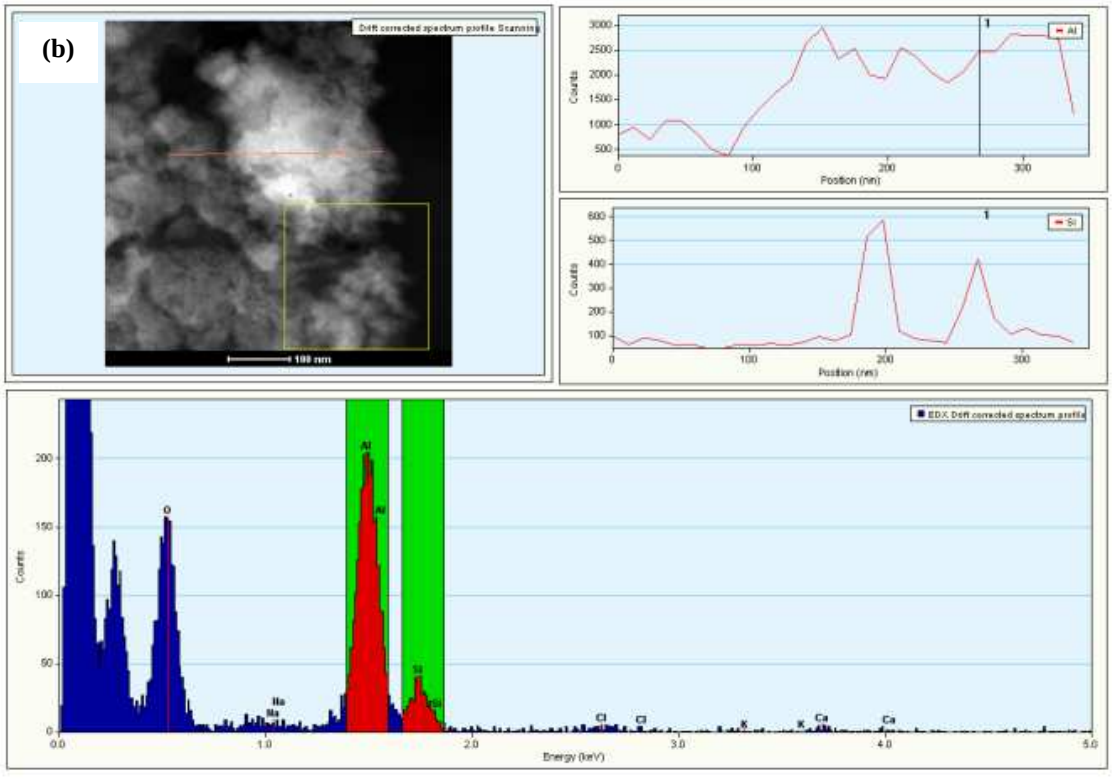

B line profile spectra2.emi - Thu Nov 28 16:19:12 2013

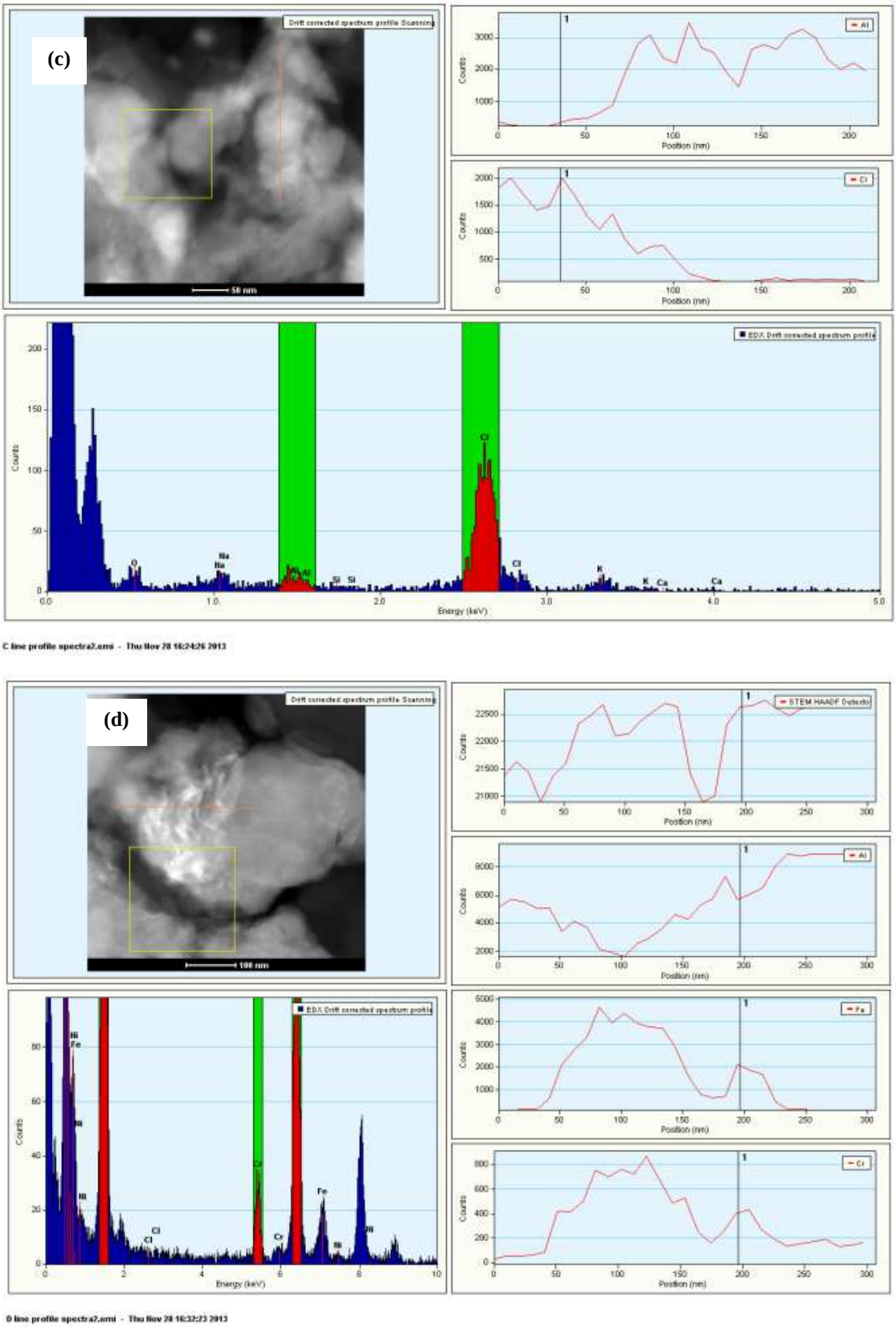

Figure 5.15: TEM-EDX analysis of material study samples showing samples milled in (a) Zirconia, (b) Agate, (c) Alumina and (d) Stainless Steel

Solid-state NMR was also carried out to anayse the effects of milling in different materials. This is shown in Figure 5.16.

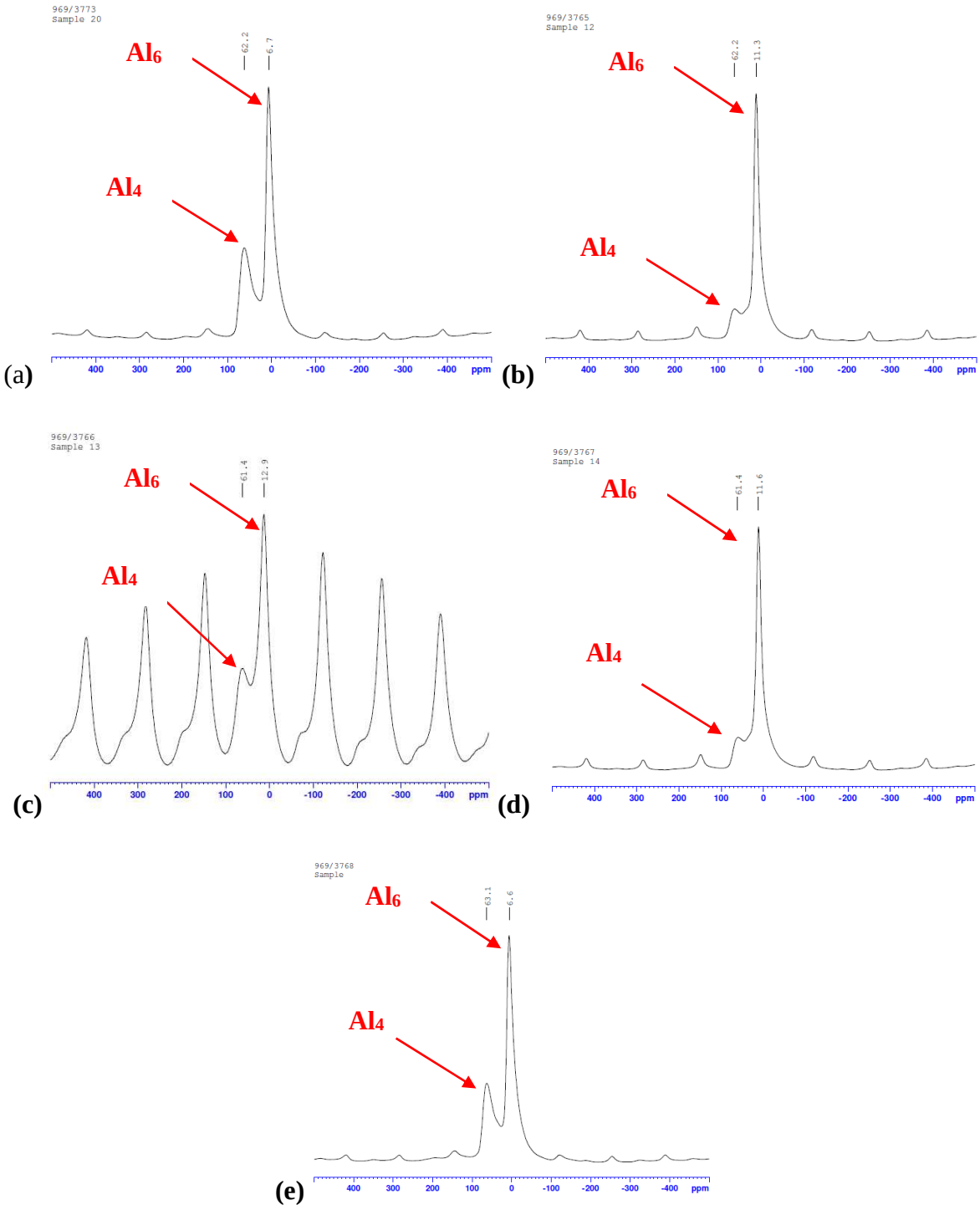

Figure 5.16: NMR results for material study showing sample (a) A-R and samples milled in (b) Zirconia, (c) Stainless Steel, (d) Alumina and (e) Agate

It can be observed that both the Agate and A-R samples look similar and have aluminium cations in both octahedral and tetrahedral sites although a small reduction in tetrahedral

aluminium cations is observed in Agate samples. The Stainless Steel results are not highly reliable due to the interference of iron but do however show a similar result. A marked reduction in the Al_4 is observed in the samples milled in Alumina and Zirconia. This result is expected as these samples have the highest amount of α-Al_2O_3 as observed by XRD Rietveld refinement. Penta-coordinated aluminium cations are still not observed in these results. Zirconia is therefore observed as the material that achieves the smallest particle size and is the most abrasion resistant of the four materials. Further study into the mechanism of phase transformation is carried out using Zirconia by a variation of milling media size.

5.5 Milling Media Size Study in the Planetary Ball Mill

Zirconia milling material has proven to initiate phase transformation from γ-Al_2O_3 to α-Al_2O_3. Further investigation into the effect of varying milling media size has been carried out to get an understanding of the energetics of the milling process. Different size media are expected to dissipate different energies per impact during milling. If the mechanical energy supplied during milling is responsible for the phase transformation, it is essential to understand whether it is the bulk energy from the milling media or the energy supplied in each and every impact that occurs in a given milling duration. A larger size milling ball is expected to dissipate a larger amount of energy than a smaller milling ball. Here, the milling media sizes used are 20 mm, 10 mm, 5 mm and 1.5 to 2.5 mm. The sample mass, milling duration and BPR are kept constant in order to analyse the effect of media size on size reduction and phase transformation. Table 5.6 shows the variables for the experiments carried out.

Table 5.6: Variables for milling media size study in the planetary ball mill

Dependant variables	Controlled variables		Independent variable	
% of α-Al_2O_3 D_{90} particle size	Time/ hr	2	Ball size (mm)	1.5-2.5
	Material	ZrO_2		5
	Medium	Dry		10
	BPR	10:1		20

5.5.1 Particle Size and Shape Analysis of Milling Media Size Study

Analysis of size reduction in this study is of importance as it can highlight the most suitable milling media size for milling γ-Al_2O_3 samples. Figure 5.17 shows the particle size distribution derived by laser diffraction for the A-R and milled samples. The overall difference in size reduction achieved by the different milling media is not very significant.

However, a trend can be observed which shows an increase in size reduction achieved with a decrease in milling media size. This suggests that conditions in the mill with the smallest milling media are more favourable for breakage of γ-Al_2O_3 particles. It can also be observed that the larger milling media i.e. the 10 mm and 20 mm results in re-agglomeration of particles as particles larger than the A-R sample are observed. Re-agglomeration also suggests larger amounts of energy dissipated in every single impact which result in cold welding of particles.

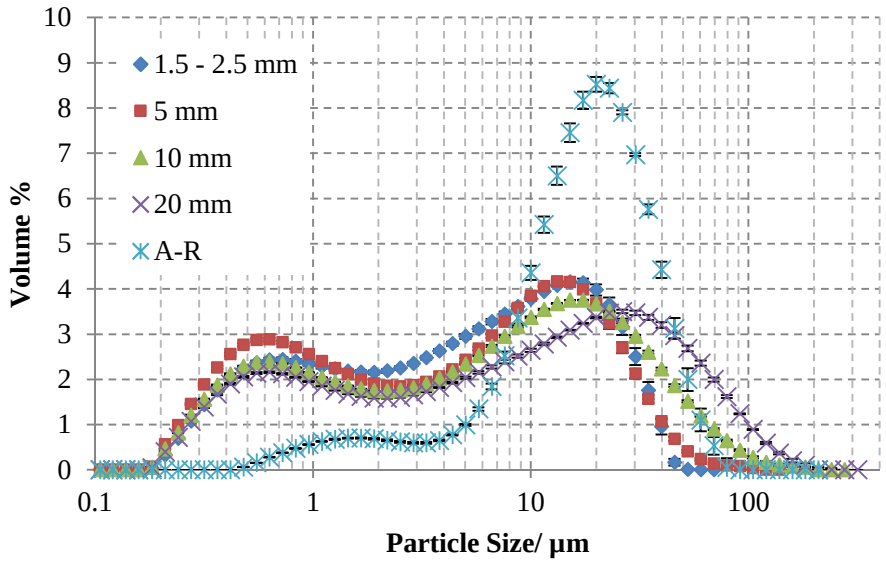

Figure 5.17: Particle size distribution for γ-Al_2O_3 samples milled in Zirconia with different milling media sizes

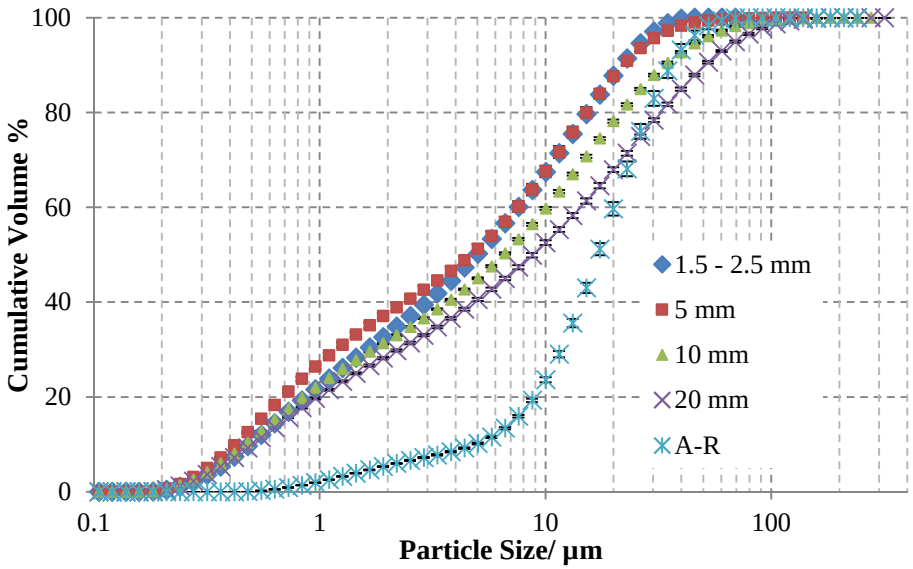

Figure 5.18: Cumulative particle size distribution for γ-Al_2O_3 samples milled in Zirconia with different milling media sizes

The cumulative plots in Figure 5.18 also show that the finest particles were achieved with the 5 mm milling media. Further particle size and shape analysis has also been carried out using SEM. Figure 5.19 shows the micrographs for the A-R sample and the samples milled with different milling media sizes. It can be observed that the particles attain rougher looking surfaces and irregular shapes due to milling.

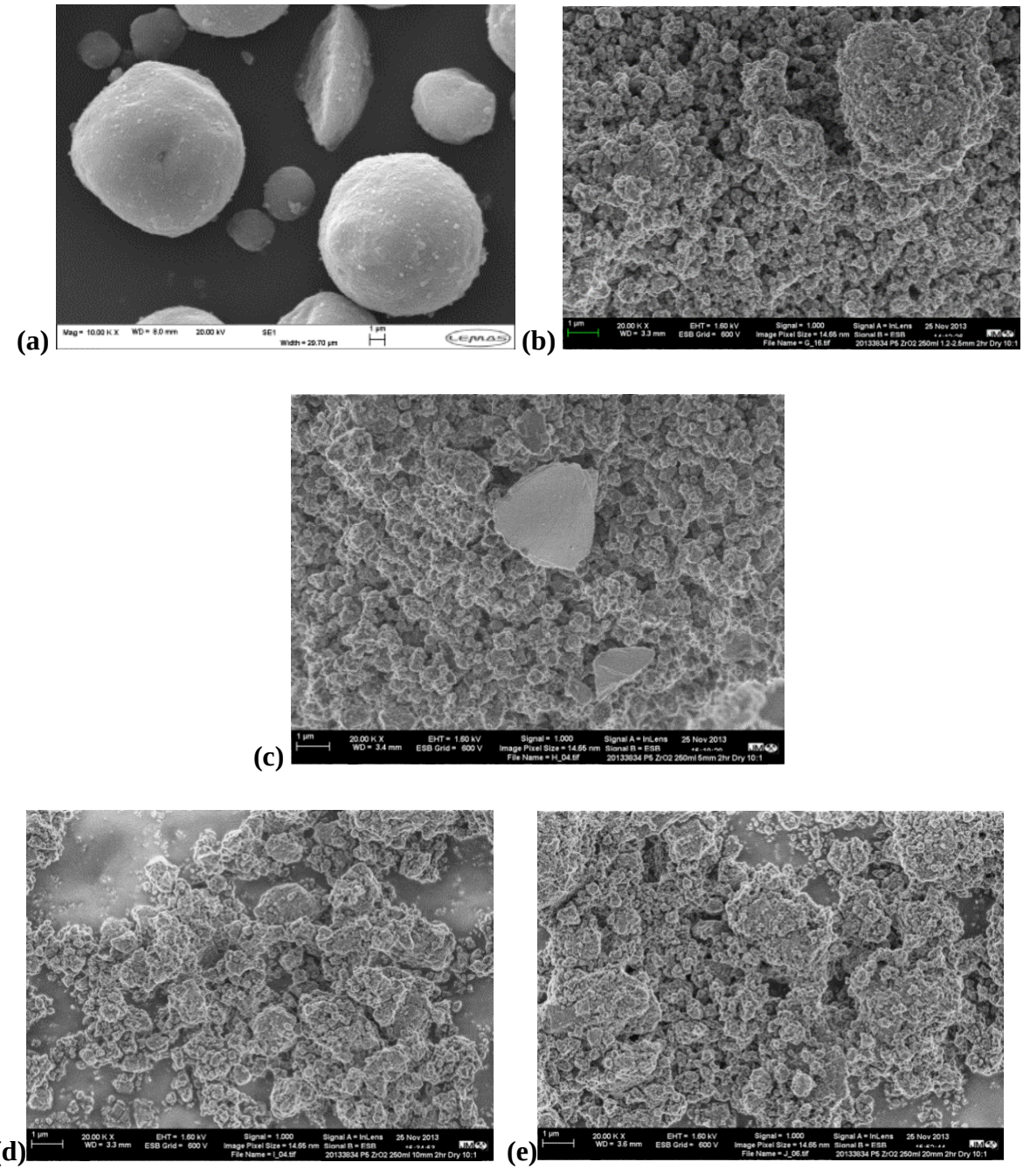

Figure 5.19: SEM imaging of γ-Al_2O_3 particles showing (a) A-R sample, and samples milled with (b) 1.5 to 2.5 mm, (c) 5 mm (d) 10 mm and (e) 20 mm milling media

It can also be observed from the SEM micrographs that larger particles exist in the 10 mm and 20 mm media samples. A number based particle size distribution analysis has also been carried out using DigitalMicrograph software. This is not representative of a full sample but can shed light into the range of particle sizes observed using electron microscopy. As shown in Figure 5.20, the sample milled with the 5 mm milling media has the largest amount of small particles below 10 μm. The SEM and laser diffraction results are in agreement and show a similar relationship. In order of size reduction efficiency for γ-Al_2O_3 powders, the observed trend is 5 mm → 1.5 -2.5 mm → 10 mm → 20 mm.

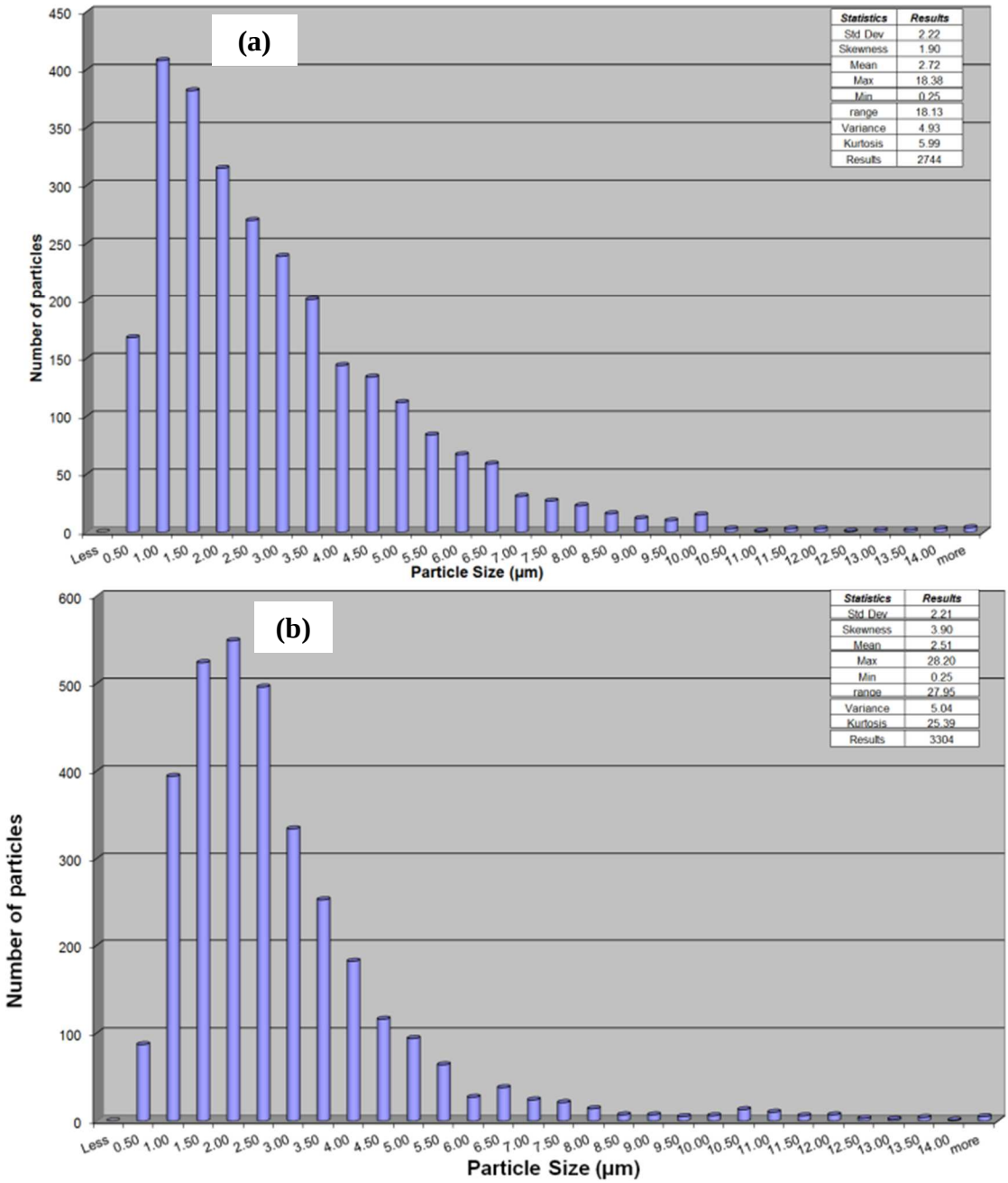

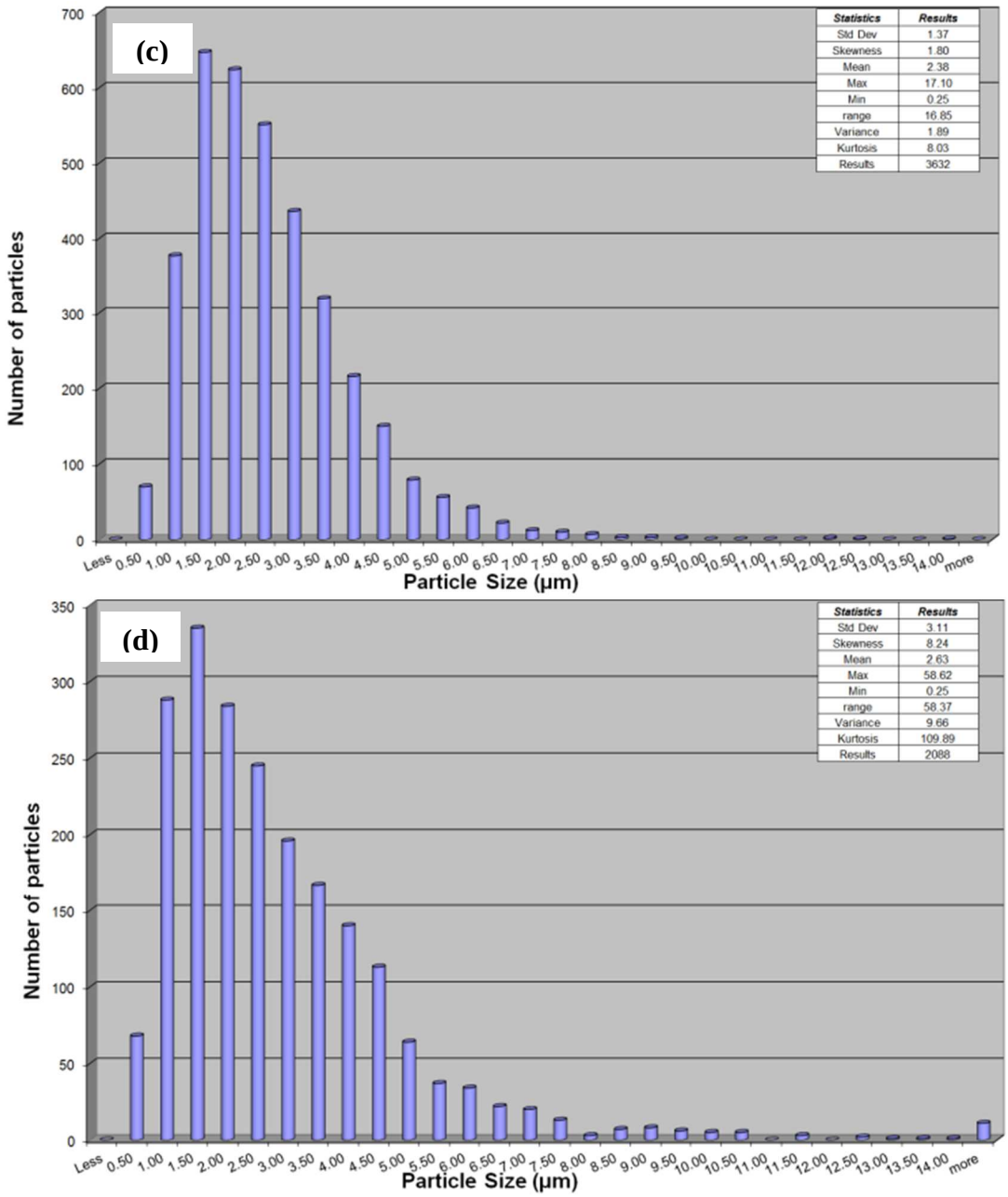

Figure 5.20: Number based particle size distribution of γ-Al_2O_3 samples milled with (a) 1.5-2.5 mm, (b) 5 mm, (c) 10 mm and (d) 20 mm diameter milling media

5.5.2 Phase Identification by XRD Analysis

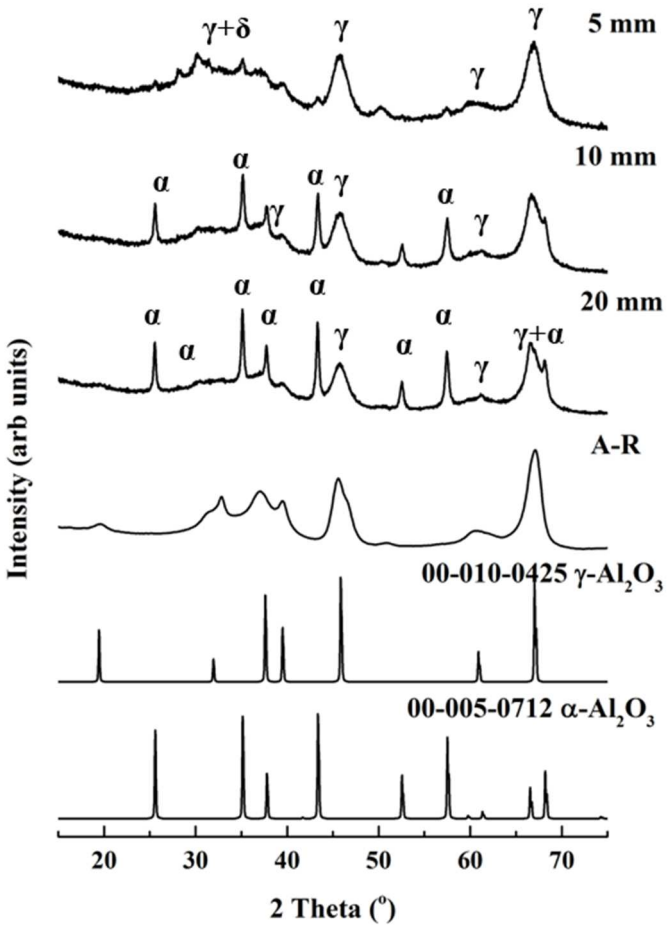

Figure 5.21: XRD patterns of Al_2O_3 showing α-Al_2O_3 ICDD reference pattern 00-005-0712, γ-Al_2O_3 ICDD reference pattern 00-010-0425, as-received γ-Al_2O_3 and γ-Al_2O_3 after milling with 5 mm, 10 mm and 20 mm milling media

The crystal morphology of milled powders were analysed by XRD to observe the effect of milling with different milling media sizes. It can be seen in Figure 5.21 that as the milling media size increases, the phase transformation is enhanced. The 5 mm sample shows initial stages of phase transformation. Small peaks matching to α-Al_2O_3 can be seen. When the 10 mm milling media size is used, stronger peaks of α-Al_2O_3 can be seen and these peaks intensify with the 20 mm milling media. Rietveld refinement has also been used to calculate the amount of each phase in the milled powders. The phase percentages are shown in Table 5.7 and it can be observed that the percentage of α-Al_2O_3 increases as the milling media size used increases. It is also interesting to note that no phase transformation is observed in the 1.5 to 2.5 mm milling media. However, 19.5% of the sample is composed of θ-Al_2O_3. This suggests that a mechanism of phase transformation similar to that of calcination of γ-Al_2O_3 is occurring during this experiment.

Table 5.7: Percentage of γ-Al_2O_3 and α-Al_2O_3 phases in media size study samples milled with 1.5-2.5 mm, 5 mm, 10 mm and 20 mm based on area under matched peaks by the use of Xpert Highscore software

Sample	Phase Composition		
	γ-Al_2O_3 (%)	α-Al_2O_3 (%)	θ-Al_2O_3 (%)
1.5-2.5 mm	80.5	0	19.5
5 mm	80.1	19.9	-
10 mm	75.4	24.6	-
20 mm	34.4	28.6	-

Solid-state NMR was also used to characterise the samples after the media size study and results are shown in Figure 5.22.

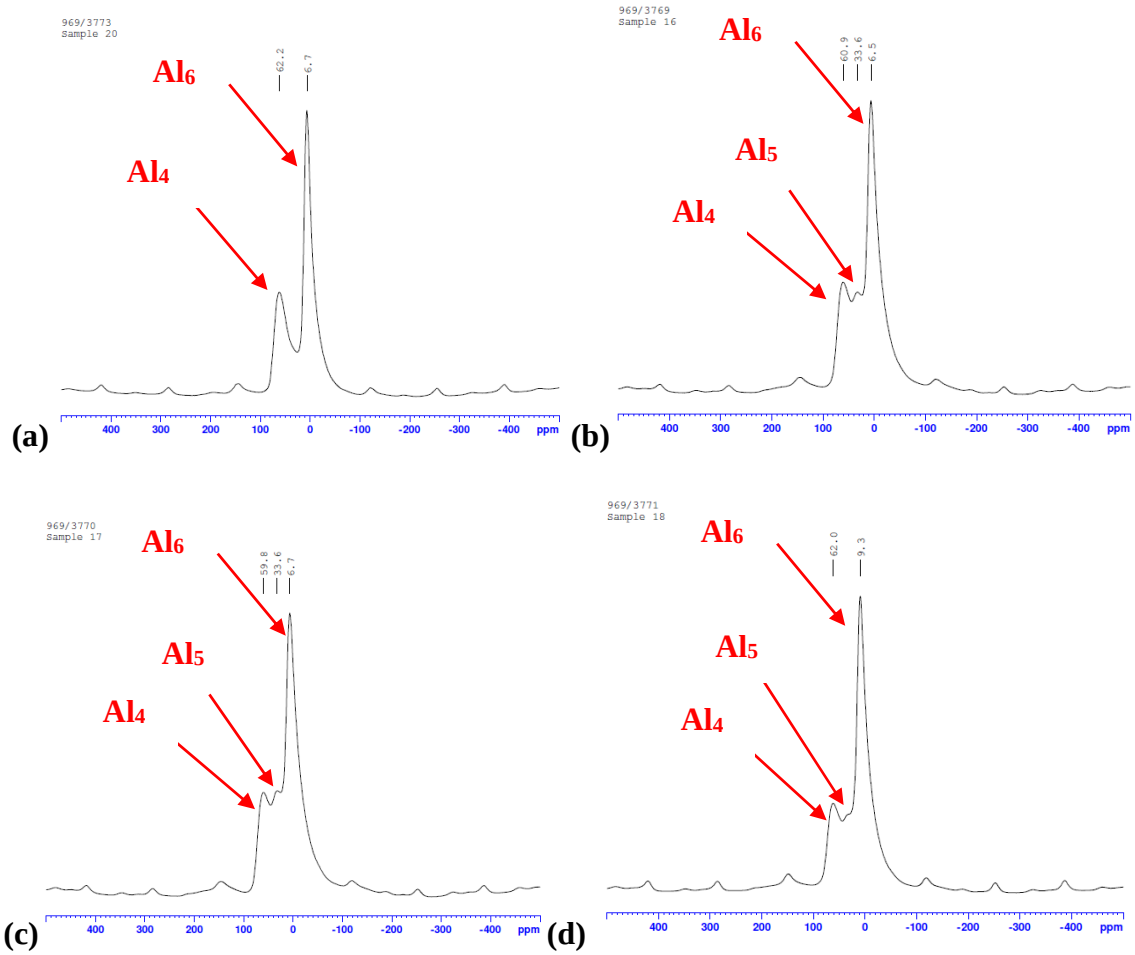

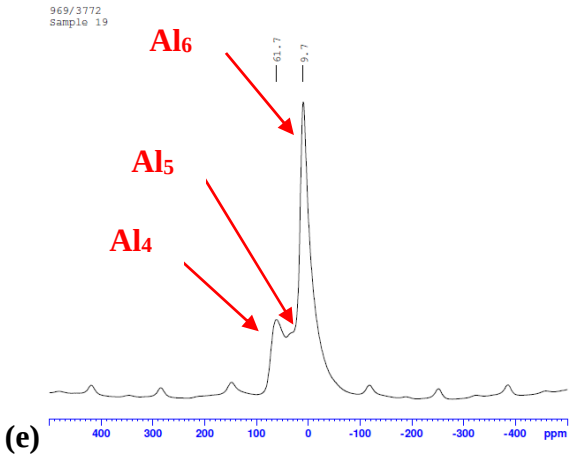

Figure 5.22: NMR results for media size study showing (a) A-R sample and samples milled using (b) 1.5 -2.5 mm, (c) 5 mm, (d) 10 mm and (e) 20 mm milling media

These results are interesting as they show the location of aluminium cations within the structure of the material in the different samples. These samples are of particular interest because not only do they show the presence of Al_4 and Al_6 aluminium cations as previously observed, but also the presence of Al_5 which have been observed by Duvel *et al*. (2011). As the energies supplied by the different milling media is expected to show a difference in the structural effects, it is interesting to note that a greater variation in results has been observed by varying the milling media more than other studies where time and milling materials were varied.

5.6 Milling Aids Study

5.6.1 Addition of water (wet milling)

The effect of adding water during milling has been reviewed in Chapter 2. Wet milling of γ-Al_2O_3 in the planetary ball mill is investigated. An initial study into the effect of adding water on size reduction is investigated. This is followed by a variation of the milling material with constant BPR and Solids-to-liquids ratio (SLR) to assess both the effect of water as well as the effect of wet milling in materials with different properties by XRD analysis. Figure 5.23 shows the cumulative PSD for samples milled in the Fritch P5 planetary ball mill. A d_{90} of ~5 microns is achieved. This shows that wet milling in the planetary ball mill can achieve the desired particle size reduction for γ-Al_2O_3. The issue of whether this is accompanied by insignificant microstructural changes is investigated further by XRD analysis. XRD diffractograms showing samples milled in Stainless Steel and Zirconia are shown in Figure 5.24. It can be observed that aluminium hydroxide is formed during wet milling with water. This is shown by the peaks on the diffractograms matching 00-001-0287 for bayerite.

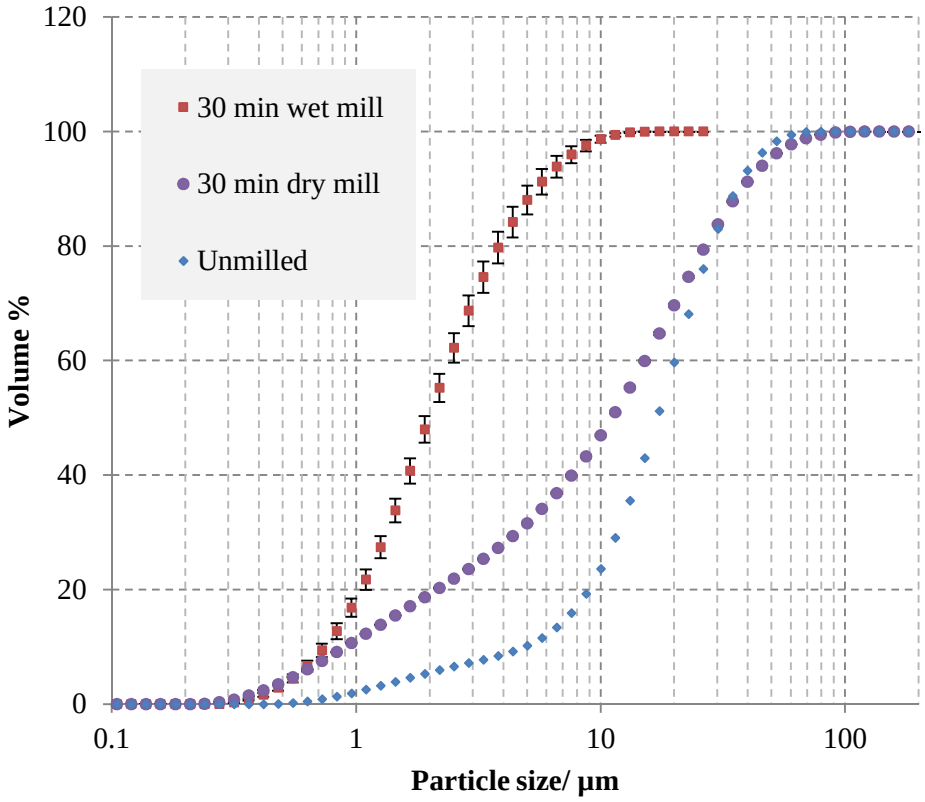

Figure 5.23: Laser diffraction results showing (a) PSD and (b) cumulative PSD of wet milled samples in the Fritsch P5 planetary ball mill

It is interesting to note that bayerite is the favoured hydroxide despite the material originating from boehmite. Initial stages of the formation of α-Al_2O_3 are also observed in the material milled in Zirconia. The comparison between dry and wet milling for the same conditions is shown in Figure 5.25. As these samples were milled for 60 min, the presence of water appears to reduce the rate at which α-Al_2O_3 is formed. This may be due to the presence of liquid bridges provided by water. The intensities of the α-Al_2O_3 peaks are higher in the dry PBM samples.

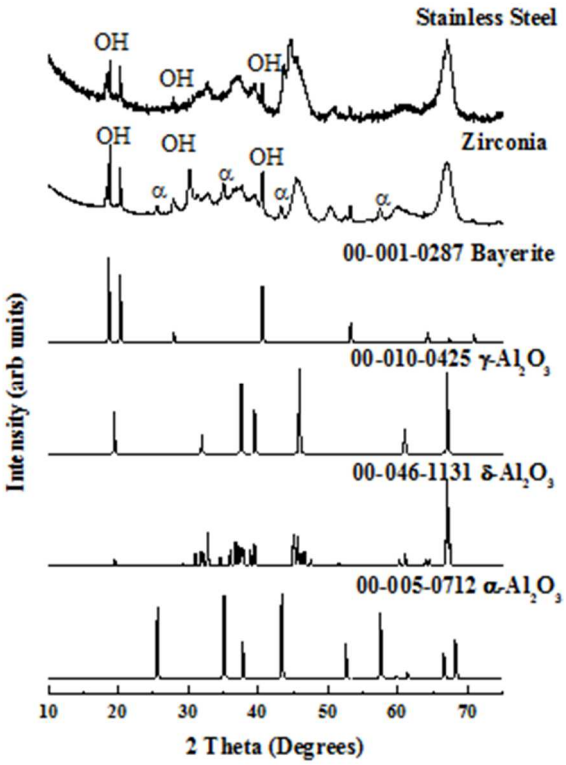

Figure 5.24: Effect of wet milling with Zirconia and Stainless Steel milling tools in the Fritsch P5 planetary ball mill for 60 min

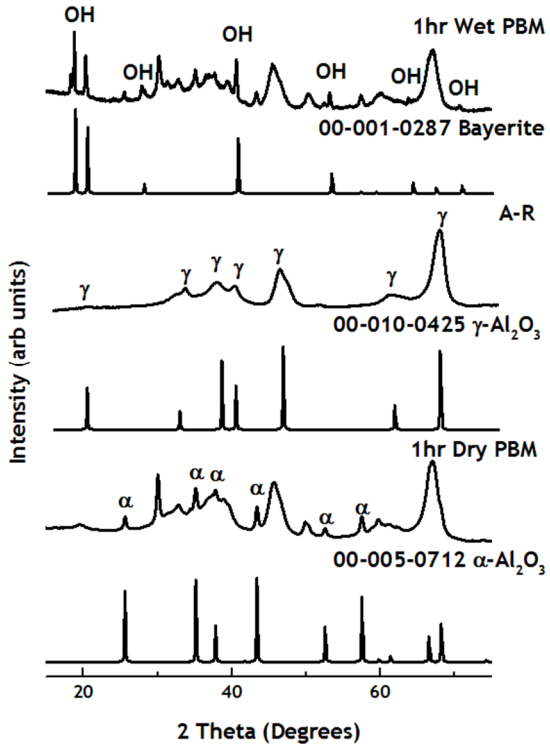

Figure 5.25: Comparison between dry and wet milling in the Fritsch P5 mill with Zirconia milling tools

5.6.2 Addition of lubricants (Zinc stearate)

Another additive that can possibly have an effect on the energy transfer between milling tools and milling material is a lubricant. Zinc stearate (ZnSt) has been investigated by adding 1% to samples and milling to observe any effects. The study was conducted in Zirconia milling tools with the Retsch PM100 planetary ball mill at 400 rpm for 60 min. The XRD diffractograms of the results are shown in Figure 5.26. The addition of dry lubricant has minimal effect on inhibiting phase change. The Zirconia contamination peak has a lower intensity in the ZnSt seeded sample suggesting that the lubricant reduces abrasion of the milling tools. The peaks of α-Al_2O_3 also show slightly lower intensities. All results highlight that amount of energy is more predominant over the mode of energy e.g. shear. Surface interacting PCAs may be more effective in inhibiting phase transformation by binding to nucleation sites such as lanthanum oxide (La_2O_3) as reported by Duvel *et al*. (2011).

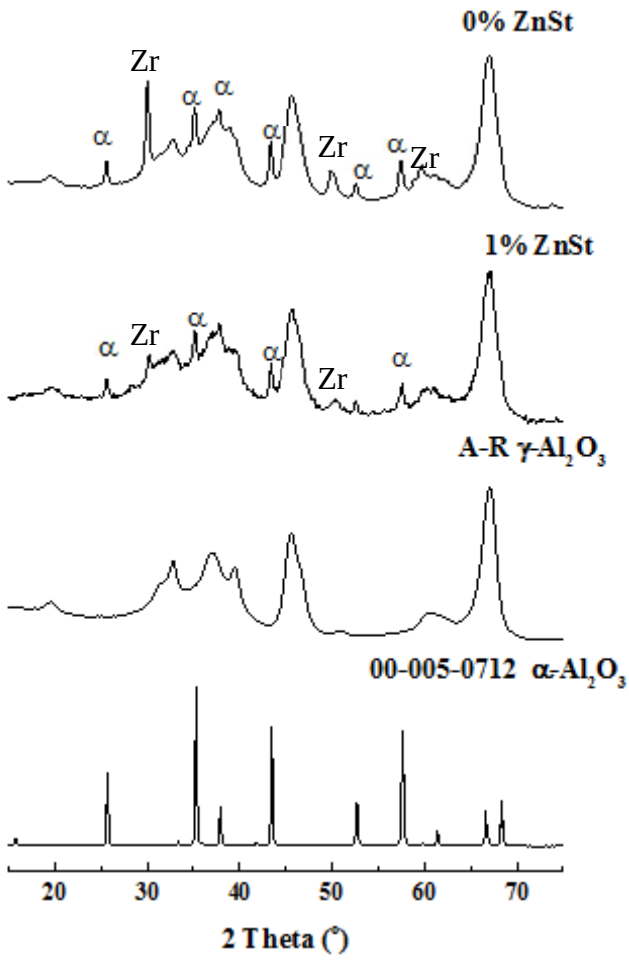

Figure 5.26: Effect of adding zinc stearate during dry milling in the Retsch PM100 planetary ball mill

5.7 Discussion

The BPR study has revealed that a higher BPR i.e. lower powder loading results in better size reduction. This can be assumed to be due to increased contacts between the powder and the milling media and milling vessel walls. The 10:1 BPR is more favourable for use with the P5 planetary mill than the 5:1 ratio. It is also noted that contamination is higher with a higher BPR. This is caused by higher energy impacts of the milling tools due to lower powder loading and a higher frequency of these impacts as less powder allows more interaction of powder and milling tools. Characterisation of the morphologies of the BPR samples milled in Agate is carried using XRD and no phase transformation to α-Al_2O_3 is observed.

This can related to the mechanical properties of the milling material, Agate. Because Agate has a low hardness value, it can be assumed that it does not provide enough energy to overcome the energy barrier for phase transformation. A material with a higher density or hardness value is therefore required for the mechanism of phase transformation to be understood further. The energy intensity in the Agate mill allows for transformation to δ-Al_2O_3 only.

The material study that is carried out after the BPR involves the use of Agate, Stainless Steel, Alumina and Zirconia materials. These four materials are tested together to derive the best conditions for size reduction as well as to understand better the conditions that initiate phase transformation. The Agate material used in the BPR study again shows the poorest size reduction efficiency as it has the largest milled particles of the four samples. Zirconia milling material shows the best size reduction efficiency whilst Alumina and Stainless Steel show size reduction not largely different to Zirconia but less efficient. No phase transformation to α-Al_2O_3 is observed with Agate in this study. Only peaks of to δ-Al_2O_3 are observed. Phase transformation to α-Al_2O_3 is observed in Zirconia and Alumina and initial stages of phase transformation are observed in Stainless Steel.

These results show that mechanical properties of the materials used for milling have an effect on the phase transformation that is achieved. Zirconia, Alumina and Stainless Steel have a higher density value than Agate and initiate faster phase transformation to the final transitional phase. It can, however be observed that density is not the only factor that affects phase transformation. The hardness and Young's modulus of a material also play a role in the phase transformation. Although Stainless Steel has a higher density than Zirconia and Alumina, it affects the crystal structure with less intensity than Zirconia and Alumina,

because it has a lower hardness value. The hardness values of the materials have been tested and are shown in Figure 5.27 and Table 5.8. The comparison of the hardness, Young's modulus and density is an interesting concept in these results and these values are given in Table 5.1.

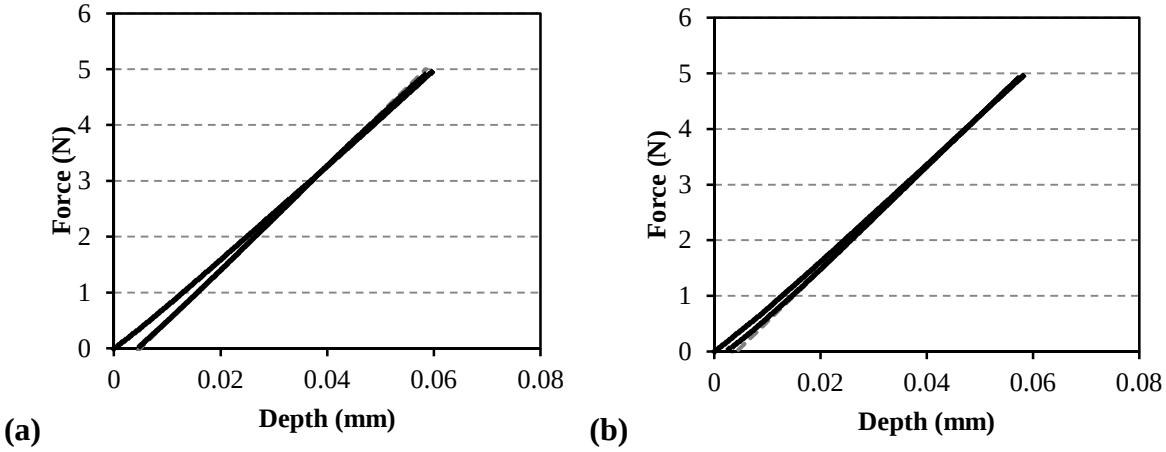

Figure 5.27: Load-displacement curves for (a) Stainless Steel milling media and (b) Zirconia milling media as measured using the Instron Test Bench

The comparison of hardness, Young's modulus and density is an interesting concept in these results. These values are given in Table 5.1.

Table 5.8: Vicker's hardness values for the Stainless Steel and Zirconia milling media used in planetary ball milling as derived from the manufacturer and the load-displacement curves in Figure 5.27

Vicker's Hardness Values (H_v)		
Milling Material	**Exp. H_v (GPa)**	**Man. H_v (GPa)**
Stainless Steel	8.45	5.30-6.47
Zirconia	11.74	11.77
	Man. H_v (GPa)	
Agate	7.85	
Alumina	15.00	

Although a higher density material such as Stainless Steel is expected to result in higher energy milling, the results show that a higher Young's modulus with a lower coefficient of restitution such as that of Alumina and Zirconia, especially coupled with a high hardness value results in higher energy dissipation into the crystal structure of the material being milled. On comparing Zirconia and Alumina, Alumina has a higher hardness value than Zirconia but a faster rate of phase transformation is observed in the Zirconia vessel. This may be due to a higher density of Zirconia coupled with a high hardness and Youngs modulus.

There is, however, a chance that the material of the milling vessel itself, corundum Alumina may be playing a role in the phase transformation from γ-Al_2O_3 to α-Al_2O_3. This is investigated further in Chapter 6 where γ-Al_2O_3 powders are seeded with small amounts of α-Al_2O_3 before milling and characterisation is carried out. High levels of contamination in materials with lower hardness values is also observed in the material study suggesting that a lot of shearing occurs during planetary ball milling and the walls of the mill and milling media are abraded. It is also interesting to note that δ-Al_2O_3 was observed in the Agate sample. This shows that the mechanism of phase transformation occurring in this sample is similar to that observed during dehydration of γ-Al_2O_3. The lower intensity of milling supplied by Agate milling tools appears to result in a reduction of Al_4 cations, which in turn results in the formation of the next transition Alumina after γ-Al_2O_3, δ-Al_2O_3.

As Zirconia shows to initiate phase transformation and has no enhancement effects on the material as observed with Alumina, it is used for a milling media size study. This is done to assess the effect of varying the impact energy per impact from different sized milling balls. From using 1.5-2.5 mm, 5 mm, 10 mm and 20 mm milling media, it is observed that the 5 mm media size has the smallest particles in terms of size reduction. When phase transformation is investigated in the media size study samples by characterisation using XRD, no phase transformation to α-Al_2O_3 is observed in the 1.5-2.5 mm samples. Only small peaks of θ-Al_2O_3 are observed. Initial stages of phase transformation are observed in the 5 mm samples with the presence of δ-Al_2O_3 and the phase transformation to the final phase is observed to become more evident as the milling media size is increased. The peaks of α-Al_2O_3 have higher intensity values in the 20 mm milling media than the 10 mm sample. It can be deduced that a variation of the milling media size and hence the energy per impact by every milling ball during milling can result in the sample reaching different stages of phase transformation.

Table 5.9 can be used to summarise the variables observed to affect phase transformation and shows how each property has an effect on the powders milled. The variables listed also show that the phase transformation is related to the mechanical energy supplied during milling. Although the effect of temperature can be raised as a contributing factor, it is not considered in this work because a higher temperature is observed in the Stainless Steel vessel than the Zirconia vessel of ~80^oC but phase transformation is observed with Zirconia. It is however not disregarded as temperatures at every collision were not measured. It is however not focussed on as the main initiator of transformation but rather a secondary effect or product of

mechanical energy at every collision. The effect of milling aids has also been analysed. Water has been observed to reduce the intensity of milling to a certain degree. From XRD analysis, the sample also shows peaks of δ-Al_2O_3 which suggests that the energetics of the milling process are closely related to those of Agate in the material study. The addition of lubricant such as zinc stearate has shown to have little effect on the phase transformation rate. The deduction made from this is that the milling aids required to reduce phase transformation have to be materials that can interact with the surface of γ-Al_2O_3 and hence bind onto nucleation sites, preventing propagation of the phase transformation. Water in the PBM results in desirable size reduction. The only weakness is the formation of bayerite which can be avoided by lowering the pH during milling.

Table 5.9: Variables that affect phase transformation

Variable	**BPR**	**Material**	**Milling Media Size**	**Milling Aids**
Conditions	Higher BPR	Higher hardness	Larger media diameter	**Water**
Outcome	Increased contacts of powder with milling media and milling vessel	Increased shear effect resulting in higher energy promoting phase transformation	Increased energy dissipated per contact between powder and milling media/ milling vessel	Liquid bridge reduces rate
				Zinc Stearate
				No effect due to lack of surface interaction

5.8 Conclusion

The results of the planetary ball mill study highlight the variables that affect size reduction and phase transformation of γ-Al_2O_3 to α-Al_2O_3. It can be concluded that time (as shown in Chapter 5), BPR, milling material and milling media size all have an effect on the size reduction efficiency and the amount of γ-Al_2O_3 that transforms to α-Al_2O_3 during milling. A higher BPR, longer time, harder material and larger milling media have been shown to promote phase transformation. Phase transformation of γ-Al_2O_3 can therefore be related to the level of mechanical energy supplied by the selected milling conditions during any milling activity. Although the stress mode has been highlighted as an important factor in Chapter 4, the extensive work in this chapter has shown that the amount of energy dominates over the stress mode applied. The successful transfer of this high energy from the milling tools is equally important. A material with properties that can allow dissipation of high energy into

gamma-Alumina particles can initiate and propagate phase transformation. The planetary ball mill study has highlighted the effect of milling in Alumina on the enhancement of the phase transformation. This is further investigated by seeding experiments in Chapter 6 to gain an understanding of how γ-Al_2O_3 interacts α-Al_2O_3 during milling. It is a natural step to assess the range of impact energies that are supplied during the experimented milling tests. DEM has been chosen to assess the impact energies and the analysis is shown in Chapter 7.

Chapter 6

Seeding Experiments and Compression Testing

The effect of milling vessel and media material observed in the Alumina vessel during planetary ball milling is investigated by adding alpha-Alumina seeds to gamma-Alumina during milling. Compression testing is also carried out to investigate lattice strain effects and initial stages of phase transformation observed in Chapter 5 and 6 by mimicking impact energy.

6 Seeding Experiments and Compression Testing

6.1 Introduction

When γ-Al_2O_3 powders are milled in a corundum Alumina vessel using the planetary ball milling, the characterised product shows signs of enhanced phase transformation. This assumption is brought about by the observations of a larger percentage of α-Al_2O_3 in the samples after milling. The large amount of α-Al_2O_3 can be assumed to originate from abrasion of the milling vessel and media but this cannot be made conclusive unless a study is carried out to rule out the effect of adding α-Al_2O_3 to γ-Al_2O_3 powders during milling. Adding a small amount of α-Al_2O_3 as seed to γ-Al_2O_3 powder in a control milling vessel such as one made of Stainless Steel or Zirconia followed by milling, can shed light into any effects α-Al_2O_3 may have on assisting the phase transformation.

Bodaghi *et al.* (2008) investigated this effect and found that adding small amounts of α-Al_2O_3 can aid in transforming γ-Al_2O_3 to α-Al_2O_3. This study was, however, carried out without much focus on the mechanism of phase transformation including the role the α-Al_2O_3 seed acts as well as the morphology of the product formed. In order to understand how mechanical energy aids phase transformation, it is necessary to carrying out a seeding study on γ-Al_2O_3 powders.

The results in *Chapter 4* have shown that a high impact energy mill such as the single ball mill can affect the morphology of γ-Al_2O_3 powders. Growth of crystals has been observed as well as the emergence of a peak that can be related to the initial stages of phase transformation from γ-Al_2O_3 to α-Al_2O_3. Compression testing can be used as a way of mimicking impact energy and characterisation of the compressed product can show the effect of impact energy on γ-Al_2O_3. If similar behaviour between compression testing and single ball milling is observed, this can be a step further into understanding how different stress modes affect the structure of γ-Al_2O_3 powders.

In this chapter, the experimental devices and procedures for seeding of γ-Al_2O_3 powders with α-Al_2O_3 and compression testing of γ-Al_2O_3 powders are presented. The results from the seeding and compression testing work are also given. A detailed discussion of the results follows. This includes deriving a relationship between previous milling work results and compression testing and seeding results. A conclusion is given at the end of the chapter.

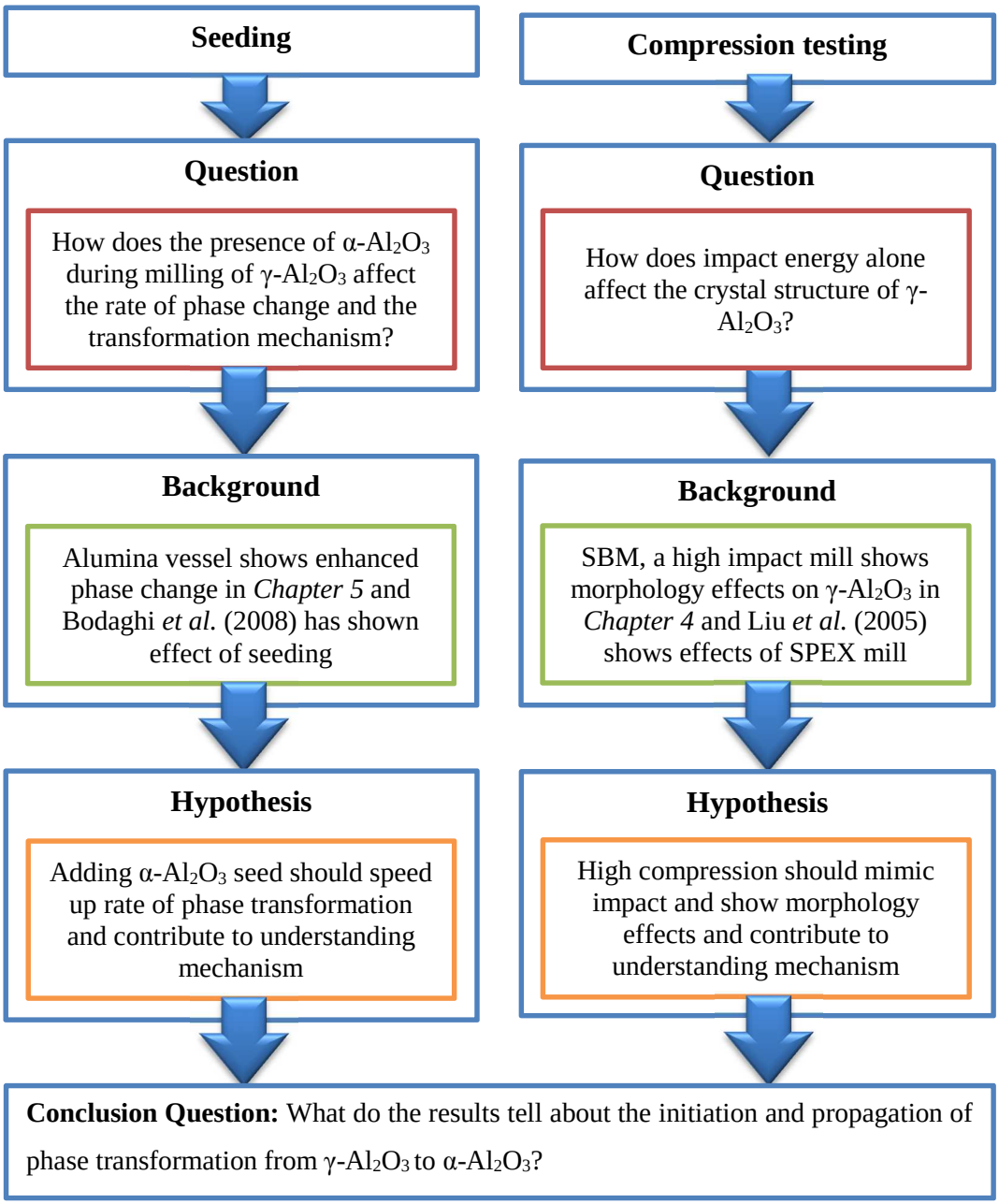

Figure 6.1: Hypothesis formulation for *Chapter 6*

6.2 Seeding Experiments

6.2.1 Experimental Devices and Procedures

Seeding experiments were carried out using mixtures of α-Al_2O_3 and γ-Al_2O_3 powders. The Retsch PM100 planetary ball mill shown in Figure 6.2(a) is used for seeding experiments. The mill is operated at a speed of 400 rpm and experiments are run for 15, 30, 45 and 60 minutes. The BPR used is 20:1 and the milling vessels and milling media used are shown with a red asterisk in Figure 6.2(b). A 10 g sample of powder is prepared by mixing 8 g γ-Al_2O_3 with 2 g α-Al_2O_3. The sample mixture is added into a 125 ml Stainless Steel vessel containing fifteen 15 mm diameter Stainless Steel milling balls and milling is carried out for the set duration. After milling, the product is characterised for morphology effects by XRD and TEM analysis. A similar experiment was carried out in a Zirconia milling vessel with 20 mm diameter Zirconia milling balls.

(a) **(b)**

Figure 6.2: Photographs showing (a) Retsch PM100 planetary ball mill and (b) various milling vessels and milling media with the Stainless Steel and Zirconia milling vessels and milling media used in experiments shown by a red asterisk

The Retsch MM200 single ball mill demonstrated in detail in *Chapter 4* and shown in Figure 6.3(a) is also used for seeding experiments. A similar BPR to that used with the planetary ball mill of 20:1 is also employed. A single 10 mm Stainless Steel ball is loaded into a 11 ml Stainless Steel milling vessel shown in Figure 6.3(b). A mixture with 20 % α-Al_2O_3 seed is added to the milling vessel and milling is commenced for durations of 15, 30, 45 and 60 minutes. The milled product is characterised for morphology using XRD and TEM analysis.

(a)

(b)

Figure 6.3: Photographs of (a) Retsch MM200 single ball mill and (b) Stainless Steel 12 ml milling vessel with a 10 mm Stainless Steel milling ball

All seeding experiments carried out with the single ball mill and the planetary ball mill are summarised in Table 6.1. The α-Al_2O_3 powder used was composed of 10 micron particles.

Table 6.1: Seeding experiments carried out with Retsch MM200 single ball mill and Retsch PM100 planetary ball mill

Experiment No.	Mill Type	% α-Al_2O_3 seed	Mill Material	Duration/ min
1	Planetary Ball Mill	20	Stainless Steel	15, 30, 45, 60
2	Single Ball Mill	10	Stainless Steel	15, 30, 45, 60
3	Single Ball Mill	20	Stainless Steel	15, 30, 45, 60

6.2.2 Seeding Experiments Results

6.2.2.1 Characterisation of Planetary Ball Mill Seeding Experiments

When 20% of α-Al_2O_3 is mixed with γ-Al_2O_3 powder and milled in a planetary ball mill, an increase in the amount of α-Al_2O_3 in the sample with increased milling time can be observed. This effect is shown in Figure 6.4. It is clear that the α-Al_2O_3 peaks increase in intensity while the γ-Al_2O_3 peaks diminish. Rietveld refinement can be used to estimate the percentage of each Alumina phase in the sample after milling. The results of the refinement carried out are shown in Table 6.2. It can be seen that the percentage of α-Al_2O_3 increases despite the fact that the milling vessel used is made of Stainless Steel and no extra α-Al_2O_3 is added during milling. Contamination of samples during milling with iron from the milling vessel is also observed. It can be assumed that a mechanism similar to that of phase transformation is occurring during milling where some of the γ-Al_2O_3 particles in the sample are transforming.

The peaks of α-Al_2O_3 appear sharp after 15 minutes suggesting a cold welding effect which suppresses the presence of γ-Al_2O_3 in the sample. Further experimental work is required and has been carried out to confirm this assumption. As observed in Table 6.2, despite the strong peaks of α-Al_2O_3, there is a small increase in α-Al_2O_3 of 10.2% after 60 min of milling.

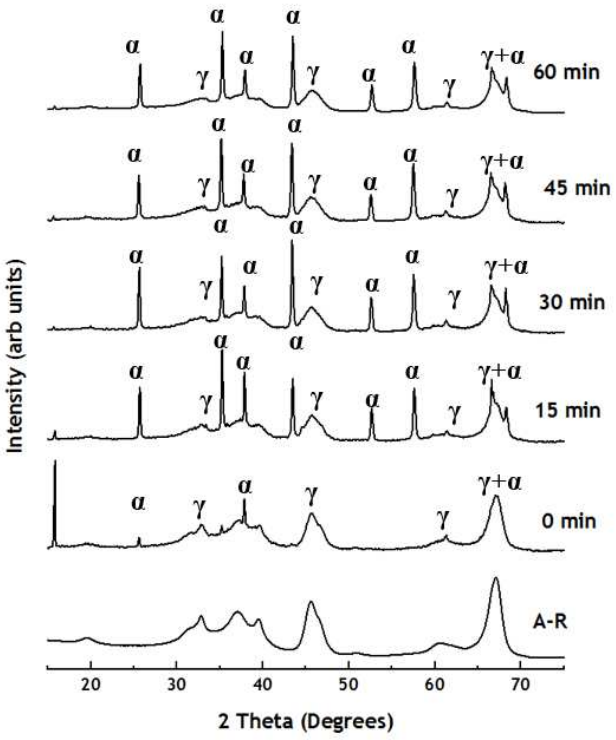

Figure 6.4: XRD diffractograms showing A-R sample and seeded samples from the Retsch PM100 planetary ball mill using 20% of Seed A

Table 6.2: Percentage of γ-Al_2O_3 and α-Al_2O_3 phases in PBM milled samples with 20% α-Al_2O_3 Seed A at 0, 30, 45 and 60 min based on area under matched peaks by the use of Xpert Highscore software

Sample	α-Al_2O_3 (%)	γ-Al_2O_3 (%)
15 min	26.4	73.6
30 min	29.5	70.0*
45 min	29.9	69.6*
60 min	30.2	69.3*

*where total is not 100%, contamination by mill material was observed

6.2.2.2 Characterisation of Single Ball Mill Seeding Results

The planetary ball mill and the single ball mill provide different ranges of energies which are focussed on in *Chapter 7* of this thesis. Both mills cause breakage by a combination of impact and shear. It can be assumed that the level of shear stress provided by the planetary ball mill would be higher than that supplied by the single ball mill due to a difference in mill

sizes and milling media sizes as well as mechanism of the mills. This variation in level of shear stress can be hypothesized as one of the reasons why the degrees of phase transformation from γ-Al_2O_3 to α-Al_2O_3 are different i.e. the planetary ball mill shows a greater extent of phase transformation with a higher percentage of α-Al_2O_3 in the milled sample. In order to understand the mechanism of phase transformation and the role of α-Al_2O_3, the single ball mill has also been used for a seeding study. Figure 6.5 shows the XRD results when 10% of α-Al_2O_3 was added to γ-Al_2O_3 before single ball milling for up to 300 minutes. A similar trend to the planetary ball mill seeding study is observed where an increase in α-Al_2O_3 peak intensity with milling time can be seen. The milling time is, however longer with the single ball mill. These results alone reflect the importance of a knowledge of the actual impact energies as these can reflect the effect of varying energies and stress modes.

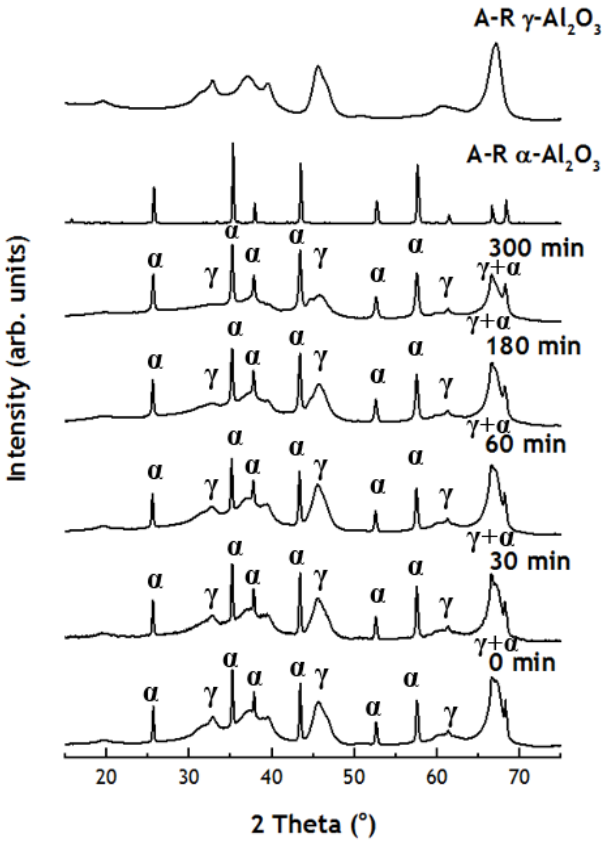

Figure 6.5: XRD diffractograms showing A-R sample for γ-Al_2O_3 and α-Al_2O_3 and seeded samples from the Retsch MM200 single ball mill using 10% of Seed B

The percentages of γ-Al_2O_3 and α-Al_2O_3 in the samples were also estimated using Rietveld refinement and are shown in Table 6.3. The percentage of α-Al_2O_3 in the sample is observed

to increase up to 30.2% after 300 minutes of milling. The SBM sample without seed as reported in *Chapter 4*, only shows initial stages of phase transformation where γ-Al_2O_3 particles begin to coarsen. Adding α-Al_2O_3 seed with the same energetics provided by the SBM results in approximately 20 % of the γ-Al_2O_3 powder transforming.

Table 6.3: Percentage of γ-Al_2O_3 and α-Al_2O_3 phases in SBM milled samples with 10% α-Al_2O_3 seed at 0, 30, 60, 180 and 300 min based on area under matched peaks by the use of Xpert Highscore software

Sample	α-Al_2O_3 (%)	γ-Al_2O_3 (%)
0 min	14.7	85.3
30 min	18.0	82.0
60 min	15.4	84.6
180 min	21.7	78.3
300 min	30.2	69.8

The effect of increasing the percentage of α-Al_2O_3 seed is also investigated by adding 20% of α-Al_2O_3 to γ-Al_2O_3 powder before milling. Figure 6.6 shows the resultant XRD diffractograms and shows a similar trend of increase in intensity of α-Al_2O_3 peaks.

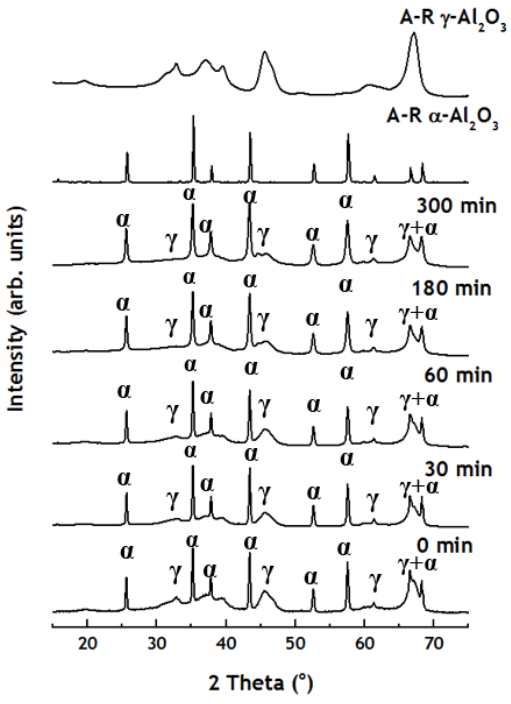

Figure 6.6: XRD diffractograms showing A-R sample for γ-Al_2O_3 and α-Al_2O_3 and seeded samples from the Retsch MM200 single ball mill using 20% of Seed B

When the Rietveld refinement of the XRD plots is carried out, the amount of α-Al_2O_3 is estimated to increase by approximately 20%. This increase is similar to that observed when 10% of α-Al_2O_3 is added and it can therefore be assumed that the mechanisms occurring are similar and increasing seed amount has no significant effect on the rate of transformation.

Table 6.4: Percentage of γ-Al_2O_3 and α-Al_2O_3 phases in SBM milled samples with 20% α-Al_2O_3 seed at 0, 30, 60, 180 and 300 min based on area under matched peaks by the use of Xpert Highscore software

Sample	α-Al_2O_3 (%)	γ-Al_2O_3 (%)
0 min	28.3	71.7
30 min	33.4	66.6
60 min	30.5	69.5
180 min	42.8	57.2
300 min	47.5	52.5

The next natural step in understanding the mechanism occurring during seeding would involve the investigation into a rate of phase transformation in the samples. This is shown in Figure 6.7. The increase in percentage of α-Al_2O_3 is plotted against milling time for both the 10% and 20% SBM seeded samples. An exponential relationship is observed and similar rates of 0.002 are observed. This suggests that the transformation mechanism occurring is similar in both samples.

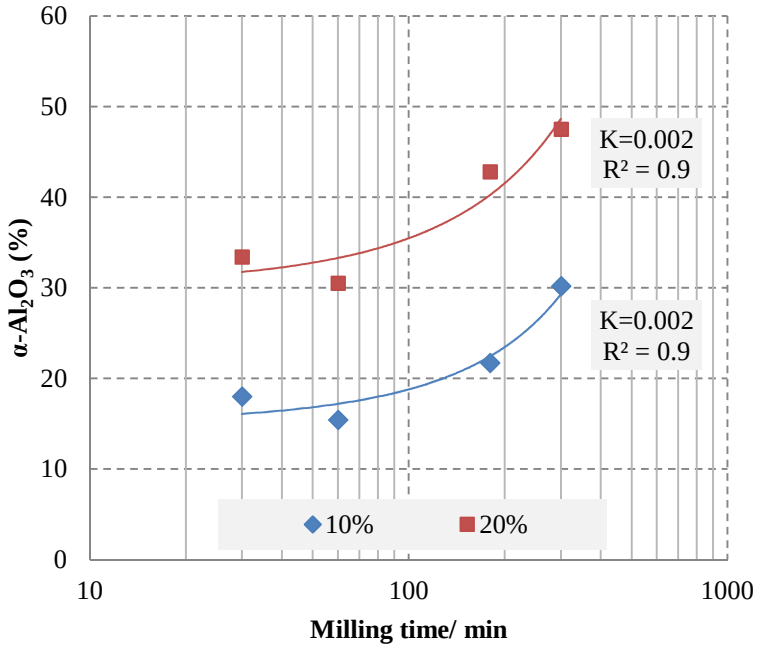

Figure 6.7: Rate of increase of α-Al_2O_3 in single ball mill seeded samples

The highest percentage of α-Al_2O_3 achieved from seeded milling experiments is 47.5% as shown in Table 6.4. If this value is compared to the graphs in McAdle and Messing (1993), it can be seen that the shape of the graphs in Figure 6.8(b) are expected for the stage at which the experiments were stopped.

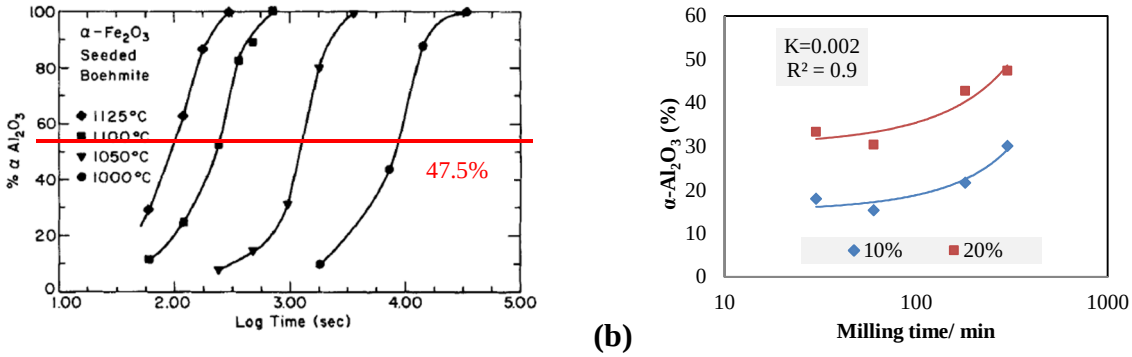

Figure 6.8: Comparison of transformation kinetics observed by McArdle and Messing (1993) with those observed by SBM seeding experiments

6.2.2.3 Characterisation of Single Ball Mill Seeded Experiments for Surface Area

The surface area values for A-R γ-Al_2O_3 and α-Al_2O_3 seed as measured by BET analysis are shown in Table 6.5. It can be observed that the surface area, pore size and pore volume of α-Al_2O_3 is smaller than that of γ-Al_2O_3. Having measured the surface area values for the materials that are physically mixed at 10% and 20% α-Al_2O_3, an analysis of the change in surface area with milling time is shown in Figure 6.9. Milling results in a decrease in surface area in the samples. The rate of reduction is initially fast between 0 min and 60 min and then reduces from 60 min up to 300 min. The surface area reduction follows an exponential relationship.

Table 6.5: Surface area, pore volume and pore size of γ-Al_2O_3 and α-Al_2O_3 A-R samples as characterised using the BET method

Sample	Surface Area (m^2/g)	Pore Volume (cm^3/g)	Pore Size (nm)
γ-Al_2O_3	145.5	0.495	13.602
α-Al_2O_3	0.5	0.001	10.924

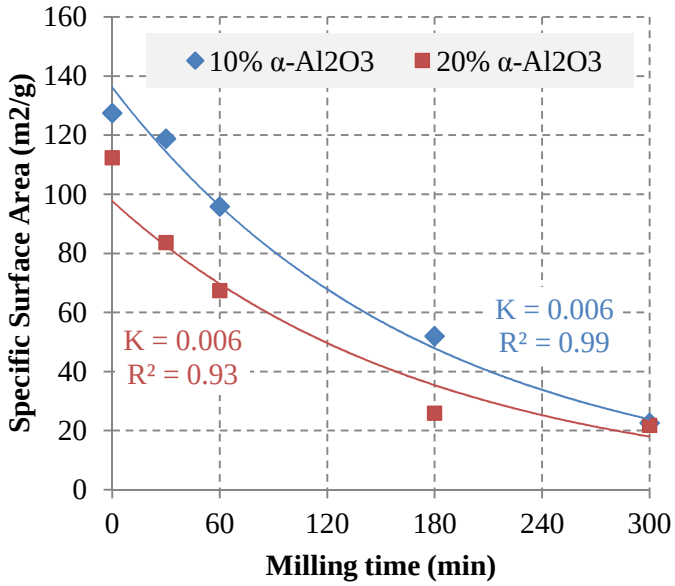

Figure 6.9: Graph showing specific surface area against milling time for single ball mill seeded experiments using Seed B at 10% and 20%

Zielinski *et al*. (1993) also observed a decrease in surface area with increase in milling time as α-Al_2O_3 is formed. If the surface area of the SBM seeded samples is plotted against the change in percentage of α-Al_2O_3, the relationship can be shown in Figure 6.10. An exponential relationship is also observed with similar rates of reduction in surface area.

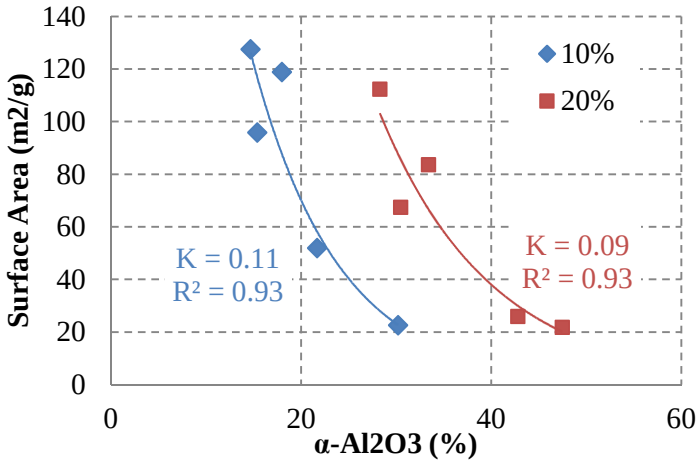

Figure 6.10: Reduction in surface area with the change of percentage α-Al_2O_3

This relationship observed through experiment is similar to that observed by Zielinski *et* al. (1993) when α-Al_2O_3 is achieved by milling γ-Al_2O_3 in a planetary ball mill. McArdle and Messing (1993) also observed a decrease in surface area with the formation of α-Al_2O_3 in seeded boehmite. An analysis is also carried for the effect of milling on pore volume. Figure 6.11 shows that pore volume reduces with an increase in milling time. The reduction follows

an exponential relationship. The pore volume of the 10% sample is initially higher as the sample has more γ-Al_2O_3 present but after 300 min of milling, the pore volumes of the 10% and 20% samples are comparable. This suggests that the initial amount of seed does not affect the phase transformation mechanism. A larger amount of seed present in the sample does not necessarily result in a faster rate of phase transformation.

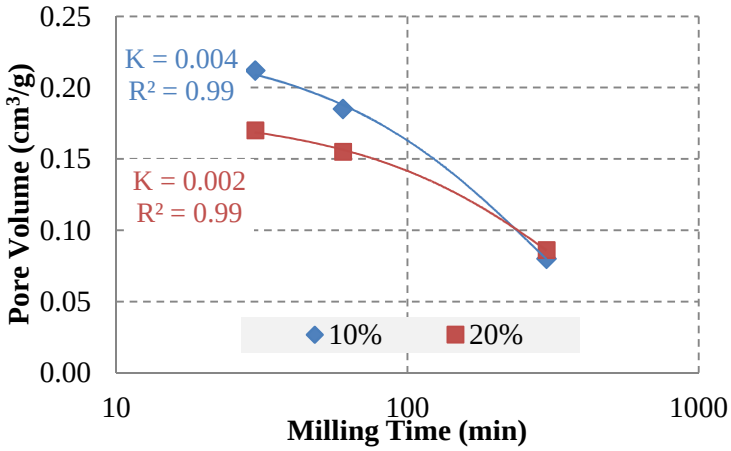

Figure 6.11: Pore Volumes of SBM Seeding Experiments

When the pore size is compared with milling time, it is observed that pore size increases and the rates of increase in pore size are similar for the 10% and 20% SBM seeded samples. The difference is only observed in that the 20% sample has larger pore sizes for all milling times when compared with the 10% sample. Pore size in BET analysis is, however, an average value and it can be expected that the average pore size of a sample with a greater amount (mass-based) of seed will have a greater average pore size as the α-Al_2O_3 sample used exists with larger pores than the γ-Al_2O_3 sample as shown in Figure 6.12.

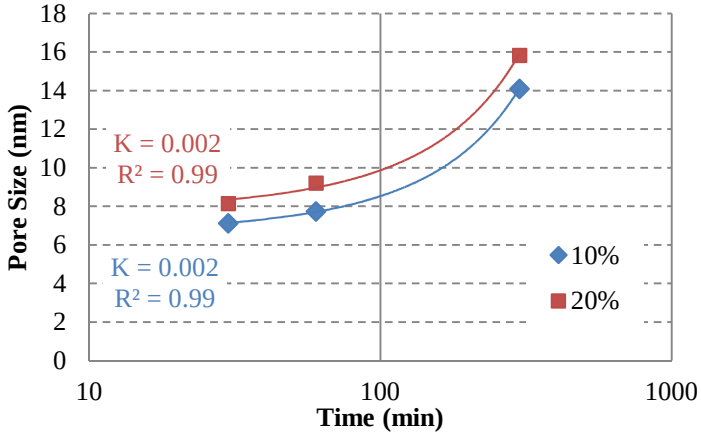

Figure 6.12: Pore Sizes of SBM Seeding Experiments

The change in pore structure with milling can also be analysed using the BET adsorption-desorption isotherms shown in Figure 6.13. When the hysteresis of the 0 min sample is compared with IUPAC classifications shown in Figure 6.14, it can be observed that the sample is mainly composed of relatively uniform pores. This can be deduced from the vertical drop on the desorption curve of the 0 min sample. The curvature of the 0 min adsorption curve is initially gentle suggesting narrow pore openings with wider internal diameters. This gives rise to the assumption that the pores are of an ink bottle shape. A similar observation was made by Zielinski *et al.* (1993). After 300 min of milling, the curvature of the adsorption and desorption suggest that the pores are slit-shaped in the micropore region. The 300 min hysteresis also suggests that the particles are aggregated. These results agree with the reduction in pore volume observed with increase in milling time.

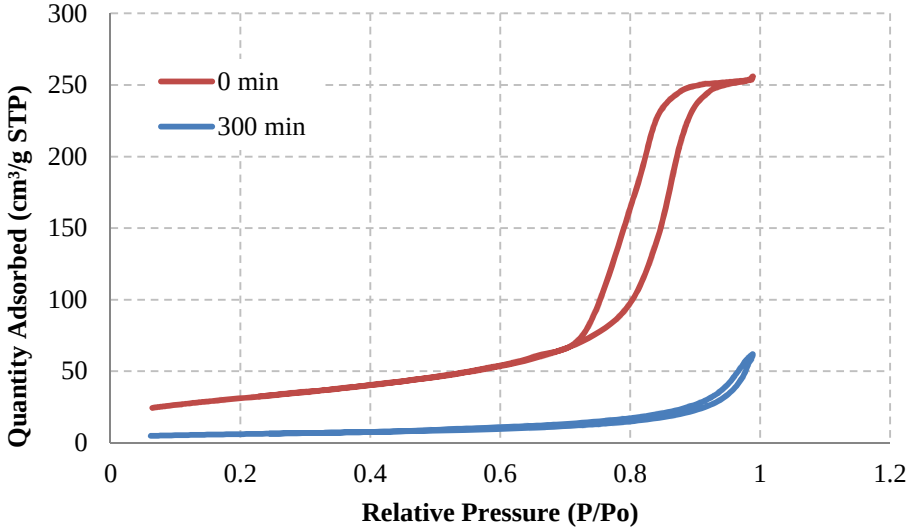

Figure 6.13: Adsorption and desorption isotherms for 20% SBM seeded samples at 0 min and 300 min milling time

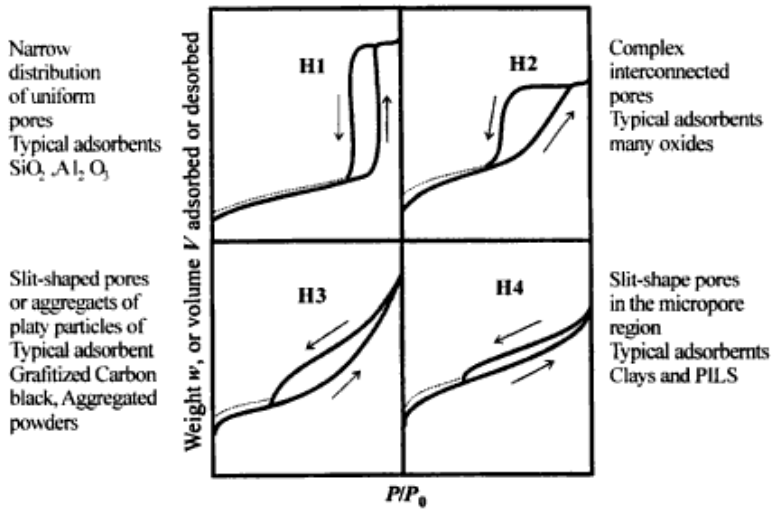

Figure 6.14: IUPAC classifications of hysteresis loops (Hubbard. 2002)

Although BET and XRD give an indication of the changes that occur to the samples during seeded milling, close observation of the samples under TEM is beneficial as it accommodates the visual aspect of the existence of the samples. Figure 6.15 shows TEM micrographs of the seed α-Al_2O_3 and A-R γ-Al_2O_3 samples. Seed samples show an average of 1.5 microns and γ-Al_2O_3 samples show 30-50 nm sized primary particles. The γ-Al_2O_3 primary particles can be observed to be between 10 and 50 nm whilst the α-Al_2O_3 samples range between 1 and 2 µm suggesting that α-Al_2O_3 primary particles are greater in size than γ-Al_2O_3 by an order of magnitude of 2.

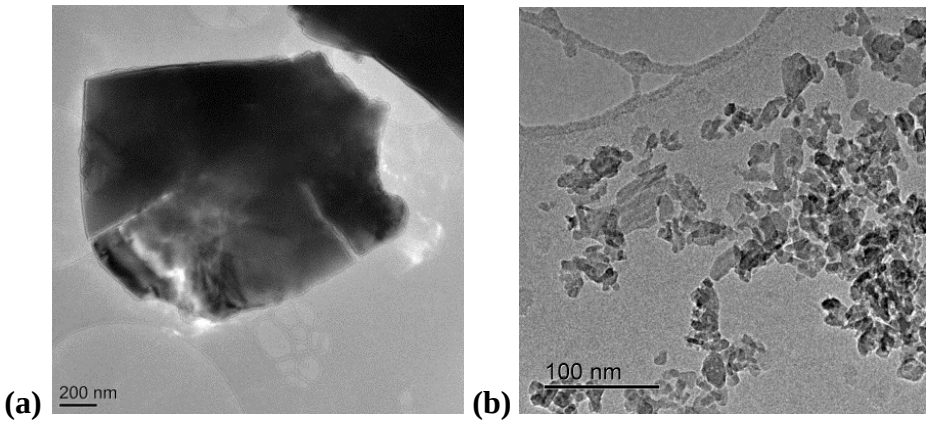

Figure 6.15: TEM imaging of A-R samples showing (a) α-Al_2O_3 Seed B and (b) γ-Al_2O_3

Further TEM imaging is shown in Figure 6.16 after 300 minutes of milling with 20% seed in a single ball mill. It can be seen that the primary particles of α-Al_2O_3 have reduced in size. The size of the primary particles in the image is in the range of 200 to 300 nm. The α-Al_2O_3 particles also appear to have a layer of smaller particles attached to their surfaces. This is

possibly γ-Al_2O_3 and the TEM images suggest that during milling, γ-Al_2O_3 primary particles bond onto α-Al_2O_3 by a cold welding process. This can also explain the rapid decline in surface area of the full sample as observed in BET analysis. It also explains the sharp peaks of α-Al_2O_3 observed by XRD despite the samples having a small amount of α-Al_2O_3.

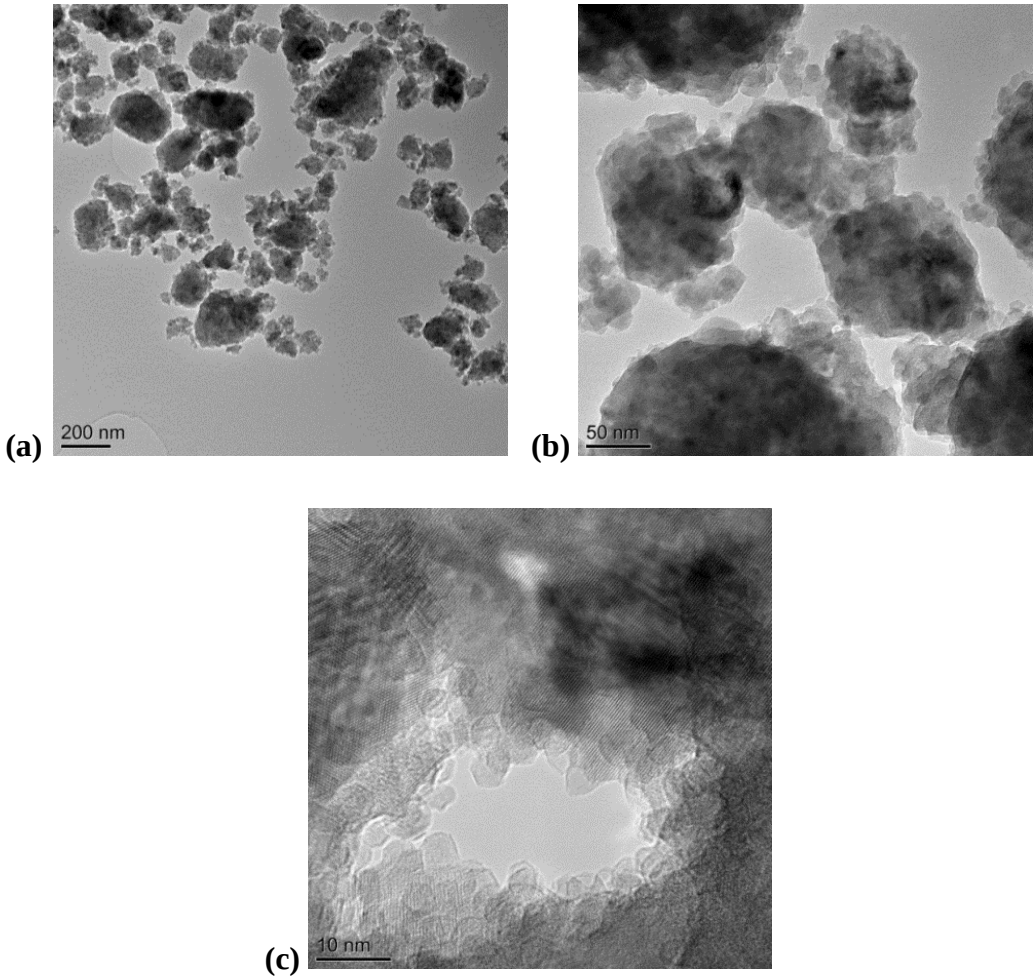

Figure 6.16: TEM imaging of single ball mill seeded samples after 300 min milling with 20% α-Al_2O_3 Seed B showing (a) x200nm mag, (b) x50 nm mag and (c) x10 nm mag

The rapid decline in surface area eventually levels off as the milling time increases. This suggests that after cold welding of the two samples, γ-Al_2O_3 primary particles are transformed into α-Al_2O_3 and amalgamated into the α-Al_2O_3 structure. This process can be encouraged by the presence of nucleation sites provided by α-Al_2O_3 and the mechanical energy supplied by the mill. Further analysis of the TEM images has been carried out in the form of line profile analysis. This was done in order to resolve the d-spacings of the observed particles. Figure 6.17 shows the line profile analysis carried out for two TEM images. The d-spacings determined are compared with d-spacings of the XRD diffractograms for both samples.

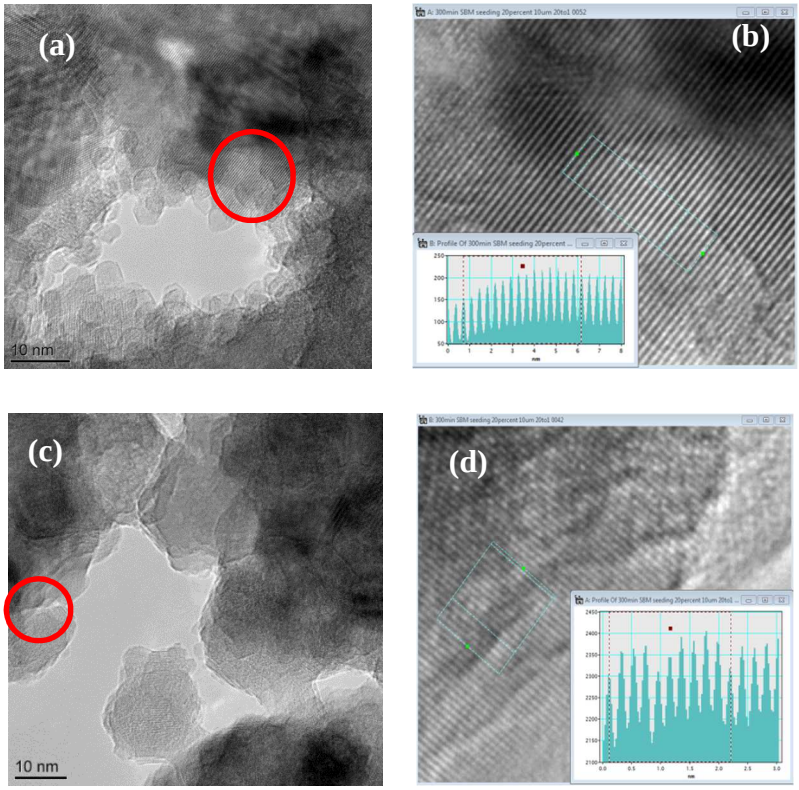

Figure 6.17: TEM images of single ball mill seeded samples after 300 min milling with 20% α-Al_2O_3 Seed B showing (a) and (c), an area on the image circled that has been used for line profile analysis shown in (b) and (d) respectively

The results in Table 6.6 show that the d-spacings obtained by line profile analysis match d-spacings from XRD diffractograms for α-Al_2O_3. The planes derived from the d-spacings are the (012) and (113) α-Al_2O_3 planes.

Table 6.6: D-spacings for two TEM images shown in Figure 6.17 of single ball mill seeded samples after 300 min milling with 20% α-Al_2O_3 Seed B derived from XRD and line profile analysis

TEM Image	Variable	Result
Figure 6.17 (b)	TEM d-spacing	0.3535 nm
	XRD d-spacing	0.3463 nm
	hkl	012 (α-Al_2O_3)
Figure 6.17 (d)	TEM d-spacing	0.2094 nm
	XRD d-spacing	0.2081 nm
	hkl	113 (α-Al_2O_3)

Observation of these surfaces by TEM imaging highlights the effects of milling on the primary particles' structures. The (012) and (113) surface terminations are common for hexagonal close packed crystals that have encountered high stresses. The applied stress results in deformation of the crystal by slip. During deformation by slip, a small region of a crystal re-orientates due to applied stresses. The process is shear stress sensitive and required a critical resolved shear stress to be overcome. The process is also common in materials with high stacking faults.

6.2.3 Wet Milling Seeding Experiments

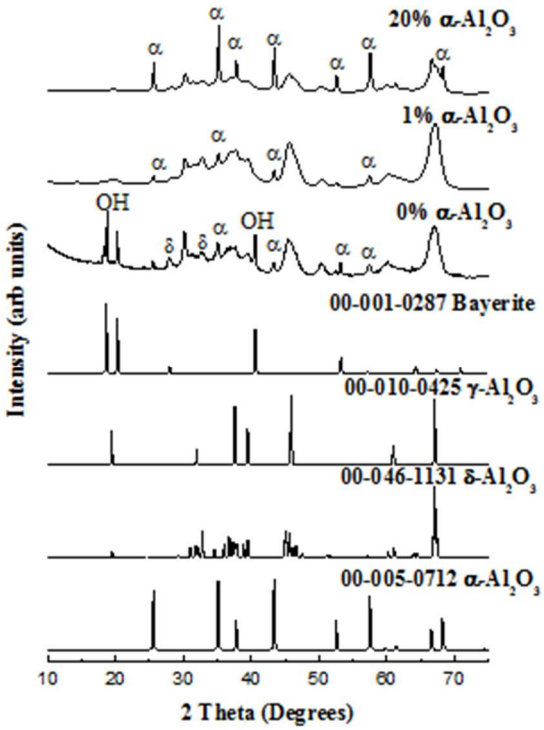

Figure 6.18: Seeded milling experiments showing the effect of adding α-Al_2O_3 during planetary ball milling with water

A short study was carried out to analyse the effects of seeding experiments in the presence of water. α-Al_2O_3 seed was added at 1% and 20% levels. This is shown in Figure 6.18. It can be observed that at 0%, bayerite is present in the sample and initial stages of α-Al_2O_3 formation are also observed. δ-Al_2O_3 is also observed which suggests that the phase transformation in this sample may be following a mechanism similar to that achieved by calcination of γ-Al_2O_3 to form α-Al_2O_3. When α-Al_2O_3 seed is added, bayerite is not observed and a mixture of γ-Al_2O_3 and α-Al_2O_3 is observed. The peaks in the 1% sample are however similar to those observed where no seed was used. At 20% seed level, stronger peaks of α-Al_2O_3 are observed

as expected. The results show that during wet milling, adding seed has minimal effect on increasing the rate of phase transformation. They also present an effect α-Al_2O_3 seed has on the surface of γ-Al_2O_3 that causes hydroxide not to form. This may be by cold welding onto γ-Al_2O_3 surfaces which inhibits attachment of hydroxyl groups on the surface.

6.2.4 Seeding Experiments Discussion

The TEM images in Figure 6.16 agree with observations by BET analysis. As observed in Figure 6.10, there is an initial fast rate of decreasing surface area. Bonding of high surface area γ-Al_2O_3 primary particles, onto low surface area α-Al_2O_3 surfaces, by cold welding, results in a rapid decrease in surface area. The initial fast decline is observed to flatten towards the 300 minutes mark and this may be attributed to consumption of γ-Al_2O_3 primary particles into the α-Al_2O_3 structure as shear stresses are continually supplied by the mill. When XRD is observed over short periods of seeded milling up to 60 minutes, an initial strong presence of α-Al_2O_3 is noted which does not increase up to 60 minutes. Further milling up to 300 minutes then shows a slow reduction in peak intensities of γ-Al_2O_3. This suggests that milling with seed can provide the nucleation sites for α-Al_2O_3 to form. The increase in amount of seed from 10% to 20% however, does not increase the rate of transformation. Surface area is observed to reduce due to cold welding of particles and consumption of γ-Al_2O_3 as milling continues. Pore structures are also observed to transform from ink bottle shapes to slit shaped pores. The reduction in pore volume proposes the destruction of the γ-Al_2O_3 structure. An initially slow rate of phase transformation from γ-Al_2O_3 to α-Al_2O_3 also suggests that before transformation can occur, the γ-Al_2O_3 particles have to be ‘readied’ for transformation. Seeding in wet milling is observed to have no effect on increasing or reducing the rate of phase transformation.

6.3 Compression Testing

6.3.1 Experimental Devices and Procedures

Compression tests were carried out using a 250 kN Compression Testing Machine. A 10 mm diameter die shown in Figure 6.19 (a) was filled up to 50% of its volume with γ-Al_2O_3 powder. The filled die was placed on the machine as shown in Figure 6.19(b). The desired load was set and the test was run. The machine pressures used and equivalent sample pressures are shown in Table 6.1. A full image of the 250 kN Compression Testing Machine used is displayed in Figure 6.19(c).

Figure 6.19: Photographs of compression testing experiments showing (a) the die 10 mm filled with γ-Al_2O_3 powder, (b) the 10 mm die on the compression testing machine during loading and (c) a full image of the compression testing machine

All compression testing experiments carried out are listed in Table 6.7.

Table 6.7: Compression testing experiments carried out using the Compression Testing Machine

Experimental Device	Experiment Type	Machine Pressure (kN)	Sample Pressure (MPa)
250 kN Compression testing Machine	Single compression	18.85	240
	Single compression	37.68	480

The Instron 5566 Test Bench was also used to get more precise data for energy calculations. The die was chosen to be smaller with a diameter of 5 mm to achieve higher pressure with a smaller load. A load equivalent to 120 MPa was tested with the Instron.

6.3.2 Compression Testing Results

XRD results for samples after compression tests with the 250 kN compression testing machine are shown in Figure 6.20 and it can be observed that a small peak emerges on the (222) γ-Al_2O_3 reflection. This emerging peak is the α-Al_2O_3 (110) reflection. This suggests that the compression stresses applied initiate phase transformation in γ-Al_2O_3. It is of interest to understand the mechanism further at the atomistic level. This mechanism may be related to the deformation twinning observed in seeded samples. However, this twinning would be initiated by compression stresses.

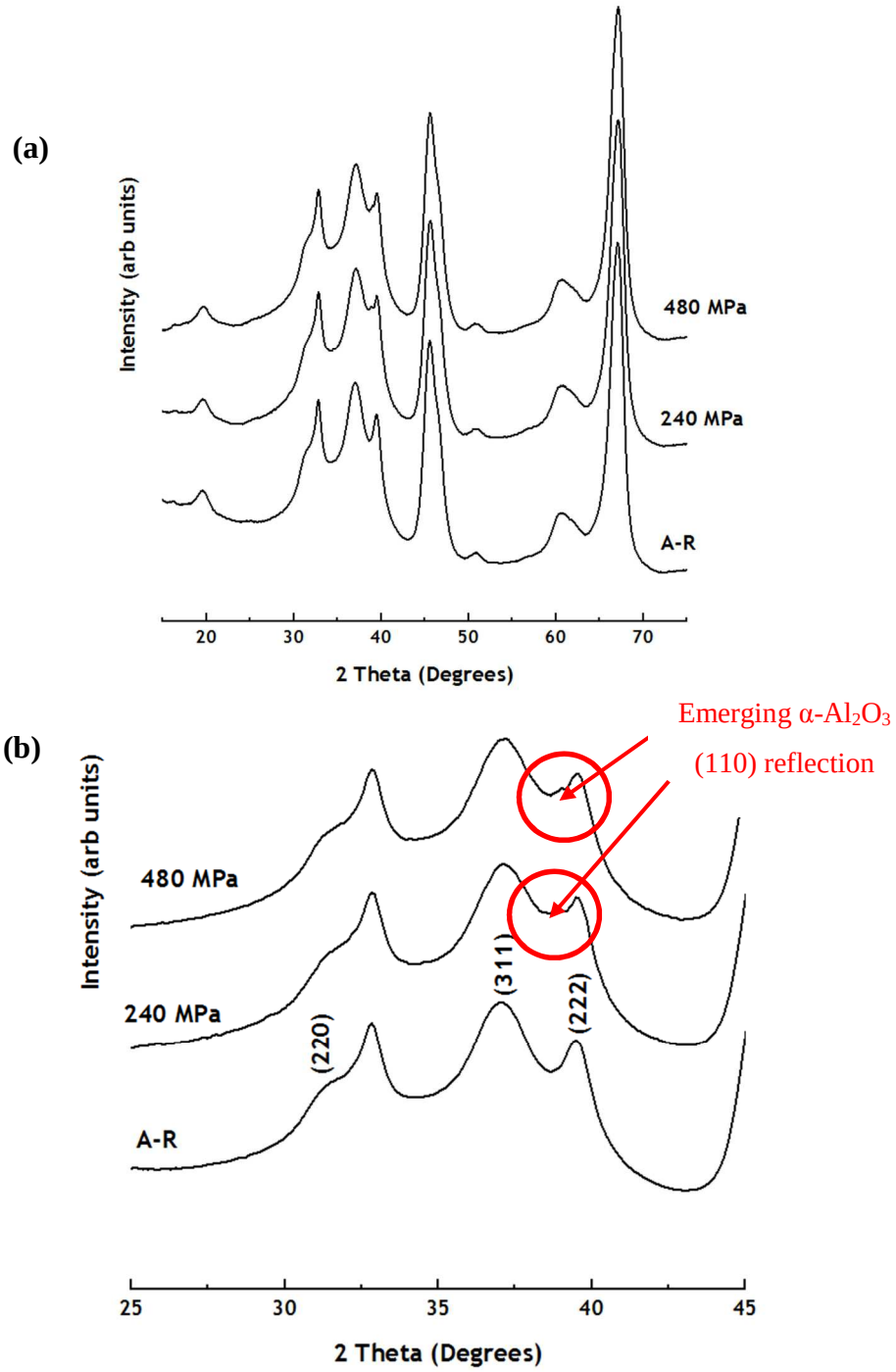

Figure 6.20: XRD Diffractograms for compression testing samples from the 250 kN Compression Testing Machine showing (a) full 2 Theta scale from 15º to 75º and (b) magnified scale from 25º to 45º showing morphology changes on the (222) γ-Al_2O_3 peak circled in red

When the compression testing XRD results are compared with XRD results for samples milled in the planetary ball mill, a similar behaviour on the (222) γ-Al_2O_3 reflection is observed as shown in Figure 6.21. Phase transformation, however, appears to occur at a faster

rate in the planetary ball mill and hence after 30 mins of milling, other small α-Al_2O_3 reflections are also observed.

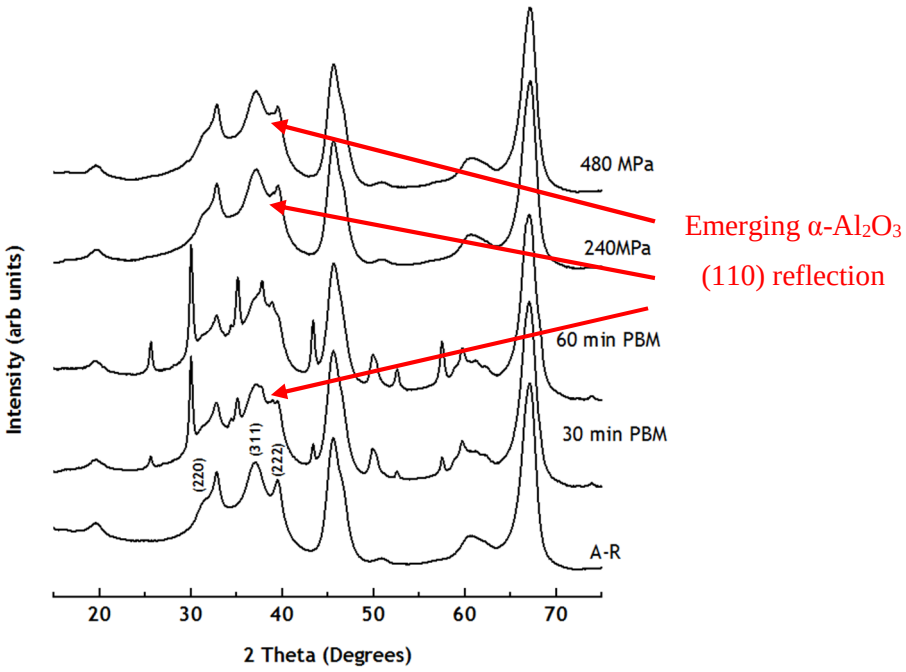

Figure 6.21: XRD diffractograms showing comparison between samples compressed using 250 kN Compression Testing Machine and samples milled in Zirconia using the Fritsch P7 planetary ball mill

It is also important to amalgamate these findings with the XRD results from the single ball mill in Chapter 4. As shown in Figure 6.22, a similar emergence of the 110 α-Al_2O_3 reflection is observed in the SBM XRD diffractogram. The load versus extension curve of the 120 MPa compression was used to calculate the energy from the compression testing. The graph is shown in Figure 6.23. The area under the graph was used to estimate the energy dissipated into the sample during a single compression. The load is labelled in newtons (N) and extension is labelled in metres (m). Each individual rectangle under the graph measures 0.0001 m by 200 N which equates to 0.02 J. The rectangles under the graph are approximately 200 in number and hence the derived energy is 4 J. As the compression time was 9.594 s and the mass of sample was 0.5 g, the specific energy is 0.83 J/s.g. The interest in this energy is that it provides a platform for comparison with the energies that are to be derived by simulation. It also gives an insight into the differences between a single impact effect and a continuous supply of impacts that a material experiences during milling. This value will therefore be compared with collision energies derived from DEM simulations.

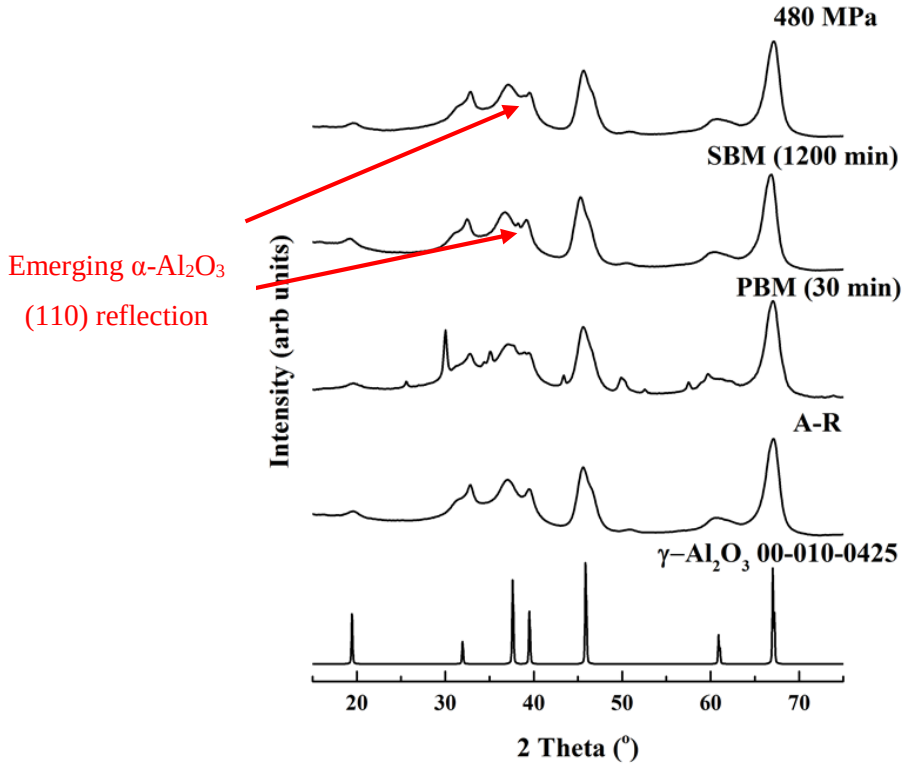

Figure 6.22: XRD diffractograms showing comparison of the 480 MPa sample compressed using 250 kN Compression Testing Machine with the A-R sample, the sample milled in Zirconia using the Fritsch P7 planetary ball mill for 30 min and the 300 min milled SBM sample

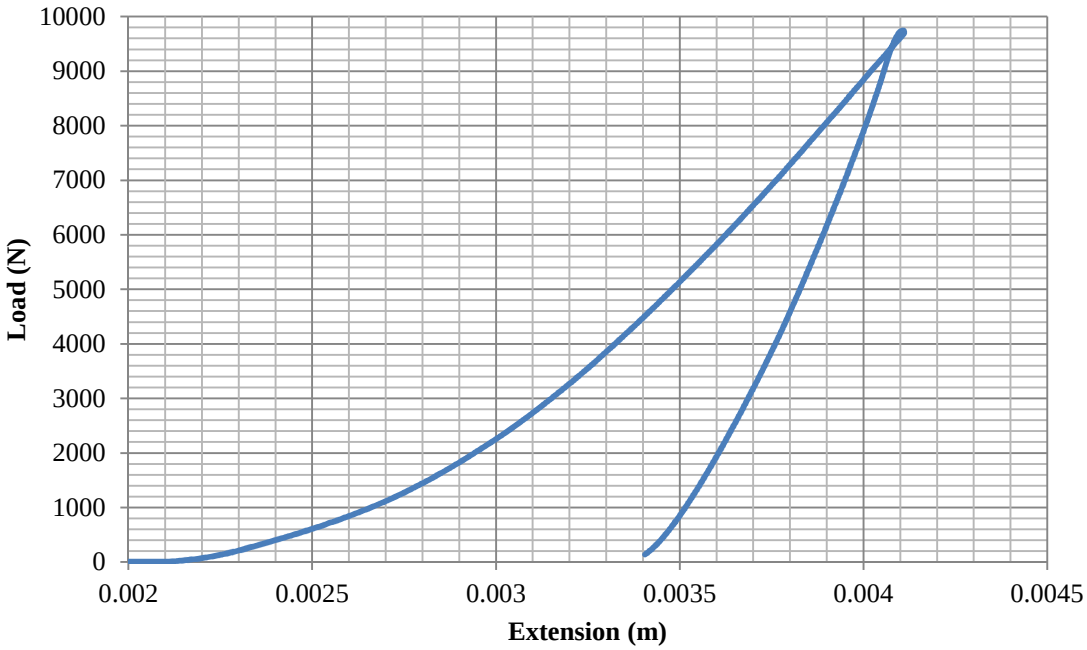

Figure 6.23: Load versus extension graph for the 120 MPa compression test sample

6.4 Discussion

When combined together, the crystallography changes observed in the single ball mill in Chapter 4, the behaviour of γ-Al_2O_3 with the presence of seed and compression testing results appear to shed more light into the initiation and propagation of phase transformation from γ-Al_2O_3 to α-Al_2O_3. Although the single ball mill mainly reduces particle sizes by impact and shear, compression forces are also present when the milling ball hits the walls of the vessel. It has been observed in the single ball mill, planetary ball mill and compression testing XRD diffractograms that the (110) reflection of α-Al_2O_3 emerges first. During a compression test, the powder bed is stagnant and pressure is applied as a uniaxial compression. In the planetary ball mill, γ-Al_2O_3 particles are in motion due to the movement of the milling vessel and the milling media. Shear, impact and compressive stresses are continually applied to them and the breakage of the material's agglomerates reveals new surface each time. This means in the planetary ball mill, phase transformation can occur at a faster rate because there are a larger number of random interactions between the applied stresses and the particles, in different directions.

On comparing the planetary ball mill with the single ball mill, the only difference that emerges is the range of energies dissipated into the particles at each interaction between milling media and the particles being milled. It is observed through compression testing that a higher compressive stress of 480 MPa shows more enhanced microstructural changes to γ-Al_2O_3 when compared with the 240 MPa compression force in Figure 6.20. This suggests that a higher energy can result in enhanced microstructural changes and the continuous supply of high energy can propagate phase transformation. The emergence of the (110) reflection of α-Al_2O_3 also suggests that transformation of γ-Al_2O_3 occurs from the surface. This is a result that ties in well with the structure of the material as it is metal terminated with Al cations on the surfaces. The metal terminated surfaces are the most close packed and they also show to be affected by the change in coordination of Al cations seen in NMR results. It can therefore be made conclusive that phase transformation from γ-Al_2O_3 occurs by a change in coordination of Al cations from tetrahedral to octahedral sites. The crystal size enlargement observed by XRD in SBM samples maybe be due to crystal deformation at surfaces and shifting of crystal planes that results in larger crystals being observed. As the energy in the SBM is not high enough to promote full phase transformation to the final phase, only minor energy effects are observed. The calculated specific energy from a 120 MPa compression is 0.83 J/s.g. This gives a benchmark for comparison with energies that will be derived with

simulation in Chapter 7. The emergence of the (110) α-Al_2O_3 peak suggests that in this process, shear induced nucleation of α-Al_2O_3 is a possibility.

6.5 Conclusion

The work that has been carried out in Chapters 4, 5 and 6 suggests that phase transformation is an energy driven process. Growth of primary particles observed in the SBM in Chapter 4 has been observed as an energy driven process. The (110) reflection observed by compression tests is a crystal surface plane that is located on the edges of a hexagonal α-Al_2O_3 crystal. From the 'synchro shear' model by Kachi *et al.* (1963), the relationship of shear nucleation observed was (111)γ//(0001)α, [110]γ//[0110]α. This shows that when stresses are applied, growth of γ-Al_2O_3 crystals can occur by interaction of close oriented crystal planes. The growth would be by the enlargement of γ-Al_2O_3 crystals on the (111) planes. In the hydroxylated state, Lodziana *et al.* (2004) presented that transitional Aluminas are stable. Instability of the lattice arises when they are dehydroxylated e.g. during calcination. The thermal energy that reduces the OH groups in the material results in rearrangement to a more stable less energetic hcp structure. During milling, the continuous breakage of particles reveals new surface and Duvel *et al.* (2011) has shown that this results in an increase in exposed pentacoordinated Al atoms (Al_5).

These Al_5 atoms have been identified as the surfaces where phase transformation originates from. Rozita *et al* (2013) concluded that the surfaces of γ-Al_2O_3 are metal terminated with aluminium atoms in octahedral and tetrahedral sites. The proposed shear nucleation occurs by change of packing of atoms from ccp to hcp structure. It can be suggested that the build-up of Al_5 atoms in octahedral sites during milling and their interaction can result in growth of crystals in an hcp structure. In this dehydroxylated state, hcp structure may be favoured as a less energetic crystal structure. The results agree with the findings of Duvel *et al.* (2011) which suggest that the process of phase transformation achieved by mechanical energy is similar to that achieved by thermal energy during milling. The key that drives the process is an adequate supply of energy to aluminium cations that exist in a dehydroxylated state. Knowledge of energetics becomes paramount in the process. Further investigation into the impact energies transferred from the milling tools for different conditions becomes a new field that can amalgamate the extensive characterization work that has been displayed with the main driver of the process.

Chapter 7

DEM Simulation of the Single Ball Mill and Planetary Ball Mill

The range of impact energies involved during milling in the jet mill, single ball mill and planetary ball mill and presented with the experimental findings on how the different mills affect the properties of gamma-Alumina are related to the impact energies dissipated during milling. The energies derived from DEM simulations also shed light into how the different stress modes i.e. impact or shear affect the crystal morphology of gamma-Alumina.

7 DEM Simulation of the Single Ball Mill and Planetary Ball Mill

7.1 Introduction

Extensive experimental work has been carried out in an attempt to understand the effects of milling on the structure of γ-Al_2O_3. The comparison of different mills has shown that different energetics yield different effects in terms of size reduction and morphological effects including those at the microscopic scale. As an example, the PBM has shown a larger degree of phase transformation than the SBM. When different milling materials are tested on the planetary ball mill, different results are yielded for each sample. The trend is showing that the harder the material used for milling, the greater the extent of phase transformation observed. Further work on applying uniaxial stress has also shown that crystallographic changes occur. With the inclusion of seeding experiments, all the work points toward energy as the main driver on the process.

It is widely known that γ-Al_2O_3 is a transitional Alumina achieved by calcination of its parent hydroxide. The thermal energy that is supplied by calcination dehydroxylates the parent hydroxide, boehmite in this case. We have shown that mechanical energy as the same effect by revealing unsaturated metal cations in hexagonal sites. The results show that α-Al_2O_3 can be achieved with an adequate supply of energy to the system that can initiate the mentioned processes. Knowledge of the range of energies supplied in different milling processes can better explain the different results that have been observed. From this, a relationship of milling energy to material effects can be achieved. Chapter 7 reports on the ranges of impact energies achieved in the SBM and PBM, two mills where material effects have been observed. The energies are compared and related to material effects from previous chapters. Conclusions are made on the relationship of the impact energies and effects achieved.

All impact energies have been quantified by the use of Discrete Element Modelling (DEM). All the planetary ball mill simulation work has been carried out by Professor Junya Kano from Tohoku University in Japan. Input parameters were supplied to Professor Kano and simulated results were produced. All the single ball mill simulation work has been carried out by Dr Colin Hare and Dr Ali Hassanpour from University of Leeds UK. No work on simulation on the planetary ball mill and single ball mill has been carried out by the author of this thesis. Only the analysis and interpretation of results is displayed.

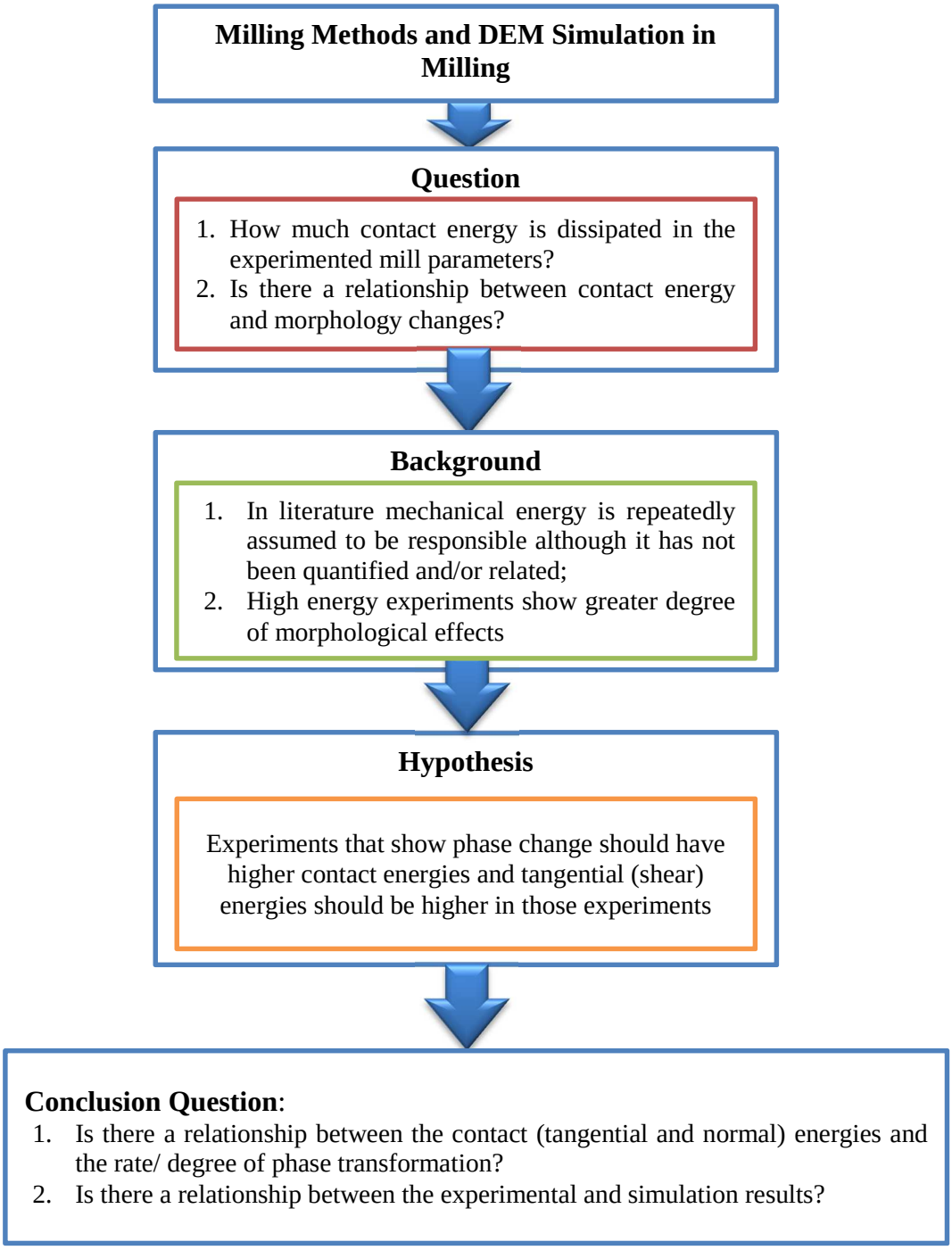

Figure 7.1: Hypothesis formulation for *Chapter 7*

7.2 Planetary Ball Mill Simulations

The simulation work on the planetary ball mill presented in this Chapter has been carried out by Professor Kano of Tohoku University. The author of this thesis has only carried out interpretation of the results provided. The simulation work has been based on previous work by Kano *et al.*, (1999, 2000, 2001). During the DEM simulation, the Voigt model was used as the contact model. This is shown in Figure 7.2.

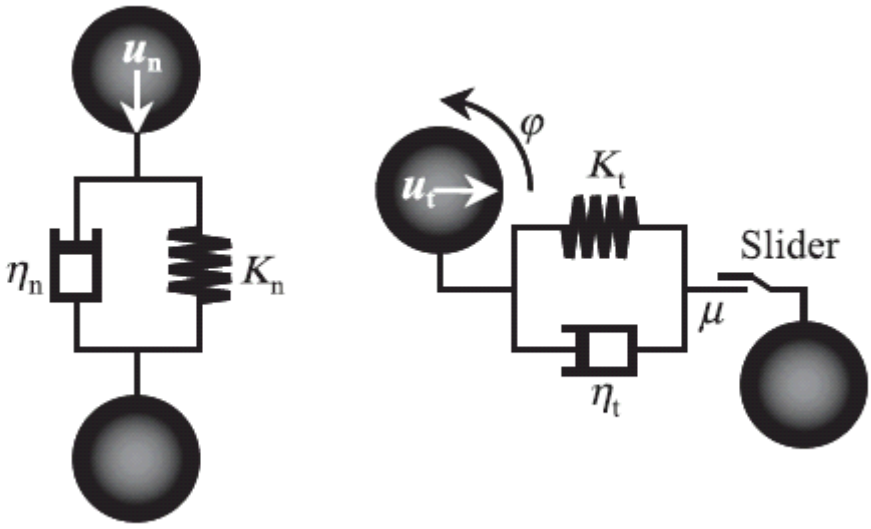

(a) (b)

Figure 7.2: Voigt Model with (a) showing normal force and (b) showing tangential force (Mori et al. 2004)

In the Voigt model, Figure 7.2(a) represents a spring-dashpot system for the normal force and Figure 7.2(b) represents the same system but with a slider for the tangential force. The equations, used for calculating the interactive forces acting on the collisions is shown below as Equation 7.1 and Equation 7.2;

$$\mathbf{F_n} = \mathbf{K_n \Delta u_n} + \boldsymbol{\eta}_\mathbf{n} \frac{\mathbf{\Delta u_n}}{\mathbf{\Delta t}} \qquad \textbf{Equation 7.1}$$

$$\mathbf{F_t} = \mathbf{min}\left\{\boldsymbol{\mu} \mathbf{F_n},\ \mathbf{K_t \Delta}(\mathbf{u_t} + \mathbf{r_B}\boldsymbol{\varphi}) + \boldsymbol{\eta}_\mathbf{t} \frac{\mathbf{\Delta}(\mathbf{u_t} + \mathbf{r_B}\boldsymbol{\varphi})}{\mathbf{\Delta t}}\right\} \qquad \textbf{Equation 7.2}$$

Where K is the spring coefficient, η is the damping coefficient, subscripts n and t and the normal and tangential components, u is the relative displacement and φ is the relative angular displacement, μ is the coefficient of friction and r_B is the radius of the milling balls. In this work, the friction coefficient is assumed as 0.68 and the impact energy of the balls, E_i, is

calculated from the relative velocity, υ_r, of ball-to-ball and ball-to-wall collisions. Equation 7.3 is used for this calculation;

$$\mathbf{E_i = \sum_{j=1}^{n} \frac{1}{2} m v_r^2} \qquad \textbf{Equation 7.3}$$

Where m is the mass of one ball and n is the number of ball-to-ball and ball-to-wall collisions in a second. In order to account for the presence of powder samples within the mill, Equation 7.4 is used were W is the mass of the sample and E_w is the specific impact energy of the balls.

$$\mathbf{E_w = \sum_{j=1}^{n} \frac{1}{2W} m v_r^2} \qquad \textbf{Equation 7.4}$$

7.2.1 Simulation parameters

DEM was used to simulate the experiments carried out with the Fritsch P5 and Fritsch P7 mill. The experimental conditions tested were inputted in the simulations and related impact energies were derived. The experimental variables used are shown in Table 7.1.The presence of powder in the simulation is taken into account by using a higher friction coefficient of 0.7 where values of 0.2 to 0.3 are usually used in the absence of powder. The effect of mechanical properties of the two materials, Stainless Steel and Zirconia, is taken into account by differing the densities. All other values are kept constant.

Table 7.1: Experimental variables for tests carried out with Fritsch P5 and P7 planetary ball mills used as input into DEM simulations

Mill		**P7**	**P5**	**P5**
Pot material		ZrO_2	ZrO_2	Stainless Steel
Pot material density	ρ (gcm^{-3})	5.7	5.7	7.8
Pot diameter	d_M (mm)	40	75	75
Pot depth	h (mm)	38	65	65
Pot volume	V_M (cm^3)	48	290	290
Pot Young's modulus	GPa	210	210	210
Poisson's ratio		0.3	0.3	0.3
Normal stiffness	Nm^{-1}	$1.40x10^{11}$	$1.40x10^{11}$	$1.40x10^{11}$
Tangential stiffness	Nm^{-1}	$5.37x10^{10}$	$5.37x10^{10}$	$5.37x10^{10}$

Normal damping coefficient	Nm^{-1}	$2.77x10^7$		$2.77x10^7$				$2.77x10^7$	
Tangential damping coefficient	Nm^{-1}	$1.72x10^7$		$1.72x10^7$				$1.72x10^7$	
Coefficient of restitution		0.16		0.16				0.16	
Friction coefficient		0.7		0.7				0.7	
Revolution radius	R (mm)	70		120				120	
Rotation-to-revolution speed ratio	r	1.00		1.18				1.18	
Ball diameter	d_B (mm)	15		2	5	10	20	10	20
Number of balls	n_B	3		1580	810	100	12	73	9
Revolution speed	N_r (rpm)	400	700	400				400	
Time step	t (sec)	$1.0x10^{-6}$							
Simulation time	t (sec)	3							
Cumulative time of impact energy	t_i (sec)	3							
Condition number		1	2	3	4	5	6	7	8

7.2.2 Results and Discussion

As shown in Figure 7.3, the Fritsch P7 planetary ball mill was simulated with three 15 mm diameter Zirconia milling balls. The condition varied was the revolution speed; 400 rpm and 700 rpm. The experimental results for this simulation are shown in Chapter 4 of this thesis.

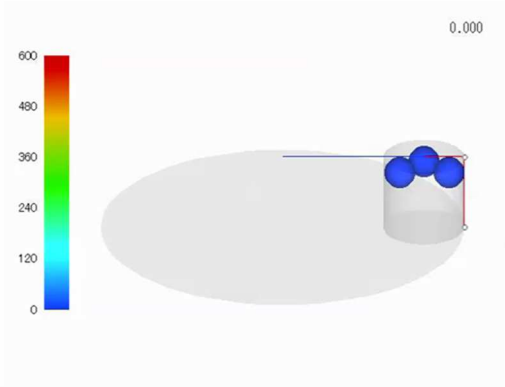

Figure 7.3: DEM simulation of Fritsch P7 planetary ball mill showing three 15 mm Zirconia milling balls

The experiments carried out in Chapter 5 on the effect of varying milling media size are also displayed in Figure 7.4. Four sizes of milling media were simulated to analyse how impact energy varies. This can give insight into the variables that affect amount of energy transferred into material being milled for any given experiment. It also assists in choice of milling

conditions suitable for the desired outcome, which can be size reduction in the case of the 5 mm milling media or phase transformation in the case of the 20 mm milling media as displayed in Chapter 5.

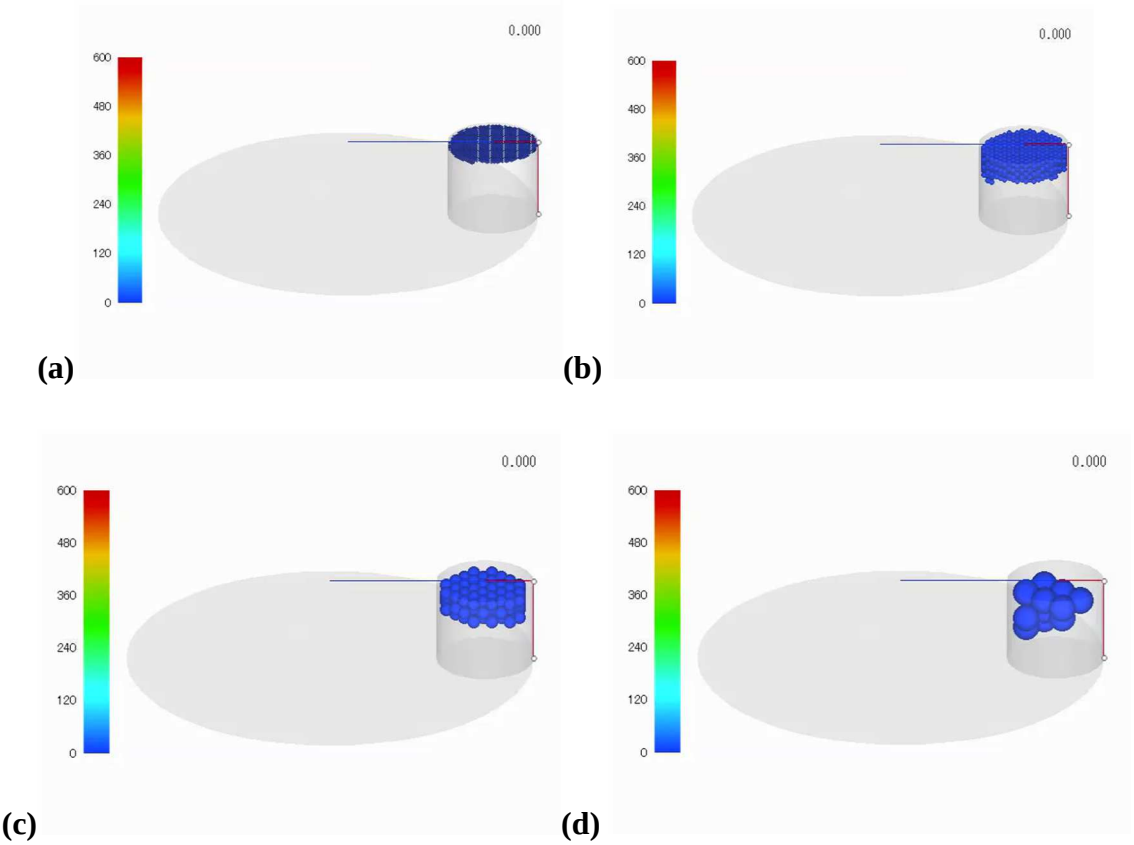

Figure 7.4: DEM simulation of Fritsch P5 planetary ball mill showing (a) 2 mm, (b) 5 mm, (c) 10 mm and (d) 20 mm Zirconia milling media in a Zirconia milling pot

For analysis of the effect of milling in different materials, milling in Stainless Steel was also simulated. In these simulations, the effect of changing milling media size was investigated by using 10 mm and 20 mm milling media in the Fritsch P5 mill. The simulation results are displayed in Figure 7.5.

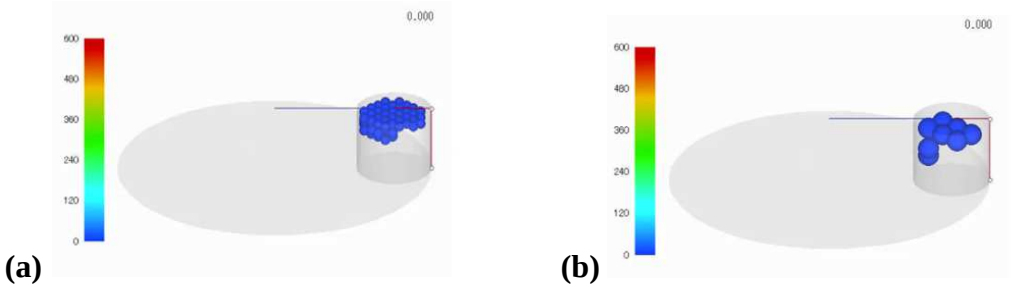

Figure 7.5: DEM simulation of Fritsch P5 planetary ball mill showing (a) 10 mm and (b) 20 mm Stainless Steel milling media in a Stainless Steel milling pot

The results of the total impact energies as well as tangential and normal energies for experiments 1 to 8 are shown in Table 7.2. Experiment 2 has the highest total specific impact energy. When the normal and tangential impact energies are compared, the tangential energies are higher. The lowest total energy is observed in the 2 mm Zirconia milling media. A high total specific impact energy is also observed in the 10 mm Stainless Steel milling media. No scale-up rule was applied between the Fritsch P5 and P7 mills. The results in Table 7.2 are also displayed in a bar chart in Figure 7.7.

Table 7.2: Specific impact energy in the PBM for 8 simulated experiments

		Experiment Number							
		1	**2**	**3**	**4**	**5**	**6**	**7**	**8**
Specific impact energy [J/s.g]	**Total**	1.3	6.0	1.4	4.7	4.3	3.4	5.1	4.0
	Normal	0.3	1.5	0.3	1.3	1.4	1.2	1.4	1.1
	Tangential	1.0	4.5	1.1	3.4	2.9	2.2	3.7	2.9

The results in Table 7.2 are also displayed in a bar chart in Figure 7.7. A high total specific impact energy is also observed in the P7 mill at 700 rpm and 10 mm Stainless Steel milling media.

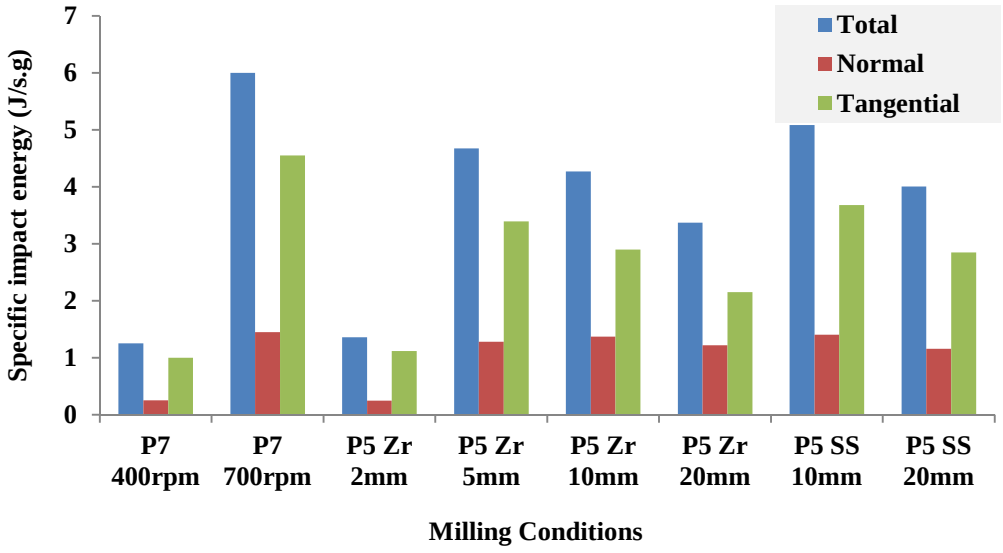

Figure 7.6: Total, normal and tangential impact energies for all conditions simulated of the Fritsch P5 and P7 planetary ball mills

Figure 7.7 shows the distribution of impact energies during the simulations displayed in Figure 7.3 for the Fritsch P7 planetary ball mill. It can be observed that increasing the milling speed results in an increased frequency of higher energy impacts. The impact energies for 400 rpm and greatly concentrated between 0.0001 J and 0.01 J whereas for 700 rpm, a large concentration of impact energies is observed between 0.01 J and 0.1 J. Bearing in mind that the sample milled at 700 rpm in the Fritsch P7 mill shows phase transformation in the experimental results in Chapter 4, the conditions used during this experiment can be concluded as conducive for phase change i.e. the combination of milling parameters such as mill pot size, milling media size, ball-to-powder ratio and milling material used facilitate the formation of α-Al_2O_3.

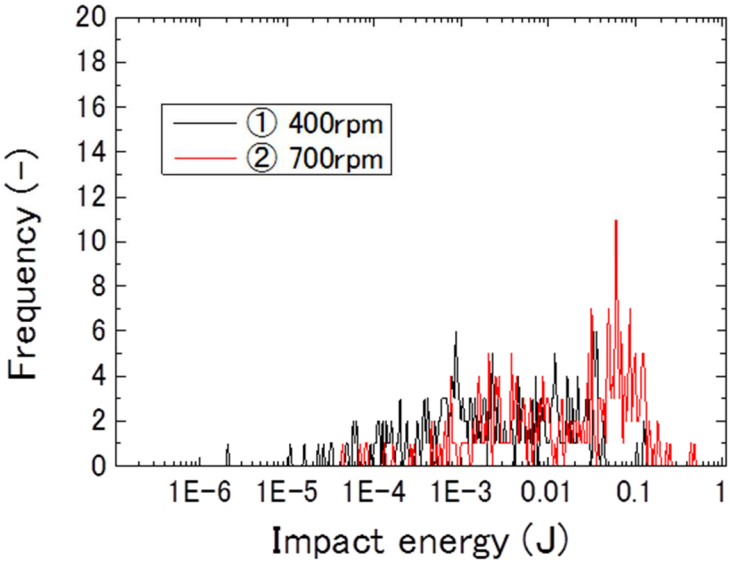

Figure 7.7: Distribution of impact energies in the Fritsch P7 planetary ball mill at 400 rpm and 700 rpm speeds

Experiments 3 to 8 are shown as distributions of impact energies in Figure 7.8. If the variation of milling media using Zirconia milling tools is analysed first (experiments 3 to 6), it is interesting to observe that there is a relationship between milling media size and distribution of impact energies. The smallest 2 mm milling media gives the widest distribution of energies and the distribution narrows as the size of milling media increases. It is also important to note that the peak of the distribution curves shift from lower to higher impact energies as the milling media size increases. The 2 mm milling media energy distribution curve peak as an example is as at 0.00001 J whereas the peak of the 20 mm milling media is at 0.1 J.

The plot also shows a variation of milling media using Stainless Steel tools. It can be seen that the frequency of impact energies in the Stainless Steel tools occurs at high energies than when Zirconia milling tools are used. This is interesting as it coincides with phase change results observed. It also favours hardness test results were a harder material dissipates more energy into the material than a softer material despite it having a higher density. This means that although SS milling media dissipates more total energy, at the point of contact with the material where hardness and Young's modulus govern the relationship, successful transference of energy results in enhanced microstructural change. The 20 mm media shows higher energies per impact than the 10 mm media for both Zirconia and Stainless Steel milling tools.

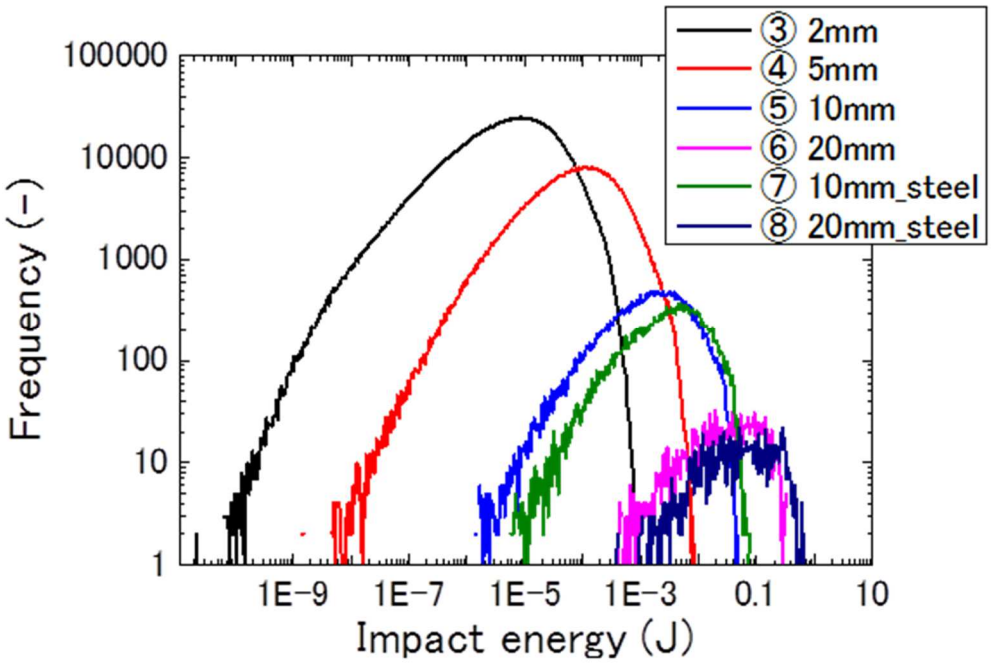

Figure 7.8: Distribution of impact energies in the Fritsch P5 planetary ball mill at 400 rpm using 2, 5, 10 and 20 mm Zirconia milling media and 10mm and 20 mm Stainless Steel milling media

Sample weight can be varied as shown in Figure 7.9 as the mass of the sample is superficially added in after impact energies are derived from the simulation. The point at which phase change is observed, in all the samples is shown in red. As the mass of the sample increases, the specific impact energy reduces.

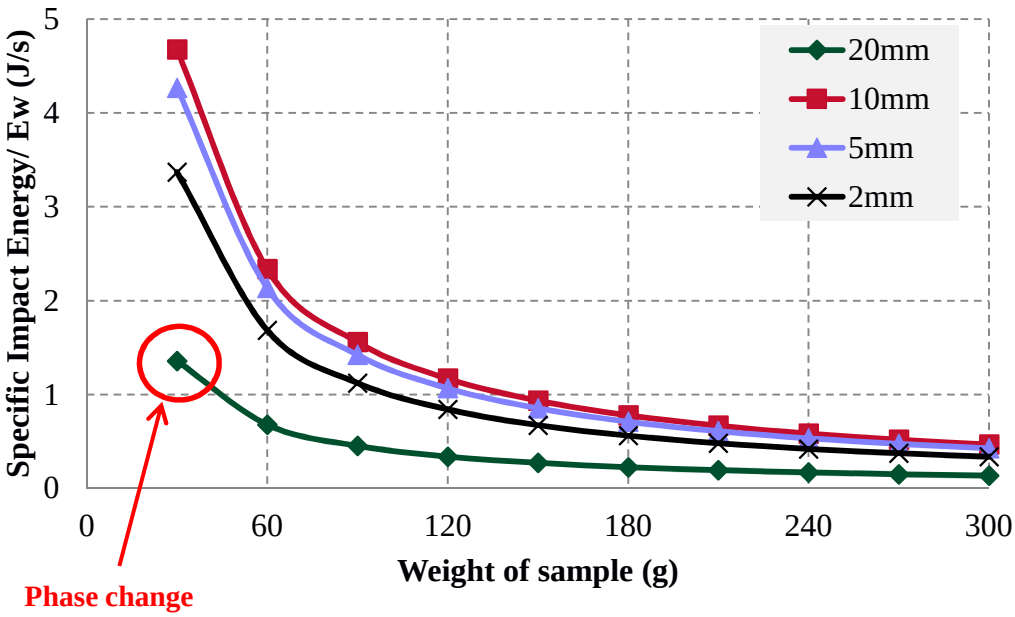

Figure 7.9: Relationship of impact energy with ball-to-powder ratio for simulations of the Fritsch P5 planetary ball mill with a variation of 2, 5, 10 and 20 mm ZrO_2 milling media

The graphs also show that at certain levels of sample mass greater than 120 g in this case, the effect of mass ceases to have an effect on the material. This is because the total specific impact energies become less varied for different milling media sizes. This can be important where phase change is not desired. The efficiency of size reduction will also be reduced. However, the system may not provide enough energy to induce phase transformation in the material. These results are only valid for the Fritsch P5 250 ml Zirconia milling jar with a variation of milling media size from 2 mm to 20 mm.

When all the total energies derived are plotted against the evolution of α-Al_2O_3, it is interesting to analyse the conditions where phase change to α-Al_2O_3 is observed and come up with variables that favour this process. The conditions where phase transformation to α-Al_2O_3 greater than 50% is observed are circled in red. The planetary ball mill simulation results show correlations between energy and phase transformation. A larger size mill, the Fritsch P7 in this case, results in a lower energy requirement for phase transformation to α-Al_2O_3 to occur. Likewise, for a smaller mill, the energy requirement is higher for phase transformation to α-Al_2O_3 to occur. When comparing the Zirconia milling tools with Stainless Steel, it can be observed that Stainless Steel produces a higher level of energy.

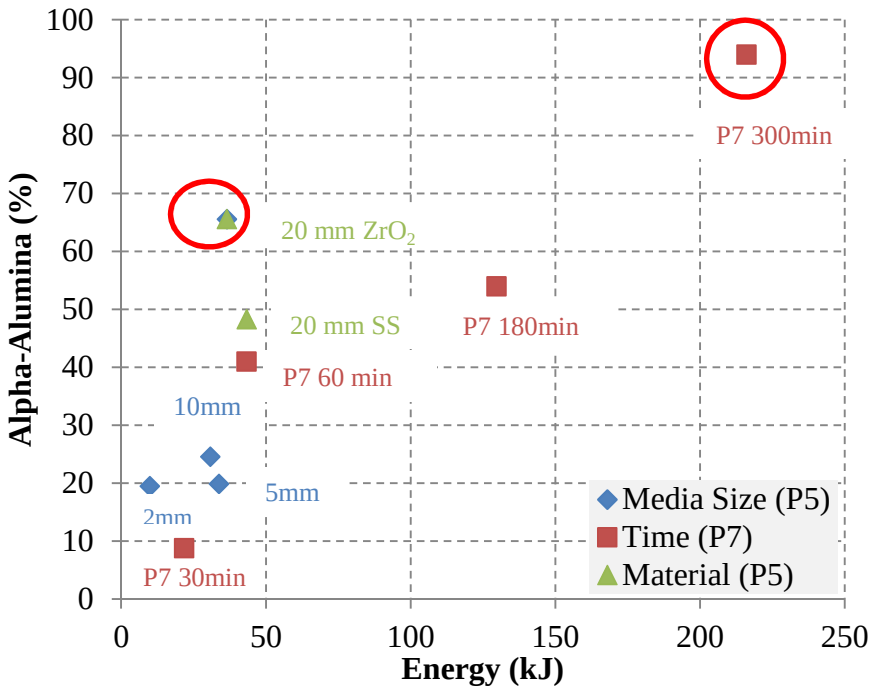

Figure 7.10: Comparison of evolution of alpha-Alumina with simulated milling energies for the Fritsch P5 and P7 planetary ball mills

Phase transformation is, however observed in Zirconia milling tools. This shows that material properties affect the amount of energy transferred from the milling tools to the powder. Zirconia has a higher hardness value and hence at every impact, more energy is transferred into the powder than with Stainless Steel. For the 5 mm and 10 mm Zirconia milling media, it can be observed that for closely related total energies of 30 kJ and 33 kJ, the percentage of α-Al_2O_3 is greater in the 10 mm sample. This shows that milling media size determines the amount of energy dissipated into the material per impact. The 10 mm Zirconia milling media sample has a higher percentage of α-Al_2O_3 despite it having a lower total energy than the 5 mm Zirconia milling media sample. Time is also a factor that determines phase transformation and its extent. It can be seen in the Fritsch P7 mill that amount of α-Al_2O_3 in the sample increases as the milling time is increased from 30 minutes to 300 minutes. It can be said that even in a small mill, prolonged repeated high energy impacts can result in high yields of α-Al_2O_3.

7.3 Single ball mill simulations

A brief attempt of simulation work was carried out on the Retsch MM200 single ball mill by Dr Colin Hare and Dr Ali Hassanpour at the University of Leeds, UK. The author of thesis interpreted the data produced. This was done in order to gain an understanding of the range of impact energies in the mill. No evolution of α-Al_2O_3 was observed in the samples; only initial stages of the phase transformation process were observed. The simulation work was carried out at Leeds using EDEM commercial software supplied by DEM-solutions, UK. The elastic contact model of Hertz-Mindlin with no adhesion forces was considered. The DEM method used applies Newtons laws of motion (shown in Equation 7.5 and 7.6) for every element and a force-displacement model is applied for every contact between elements.

$$\mathbf{F_i = ma_i} \qquad \textbf{Equation 7.5}$$

$$\mathbf{M_i = m\omega_i} \qquad \textbf{Equation 7.6}$$

F, a, M and ω are the force, acceleration, moment and angular rotation, respectively, acting on a particle of mass, *m*, in direction *i*. The movement of the milling jar induces the motion of the milling media and powder sample. Jar geometry and movement at a frequency of 30 Hz were the two defined parameters. The milling jar dimensions used for the simulation were 9 mm diameter by 38.3 mm length in the geometry of a cylinder with two half-spheres of 9 mm diameter at either end.

The velocity of an element in the simulations is considered to be constant for a short time interval (20 % of the Rayleigh time step). Elements are allowed to overlap to account for the deformation of contacts. The contact force is calculated by the force-displacement law. The Hertz-Mindlin model is used to represent elastic deformation of particles as shown in Equation 7.7.

$$F_n = -\frac{4}{3} E^* \sqrt{R^*} \left(\delta_n\right)^{3/2} n_c \qquad \textbf{Equation 7.7}$$

E^*, R^*, δ_n, and n_c are the reduced modulus, reduced radius, normal overlap and the normal contact vector, respectively. A damping force, F_n^d, is also applied to contacts as shown in Equation 7.8.

$$F_n^d = -2\sqrt{\frac{5}{6}}\beta\sqrt{S_n m^*}\, v_n^{rel} \qquad \textbf{Equation 7.8}$$

m^* is the reduced mass (Equation 7.9), v_n^{rel} is the relative normal velocity between the contacting elements, β is the damping coefficient (Equation 7.10) and S_n is the normal stiffness.

$$m^* = \frac{m_A m_B}{m_A + m_B} \qquad \textbf{Equation 7.9}$$

$$\beta = \frac{\ln e}{\sqrt{\ln^2 e + \pi^2}} \qquad \textbf{Equation 7.10}$$

e is the coefficient of restitution. A sliding friction term, μ_s, is added to retard the motion of the particles by a frictional force, F_s, as shown in Equation 7.11. A rolling friction term, μ_r, is also applied to provide a rolling resistance moment, M_r, shown in Equation 7.12 where $F_{s,max}$ is the maximum shear force that can exist in a non-sliding contact. $M_{r,max}$ is the maximum moment that can exist in a non-rolling contact.

$$\begin{aligned} &F_{s,max} = \mu_s \left|F_{n,i}\right| \\ &\text{if } F_{s,max} < \left|F_s\right| \\ &F_s = F_s \frac{F_{s,max}}{\left|F_s\right|} \end{aligned} \qquad \textbf{Equation 7.11}$$

$$\begin{aligned} &M_r = \mu_r F_i^n R_i \omega_{rel} \\ &\text{if } M_{r,max} < \left|M_{r,i}\right| \\ &M_{r,i} = M_i \frac{M_{r,max}}{\left|M_i\right|} \end{aligned} \qquad \textbf{Equation 7.12}$$

At the start of a DEM time step, the laws of motion are applied to each particle in the simulation and the particles are moved for the duration of the time step. After particle motion the particle positions are updated, followed by the list of contacts, then the force-displacement law is applied to every contact. The process is repeated until all required time steps are completed. The origin for movement of the milling jar was established at the centre of the jar. A distance of 9 mm from the origin was determined as the maximum displacement of the milling jar. A Stainless Steel milling ball of 5 mm diameter is simulated. The powder in the mill is represented by spheres with diameters of 350 to 475 μm. Only a brief analysis was carried out for an idea of the range of impact energies in the mill. A small shear modulus had to be implemented as well as bigger particle sizes to increase the time step and obtain faster simulations. An exact mimic of process variables in the SBM would have taken a long duration that was not available. An image of the mill in DEM software is shown in Figure 7.11.

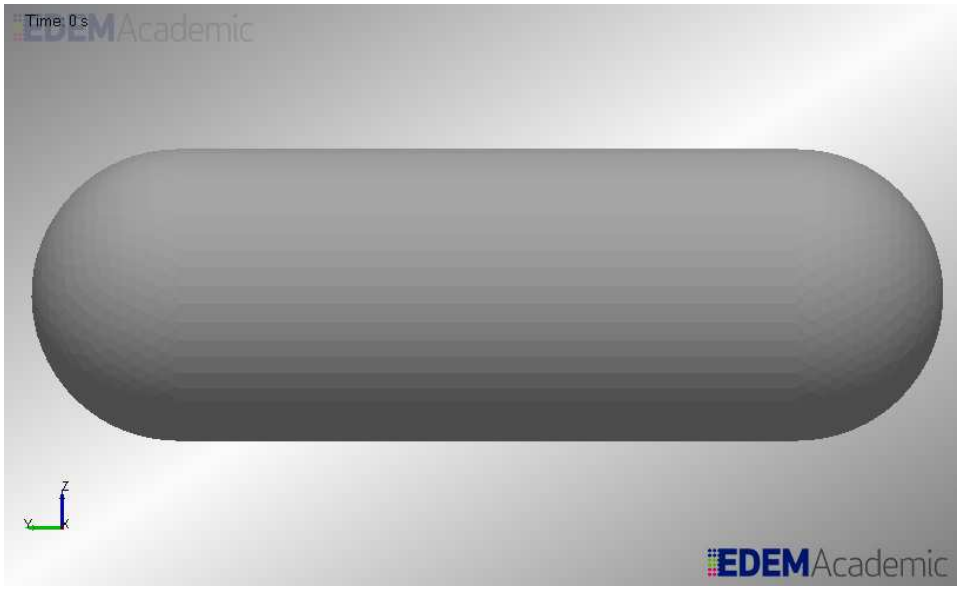

Figure 7.11: Illustration of the single ball mill in EDEM software

7.3.1 Simulation parameters

Table 7.3 shows the input data used for the DEM simulations of the single ball mill and Table 7.4. The coefficient of friction used was derived from previous work by Kano *et al.* (1999). Only one set of conditions was simulated to gain an idea of the range of energies in the single ball mill.

Table 7.3: Input data for DEM simulations of the Retsch MM200 single ball mill

Contact	Steel – Steel	Steel – Particles	Particles – Particles
Sliding friction	0.2	0.5	0.5
Rolling friction	0.01	0.1	0.1
Coefficient of restitution	0.70	0.50	0.50

Table 7.4: Properties of milling jar and milling ball used in DEM simulations

Article	Milling jar	Milling media	Particles
Material	Stainless Steel	Stainless Steel	Particles
Shear Modulus (GPa)	210	210	1
Poisson's Ratio	0.3	0.3	0.25
Density (kg m^{-3})	7800	7800	1500

During the simulation, after the mill geometry is generated, the milling ball is inserted and placed at a randomly defined location within the mill geometry. Particles generation follows this process and each particle location is randomly determined. The size of each particle is randomly selected within the specified range of 350 – 475 μm. Particles are generated at a rate of 20 grams per second, until 2 g has been generated. The process of particle generation takes 0.1 s and 37,962 particles are generated. Gravitational force is present in the simulation and acts on all particles and the milling ball and therefore both come to rest after a short period of simulation time. The process of particle generation is carried out with an initial downward velocity of 1 m/s to reduce the settling time. The oscillation of the mill is started after 0.5 sec of simulation time after particles are approximately stationary and continues for the duration of the simulation. The oscillation is a sinusoidal motion about the z axis with amplitude of 20 mm. Figure 7.12 shows an image taken during the simulation.

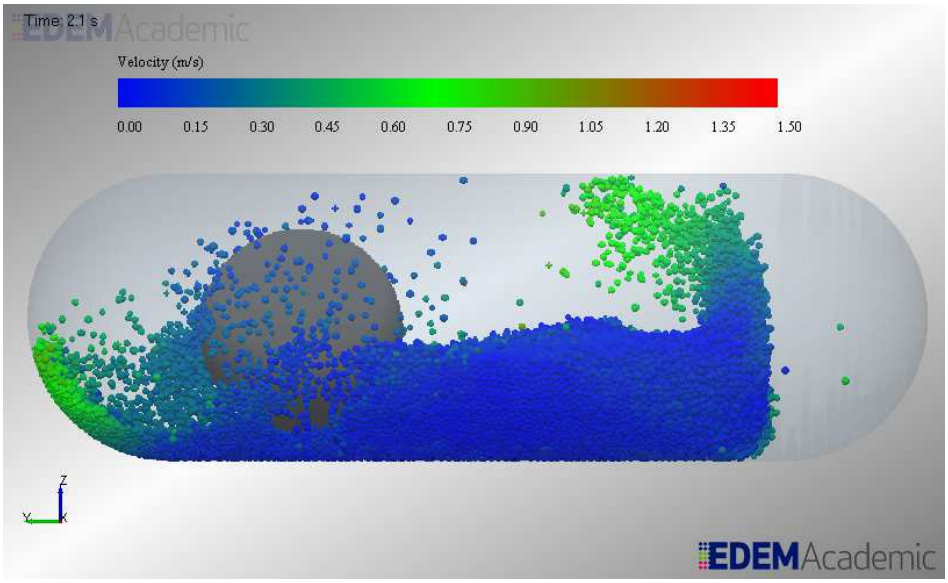

Figure 7.12: Illustration of DEM simulation of single ball mill during a period of varied velocity

7.3.2 Results

The results of the simulation run by DEM for the SBM are shown in Table 7.5. It can be observed that the tangential energies are significantly higher than the normal energies.

Table 7.5: Impact energies in the SBM

	Normal	Tangential	Total
E_i (J/s)	0.00010	0.00540	0.00550
E_w (J/s.g)	0.00005	0.00270	0.00275

7.4 Comparison of planetary ball mill and single ball mill energies

Figure 7.13 shows a comparison of the specific impact energies from the Fritsch P7 planetary ball mill at 700 rpm and the SBM at 30 Hz frequency. It can be observed that there is a significant difference in the energies. The PBM supplies a higher energy by three orders of magnitude; 6 J/s.g as compared to 0.003 J/s.g. The results can be further analysed by relating them to experimental data that has been characterised in Chapter 4.

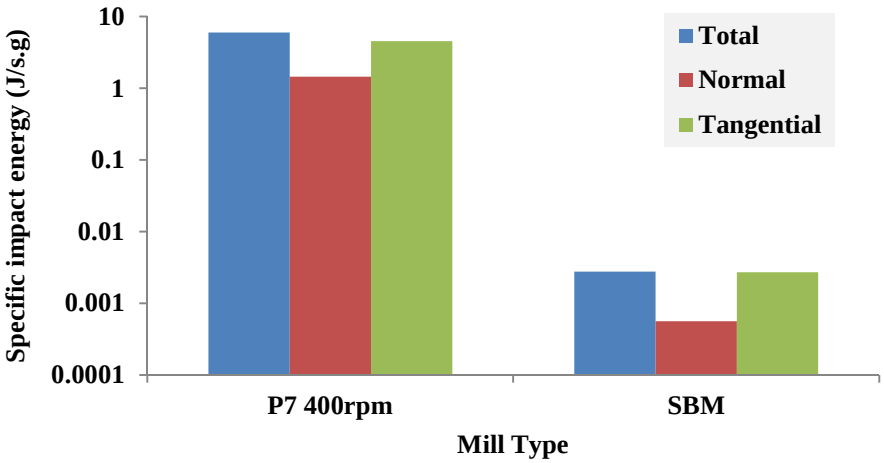

Figure 7.13: Comparison of specific impact energies for the single ball mill and the planetary ball mill

Table 7.6 shows a comparison of the total energies for the SBM and Fritsch P7 PBM. If the energies quantified from DEM are related to experiments carried out in Chapter 4, the durations of the experiments can be used to calculate total energies for the milling conditions. In the 300 min PBM sample milled in the Fritsch P7 mill, 94% α-Al_2O_3 was achieved. In the SBM sample milled for 1200 min, only early stages of phase transformation where observed by the emergence of the α-Al_2O_3 (110) peak. If total energies are compared, it can be seen that there is a significant difference; 0.198 kJ for the SBM and 108 kJ for the P7 PBM. This shows why there is a difference in the extent of microstructural changes in the two samples. It is however important to point out that the properties of the particles used for the SBM simulation (particularly particle size and density) do not match those of γ-Al_2O_3 and therefore the energy quantified is only used as a guide.

Table 7.6: Impact energies for the PBM and SBM experiments

SBM	**E_w (J/s.g)**	0.003
	1200 min E (J/g)	198
PBM P7	**E_w (J/s.g)**	6
	300 min E (J/g)	108000

7.5 Conclusions

The Fritsch P5 and P7 planetary ball mill and the Retsch MM200 single ball mill have been simulated. From experiments in Chapter 5 and 6, phase transformation has been observed in the Fritsch P7 at 700 rpm and the Fritsch P5 with 20 mm Zirconia milling media. The results show that a higher energy can initiate and propagate phase transformation. Lower energy can achieve phase transformation if the mill is a larger size and larger milling media diameter is

used. It has also been observed that although a higher total energy can achieve phase transformation, the efficiency of transfer of energy from the milling tools to the powder at every impact determines the microstructural effects achieved. The energy transferred per impact is also more important than the total energy. The simulation results correlate well with the experimental results as the higher energy conditions are the ones where the most microstructural changes are observed. The effect of hardness displayed in Chapter 6 has also been displayed as effect on energy dissipation. The results give a more complete picture of the relationship between energy and microstructural changes. The final step required in this work is an amalgamation of all the results to derive relationships between energy and changes observed as well as to provide milling process conditions for different desired outcomes during the milling of γ-Al_2O_3.

Chapter 8

Relationship between Milling Methods and Simulation

Amalgamation of experimental work carried out to define a relationship between milling methods and simulation results of impact energies

8 Relationship between Milling Methods and Simulation

8.1 Introduction

The main aim of this thesis has been to understand microstructural effects that occur during the milling of γ-Al_2O_3 by relating these effects to the energy supplied. Energy has become more and more apparent as the causal effect from Chapter 4 through to Chapter 7. Three high energy milling methods have been selected and six characterisation methods have been used to gain understanding of the existence of γ-Al_2O_3 before and after milling.

Milling with the jet mill, planetary ball mill and single ball mill (displayed in Chapter 4) was based on the hypothesis that different stress mode applications from the different mills can result in different microstructural effects in γ-Al_2O_3. Having developed a clear picture of the energy from the different mills, the main observations that can be drawn from these experiments were;

- Low energy results in minimal structural change as observed in single ball milling
- High energy results in phase transformation from γ-Al_2O_3 to α-Al_2O_3 as observed in the planetary ball mill
- Lack of shear stress and the addition of fluid during milling results in no microstructural effects as observed in the jet mill
- High energy results in surface area reduction which is possibly due to a reduction in vacancies in the crystal structure

Further experimental work was carried out to better understand microstructural effects observed by isolating different variables. In Chapter 5, the planetary ball mill was the main focus and the effect of milling material, BPR, milling media size and milling aids was investigated. The main observations drawn from this chapter was that the amount of energy as well as the transfer of the energy into particles is just as important as the stress mode with which the energy is supplied. For instance, a mill such as the jet mill is known to be a high energy mill because the energies at every impact can be assumed to be much less than in a ball mill. This assumption is due to the fact that impacts in a jet mill involve particle-to-particle collisions whereas impacts in a ball mill involve particle-to-media/vessel contacts. Because of this, particles milled by the planetary ball mill experience more energy effects to their microstructure. Other observations drawn from Chapter 5 include an understanding of variables that result in higher energy milling such as;

- milling tools with a high hardness value
- larger diameter milling media
- higher BPR
- PCAs that do not interact with the surface of the material being milled
- dry milling over wet milling
- the increase in pentacoordinated aluminium cations

Lower energy effects also observed include other phases such as δ-Al_2O_3 and θ-Al_2O_3 in the samples and the growth of crystals. Further investigation has been carried out on the effect of compression and seeding on γ-Al_2O_3. Compression tests were carried out to isolate impact energy and assess its effects. Seeding experiments were carried out to assess the effects of providing nucleation sites for the formation of α-Al_2O_3 by consuming γ-Al_2O_3 during milling. A better understanding of the behaviour of γ-Al_2O_3 during milling was derived from these experiments. The results reflected that the variation in energy dissipated to particles being milled is determined by the stress mode and milling variables.

The specific energy during a single compression was measured as 0.83 J/s.g for a time period of 9.594 s. This is less than the energies derived from the PBM simulations. As a comparison, the energy in the P7 PBM at 700 rpm for the same time period is 57.56 J/g where it is 2 J/g in the single compression. If the single ball mill was run under experimental conditions tested for the same time of 9.594 s, the total specific energy would be 0.027 J/g. In milling processes such as planetary ball milling were high energy is successfully transferred into the structure of γ-Al_2O_3 and the materials have more area for movement and constant particle breakage is occurring, the phase transformation can occur by diffusional nucleation through exposed aluminium cations in octahedral sites. In processes where there is limited movement of particles such as compression or impact events, the phase transformation can occur by shear nucleation were atoms in the region of transformation shift a short distance into a new crystal arrangement, i.e. from ccp to hcp in this case.

Having derived an understanding of the different effects energy has on the microstructure of γ-Al_2O_3, DEM simulation on the planetary ball mill and the single ball mill show that shear stresses are higher than impact stresses. When compared, the energies levels are however significantly different. The planetary ball mill has much higher energy per impact than the single ball mill. This explains why extensive phase transformation is observed in the planetary ball mill and not in the single ball mill. Other deductions that had been assumed

from characterisation work were simulated in the planetary ball mill such as a variation of speed, milling media size and different milling materials. The results correlate well with the experimental work and show that a higher speed, larger milling media and a material with a high hardness value all contribute to a high energy milling process that initiates and propagates phase transformation. The results also show that for phase transformation to occur, the energy that is successfully transferred into a particle per impact is more important than the total energy dissipated during the entire milling process. Correlations between the energy and milling parameters have been derived and are shown in the next section.

8.2 Relationship between Microstructural Changes and Energy

From the experimental and simulation results of the Fritsch P7 planetary ball mill, a relationship of energy and time can be derived and shown in Figure 8.1.

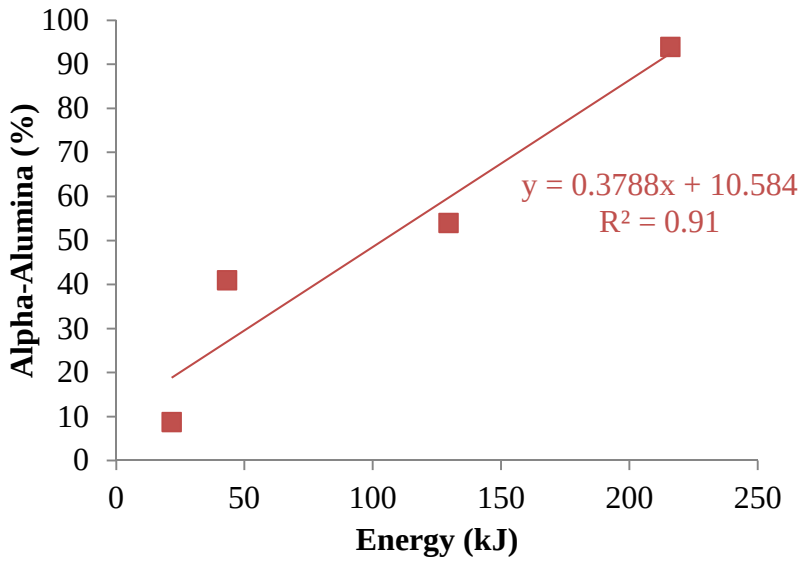

Figure 8.1: Graph showing evolution of α-Al_2O_3 with increase in energy for the time study in the Fritsch P7 planetary ball mill

It can be seen that as energy increases, the amount α-Al_2O_3 present in the samples also increases. The results also show a linear relationship between energy and transformation. This suggests that for the milling conditions used, the addition of time of milling continues the process of phase transformation and they show that prolonged milling with the right energetics has the possibility to yield 100% α-Al_2O_3 from a sample that was originally γ-Al_2O_3. Another relationship that can be looked at closely is the relationship of evolution of alpha-Alumina with an increase in milling media diameter. It can also be observed that phase

transformation increases with an increase in milling media diameter. The total energies are however higher for 5 mm and 10 mm milling media. It has been shown in Figure 7.8 that the frequency of higher energy impacts is lower despite the total energy being higher. This means that to define a relationship between energy and phase transformation, focus should lie on higher energy impacts.

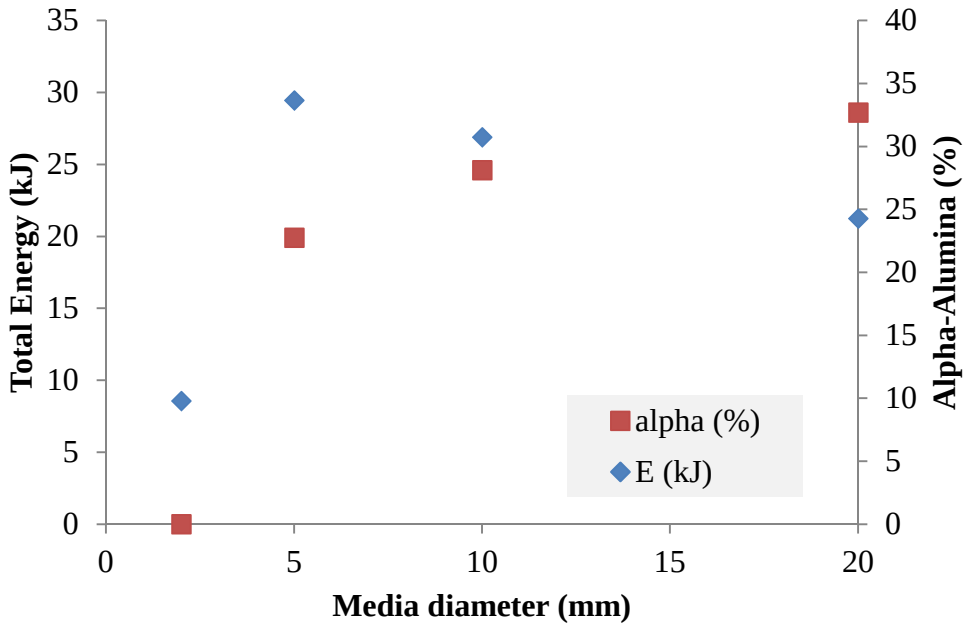

Figure 8.2: Graph showing the energy and evolution of α-Al_2O_3 with increase in milling media for experiments in the Fritsch P5 planetary ball mill

If all the results with quantified energies are combined, they can be shown in Figure 8.3. It can be observed that there is a difference in energy quantities for samples where α-Al_2O_3 is observed and where other Alumina phases are observed.

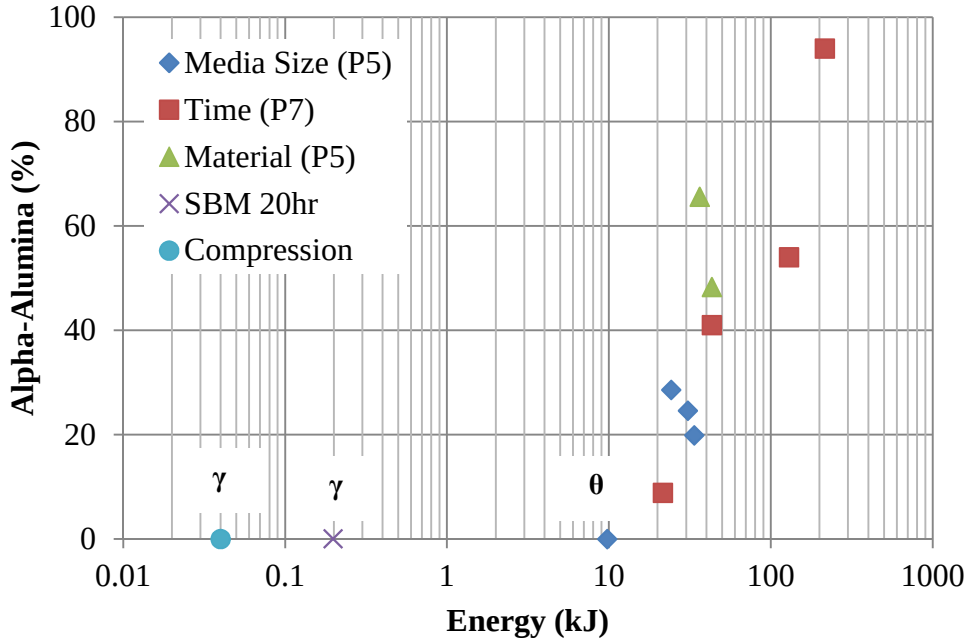

Figure 8.3: Graph showing the energy relationship with evolution of α-Al_2O_3 for different experiments using compression, single ball milling and planetary ball milling

It is also interesting to note that as energy increases, the phases of Alumina observed change according to the dehydration sequence of γ-Al_2O_3 to α-Al_2O_3, i.e. γ-Al_2O_3 →δ-Al_2O_3 →θ-Al_2O_3 →α-Al_2O_3. An amalgamation of the energy results confirm that the phase transformation of γ-Al_2O_3 is an energy driven process. From boehmite, dehydroxylation results in γ-Al_2O_3 with aluminium cations in octahedral and tetrahedral sites. The transformation from γ-Al_2O_3 →δ-Al_2O_3 →θ-Al_2O_3 →α-Al_2O_3 is mainly differentiated by the rearrangement of aluminium cations. The study by Wilson (1979) states that the rearrangement during transformation results in two outcomes; a reduction in aluminium cations in tetrahedral sites and a reduction in vacancies. It also gives a relationship of these reductions with a change in the intensity of the {220} reflections as they represent tetrahedrally coordinated cations in spinel-type structures. As shown in Figure 8.4, the (111) is a surface plane and has a high concentration of aluminium cations as shown in Figure 8.5. The (111) plane is also the slip plane for fcc crystals and slip occurs in the <110> direction. This is because the (111) plane is the most dense plane and has the highest resolved shear stress. The shear stresses in the milling processes also increase the frequency of slip events.

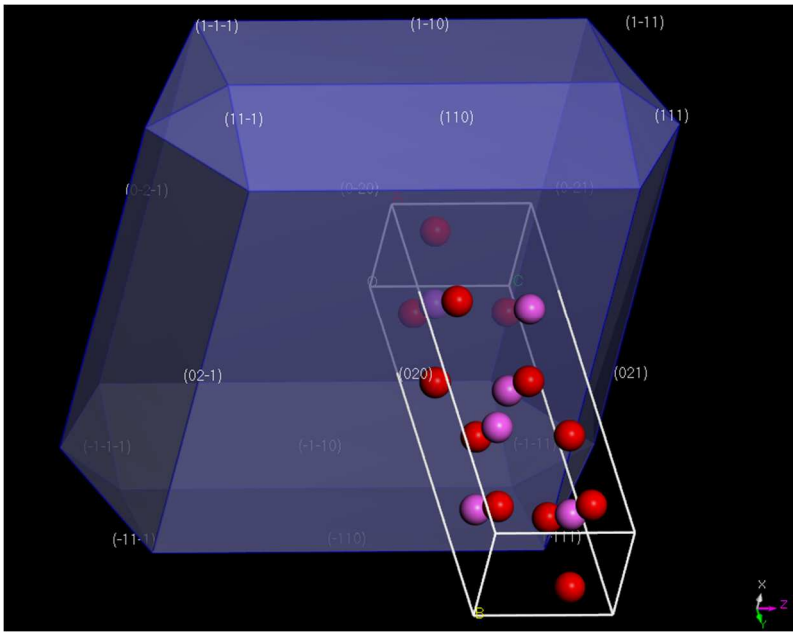

Figure 8.4: Illustration of the morphology of a gamma-Alumina crystal with Al atoms represented by purple and O atoms represented by red

It can be concluded that the mechanical energy supplied by milling is used to overcome the resolved critical shear stress resulting in slip on close packed Al-O planes. This results in an increase in octahedrally coordinated aluminium and a reduction in tetrahedrally coordinated aluminium cations. The build-up of pentacoordinated aluminium cations is highly likely due to the gradual transformation from fcc ABCABC stacking to ABABAB hcp stacking. Where high energy is in constant supply in a system, transformation occurs at a faster rate due to many slip events occurring at the same time.

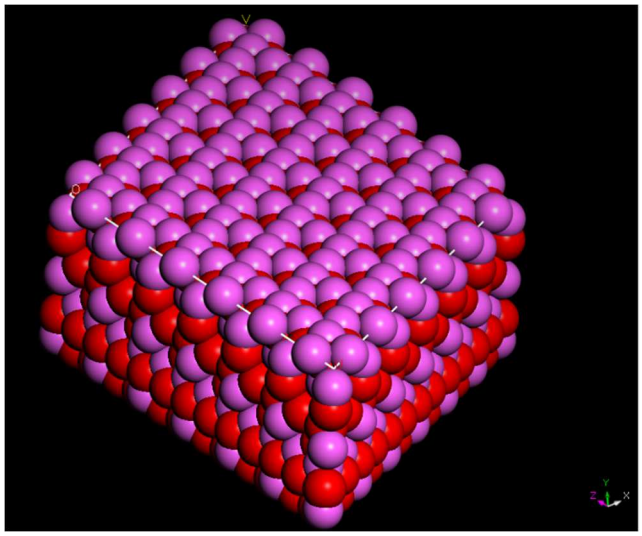

Figure 8.5: Illustration of the close packed {111} plane of gamma-Alumina with Al atoms represented by purple and O atoms represented by red

Transformed crystals also provide nucleation sites for further transformation and hence the rate of phase transformation increases as more energy is supplied to milling processes. As for an energy threshold, by using Figure 8.3, the results show that a total energy of 10 kJ or less during milling will not result in the evolution of α-Al_2O_3. Other transition Aluminas will however be observed. For the γ-Al_2O_3 structure to be preserved, the total energy needs to be kept the range of 0.1 kJ. A relationship between energy (mechanical or otherwise) and microstructural change has been established in this work. Furthermore better understanding of the effect of mechanical energy on the structure of γ-Al_2O_3 has been displayed. DEM simulation has also been displayed as a useful tool for deriving energy thresholds and this tool can be used to save time consuming experimental trials. Experiments can be simulated by the manipulation of different variables such as BPR, milling speed and milling media size to derive the best combination of variables for the desired product. In the case of γ-Al_2O_3 used for this work, a total energy of 0.1 kJ during dry during milling in the planetary and single ball mills can maintain the desired crystal structure.

Chapter 9

Recommendations and Future Work

Recommendations for milling gamma-Alumina as well as future work that can be carried out are outlined.

9 Recommendations and Future Work

9.1 Introduction

The effect of milling on the microstructure of gamma-Alumina has been thoroughly investigated. The aim of the work has been to find a relationship between the energy supplied by milling and the microstructural changes observed by characterisation. Relationships have been found and a substantial contribution to the further understanding of phase transformation from gamma-Alumina to alpha-Alumina has been made. It is important at this point to bring about the relevance of this work in terms of application.

As the gamma-Alumina investigated in this thesis is used as a catalyst support, a set of recommendations have been compiled as to how the structure of gamma-Alumina can be preserved to avoid loss of desired properties such as high surface area. Like any other piece of research work, the subject is however not fully conquered as each set of experiments builds up new variables that inspire further interest in the subject and motivate the need for more work. Hence, future relevant work is also given in this chapter.

9.2 Recommendations

The set of recommendations have been derived from the use of three different milling methods namely the planetary ball mill, the jet mill and the single ball mill. The main driver of phase transformation as well as the initiation of microstructural changes in gamma-Alumina has been identified as energy. An ideal milling process for gamma-Alumina involves achieving the desired size reduction without loss of desired properties by any change to the structure of the material. Initial thoughts on this, point toward a milling method with efficient use of energy.

In terms of milling equipment, the jet mill has proven to be a worthy candidate for size reduction. It can achieve the required size reduction of a d_{90} of 10 microns and does not induce any microstructural changes into the material. The mill also has low levels of contamination due to the mechanism of size reduction and hence can be beneficial in keeping the material from contamination by surface interacting agents. The weakness of the process used is that it involves feeding the material through the mill up to 20 times to achieve the required size. For bench top experiments, this is achievable and in shorter times than ball milling as each milling cycle lasts 10 minutes. This can however be tedious in larger scale milling processes as probably more mills will be required in sequence. The added effect of

high surface energies of particles after milling can prove to be a counteractive issue as it can encourage re-agglomeration of particles. Static can be used to reduce the charge in this case. These two weaknesses highlight the fact that the use of the jet mill is not the perfect solution for milling gamma-Alumina. It is therefore necessary to evaluate ball milling processes.

Milling in the single ball mill has shown better size reduction than milling in the planetary ball mill. The size reduction achieved is however not even close to acceptable. The microstructural changes that the material undergoes in this mill are minimal. However, signs of the initial stages of phase transformation have been observed. It is therefore recommended that any milling activity done in this mill, if carried out to the same milling variables would require a lower frequency of milling or milling tools with lower hardness values. This mill is however not recommended for size reduction purposes but rather to gain a better understanding of different milling methods on the structure of gamma-Alumina.

The planetary ball mill has been investigated both in wet and dry milling. The size reduction achieved by wet milling surpasses the desired size and therefore in wet milling, the mill is suitable for size reduction. The desired end state of the material however needs to be considered. As this is a wet process, if the material is to be dry for end use, an extra process of drying is required. The wet milled samples also show some degree of microstructural effects and therefore the energy in the process needs to be reduced to have minimal impact on the microstructure of gamma-Alumina. Variables that need to be considered to reduce energy will be discussed combined with recommendations for dry milling. Dry planetary ball mill is not recommended for size reduction required in this sample. The process results in agglomeration and production of particles larger than the sample before milling due to the combination of fines with high surface energy and other poorly milled particles. Water aids in keeping the material fluidised and hence results in more efficient use of the high energy impacts.

In order to reduce the amount of energy dissipated in particles during planetary ball mill considerations around milling variables can be made. These are listed in Table 9.1. It is important to note that the selection of variables has compromises. For instance, selecting a softer material can mean higher levels of contamination. Selecting smaller milling media can mean longer milling times and higher levels of re-agglomeration. Selecting a shorter milling time may not achieve the required size reduction and a smaller BPR may prolong milling time. This then brings the use of a predictive tool into consideration. Simulating the process

using software such as DEM before lengthy trial and error experiments can result in selection of the best variables for a milling process.

Table 9.1: Considerations for reducing highly energetic collisions in the PBM

Variable	**Action**	**Outcome**
Milling tools material	Low hardness value	Low hardness materials dissipate less energy into the particles per impact
Milling media diameter	Smaller milling media	Smaller milling media dissipate lower energies into material per impact
Milling time	Shorter milling time	Shorter milling times reduce to the total energy dissipated into the samples and can achieve product before transformation occurs
Milling speed	Slower speed	Slower milling speed results in lower energy collisions
Ball-to-powder ratio	Smaller ratio	Smaller BPR results in more sample and reduces the frequency of high energy collisions with the same particles

Another variable to consider in both wet and dry planetary ball milling is the addition of PCAs. If the selected material has no effect on end use, it can aid in reducing microstructural effects. Materials such as La_2O_3 have been reported to bind onto alpha-Alumina nucleation sites and hence inhibit the propagation of phase transformation. Lesson learnt from the milling processes show that in order to improve efficiency of energy use in the milling of gamma-Alumina, a fluidized system works better i.e. a solvent or gas. The phase transformation has also been linked with the change of aluminium cations from tetrahedral to octahedral sites. If selected gamma-Alumina samples for milling are produced with more aluminium cations in tetrahedral sites, the phase transformation rate can also be greatly reduced.

9.3 Future work

In the progression of this project, different aspects have come up during both experimentation and simulation that have not been addressed. This may have been due to time constraints or misalignment with the objectives of the project. All aspects however can provide a great contribution to knowledge as well as further understanding of the subject.

One aspect that has come up is an interest in investigation compression tests of gamma-Alumina under cyclic loading. This can give mimic repeated impacts and give insights into whether phase transformation can be achieved this way. On the same subject matter, the analysis of single compression tests by TEM can provide more in depth analysis as to whether the compression causes any stacking faults within the material.

The investigation on milling in the single ball mill has been carried out up to 20 hours. There is interest into whether longer mill times would results in phase transformation to alpha-Alumina. Shorter milling times are also of interest in the planetary ball mill as characterisation of the samples would result in an understanding of the initial stages of phase transformation.

The simulation of the jet mill is another interesting piece of work that can further contribute into understanding how energies per impact affect the microstructure of gamma-Alumina. A comparison with the planetary ball mill simulations as well as more extensive simulations on the single ball mill would give more insight on the effects of energy. The use of a scale-up rule in the use of different planetary ball mills can also introduce the effect of varying mill size and provide a predictive tool for scaling up the planetary ball milling process. A simulation of wet milling in the planetary ball mill can also contribute to understanding how energy and hydroxyl groups interact on the surface of gamma-Alumina during milling.

One final aspect that has not been looked at in this work is the addition of surface interacting PCAs. It is of interest to investigate how PCAs interact with the surface of gamma-Alumina and how they can inhibit phase transformation.

10 References

Aliofkhazraei, M. 2015. *Handbook of Mechanical Nanostructuring*. John Wiley & Sons.

Angelo, P. C. and R. Subramanian. 2008. *Powder Metallurgy: Science, Technology and Applications.* PHI Learning. 22-23

Argonne National Laboratory. 2009. *Argonne scientists discover new platinum catalysts for the dehydrogenation of propane.* Available: http://www.anl.gov/articles/argonne-scientists-discover-new-platinum-catalysts-dehydrogenation-propane

Askeland, D and W. Wright. 2013. *Essentials of Materials Science & Engineering*. SI Edition. Cengage Learning

Augsburger, L.L and S. W Hoag. 2008. *Pharmaceutical Dosage Forms – Tablets*. Third Edition. CRC Press

Bagwell, R.B, G. L. Messing, P. R. Howell. 2001. J.Mater.Sci.. 6. 1833-1841.

Balaz, P., Achimovicova, M., Balaz, M., Billik, P., Cherkezova- Zheleva, Z.l, Criado, J. M., Delogu, F., Dutkova, E., Gaffet, E., Gotor, F. J., Kumar, R., Mitov, I., Rojac, T., Senna, M., Streletskii, A. and K. Wieczorek- Ciurowa. 2013. Chem. Soc. Rev. 42. 7571 – 7637.

Bettelheim, F., Brown W., Campbell, M. and Farrell, S. 2009. *Introduction to General, Organic and Biochemistry*. Cengage Learning

Blachou, V., Goula, D. and C. Philippopoulos. 1992. *Wet Milling of Alumina and Preparation of Slurries for Monolithic Structures Impregnation*. Industrial & Engineering Chemistry Research. 31. 1.364-369

Bodaghi, M., Mirhabibi, R., Zolfonun, H., Tahriri, M. and M. Karimi. 2008. 81(6). 571-580.

Cardarelli, F. 2008. *Materials Handbook: A Concise Desktop Reference*. Springer Science & Business Media

Callister, W. D. 2007. *Material Science and Engineering: An Introduction* (Seventh Edition). John Wiley and Sons

Campbell, S. J., Kaczmarek', W. A. and G. M. Wang. 1995. *Mechanochemical Transformation of Haematite to Magnetite*. Science. 6(95). 735-738

Chauruka, S. R., Hassanpour, A., Brydson, R., Roberts, K.J., Ghadiri, M and H. Stitt. 2015. *Effect of mill type on the size reduction and phase transformation of gamma-Alumina*. Chemical Engineering Science, Volume 134, Pages 774–783

Chorkendorff, I and Niemantsverdriet, J. W. 2006. *Concepts of Modern Catalysis and Kinetics*. John Wiley and Sons

Colombo, P., Traini, D and F. Buttini. 2012. *Inhalation Drug Delivery: Techniques and Products.* John Wiley and Sons

Cullity, B.D and S.R. Stock. 2001. *Elements of X-Ray Diffraction*. Prentice-Hall Inc. 167-171

Damm C. and Peukert W. 2011. *Mechano-Chemical Radical Formation and Polymerization Initiation during Wet Grinding of Alumina*. Journal of Colloid and Interface Science, 363(1), pp.386-392.

Digne M, Sautet P, Raybaud P, Euzen P, Toulhoat H. 2004. *Use of DFT to achieve a rational understanding of acid-basic properties of [gamma]-Alumina surfaces*. Journal of Catalysis [Internet]. 226(1):54–68

Digne M, Sautet P, Raybaud P, Euzen P, Toulhoat H. 2002 Oct. 1. *Hydroxyl Groups on γ-Alumina Surfaces: A DFT Study*. Journal of Catalysis [Internet]. [Cited 2014 Mar 20]; 211(1):1–5

Duvel, A., Romanova, E., Sharifi, M., Freude, D., Wark, M., Heitjans, P. and M. Wilkening. 2011. The J.Phys.Chem C. 115(46). 22770-22780.

Dwyer, T.; Pesansky, D. U.S. Patent 3,873,350,1975.

Dynys, F.W and J. W Halloran. 1979. 65(9). 442–8.

Fadhel H. B. and Frances C. 2001. *Wet Batch Grinding of Alumina Hydrate in a Stirred Bead Mill*. Powder Technology, 119(2-3), pp.257-268.

Gad, S. C. 2008. *Pharmaceutical Manufacturing Handbook: Production and Processes*. John Wiley and Sons

Gatan Digital Micrograph Offline. 2014. Accessed from the World Wide Web; 6 September 2014. Available: http://www.gatan.com/resources/scripting/demo/

Günther, H. 2013. *NMR Spectroscopy: Basic Principles, Concepts and Applications in Chemistry.* John Wiley and Sons

Hubbard, A. T. 2002. *Encyclopedia of Surface and Colloid Science*. CRC Press

Jefferson D. A. 2000. *The surface activity of ultrafine particles*. Philosophical Transactions of the Royal Society of London Series a-Mathematical Physical and Engineering Sciences, 358(1775) .2683-2692

Juhász Z. A. 2007. *Particulate Science and Technology : An International COLLOID-CHEMICAL ASPECTS OF MECHANICAL ACTIVATION*. Science. 37–41

Kachi, S. Momiyama, K and S. Shimizu. 1963. J. Phys. Soc. Japan 18. 106.

Kim, S.M, Y. J. Lee, K. W. Jun, J. Y. Park, H. S. Potdar. 2007. *Materials Chemistry and Physics.* 104(1). 56–61.

Knozinger, H and P. Ratnasamy. Catal. 1978. Rev .Sci. Eng. 17. 31-70.

Kostic, E., Kiss, J., Zec, S., and S. Boskovic. 2000. *Powder Technology*. 107. 48–53

Kwan, C.C., Mio, H., Chen, Y. Q., Ding, Y. L., Saito, F., Papadopoulos, D., Bentham, A. C and M. Ghadiri. 2005. Chemical Engineering Science. 60(5). 1441–8

Levin, I., Bendersky, L. A., Brandon, D. G. and M. Ruhle. 1997. *Cubic to Monoclinic Phase Transformations in Alumina*. Acta mater. 9. 3659-3669

Liu S. F., Zhang L. G. and An L. N. 2005. *Phase Transformation of Mechanically Milled nano-sized Gamma-Alumina*. Journal of the American Ceramic Society. 88. 9. 2559-2563

Liu, R. 2008. *Water-Insoluble Drug Formulation*: Second Edition. CRC Press

Lloyd, L. 2011. *Handbook of Industrial Catalysts*. Springer Science & Business Media

Lü, L and M. O. Lai. 2013. *Mechanical Alloying*. Springer Science & Business Media. New York

McPherson, R. 1973. *Formation of metastable phases in flame and plasma-prepared Alumina*. Journal of Materials Science. 8. 851-858

Midoux, N. and P. Hosek. 1999. Powder Technology. 2–9

Mio, J.K.H., Saito, F. and M. Miyazaki. 2001. Science. 14(10). 1213–23

Neikov, O. D., Naboychenko, S., Mourachova, I. B., Gopienko, V. G., Frishberg, I. V. and D. V. Lotsko. 2009. *Handbook of Non-Ferrous Metal Powders: Technologies and Applications*. Elsevier. 56-62

Oberlander, K. 1984. *Applied Industrial Catalysis*. Academic Press. New York. 63. 9

Paglia G., Buckley C. E., Rohl A. L., Hart R. D., Winter K., Studer A. J., Hunter B. A. and J. V. Hanna. 2004a. Boehmite *Derived γ-Alumina System. 1. Structural Evolution with Temperature , with the Identification and Structural Determination of a New Transition Phase , γ ′ -Alumina*. Chem. Mater. 13. 220–236

Paglia G., Buckley C. E., Udovic T. J., Rohl A. L., Jones F., Maitland C. F. and J. Connolly. 2004b. *Boehmite-Derived γ-Alumina System. 2. Consideration of Hydrogen and Surface Effects*. Chem. Mater.16. 1914-1923

Panalytical B.V. Highscore with Plus Option. 2014. Accessed from the World Wide Web; 3 September 2014. <http://www.panalytical.com/Xray-diffraction-software/HighScore-with-Plus-option.htm>

Pourghahramani, P., Altin E., Mallembakam M. R., Peukert W. and Forssberg E. 2008. *Microstructural Characterization of Hematite during Wet and Dry Millings using Rietveld and XRD line Profile Analyses*. Powder Technology, 186(1), pp.9-21.

Rahman, A., Choudhary M. I. and A. Wahab. 2015. *Solving Problems with NMR Spectroscopy.* Academic Press

Ramesh, K. T. 2009. *Nanomaterials: Mechanics and Mechanisms.* Springer Science and Business Media

Regalbuto, J. 2006. *Catalyst Preparation: Science and Engineering*. CRC Press

Reid, C. B., Forrester, J. S., Goodshaw, H. J., Kisi, E. H., and G. J. Suaning. 2008. Ceramics International. 34(6). 1551–6.

Richerson, D and W. E Lee. 2005. *Modern Ceramic Engineering: Properties, Processing, and Use in Design:* Third Edition. CRC Press

Rosenqvist, T. 2004. *Principles of Extractive Metallurgy*. Tapir Academic Press. 177

Rozita Y., Brydson R. and Scott A. J. 2010. *An Investigation of Commercial Gamma-Al2O3 Nanoparticles*. Journal of Physics: Conference Series. 241. 12096

Rozita, Y., Brydson, R., Comyn, T. P., Scott, A., Hammond, C., Brown, A., Chauruka, S., Hassanpour, A., Young, N. P., Kirkland, A.I., Sawada, H., and R. I. Smith. 2013. ChemCatChem. 2695-2706

Šepelák, V., Indris, S., Heitjans, P. and K. D. Becker. 2007. Journal of Alloys and Compounds. 776–778

Sinha K. P. and A. P. B. Sinha. 1956. *Vacancy Distribution and Bonding in some Oxides of Spinel Structure*. Acta Crystallogr. 47. 617–630

Somasundaran, P. 2006. *Encyclopedia of Surface and Colloid Science*. CRC Press

Sopicka-Lizer, M. 2010. *High-Energy Ball Milling: Mechanochemical Processing Of Nanopowders.* Elsevier. 1-13.

Stenger F., Mende S., Schwedes J. and Peukert W. 2005a. *The Influence of Suspension Properties on the Grinding behaviour of Alumina Particles in the Submicron Size Range in Stirred Media Mills.* Powder Technology, 156(2-3), pp.103-110.

Stenger F., Mende S., Schwedes J. and Peukert W. 2005b. *Nanomilling in Stirred Media Mills*. Chemical Engineering Science, 60(16), pp.4557-4565.

Tonejc, A. M. Tonejc, D. Bagovid, C. Kosanovid. Materials Sci and Eng. 1994. 182. 1227–31.

Trueba, M. and S. P. Trasatti. 2005. *γ-Alumina as a Support for Catalysts: A Review of Fundamental Aspects*. European Journal of Inorganic Chemistry. (17). 3393–3403. Available from: http://doi.wiley.com/10.1002/ejic.200500348

Tsuchida, T., Furuichi, R. and T. Ishii. 1980. *Kinetics of the dehydration of boehmites prepared under different hydrothermal conditions*. Thermochimica Acta. 39. 103–115

Varin, R. A, Czujko, T. and Z. S. Wronski. 2009. *Nanomaterials for Solid State Hydrogen Storage*. Springer Science & Business Media. New York

Wadhwa, A. S. and H. S. Dhaliwal. 2008. *A Textbook of Engineering Material and Metallurgy*. Firewall Media

Wang, Y. and C. Suryanarayana. 2005. L. An. J. Am. Ceram. Soc. 88. 780–783

Wang Y. G., Bronsveld P. M., Dehosson J. T. M., Mcgarry D. and S. Pickering. 1998. *Ordering of Octahedral Vacancies in Transition Aluminas*. 81. 1655–1660

Wefers, K. 1990. *Alumina Chemicals: Science and Technology Hand- book*. The American Ceramic Society. Westerville, Ohio. 13.

Wilson S. J. 1979. *The Dehydration of Boehmite, γ-AlOOH, to γ-Al_2O_3*. Journal of Solid State Chemistry. 1. 247–255

Wilson S. J. and J. D. C. Mc Connell. 1980. *A Kinetic Study of the System γ-AlOOH/Al_2O_3*. Journal of Solid State Chemistry. 34. 315-322

Zhou, R. S and R. L. Snyder. 1991. *Structures and Transformation Mechanisms of the η, γ and θ Transition Aluminas*. New York. 2(2)

Zielin´ski, P. A., Schulz, R., Kaliaguine, S. and A. Van Neste. 1993. J. Mater. Res. 8. 2985–2992.

Appendix A

A.1 Stress Energy Comparison between SBM and PBM

A comparative analysis of the effect of energy on the lattice strain, relative intensity and crystallite size on the material in the PBM and SBM was carried out. This was done after data analysis of XRD diffractograms obtained from SBM and PBM milling. The SBM sample analysed is the 1200 min milled sample discussed in Chapter 4 and the PBM sample is the 300 min sample also discussed in Chapter 4. This was done to attempt to further understand the effects of milling energy on the crystal structure of the material.

A.1.1 Lattice Strain

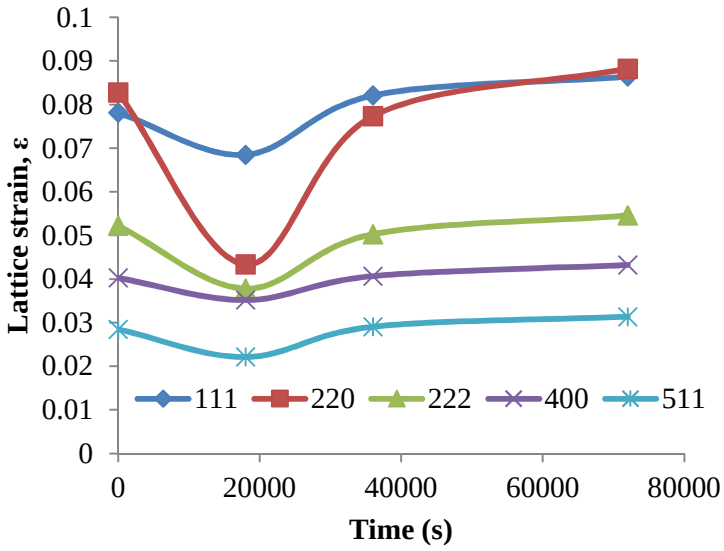

Figure A1: Lattice strain in various planes in the SBM milled sample derived from XRD difractograms

It can be observed from Figure A1 that the most affected plane is the (220) reflection. The largest effect happens in the first 300 min of milling which suggests that the microstructural surface effects happen in the initial stages of milling. This coincides with observations made in Chapter 6 where the surface planes of γ-Al_2O_3 are the most affected by milling energy. The peaks represented in Figure A1 are for γ-Al_2O_3 as the material is predominantly γ-Al_2O_3 after SBM milling. Figure A2 shows peaks from α-Al_2O_3 as it is the predominant phase in the sample. It can be observed that lattice strain increases in the (111) plane signifying that milling energy affects this plane the most. This is expected as the observations from Chapter

6 have shown that phase transformation from γ-Al_2O_3 to α-Al_2O_3 occurs at the surface of the material. As the SBM sample does not result in phase transformation, it is possible that energy supplied by the SBM is not enough propagate the phase transformation. Longer milling times have not been investigated and therefore cannot be commented on.

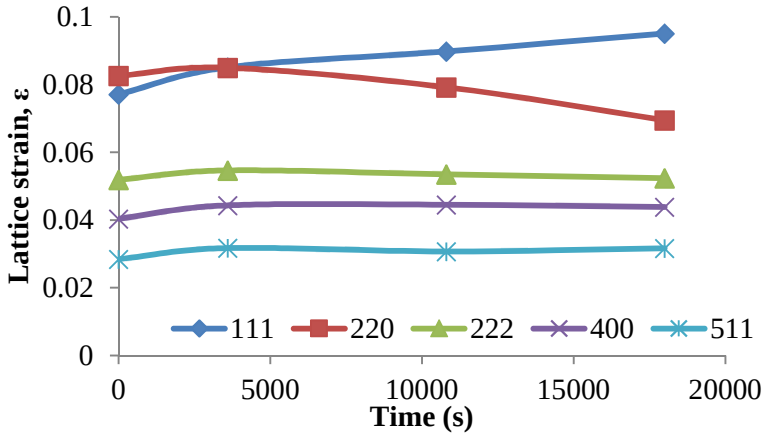

Figure A2: Lattice strain in various planes in the PBM milled sample derived from XRD difractograms

A.1.2 Average Relative Intensity

The average relative intensity can show any changes to peak intensities. This can reflect changes to the crystal structure of a material although it can also be affected by stronger peak intensities of a material with a mixture of very small and very large crystals. Figure A3 shows that in the planes analysed, there was no effect to the average relative intensity after milling. This is expected as there was no phase change in the material.

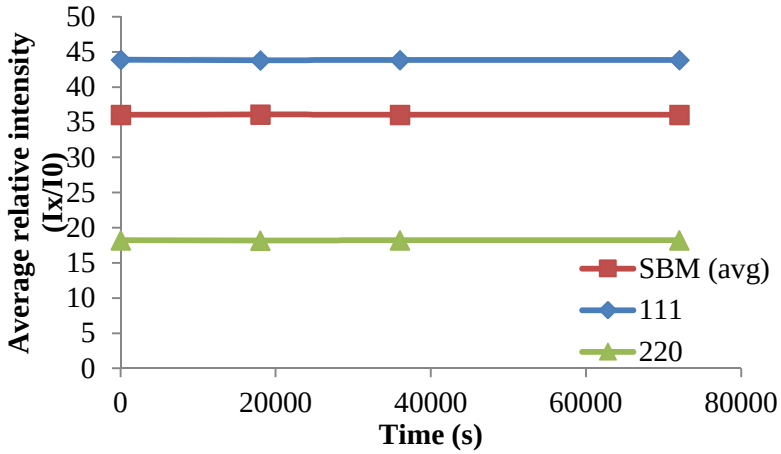

Figure A3: Average relative intensity in various planes in the SBM milled sample derived from XRD difractograms

Figure A4 shows the average relative intensities of the same γ-Al_2O_3 peaks after milling in the PBM. It can be observed that the average relative intensity decreases with an increase in milling time which shows that the γ-Al_2O_3 crystals appear to reduce in size. This may well be an effect of the intensities of the larger α-Al_2O_3 crystals that emerge in the sample. Further analysis can be carried out by an analysis of crystallite size from the individual peaks. Crystal size refinement can also occur in crystals of γ-Al_2O_3 that have not transformed.

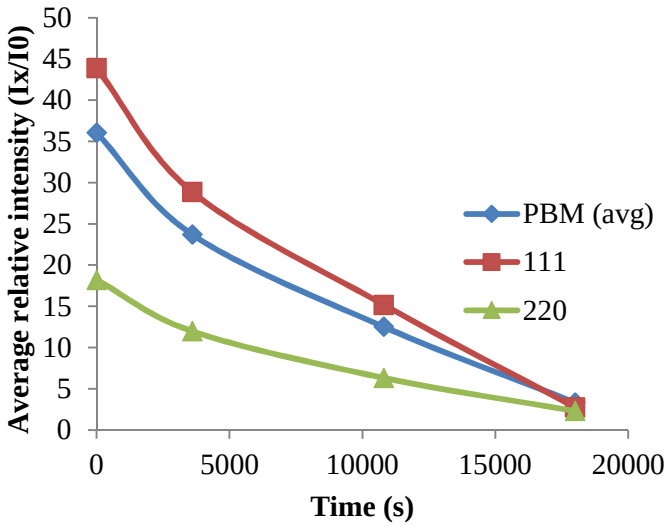

Figure A4: Average relative intensity in various planes in the PBM milled sample derived from XRD difractograms

A.1.3 Crystallite Size

The crystallite sizes on the different reflections in the SBM milled sample are shown in Figure A5. It can be observed that the crystallite size increases in the (220) reflection. This coincides with surface effects observed in milled samples in Chapter 6. The crystallite size increase can be linked to shift of planes from ccp to hcp structure on the Al rich surfaces of γ-Al_2O_3. These result in crystal enlargement and reflect as larger crystals in XRD analysis. This may also be linked to the suggestion of crystal coarsening mentioned in Bagwell *et al* (2001).

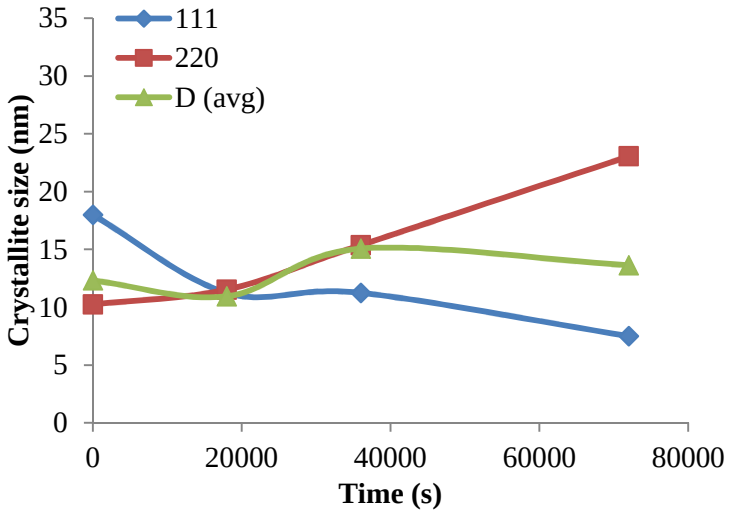

Figure A5: Crystallite sizes of various planes in the SBM milled sample derived from XRD difractograms

Figure A6 shows the crystallite sizes of reflections in the PBM sample. It can be observed that the crystallites initially grow in size in the first 60 minutes and then refine to smaller sizes. The same as for SBM samples can be said for the PBM samples. During transformation, when the critical resolved shear stresses of the affected planes is reached, the atoms shift from ccp to hcp at surface planes resulting in the formation of larger crystals. Further milling energy refines the sizes of these crystals. Crystal refinement of α-Al_2O_3 has also been observed in Chapter 6 during seeded milling experiments.

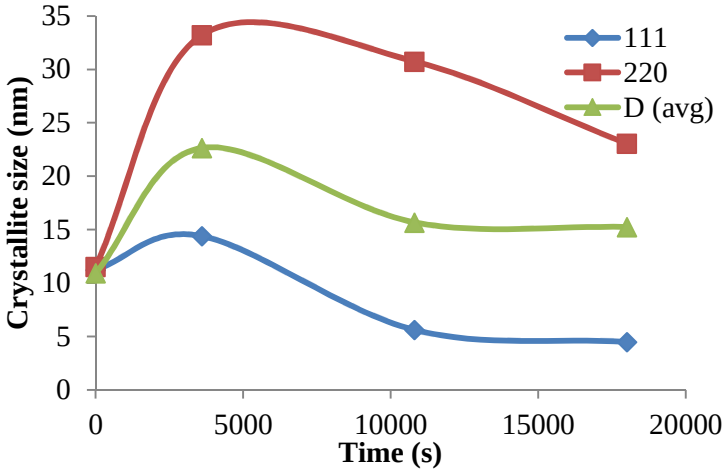

Figure A6: Crystallite sizes of various planes in the PBM milled sample derived from XRD difractograms